
Binding of Proteins to Nanoparticles in Complex Fluids Probed by Fluorescence Correlation Spectroscopy

Judith Julia Mittag



München 2017

Binding of Proteins to Nanoparticles in Complex Fluids Probed by Fluorescence Correlation Spectroscopy

Judith Julia Mittag

Dissertation
zur Erlangung des Grades
Doktor der Naturwissenschaft (Dr. rer. nat.)
an der Fakultät für Physik
der Ludwig–Maximilians–Universität
München

vorgelegt von
Judith Julia Mittag
aus Regensburg

München, den 01.03.2017

Erstgutachter: Prof. Dr. Joachim O. Rädler

Zweitgutachter: Prof. Dr. Jan Lipfert

Tag der mündlichen Prüfung: 12.04.2017

Contents

Zusammenfassung	vii
Abstract	ix
1 Motivation	1
2 Fluorescence Correlation Spectroscopy	5
2.1 Photoluminescence	5
2.2 Fluorescence Correlation Spectroscopy	7
3 Analysis of Binding Affinity Reactions	23
3.1 Law of Mass Action and Binding Constants	23
3.2 Association and Dissociation Rates	26
3.3 Strength of Binding and Strong Binding Model	28
3.4 Binding Probed by Fluorescence Correlation Spectroscopy	29
3.5 Binding Probed by Microscale Thermophoresis	30
4 Proteins and Plasma	35
4.1 Biomolecular Corona	35
4.2 Plasma Proteins	37
4.3 Amyloidogenic Proteins	40
4.4 Blood Plasma and Serum	42
4.5 Viscosity of Mixtures of Fetal Bovine Serum and Phosphate Buffered Saline	43
5 Interaction of Proteins with Solid Nanoparticles	47
5.1 Solid Nanoparticles	47
5.2 Understanding the Kinetics of Protein-Nanoparticle Corona Formation . .	49
5.3 Hierarchy of Protein Nanoparticle Binding Affinities	58

6	Thermosensitive Liposomes as Drug Delivery Systems	69
6.1	Motivation	69
6.2	Evaluation of Basic Parameters of Thermosensitive Liposomes	71
6.3	Release from Thermosensitive Liposomes	75
6.4	Binding of Proteins to Thermosensitive Liposomes and its Reversibility . .	79
6.5	Conclusion	82
7	Protein Self-assembly in Health and Disease	85
7.1	Background on Self-assembly	85
7.2	Quantification of Amyloid β_{1-42} Fibrillogenesis Using FCS	88
7.3	Quantitative Study of α -synuclein Aggregates	94
8	Conclusion and Future Prospects	101
	Publications and Manuscripts	107
P1	· Understanding the Kinetics of Protein-Nanoparticle Corona Formation . .	109
M2	· Hierarchy of Protein Binding to Nanoparticles	125
M3	· Impact of Plasma Protein Binding on Cargo Release by Thermosensitive Liposomes Probed by Fluorescence Correlation Spectroscopy	141
P4	· Simultaneous Measurement of a Range of Particle Sizes During Abeta Fibrillogenesis Quantified Using Fluorescence Correlation Spectroscopy .	155
M5	· Peptide Self-assembly Measured by Fluorescence Correlation Spectroscopy	163
P6	· Quantitative Thermophoretic Study of Disease-related Protein Aggregates	173
	Abbreviations	191
	Bibliography	195

Zusammenfassung

Der Einsatz von Nanomaterialien für den zielgerichteten Medikamententransport ist ein Schwerpunkt aktueller Forschung. Wenn Nanopartikel (NP) mit Proteinen in Kontakt kommen, können diese auf den NP adsorbieren und bilden eine Schicht, die Proteinkorona, die die Wechselwirkungen des NP mit seiner Umgebung steuert. Für die Entwicklung von Nanotransportern ist es daher von Interesse, die Bindung von Proteinen an NP, den Effekt der adsorbierten Moleküle auf die Funktionsweise des NP und die Wechselwirkung von Proteinen miteinander zu verstehen. Quantitative Messungen dieser molekularen Wechselwirkungen sind für das optimale Design neuartiger Arzneimittel und Diagnoseverfahren von großer Bedeutung.

In dieser Arbeit wird die Kinetik der Proteinkorona-Bildung mittels Fluoreszenzkorrelationspektroskopie (FCS) untersucht. Die Technik erlaubt die Bestimmung der hydrodynamischen Größe und des Anteils an gebundenen Proteinen bei geringem Materialverbrauch sowie der Möglichkeit in komplexen physiologischen Flüssigkeiten wie Blutplasma oder -serum zu messen.

Im ersten Teil wurde die Entwicklung der Korona von Festkörper-NP in einem sich über die Zeit ändernden Modellplasma untersucht. Die Ergebnisse von Einzelprotein-NP-Experimenten dienten als Startparameter für den kombinierten Simulations-Theorie-Ansatz. Es wurde gezeigt, dass die auf Nicht-Langmuir-Differentialratengleichungen (NLDRE) beruhende Theorie die Entwicklung der experimentell bestimmten Proteinkorona auf Siliziumoxid-NP unter kompetitiver Proteinbindung vorhersagen kann. Der Nachweis eines "memory" Effekts der Korona während ihrer Weiterentwicklung durch sich verändernde Umgebungsbedingungen wurde erbracht.

Darauf aufbauend wurde eine systematische Untersuchung von Einzelprotein-NP Wechselwirkungen mit repräsentativen Proteinen und NP durchgeführt. Das Ziel ist, die Erstellung einer Datenbank solcher Wechselwirkungen in Kombination mit Modellen, wie dem in der vorherigen Studie verwendeten. Dies könnte Vorhersagen über die

Bildung der Proteinkorona erlauben. Drei Interaktionsklassen wurden identifiziert: Aggregation, starke Bindung und schwache bzw. keine Bindung. Die aggregierenden Kombinationen sind für die quantitative Analyse nicht zugänglich, wohingegen sich die Bindung und Desorption der starken Binder charakterisieren ließ. Die Desorptionsraten in Gegenwart von Serum wurden bestimmt und mit der hierarchischen Ordnung der Bindungsaffinitäten verknüpft. Dies ermöglicht erste Annahmen darüber wie diese NP im Körper reagieren und ob sie ihren Wirkstoff zielgerichtet transportieren könnten.

Aufgrund ihrer Eigenschaft eingekapselte Arzneimittel zielgerichtet freizusetzen und damit eben jenen zielgerichteten Transport zu erlauben, gelten thermosensitive Liposomen (TSL) als vielversprechende Nanotransporter. Allerdings ist die Untersuchung der Auswirkungen von Proteinen auf den Abgabemechanismus und die Freisetzung notwendig, um die Dosierung zu kontrollieren und eine unspezifische Abgabe zu vermeiden. Deshalb wurde ein neuartiger Test für die Quantifizierung der temperaturabhängigen Freisetzung für TSL entwickelt und validiert. Um zu klären, ob die Anwesenheit von Proteinen das Verhalten bei gesteuerter Freisetzung verändert, wurden die Freisetzungsprofile von TSL in Puffer, Serum oder Plasma verschiedener Spezies sowie in Einzelproteinlösungen gemessen. Die Bindungsaffinitäten von Blutproteinen und die Reversibilität ihrer Bindung wurden bestimmt. Eine mögliche Korrelation zwischen dem Abgabeverhalten und den Bindungsaffinitäten wurde untersucht.

Bei der Entstehung von Amyloidosen spielt das Auftreten von intermediären Aggregaten während der Selbstorganisation von amyloidogenen Proteinen eine entscheidende Rolle. Trotz ihrer Bedeutung ist die Kinetik dieses Prozesses noch nicht gut verstanden. So wurde in dieser Arbeit FCS verwendet, um die Selbstorganisation über die Zeit zu charakterisieren. Zu diesem Zweck wurde ein neuer Auswertalgorithmus zur gleichzeitigen Analyse einer Reihe von Teilchengrößen, das Gaussian Distribution Modell (GDM), implementiert und durch den Vergleich mit dem etablierten MEMFCS-Algorithmus validiert. Dieser Ansatz könnte auf α -Synuclein übertragen werden, das als Modellsystem bei der Weiterentwicklung der Thermophorese von Polymeren in Elektrolytlösungen diente. FCS lieferte hierzu komplementäre Parameter wie die Größe und die Diffusionskonstanten verschiedener α -Synuclein-Multimere. Die Kombination von FCS und Thermophorese könnte zum Verständnis auf dem Gebiet der Amyloidosen beitragen. FCS ermöglichte die Bestimmung von Bindungsaffinitäten, Desorptionsraten und Größenverteilungen und damit ein besseres biophysikalisches Verständnis der Wechselwirkungen von Proteinen und NP sowie Proteinen untereinander.

Abstract

Current research focuses on the usage of nanocarriers as specifically acting, targeted drug delivery vehicles. When proteins are present in conjunction with nanoparticles (NPs) they adsorb to them, forming a layer called the protein corona, which controls the interactions of the NP with their environment. Thus, for the development of nanocarriers it is of interest to understand binding of proteins to NPs, the impact of the adsorbed molecules on the functioning of the NP and the interaction of proteins with each other. A quantitative measurement of these molecular interactions is of eminent importance to the rational design of novel drug and diagnostic tools.

In this thesis, the kinetics of the protein corona formation are investigated using fluorescence correlation spectroscopy (FCS). The technique provides a means to determine the hydrodynamic size and the fraction of bound proteins, with the advantage of low sample consumption, as well as the possibility to measure in complex physiological fluids, e.g. blood plasma or serum.

In the first part, the development of the corona of solid NPs in a temporally changing model plasma was studied. The results of single protein-NP experiments served as input for the combined simulation-theory approach. It was demonstrated that non-Langmuir differential rate equation (NLDRE) theory is capable of predicting the evolution of the experimentally determined protein corona on silica NPs under competitive protein binding conditions. Evidence of “memory” in the evolution of the corona was found upon changes in the molecular composition of the environment, which would have significant implications for medical applications.

Building on this, a systematic study of single protein-NP interactions was performed using representative proteins and NPs. The goal here is the creation of a database of such interactions combined with models, such as e.g. the one used in the previous study, which would eventually allow predictive power concerning the protein corona formation. Three classes of interactions were identified: aggregation, strong binding,

and weak or no binding. While the class of aggregating combinations is not accessible to quantitative evaluation, the binding and desorption were characterized for strong binders. Desorption rates were measured in the presence of serum and linked to the hierarchical order of the binding affinity enabling first assumptions on how these NPs would react in the body and whether they would be capable of delivering a payload to a specific site.

This possibility of specificity is also why thermosensitive liposomes (TSLs), which are capable of controlled release of the encapsulated drug, are seen as promising nanocarriers. However, evaluation of the impact of proteins on the trigger mechanism and release is necessary for controlling the dosage and avoiding non-specific release in the final application. Thus, a novel assay for the quantification of the temperature-dependent release for TSLs was established and validated as part of this thesis. To clarify whether the presence of proteins alters the behavior upon intentional release, the release profiles of TSLs were measured in buffer, serum or plasma from different species, as well as in single-protein solutions. The binding affinities of blood proteins and the reversibility of their binding were determined. A possible correlation between the release behavior and the binding affinities was probed.

In the development of amyloidosis, the appearance of intermediated sized species during self-assembly of amyloidogenic proteins plays a crucial role. Despite its importance, the kinetics of this process are not yet well understood. Thus, in this thesis FCS was used to characterize this self-assembly process over time. To this end, a novel fitting algorithm to enable the simultaneous measurement of a range of particle sizes, the Gaussian distribution model (GDM), was implemented and validated by comparison to the established MEMFCS algorithm. This approach, could be applied to α -synuclein (α -syn) which served as a model system in the further development of thermophoresis of polymers in electrolyte solutions. FCS provided complementary data and parameters such as size and the diffusion constants of different species of α -syn. The combination of FCS and thermophoresis might contribute to progress in the field of amyloid diseases.

FCS enabled the determination of binding affinities, desorption rates and size distributions, and thus, a better biophysical understanding of interactions of proteins and NPs and of proteins with each other in complex fluids.

Chapter 1

Motivation

Nanomaterials are part of our modern, everyday life. In industry, they are employed as catalysts, photovoltaic devices or for gas storage [1–3]. In addition to regular debates on limits for fine dust and their related health risks, the potential hazards of NPs that are present in food are heatedly discussed [4–6]. For instance, silicon dioxide (E551) is added as an anti-caking agent to powdery food such as dried spices, salt or instant soups, or as a flow enhancer in ketchup. Titania (E171) is applied to make the coating of chocolate more shiny, but also acts as a sun blocker in sunscreen. In cosmetics, NP are used to increase the stability of products or to improve absorption of nutrient-enriched skin care products [7].

The characterization of all of these materials is of key importance in terms of nanosafety and precaution, however, this aspect is not always considered and NPs are used as additives without intense scientific testing for potential hazards. Furthermore, it is not only bare nanomaterials whose physico-chemical characteristics need to be considered in such studies. There is growing evidence that the molecules that adsorb to the NP's surface, building the so-called "biomolecular corona", dominate the interactions of the nanomaterial with its environment and thus influence the fate of the NP within living organisms (Figure 1.1) [8–11]. For example, if certain signaling proteins bind to the NP, cellular uptake can be enhanced for specific types of cells [12]. This impact of the corona is negative if the NP has a suspected toxic effect, but it can be positive as well if the NP is being used as a drug nanocarrier that reaches its target area in this way. It is not yet understood how the physico-chemical properties of NP and the proteome of the medium affect the composition of the protein corona and how the protein corona is built upon first contact with biological fluids. The underlying mechanisms of the following evolution of

the corona over time and with change of the surrounding environment, while traveling through the body, are under discussion as well.

There is phenomenological evidence that all of these processes take place, but they are far from being understood in a way that they can be controlled and applied in a target-oriented manner. In the beginning, a better knowledge of basic patterns and principles of these combined effects might help to at least classify nanomaterials.

Insights into these interactions are, moreover, of interest for deliberate administration in medical applications of nanomaterials such as thermosensitive liposomes (TSLs). Due to their versatility, NPs enjoy great popularity in medicine, pharmacology and related life sciences. A lot of effort is put into developing novel smart drug nanocarriers [13–17]. For instance, NPs offer the possibility to transport water insoluble drugs, their surface can be decorated with molecules that allow a targeted delivery of drugs or they can be used as contrast agents [18]. In many cases, several of these functions can be united in a single NP. In addition to issues regarding the corona composition, questions of how to use NPs effectively as a delivery vehicle are of interest: How can a drug be loaded into a drug nanocarrier? How does the drug stay inside the NP during movement to the target region? How does one go about designing targeting? How can the release be controlled? How does the corona affect the transport and the release? How do NPs interact with cells? How do NPs pass biological barriers such as the blood-brain barrier?

Such multi-faceted questions call for versatile tools and efforts from mixed research disciplines including physics. The evaluation and quantification of many of the listed topics may be tackled effectively by *in vitro* experiments using fluorescence correlation spectroscopy (FCS). FCS is a highly sensitive optical technique used to study interactions of fluorescently labeled molecules on a single molecule level in strongly diluted solutions. A broad range of research issues are addressed by FCS, such as the determination of the size of complexes, the determination of the concentration of proteins in solution, or studies of chemical reactions such as binding or cleavage or the interaction of NP with proteins [19–22]. Since only small sample sizes with concentrations in the pico- to nanomolar range are needed, FCS is highly attractive for expensive or rare materials. Additionally, this also leads to a high sensitivity. Apart from these extremely dilute conditions, its "non-invasiveness" is a further advantage of FCS. This means that the act of measuring hardly affects the sample. This fact makes FCS an ideal tool for measuring processes that are easily influenced in an undesired way by changes in their environment.

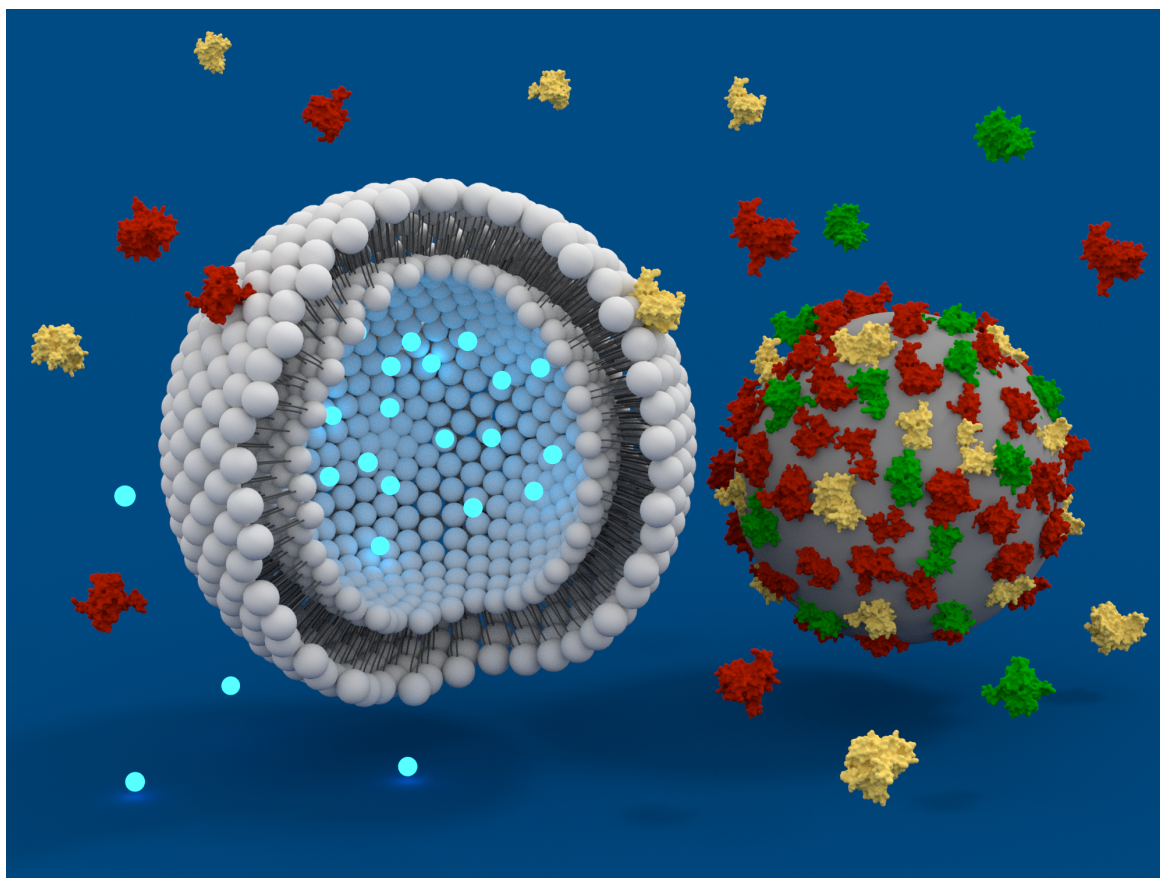


Figure 1.1: Biomolecules form a corona by adsorption to a solid NP and a liposome filled with a fluorescent dye in a biological fluid. The release of dye from the liposome is indicated. The identity of the NPs is formed by the corona which interacts with the biological environment. The relevance of the layer of adsorbed proteins has been seen in biomaterial implants and cell scaffolds.

One of these processes is the self-assembly of proteins. Understanding this is relevant on multiple levels. On the one hand, self-assembly of amyloidogenic proteins such as amyloid beta ($A\beta$) or α -synuclein (α -syn) play a pivotal role in the onset of severe neurodegenerative diseases such as Alzheimer's or Parkinson's Disease. In order to find effective therapeutic approaches, the underlying protein-protein interactions need to be quantified and related to the clinical picture. On the other hand, the structures built, the so-called amyloid fibrils, are highly ordered and enormously stable. Understanding and control of the self-assembly process would allow construction of artificial nanostructures with these properties [23–26]. For instance, hybrid membranes to remove heavy metal ions and radioactive waste from water are constructed from protein amyloid fibrils and

activated porous carbon and the size of nanotubes that self-assemble in a similar way as amyloid fibrils do, could be controlled.

In this thesis, FCS is applied to elucidate the aggregation kinetics of $A\beta$ (Chapter 7). For this purpose a novel fitting algorithm for the analysis of polydisperse systems is introduced. In Chapter 6, an innovative approach to quantify the release of TSLs at low temperatures is suggested. The binding of plasma proteins as well as their impact on the release profile are investigated. The interactions of proteins and solid NPs are the focus of Chapter 5. An approach that combines experiments with simulations and theory that paves the way for a deeper understanding of the kinetics of the biomolecular corona is presented. In order to perform and analyze experiments in complex fluids, such as body fluids, correctly, the physical properties of mixtures of phosphate buffered saline (PBS) and fetal bovine serum (FBS) are determined (Chapter 4).

Chapter 2

Fluorescence Correlation Spectroscopy

The focus of this dissertation lies on binding measurements. FCS is a highly sensitive optical technique that enables gaining information on interactions such as binding or cleavage of fluorescent molecules or particles in highly diluted solutions. Translational or rotational diffusion are further dynamics that become accessible to FCS. In order to study them, these processes need to cause fluctuations in the local concentration of particles leading to measurable changes in the fluorescence intensity. Under the assumption of a uniform illumination of the sample volume, even measurements in complex media such as blood plasma, cells or bacteria are possible [27]. In this chapter, the basic principles of fluorescence and FCS, as well as different approaches to data analysis are presented.

2.1 Photoluminescence

Photoluminescence denotes a process during which a physical system like a molecule is excited by incoming photons of a specific wavelength, followed by the emission of red-shifted photon during relaxation to the ground state S_0 . The absorption of light occurs very fast, on the order of femtoseconds. There are two types of photoluminescence: fluorescence and phosphorescence. These processes differ by the pathway the excited electron uses to return to the ground state S_0 as summarized by a Jablonski diagram (Figure 2.1). Fluorescence describes the transition from the excited singlet state S_1 to the ground state S_0 under the emission of a photon. This process occurs very fast (typical lifetime of $S_1 \sim 0.5 - 20$ ns) and therefore the emission of light ends quasi immediately after turning off the source of excitation [28]. In Figure 2.1 this process is indicated by the dark green arrow.

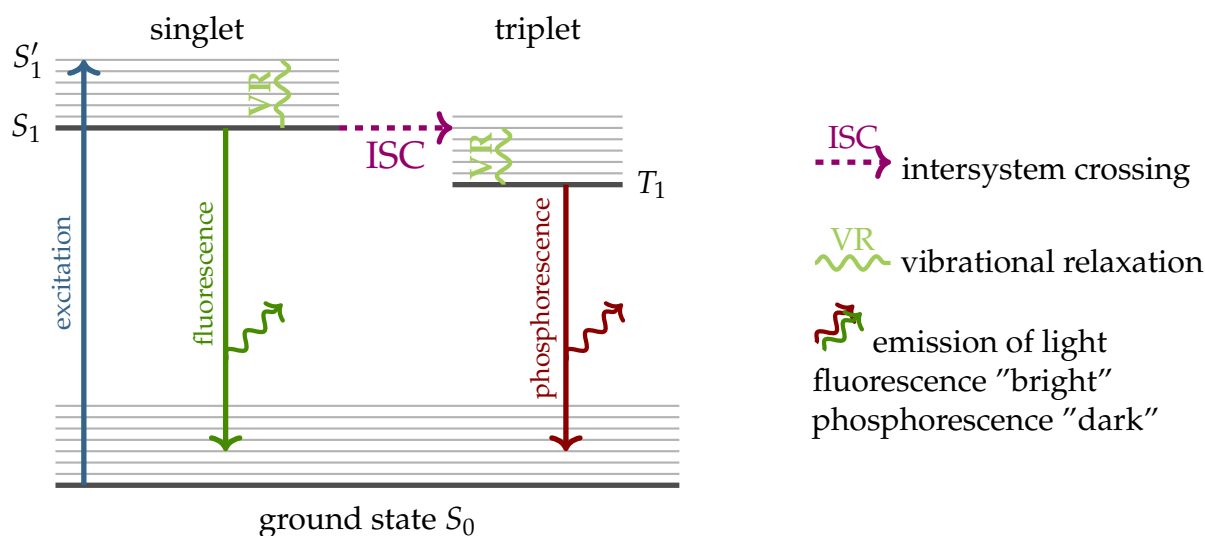


Figure 2.1: Jablonski diagram. By absorption of a photon, a system is excited to a higher energy level in the singlet state S_1' (blue). Due to subsequent internal radiationless vibrational relaxation processes (VR), the molecule reaches the excited relaxed singlet state S_1 . The direct transition from S_1 to the ground state S_0 while emitting a photon is termed fluorescence (green). The intersystem crossing (ISC) to the triplet state T_1 and the subsequent quantum mechanically prohibited transition to the ground state S_0 during emission of a photon is called phosphorescence (dark red).

Phosphorescence includes the intersystem crossing (ISC) from the lowest excited singlet state S_1 via the state T_1 to the ground state S_0 (see Figure 2.1, dark red arrow). The transition from T_1 to S_0 is quantum mechanically prohibited, which results in a long lifetime of the state T_1 . During the period of time which the electron spends in the triplet state T_1 , no light is emitted ($\lesssim 10 \mu\text{s}$), and the molecule cannot be excited again. Thus, the system is situated in an “optical dark state” [29]. This effect is the origin of blinking of a fluorophore while it diffuses through the observation volume (see Section 2.2.4). Phosphorescence takes place on a much longer timescale than fluorescence (milliseconds to seconds *versus* nanoseconds), since the electron remains in the triplet state longer than in the excited singlet state. An afterglow can be detected, after turning off the exciting light.

The so-called Stokes shift describes the difference in the exciting and the emitted wavelength. In most cases, a system absorbs more energy than is actually needed to reach the lowest excited state S_1 , so the system is excited to a higher energy level S_1' . A molecule reaches the excited relaxed singlet state S_1 by radiationless processes such as vibrations or rotations within picoseconds [28]. In this way, energy is released and the subsequently

reduced energy the red-shift in the wavelength from incoming to emitted light is caused. This phenomenon allows distinguishing and separating light used for excitation and fluorescent light. Further factors which may influence the characteristics of the Stokes shift are interactions of the excited fluorophores with solvents or the formation of complexes.

2.2 Fluorescence Correlation Spectroscopy

2.2.1 Experimental Background of FCS

An exemplary set-up of a fluorescence correlation spectroscope is shown in a schematic representation in Figure 2.2. A confocal microscope provides the foundation of the set-up. Laser light with a specific wavelength is directed via a dichroic mirror into the objective of the microscope to excite the fluorophores inside the sample. The objective obtains a high numerical aperture ($NA > 0.9$) to achieve a small focal spot size. Typically, water immersion objectives are used because of their high numerical apertures and their better resolution. The laser light is focused into the sample, where fluorescent molecules that cross the illuminated volume are excited. The fluorescence light emitted from these molecules is guided back to the dichroic mirror along the same path. In order to separate remaining laser light from fluorescence light, an emission filter is used. Finally, the fluorescence light is focused through a pinhole onto an avalanche photodiode (APD). The pinhole is positioned in the image plane to reject light that does not originate from the observation volume. Thus, only fluctuations from within the confocal volume are measured. A hardware correlator correlates the intensity fluctuations to obtain the autocorrelation curves $G(\tau)$. These data sets can be further analyzed by adequate fitting algorithms to extract physically relevant parameters such as the diffusion constant D or the concentration c .

The size of the detection volume is typically below 1 fl. Its shape is an ellipsoid, but its exact size depends on the properties of the specific set-up used (laser and pinhole diameter). The structure parameter S describes the proportions of the diffraction-limited three dimensional observation volume (inset in Figure 2.2). A low concentration of fluorescent molecules is desirable to obtain clear variances in the fluctuating fluorescence signal. With increasing number of particles inside the confocal volume, the relative fluctuations are less pronounced. In the ideal case, only a small number of particles

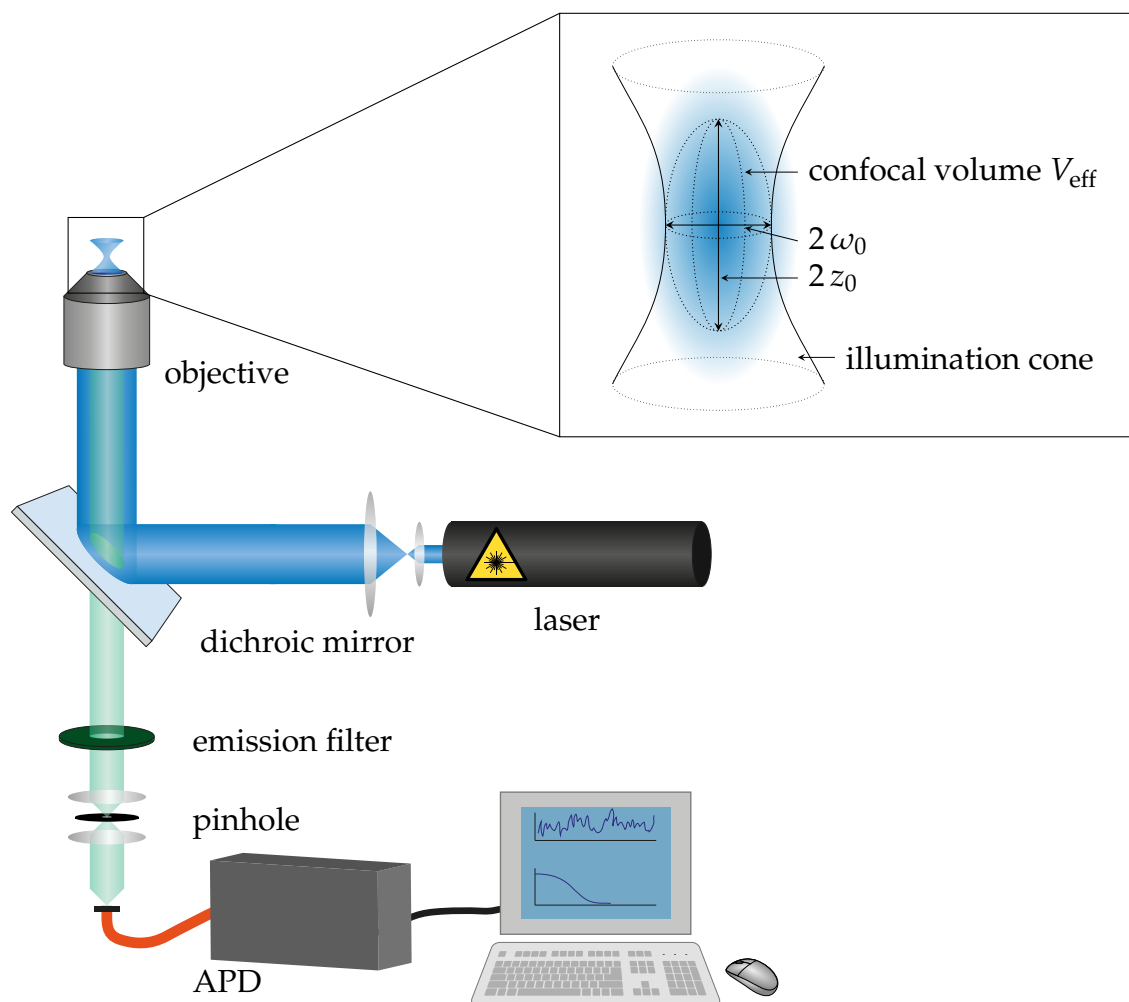


Figure 2.2: Schematic representation of the set-up of a fluorescence correlation spectroscopy and a detailed sketch of the confocal volume. Laser light is focused into a sample via a dichroic mirror and an objective. Here, fluorescent molecules are excited. Emitted light is collected by the objective, passes the dichroic mirror, an emission filter and a pinhole and finally hits an avalanche photodiode (APD). The signal is correlated by a correlator. The resulting autocorrelation curve can be further analyzed. Inset: Visualization of the shape and size of the confocal volume and the definition of the structure parameter S . z_0 describes the half height of the observation volume and ω_0 the radius of the beam waist.

diffuse through the confocal volume at any time, allowing the realization of single molecule studies [28].

2.2.2 Instrumentation

An Axiovert 200 microscope with a ConfoCor2 unit (Carl Zeiss Jena, Germany) was used for the experiments performed in the course of this thesis. Available lasers for excitation were an argon ion laser (488 nm) and two helium-neon lasers (543 nm and 633 nm). Fluorescence emission was filtered from the excitation light using corresponding band- and long pass filters. A 40x water immersion apochromat objective (Carl Zeiss) was used with a numerical aperture of 1.2. Samples were measured in 8-well LabTek II chamber slides (Nunc, Thermo Scientific) or in 384-well plates (Greiner Bio one). The measured fluctuations were correlated with a hardware correlator. As default an argon ion laser was used for excitation and a bandpass filter ranging from 500-550 nm for separation of emission and excitation light. The set-up is located in a temperature-controlled room (22°C). For calibration fluorescent dyes with known diffusion constants, Alexa488 and Alexa633, were used [30, 31]. The ConfoCor2 software was used for analysis when not stated differently. Fitting procedures employing equations that are not implemented in the software package were carried out using Igor Pro (WaveMetrics) or Matlab (MathWorks).

2.2.3 Theoretical Background of FCS

FCS is a statistical analysis of a fluctuating fluorescence signal. Poisson statistics describe the probability $P(n, N)$ to detect a defined number of point-like particles (n) at a certain time inside the confocal volume

$$P(n, N) = \frac{N^n}{n!} e^{-N}, \quad (2.1)$$

where N is the average number of particles in the observation volume. In this context, point-like means much smaller than the beam waist of the observation volume ($d \ll 2\omega_0$). The fluctuations are initiated by movement of particles due to Brownian motion. The number of fluorophores n inside the observation volume affects the fluorescence intensity $F(t)$ strongly. If fluorophores diffuse into the detection volume, the fluorescence signal becomes more intense and if they diffuse out of the confocal volume the intensity is

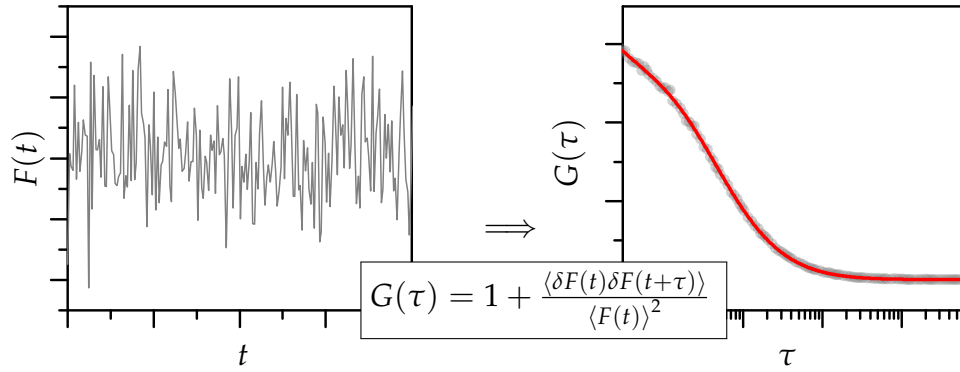


Figure 2.3: Basic principle of FCS. The intensity time trace of fluorescent particles in the observation volume is measured (left). Information on the molecules is gained by autocorrelation of the fluorescence signal and analysis of the resulting autocorrelation function (right). A model fitting function (red line) is needed to extract physically relevant information from the correlation data (gray circles).

reduced (Figure 2.3). The autocorrelation function $\tilde{G}(\tau)$ is determined by temporal correlation of the fluorescence intensity $F(t)$ and the fluorescence intensity $F(t + \tau)$ at a later time $t + \tau$:

$$\tilde{G}(\tau) = \frac{1}{T} \int_T^0 F(t)F(t + \tau)dt = \langle F(t + \tau)F(t) \rangle . \quad (2.2)$$

The angular brackets denote averaging over time t and the parameter τ is called correlation time or delay time. $\tilde{G}(\tau)$ is a means of describing the self-similarity between the fluorescence intensity $F(t)$ and itself at a later time $t + \tau$. Alternately, one can interpret $\tilde{G}(\tau)$ as a measure for the probability that the signal at various times still belongs to the same molecule.

The normalized autocorrelation is defined as

$$\tilde{G}(\tau) = 1 + \frac{\langle F(t)F(t + \tau) \rangle}{\langle F(t) \rangle^2} = 1 + \frac{\langle \delta F(t)\delta F(t + \tau) \rangle}{\langle F(t) \rangle^2} = 1 + G(\tau) \quad (2.3)$$

using the fluctuations of the intensity

$$\delta F(t) = F(t) - \langle F(t) \rangle . \quad (2.4)$$

For the remainder of this chapter the summand 1 will be dropped to obtain a clear notation.

$G(\tau)$ is an empirically determined and dimensionless function which contains no information on the sources of the observed intensity fluctuations. Therefore, a theoretical model fit is needed to interpret the correlation curves.

Generally, the required analysis model is based on the assumption that point-like particles freely diffuse in three dimensions without constraints or external influence such as directed flow. The fluorescence intensity $F(t)$ is then defined to be

$$F(t) = B \int I(\mathbf{r}) \cdot O_{\text{eff}}(\mathbf{r}) \cdot C(\mathbf{r}, t) \, d\mathbf{r} \quad (2.5)$$

using the following parameters:

B : brightness, the average number of photon counts during a defined period of time resulting from a single fluorophore.

$I(\mathbf{r})$: spatial distribution of the illumination intensity

$O_{\text{eff}}(\mathbf{r})$: detection probability of the set-up which is defined by the spatial positioning of the optical components (objective and pinhole) in the beam line.

$C(\mathbf{r}, t)$: spatial distribution of the fluorescent particles at time t .

The expression

$$\Omega(\mathbf{r}) = O_{\text{eff}}(\mathbf{r}) \cdot I(\mathbf{r}) \quad (2.6)$$

is also known as fluorescence detection profile and the brightness is defined by

$$B = \kappa \cdot \epsilon \cdot Q \quad (2.7)$$

with κ being the efficiency of the detector including its quantum efficiency and wavelength dependency, the molar extinction coefficient ϵ of the fluorophore at the excitation wavelength and the quantum efficiency of the fluorophore Q . The brightness should be constant during the measurement.

Inserting Equation 2.6 in Equation 2.3, we obtain

$$G(\tau) = \frac{B^2 \int \int \Omega(\mathbf{r}) \langle \delta C(\mathbf{r}, t) \delta C(\mathbf{r}', t + \tau) \rangle \Omega(\mathbf{r}') \, d\mathbf{r} d\mathbf{r}'}{(B \langle C \rangle \int \Omega(\mathbf{r}) \, d\mathbf{r})^2} . \quad (2.8)$$

Assuming an ideal Gaussian laser profile, the detection profile can be approximated by a three-dimensional Gaussian distribution described by:

$$\Omega(\mathbf{r}) = \Omega_0 \cdot \exp\left(-2 \cdot \frac{x^2 + y^2}{\omega_0^2}\right) \cdot \exp\left(-2 \cdot \frac{z^2}{z_0^2}\right) \quad (2.9)$$

with the maximum of intensity Ω_0 , the spatial Cartesian coordinates x, y, z , the radius of the laser beam ω_0 and the half length of the confocal volume in z -direction z_0 .

The structure parameter

$$S = \frac{z_0}{\omega_0} \quad (2.10)$$

describes the ratio of the axial and radial axes. As shown in Figure 2.2, there are no hard edges of the confocal volume. Under the above assumption of a Gaussian beam profile, the axes are defined as the distances from the center of the confocal volume to the position at which the laser intensity has decreased by a factor of e^{-2} in their corresponding directions [27, 32]. The size of the confocal volume is typically less than 1 fl ($< 1 \mu\text{m}^3$).

The fluctuations of the concentration $\langle \delta C(\mathbf{r}, t) \delta C(\mathbf{r}', t + \tau) \rangle$ contain the correlation within time. For three-dimensional translational diffusion - without considering rotation - the following expression is obtained

$$\langle \delta C(\mathbf{r}, t) \delta C(\mathbf{r}', t + \tau) \rangle = \langle C \rangle (4\pi D\tau)^{3/2} \exp\left(-\frac{|\mathbf{r} - \mathbf{r}'|}{4D\tau}\right) \quad (2.11)$$

with the diffusion coefficient D , which is a measure for the mobility of a particle and the correlation time τ [28].

Using Equations 2.9, 2.11 and 2.8, the autocorrelation function is derived

$$G(\tau) = G(0) \cdot \left(1 + \frac{4D\tau}{\omega_0^2}\right)^{-1} \cdot \left(1 + \frac{4D\tau}{z_0^2}\right)^{-1/2}. \quad (2.12)$$

We can simplify this relation further to

$$G(\tau) = G(0) \cdot \left(1 + \frac{\tau}{\tau_D}\right)^{-1} \cdot \left(1 + \frac{\tau}{S^2 \tau_D}\right)^{-1/2}, \quad (2.13)$$

using Equation 2.10 and

$$\tau_D = \frac{\omega_0^2}{4D}. \quad (2.14)$$

The translational diffusion time τ_D represents the average dwell time of a fluorophore inside of the detection volume.

Using $\tau = 0$ and Equation 2.3, we obtain

$$G(0) = \frac{\langle \delta F(t) \delta F(t) \rangle}{\langle F(t) \rangle^2} = \frac{\langle \delta N \delta N \rangle}{\langle N \rangle^2} = \frac{1}{\langle N \rangle} \quad (2.15)$$

using the relative deviation of the average for Poissonian statistics

$$\frac{\delta N}{N} = \frac{1}{\sqrt{N}}. \quad (2.16)$$

At the same moment in time, positions can only be correlated with themselves. So, $G(0)$ is determined by replacing $\langle \delta C(\mathbf{r}, 0) \delta C(\mathbf{r}', 0) \rangle$ by $\langle C \rangle \delta(\mathbf{r} - \mathbf{r}')$ in Equation 2.8.

The maximum amplitude of the autocorrelation function is then

$$G(0) = \frac{1}{\langle N \rangle} \quad (2.17)$$

with $\langle N \rangle$ being the average number of particles inside the detection volume.

Finally, we obtain the fitting function for a three-dimensional freely diffusing species as

$$G(\tau) = \frac{1}{N} \left(1 + \frac{\tau}{\tau_D}\right)^{-1} \left(1 + \frac{\tau}{S^2 \tau_D}\right)^{-1/2} = \frac{1}{N} g(\tau) \quad (2.18)$$

with N representing the number of particles inside the confocal volume, τ the correlation time, S the structure parameter, τ_D the translational diffusion time of the molecule and $g(\tau)$ the normalized correlation function.

2.2.4 Triplet State

Phosphorescence, or the so-called “optical dark state” was mentioned in Section 2.1. This state is detected by the used photodetectors and therefore has to be taken into consideration for analysis by adding an extra factor to the fitting function $G(\tau)$. The triplet state is represented by the triplet function

$$G_{\text{triplet}}(\tau) = \left(1 + \frac{T}{1-T} \exp\left(-\frac{\tau}{\tau_T}\right)\right) \quad (2.19)$$

where τ_T describes the triplet state relaxation time and T the mean fraction of fluorophores in the dark state [32, 33]. The total correlation curve is a product of the triplet

function and the model function $G(\tau)$:

$$G_{\text{total}}(\tau) = G_{\text{triplet}}(\tau) \cdot G(\tau) . \quad (2.20)$$

The triplet contribution is an individual characteristic of each type of dye. A high-quality dye shows a triplet fraction of only a few percent. The typical lifetime of a fluorophore in the triplet state is in the range of 0.5-10 μs . The effect that a molecule is switched on and off several times during its way through the confocal volume is called blinking. These are fluctuations on their own that lead to an additional contribution in the autocorrelation curve. While $G_{\text{triplet}}(\tau)$ was included into the fitting to obtain stable results, triplet kinetics were not subject of this work.

2.2.5 Polydispersity and Multicomponent Fitting

Since the focus of this thesis is the study of binding processes, we typically deal with samples that contain more than one single species, such as solutions containing free and bound proteins. In order to analyze such polydisperse systems, the model presented above has to be extended. Polydispersity describes the fact that a sample contains particles of various size. Each particle size is associated with its own diffusion time τ_{Di} . The fluorescence intensities are added because the emission of the different types of particles is not spatially correlated. In practice, this means that the correlation function now becomes a weighted sum of the correlation functions of each particle species [29],

$$G(\tau) = \frac{\sum q_i^2 N_i g_i(\tau)}{(\sum q_i N_i)^2} \quad (2.21)$$

with q_i being the brightness, N_i the number of particles, f_i the fraction and $G_i(\tau)$ the correlation function of the i^{th} species. In the case of equal brightness of the different species, this equation simplifies to

$$G(\tau) = \frac{1}{N} \sum_i f_i g_i(\tau) . \quad (2.22)$$

For systems with unequal brightness of the various components, Equation 2.21 has to be used for analysis. Alternatively, empirically determined correction factors need to be applied to Equation 2.22 [34], if not all parameters of Equation 2.21 are accessible. Difference in brightness can be caused, for instance, by quenching of the fluorescent

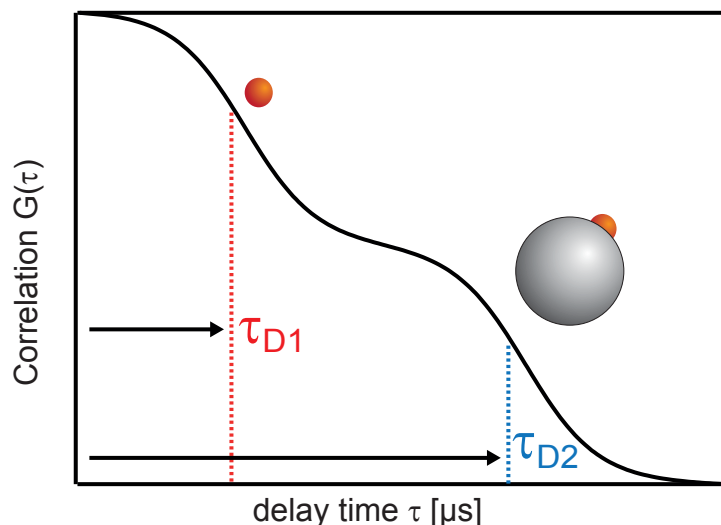


Figure 2.4: Two-component autocorrelation function showing the correlation times τ_{D1} and τ_{D2} . A freely diffusing fluorescent particle (red) has a diffusion time τ_{D1} while small particles bound onto the significantly larger NP (gray) have a much longer diffusion time τ_{D2} .

molecules upon binding or when two dyes with the same spectral properties are present, e.g. Alexa488 and fluorescein.

For only a few different species a multicomponent fit is appropriate, whereas for heterogeneous systems more sophisticated models are adequate. Among them are a maximum entropy method for FCS data analysis (MEMFCS), a Gaussian distribution model (GDM) based approach or other fitting algorithms like CONTIN [35–38]. MEMFCS and GDM are used in this dissertation in Chapter 7, thus they are introduced in more detail in the following.

Two-component Fitting

The most frequently multicomponent fit is the two-component fit. It is especially useful to measure binding of a small fluorescent component - e.g. a protein - to a large non-fluorescent component such as a NP or a liposome (see Figure 2.4). Two-component fitting allows us to determine the fraction of protein bound to NPs in the case of equal brightness of bound and unbound protein. The fitting function of a two-component fit is defined as

$$G(\tau) = \frac{1}{N} \sum_{i=1}^2 f_i g_i(\tau) = \frac{1}{N} ((1 - f_2) g_1(\tau) + f_2 g_2(\tau)) \quad (2.23)$$

with the constraint

$$\sum_{i=1}^2 f_i = f_1 + f_2 = 1 \quad (2.24)$$

and with N being the total number of particles inside the confocal volume, f_2 representing the fraction of the second component, and $g_1(\tau)$ and $g_2(\tau)$ denoting the normalized correlation functions of the first and the second component, respectively. For two components, it is possible to obtain a good and reasonable fit, but even with as little as three components it is already more complicated due to the steadily increasing number of free fitting parameters.

Multicomponent Fitting

A multicomponent fit is defined as the weighted sum of the characteristic correlation functions of the single species i described by

$$G(\tau) = \sum_{i=1}^m x_i \left(1 + \frac{\tau}{\tau_{Di}}\right)^{-1} \left(1 + \frac{\tau}{S^2 \tau_{Di}}\right)^{-1/2} \quad (2.25)$$

with weight x_i and the diffusion time of the i^{th} species τ_{Di} . The weight x_i is defined as the number of the i^{th} particle species N_i divided by the total number of particles $N = \sum_i N_i$ and is a measure of the abundance of this species. Even if one obtains a good fit, it might not be considered a physically meaningful result. For instance, diffusion times which are shorter than the one of a free fluorophore are obtained. On these grounds this type of fitting is limited to systems with a really small discrete number of differently diffusing species and is not suited for highly polydisperse systems.

Maximum Entropy Method for FCS Data Analysis (MEMFCS)

For polydisperse systems the number of free fitting parameters in a discrete multicomponent-model becomes too high to achieve meaningful fitting results. Thus, other fitting methods are required. The method of maximum entropy enables extracting information from noisy data. A maximum entropy method for FCS data analysis (MEMFCS) allows analyzing samples that contain multiple species. A lack of information can be compensated by maximum entropy method based algorithms which chose the most uniform solution that is consistent with the data. In 2003, Sengupta *et al.* developed the concept of maximum entropy method for FCS data analysis (MEMFCS) [39]. A simple model

system, green fluorescent protein (GFP) in aqueous solution, and a set of simulated highly polydisperse data were used to validate the functioning of MEMFCS. The results of the fitting were compared to conventional fitting with a small number of different species. Since then it has been used to study the aggregation of proteins [40–42], the size of NPs [43, 44] or the interaction of biomolecules and NPs [45, 46]. MEMFCS uses a quasicontinuous distribution of a large number of diffusing components to obtain an unbiased fitting. Moreover, it guarantees a maximally wide distribution that is consistent with the data. The formula is a sum of i different species weighted by their corresponding amplitudes $a_i(\tau_{Di})$ [47].

According to these publications, the triplet can be neglected in biological diffusion studies by separating it out in time. The model function is stated to be

$$G(\tau) = \sum_{i=1}^m a_i(\tau_{Di}) \left(1 + \frac{\tau}{\tau_{Di}}\right)^{-1} \left(1 + \frac{\tau}{S^2 \tau_{Di}}\right)^{-1/2} \quad (2.26)$$

with the number of species m , a_i the relative amplitude of the i^{th} species that is related to its brightness and average number in the observation volume, τ_{Di} the diffusion time of the i^{th} species available, τ the delay time and the structure parameter S .

A range of possible diffusion times on a logarithmic time-scale is divided into m parts. During the fitting process, the resulting distribution of possible diffusion times τ_{Di} is fixed. In order to obtain a fit that is consistent with the data, the algorithm varies the amplitudes a_i . In comparison to other methods, MEMFCS does not use any *a priori* assumptions on the distribution of the amplitude. Initially, the amplitudes $a_i(\tau_{Di})$ are uniformly distributed. A least-squares fitting algorithm is applied for fitting, ideally a Levenberg-Marquardt algorithm. The result of MEMFCS is a distribution of a_i that maximizes the entropy H and minimizes the difference of the measured data and the fit at the same time. The entropy is defined as

$$H = - \sum_i p_i \ln p_i \quad (2.27)$$

using

$$p_i = \frac{a_i(\tau_{Di})}{\sum_i a_i(\tau_{Di})}. \quad (2.28)$$

This method results in the most acceptable distribution. For a discrete solution for τ_D , the entropy is minimal. Minimal entropy is associated with complete knowledge of

the system. So for noisy data, minimal entropy is the least acceptable solution, while maximal entropy gives a solution that is consistent with the data available. MEMFCS provides a safe limit for the interpretation of data without any *a priori* assumptions and thus prevents the risk of overinterpreting the data of highly polydisperse systems. It is disadvantageous that the input distribution of τ_{Di} spans several decades. As a result, not all values for τ_D that correspond to physically relevant diffusion times of various particle size, are precisely available during the fitting process. On the other hand, it is argued that the absence of a particular diffusion constant in this analysis is a reliable indicator of the absence of that specific species [48].

Gaussian Distribution Model (GDM)

An alternative to MEMFCS is provided by the Gaussian distribution model (GDM) [49]. It functions in a comparable way, except that an assumption is made on the form of the initial distribution of the amplitude. The idea is that a component is not only represented by a single sharp value for τ_D . Instead, a Gaussian distribution around a peak diffusion time τ_p is assumed. A polydisperse system is analyzed and therefore the amplitude is described as a sum of n Gaussian distributions, so a multimodal size distribution. The total model function is then once more a sum of m one-component functions. As for MEMFCS, the range of possible diffusion times τ_D is logarithmically scaled and divided into m parts. The obtained set of τ_{Di} , $i = 1 + m$, is kept fixed during the fitting procedure. In order to obtain a fit that minimizes the difference between measured data and fit, only the amplitude a_i is varied. More specifically, the parameters A_k , b_k and τ_{pk} in Equation 2.30 are varied during fitting. A_k describes the relative amplitude of the components, τ_{pk} is the peak diffusion time of the k^{th} component and b_k is related to the width of the distribution.

The model is described by

$$G(\tau) = \sum_{i=1}^m a_i(\tau_{Di}) \left(1 + \frac{\tau}{\tau_{Di}}\right)^{-1} \left(1 + \frac{\tau}{S^2 \tau_{Di}}\right)^{-1/2} \quad (2.29)$$

using

$$a_i(\tau_{Di}) = \sum_{k=1}^n \exp(A_k) \cdot \exp\left(-\left(\frac{\tau_{Di} - \tau_{pk}}{b_k}\right)^2\right) \quad (2.30)$$

with peak diffusion time of the k^{th} Gaussian τ_{Pk} , b_k is related to the width of the k^{th} Gaussian, a_i is the relative amplitude of the i^{th} species, τ_{Di} is the diffusion time of the i^{th} species, n the total number of Gaussian peaks and S is the structure parameter [49]. By also including the triplet into the fitting, one obtains

$$G(\tau) = \underbrace{\left(1 + \frac{T}{1-T}\right) \exp\left(-\frac{\tau}{\tau_T}\right)}_{\text{triplet}} \cdot \sum_{i=1}^m a_i (\tau_{Di}) \left(1 + \frac{\tau}{\tau_{Di}}\right)^{-1} \left(1 + \frac{\tau}{S^2 \tau_{Di}}\right)^{-1/2}. \quad (2.31)$$

The areas under the single Gaussian peaks are calculated and divided by the sum over the areas under all Gaussian peaks to follow the development of the various species:

$$\text{percentage of } k^{\text{th}} \text{ component} = \left(\frac{\text{area}_k(\tau_{Pk})}{\sum_{k=1}^n \text{area}_k}\right) \cdot 100\% \quad (2.32)$$

with $k = 1, 2, \dots, n$. The major advantages of this type of fitting are that it is much faster and that it gives better resolved information on the distribution of particles than MEMFCS. The disadvantage is that some *a priori* knowledge of the system under observation is needed to choose a number of Gaussians n that works for the complete fitting process. Moreover, the starting values for the fitting procedure are educated guesses that depend on *a priori* knowledge from literature or complementary experiments. Where such *a priori* values are known or can be independently measured, however, GDM can lead to better understanding of the kinetics of the measured process.

2.2.6 Analysis

The appearance of the correlation function can give first insights into the sample. The shape of $G(\tau)$ gives a first hint on the particle size and on the number of particles inside the confocal volume. For a monodisperse system, the point of the correlation curve, where the maximal amplitude $G(0)$ has decreased to half its value gives the size of the particles. The amplitude of $G(\tau)$ is inversely proportional to the number of particles inside the sample (see Equation 2.17).

Determination of Concentration

Binding processes are related to changes in size and concentration. Determination of the kinetics of both parameters allows quantification of the underlying processes. The

concentration of the particles in solution can be determined from fitting by

$$\langle C \rangle = \frac{\langle N \rangle}{V} = \frac{1}{G(0) \cdot V_{\text{eff}}} \quad (2.33)$$

with the effective volume

$$V_{\text{eff}} = \pi^{3/2} \omega_0^2 z_0 = \pi^{3/2} \omega_0^3 S, \quad (2.34)$$

using the dimensions of the observation volume described by Equation 2.10 and shown in Figure 2.2.

Hydrodynamic Size Determination

The particle size can be calculated from the diffusion time τ_D or coefficient D determined by successful fitting, respectively. For spherical molecules, the Stokes-Einstein equation links the diffusion properties D to the hydrodynamic radius R_H using the Boltzmann constant $k_B = 1.38064852 \cdot 10^{-23}$ J/K, the viscosity η and the temperature T of the surrounding medium:

$$D = \frac{k_B T}{6\pi\eta R_H}. \quad (2.35)$$

The hydrodynamic radius R_H describes a hypothetical sphere which obtains the same properties of diffusion as the particle under observation. If the real geometry of a particle deviates strongly from a sphere, R_H can only give a rough estimation of the size and not a precise value.

Not all particles studied in this thesis can be considered spherical. For instance, short deoxyribonucleic acid (DNA) filaments or fibrils are more shaped like a rod. In order to consider the differences in geometry of rigid rod-like molecules, the above formula is modified to

$$D = \frac{A k_B T}{3\pi\eta L} \quad (2.36)$$

using the correction factor

$$A = \ln\left(\frac{L}{d}\right) + 0.312 + 0.565\left(\frac{d}{L}\right) - 0.1\left(\frac{d}{L}\right)^2. \quad (2.37)$$

L is the length and d the diameter of the rod-like object, respectively [50]. In order to

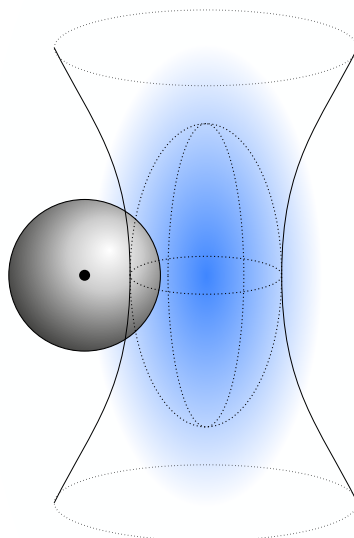


Figure 2.5: Illustration of the impact of the finiteness of a particle. While a fluorescent particle of finite size (gray) enters the confocal volume, its center of mass (black dot) is still located outside of the detection area. Due to this, a fluorescence signal is detected for a longer time and the apparent diffusion time τ_A is prolonged compared to a point-like particle with the same diffusion properties.

reduce the number of free parameters and to receive meaningful results from fitting, *a priori* information on the object is required, such as knowledge of the diameter d . This data is often determined with a complementary imaging technique, such as transmission electron microscopy or atomic force microscopy (AFM). For semiflexible long polymers, more sophisticated approaches would need to be applied [51, 52].

Finite Size Correction

Up until now, nearly point-like spherical particles are considered. But NPs are particles with a finite size that has to be taken into account in the analysis. The impact of the finiteness of particles was first discussed by Starchev *et al.* [53]. If a particle obtains a diameter that is comparable to the size of the beam waist of the confocal volume ($d \approx 2\omega_0$), then the shape of correlation curve $G(\tau)$ is influenced by the geometrical size as well as the arrangement of the fluorophores on the particle. The time a particle is detected inside the confocal volume increases with increasing particle size. While its center of mass is still outside of the observation volume, the edge of the particle is already inside the detection region (Figure 2.5). This apparent prolonged diffusion time τ_A has to be corrected to obtain the actual hydrodynamic size of the particle using the

Stokes-Einstein Equation (2.35) [54].

There are two cases of label positioning that have to be considered. On the one hand, for a sphere that is only labeled on the surface (shell), the apparent diffusion time τ_A is related to the actual diffusion time τ_D by

$$\tau_A = \tau_D \cdot \left(1 + \frac{8}{3} \frac{R^2}{\omega_0^2} \right). \quad (2.38)$$

On the other hand, a particle can be a uniformly volume-labeled sphere. In this case, the correction term is described by

$$\tau_A = \tau_D \cdot \left(1 + \frac{8}{5} \frac{R^2}{\omega_0^2} \right). \quad (2.39)$$

It is recommended to use these corrections for a ratio of the radius of the particles R to the radius of the beam waist $R/\omega_0 > 0.2$. For values above this threshold the error is larger than 10 %.

For particles that obtain an even larger diameter than the beam waist, $d \gg 2\omega_0$, corrections according to Gapinski *et al.* have to be considered [55, 56]. This case did not occur in present thesis.

Chapter 3

Analysis of Binding Affinity Reactions

In this chapter the analysis of titration experiments to quantify binding of proteins to solid NPs and liposomes is discussed. With FCS it is possible to measure the fraction of bound proteins as a function of the concentration of NPs, which can be used to determine the equilibrium binding constant or binding affinity K . The underlying theory for equilibrium binding constants is explained. Knowledge of the value of K and its dependence on additional experimental parameters is crucial to elucidate mechanisms of interactions of biophysical matter.

3.1 Law of Mass Action and Binding Constants

3.1.1 Monovalent Receptors

A biomolecular interaction of a single ligand L and a single receptor R leading to the formation of a complex RL (Figure 3.1) is described by the following reaction equation



If the interaction is an equilibrium reaction, it is determined by the law of mass action. The fraction of receptors occupied is given by

$$Y = \frac{[RL]}{[R]_{\text{tot}}} = \frac{[RL]}{[R] + [RL]} = \frac{K \cdot [R]}{1 + K \cdot [R]} \quad (3.2)$$

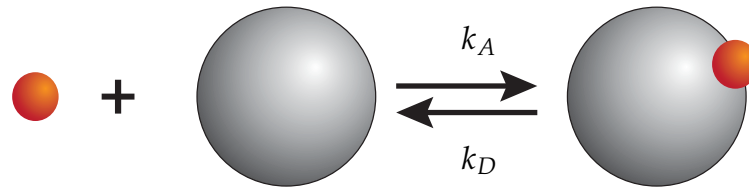


Figure 3.1: Illustration of binding process. A single ligand (gray) binds to a receptor (red), building a complex.

using the definition of the equilibrium binding constant

$$K = \frac{[RL]}{[L] \cdot [R]} \rightarrow [R] = \frac{[RL]}{K \cdot [L]}, \quad (3.3)$$

where $[X]_{\text{tot}}$ describes the total available amount of species X ($X = R, L$), so the initial concentration used for the experiment, and $[X]$ is the amount of unbound X in solution [57]. The binding affinity K provides information on the thermodynamic properties of the reaction. Its value allows making a statement on the strength of binding, but it does not say anything about the dynamics of the reaction. To this end, time-resolved measurements are needed as discussed in Section 3.2.

In order to express Y in terms of the experimentally easier accessible parameters $[L]_{\text{tot}}$, $[R]_{\text{tot}}$ and K , the following relations are applied:

$$[L]_{\text{tot}} = [L] + [RL] \rightarrow [L] = [L]_{\text{tot}} - [RL] \quad (3.4)$$

and

$$[R]_{\text{tot}} = [R] + [RL] \xrightarrow{(3.3)} [R]_{\text{tot}} = \frac{[RL]}{K \cdot [L]} + [RL]. \quad (3.5)$$

If the last two expressions are combined, we obtain the following relation:

$$[R]_{\text{tot}} = [RL] + \frac{[RL]}{K \cdot [L]} = [RL] + \frac{[RL]}{K \cdot ([L]_{\text{tot}} - [RL])}. \quad (3.6)$$

Solving the resulting quadratic equation for $[RL]$ and inserting the result in Relation 3.2, we obtain

$$Y = \frac{([R]_{\text{tot}} + [L]_{\text{tot}} + K^{-1}) - \sqrt{([R]_{\text{tot}} + [L]_{\text{tot}} + K^{-1})^2 - 4[R]_{\text{tot}}[L]_{\text{tot}}}}{2[R]_{\text{tot}}}. \quad (3.7)$$

In the limit of $[L]_{\text{tot}} \gg [R]_{\text{tot}}$, $[L]_{\text{tot}} \approx [L]$ the above Relation 3.7 simplifies to

$$Y = \frac{[RL]}{[R]_{\text{tot}}} = \frac{[RL]}{[R] + [RL]} = \frac{K \cdot [L]_{\text{tot}}}{1 + K[L]_{\text{tot}}}. \quad (3.8)$$

These expressions can be used to experimentally determine the equilibrium binding constant K of a ligand receptor interaction. The fraction bound, as a function of the concentration of the titrated ligand, gives an S-shaped curve, the so-called binding isotherm. Fitting with the above equations allows extracting a value of K from this graph.

In pharmacology or biochemistry, Relation 3.8 is also known as the Langmuir binding isotherm. The Langmuir binding isotherm describes the state of equilibrium of adsorption and desorption at an interface at constant temperature. It is the simplest model of adsorption that describes the complete adsorption on a surface. K is often noted as K_L and called Langmuir sorption coefficient [58].

Moreover, Equation 3.8 is known as a limit of the so-called Hill equation for the case of $n = 1$:

$$Y_{\text{Hill}} = \frac{K \cdot [L]_{\text{tot}}^n}{1 + K \cdot [L]_{\text{tot}}^n} \quad (3.9)$$

The Hill coefficient n is an indicator of cooperativity. If $n = 1$, the binding of two ligands is independent of each other. In the case of $n \neq 1$, the cooperativity is either positive ($n > 1$) or negative ($n < 1$). For positive cooperativity, the affinity of the receptor for further ligand molecules increases if one ligand is bound, and *vice versa* for negative cooperativity. Hill himself refused a physical interpretation of n [59]. Only for the special case of strong positive cooperativity, the Hill coefficient gives an exact estimation of the number of binding sites, because n particles bind in an all-or-nothing fashion without any intermediate states. But this assumption does not hold true for all cases and therefore n only provides a lower limit of the number of binding sites [60–63].

3.1.2 Polyvalent Receptors

The above relations are derived under the assumption that a single ligand only binds to a single receptor. This assumption is not, however, universally valid for all biophysical interactions. Frequently, receptors provide more than one binding site to the available ligands. The theory above can be expanded for the universal case of ligands binding to receptors with m binding sites to which between 1 and m ligands can adsorb. Applying a statistical description of the bimolecular binding process, the theory can be generalized.

This allows the integration of special cases such as cooperative processes including different binding constants for different population of the receptor's binding sites [57]. The fraction of bound ligands can be defined as the probability that a ligand is adsorbed to a receptor. The probability p_j of a ligand binding to a receptor with m binding sites which are occupied by j ligands is identical for all $j=0, 1, \dots, m-1$, if we assume that the binding affinity K does not depend on the current number of filled binding sites on the receptor. The same assumption is made for the analysis with the Langmuir binding isotherm mentioned above. From this we can deduce an expression for the probability p_{bound} that a ligand is bound to a receptor with m possible binding sites:

$$p_{\text{bound}} = \sum_{j=0}^{m-1} p_j = \sum_{j=0}^{m-1} p = m \cdot p. \quad (3.10)$$

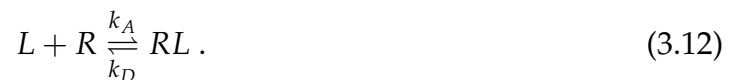
Due to the assumption that the probability of binding p is independent of the number of occupied binding sites on the receptor, we can replace p by using Equation 3.8. The probability p_{bound} can then be rewritten as

$$p_{\text{bound}} = m \cdot p = m \cdot \frac{K \cdot [L]_{\text{tot}}}{1 + K[L]_{\text{tot}}}. \quad (3.11)$$

This equation enables us to extract the binding constant K from a titration series of proteins (ligands) and a fixed concentration of NPs acting as receptors with an average of m binding sites.

3.2 Association and Dissociation Rates

Equilibrium does not describe a static state in which the reaction has stopped. On the contrary, in equilibrium there are as many ligands binding to the receptors as unbind from them, so the association rate k_A and dissociation rate constants k_D are simply the same. To add these new parameters to our considerations, Equation 3.1 is noted as



The kinetics of the binding process are described by

$$\frac{d[RL]}{dt} = k_A \cdot [R] \cdot [L] - k_D \cdot [RL]. \quad (3.13)$$

With this equation we are able to analyze time-resolved measurements of the amount of free protein [64]. This is possible because the underlying law of mass action describes reactions that are reversible. The affinity constant K is related to k_A and k_D via

$$K = \frac{k_A}{k_D}. \quad (3.14)$$

Most reactions are determined by the dissociation rate constant k_D which has, for instance a value of 10^{-1}s^{-1} for the desorption of proteins from NPs as shown in Chapter 5.3.4. In case of high values for K , the values for k_D can decrease to 10^{-6}s^{-1} . These reactions are nearly irreversible such as Avidin-Biotin, and often described by the strong binding model presented in Section 3.3. Besides the dissociation rate constant k_D , the dissociation constant K_D is also frequently used to describe binding reactions:

$$K_D = \frac{[L] \cdot [R]}{[RL]} = \frac{k_D}{k_A} = K^{-1}. \quad (3.15)$$

K_D is a measure of equilibrium of the dissociation reaction and can be considered a special case of the equilibrium constant of the law of mass action.

3.2.1 Diffusion-limited Reactions

If there are no serious conformational changes of the reaction partners, then the binding itself is very fast due to the nature of interaction forces and low activation barriers. The binding reaction is often only limited by the frequency of encounters of ligands and receptors. In an unbiased reaction volume ligands and receptors move by diffusion, and thus such binding reactions are called diffusion-limited.

Under these assumptions, the association constant is given by

$$k_A = 4 \cdot \pi \cdot D_{RL} \cdot (r_R + r_L) \cdot N_A \quad (3.16)$$

with the diffusion constant $D_{RL} = D_R + D_L$, the radii of the receptor and the ligand r_R and r_L , respectively, and the Avogadro constant N_A .

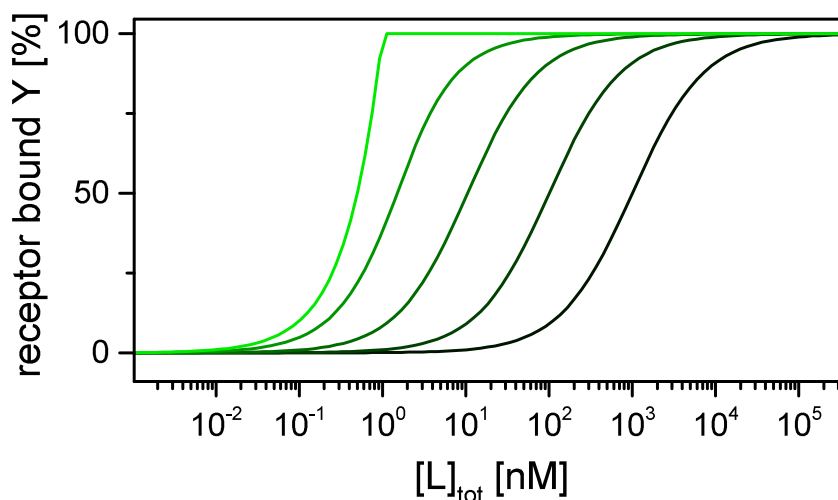


Figure 3.2: Theoretical evaluation of the concentration of bound receptor $[RL]$ in dependence of the total ligand concentration $[L]_{\text{tot}}$ for various binding affinities. The affinity K increases with brightness of color from dark to light green. Total concentration of receptor $[R]_{\text{tot}} = 1 \text{ nM}$.

3.3 Strength of Binding and Strong Binding Model

First conclusions can be drawn from the shape and the position of the binding curve. In Figure 3.2, theoretical titration curves for a fixed concentration of receptors $[R]_{\text{tot}}$ and various binding affinities K are shown. If the curve increases weakly with concentration and transits very smoothly into the plateaus, then the binding affinity is low. If the increase is very steep, this indicates a high affinity. In this case, the position of the curve depends only on the concentration of the receptor $[R]_{\text{tot}}$. In the special case of strong binding, the position of the kink reaching saturation, gives an estimate of the concentration of binding sites. If the value for K is very high due to low values of k_D , the process can be considered irreversible on microscopic time-scales. For such interactions the usage of equilibrium concepts to describe adsorption may no longer be appropriate [65]. A strong binding model as proposed by Milani *et al.* seems to be more suited [21]. The model assumes a strong interaction of proteins with the bare NP surface and a negligible interaction of proteins and NPs covered with proteins. Resulting from this, proteins (P) bind to the NP until the surface is completely covered. In order to apply the strong binding analysis, the fraction bound is plotted against the molar ratio $x = [P]/[NP]$. Data that is represented in this way falls on a single universal curve as shown in Figure 3.3. A full adsorption up to x_c^* with a decreasing fraction bound is

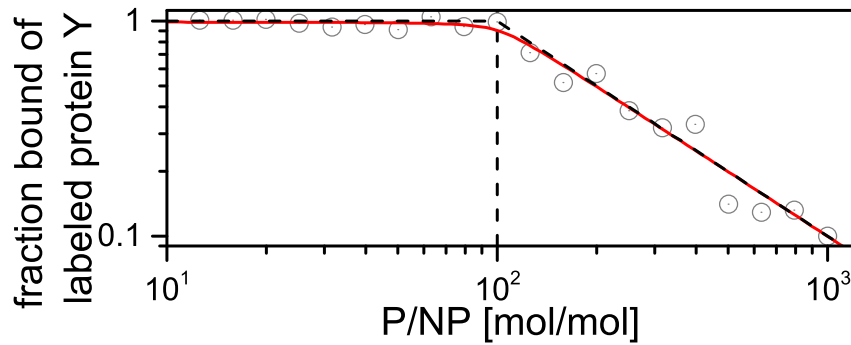


Figure 3.3: Comparison of the strong binding model for protein-NP interactions (dashed black line) and analysis using the law of mass action described by Equation 3.7 (solid red line). Gray circles represent generic data.

observed. The fraction bound according to the strong binding model is defined by

$$Y = \frac{[P/NP]}{[P]_{\text{tot}}} = \begin{cases} 1 & \text{if } x \leq x_c^* \\ x_c^*/x & \text{if } x > x_c^* \end{cases} \quad (3.17)$$

where x_c^* is the critical molar ratio of a full monolayer coverage and additionally gives an estimation of the average number of available binding sites per NP. The advantage of this approach is, that there is no need to measure a complete binding isotherm as necessary for Langmuir adsorption isotherms. This is especially useful, if one is only interested in the stoichiometry and not the exact value of the binding affinity K .

3.4 Binding Probed by FCS

FCS uses the fact that the diffusion of particles depends on their size and that binding causes a change of this diffusion behavior. In a typical FCS experiment, the smaller proteins are fluorescently labeled and kept at a fixed concentration - so they act as receptors. This way, we are able to observe a more pronounced change in diffusion behavior, if a fast diffusing protein binds to a slower NP. We measure the number of free proteins N_{free} with respect to the initial amount of proteins in solution (N_0). The fraction bound is given by

$$Y = 1 - \frac{N_{\text{free}}}{N_0} . \quad (3.18)$$

We determine the binding isotherms as a function of the concentration of NP. From the isotherms we can extract the binding affinity K with a fit according to Equation 3.7 if we assume that the binding constants are always independent of the state of occupation of the s ligand's binding sites [66–69].

In this thesis, interactions of proteins with solid NPs and TSLs are studied. Both types of ligands have a diameter of about 100 nm and can be considered as ligands with s independent binding sites for proteins. So, the fraction of proteins bound to the ligand NPs can be expressed in terms of free ligands $[L]_{\text{tot}}$ using Relation 3.8. In this case, the value of K relies heavily on the homogeneity of the size and the related available surface of the nanocarrier under observation. In order to overcome this limitation, a more general form is desirable which is independent of the size of the ligand. The total number of available ligand binding sites S is defined by the product of the average number of binding sites per ligand s and the total concentration of ligands $[L]_{\text{tot}}$ in solution

$$[S] = s \cdot [L]_{\text{tot}} . \quad (3.19)$$

In the case of TSL, it is assumed that every lipid can act as a potential binding site. Thus, the binding constant is often defined in terms of the lipid concentration instead $[S]$ of the concentration of liposomes $[L]_{\text{tot}}$. This leads to the following definition of the fraction of proteins bound to TSLs:

$$Y = \frac{K \cdot [L]_{\text{tot}}}{1 + K[L]_{\text{tot}}} = \frac{K \cdot s \cdot [L]_{\text{tot}}}{1 + K \cdot s \cdot [L]_{\text{tot}}} = \frac{K \cdot [S]}{1 + K[S]} . \quad (3.20)$$

$[L]_{\text{tot}}$ is the initial concentration of TSLs in solution and $[S]$ represents the total concentration of lipids in the sample. Liposomes consist of a lipid bilayer. Due to this, only half of the lipids are accessible for binding. This fact can be considered by expressing K in terms of accessible lipids $[S]/2$ instead of the total lipid concentration $[S]$ [70].

Since measurements mainly dealt with binding under the excess of available ligand binding sites $[S]$, Equation 3.20 was used for analysis of the binding isotherms. Where the limit $[L]_{\text{tot}} \gg [R]_{\text{tot}}$ was not valid, Equation 3.7 was applied.

3.5 Binding Probed by Microscale Thermophoresis

In microscale thermophoresis (MST), the directed movement of fluorescent molecules in a local temperature gradient is measured. The underlying effect is called thermophoresis

and was first mentioned by Carl Ludwig in 1856 [71]. MST is a technology that allows the evaluation of the interaction of molecules such as binding or unbinding by studying the changes in the characteristic motion of the sample molecules [72, 73].

3.5.1 Basics of Microscale Thermophoresis

In a temperature gradient ∇T in a liquid, molecules with thermophoretic mobility D_T move with pace $v = D_T \cdot \nabla T$. Differences in the local concentration c are induced by the thermophoretic motion, which causes diffusion of the molecules along the gradient. The resulting total molecular flow is described by [71]:

$$\mathbf{j} = \mathbf{j}_D + \mathbf{j}_{D_T} = -\nabla c \cdot D - c \cdot \nabla T \cdot D_T. \quad (3.21)$$

D is the diffusive mobility. In equilibrium, thermophoresis and ordinary mass diffusion ($\mathbf{j} = 0$) compensate each other:

$$\frac{dc}{c} = -\frac{D_T}{D} \cdot dT. \quad (3.22)$$

From this relation the equilibrium distribution of the concentration can be obtained:

$$\frac{c(x)}{c_0} = \exp \left[-\frac{D_T}{D} \cdot (T(x) - T(x_0)) \right]. \quad (3.23)$$

c_0 describes the concentration at site x_0 . The Soret coefficient S_T , a measure for the intensity of thermodiffusion in the stationary state, is defined as

$$S_T = \frac{D_T}{D}. \quad (3.24)$$

The distribution of the concentration caused by thermophoretic motion can be interpreted as a local change in the Gibbs free enthalpy G using a Boltzmann distribution for small, quasi-continuous temperature steps [74]:

$$\frac{c(T_1)}{c(T_2)} = \exp \left[-\frac{G(T_1) - G(T_2)}{k_B T} \right]. \quad (3.25)$$

From the last two equations, we deduce an expression that relates the Soret coefficient to the overall entropy H :

$$-H = \frac{\Delta G}{\Delta T} = S_T \cdot k_B T. \quad (3.26)$$

H describes the local negative entropy of the solvent-solute system for individual particles at constant pressure. For biophysical experiments, this solvent is ordinarily water or watery solutions. In this case, the entropy of the particles is determined by the entropy of ionic shielding and the entropy of hydration, described by

$$S_T = \frac{A}{k_B T} \left(-s_{\text{hydr}} + \frac{\beta \sigma_{\text{eff}}^2}{4\epsilon\epsilon_0 T} \cdot \lambda_{DH} \right) \quad (3.27)$$

with the hydration entropy s_{hydr} per surface area A , the effective surface charge density σ_{eff} , the dielectric constant of water ϵ , the vacuum permittivity ϵ_0 and the Debye screening length λ_{DH} . λ_{DH} depends on the concentration of salt of the solution. The relative change of the solvent's dielectric constant $\epsilon(T)$ and λ_{DH} with temperature is characterized by β .

3.5.2 Analysis of Binding

The Soret coefficient S_T depends on several parameters: size, conformation, charge and solvation entropy of a particle. Interactions such as binding may alter some or all of the named characteristics. The impact on at least one of these parameters is used in MST to put the interaction of molecules on a quantitative level. The change in concentration in the stationary state with the temperature change $\Delta T = T(x) - T(x_0)$ at the respective position x is determined by S_T [75]:

$$c_{\text{hot}} = c_{\text{cold}} \cdot \exp(-S_T \cdot \Delta T) . \quad (3.28)$$

In practice, the temperature gradient inside the sample chamber is generated by a low-powered infrared laser [76]. Usually, the sample chamber is a capillary. Fluorescent labelling of the molecules under observation allows the visualization of the thermophoretic motion as a change in the fluorescence intensity detected (see Figure 3.4). The ratio $F_{\text{hot}}/F_{\text{cold}} = F_{\text{norm}}$ of the averaged fluorescence intensity during the times when the laser is switched on (F_{hot}) and off (F_{cold}), respectively, is used to quantify the thermophoretic behavior. Normally, the amount of the unlabeled interaction partner is titrated against a fixed concentration of the fluorescently labeled partner. This unlabeled partner acts as receptor. If the thermophoretic depletion is plotted against the concentration of receptors, we obtain a binding isotherm that can be analyzed using the formalism presented in the previous section (Equation 3.7 or 3.8, respectively).

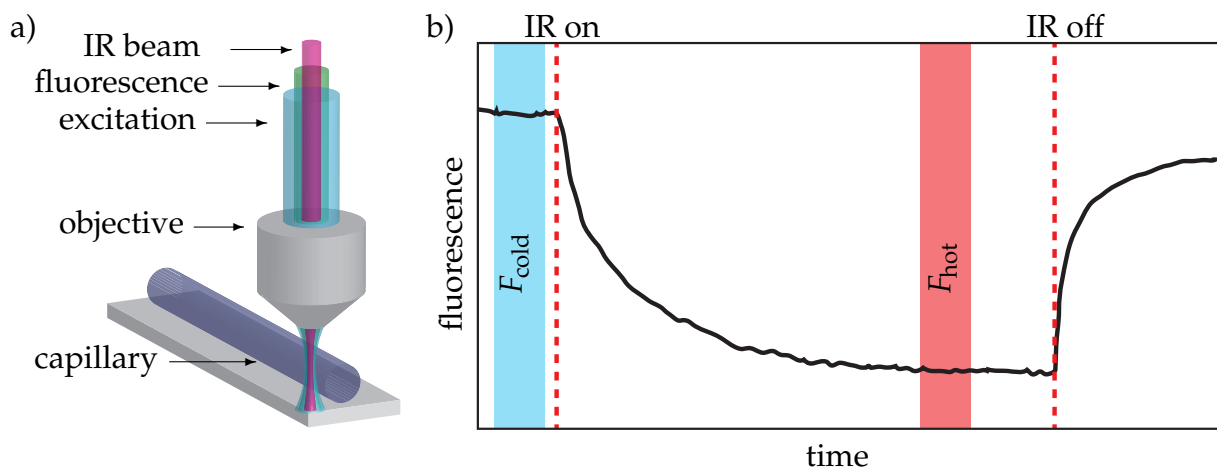


Figure 3.4: MST. a) Thermophoresis in a sample solution containing biomolecules is induced by a focused infrared laser. The directed motion of the molecules in the established temperature gradient is detected via the local change in fluorescence. The fluorescent particles are excited using an LED. The thermophoretic motion causes a concentration gradient inside the capillary. b) Fluorescence time trace. Before the infrared laser is switched on, the cold fluorescence F_{cold} is measured. After starting heating, a steep decrease in fluorescence is detected. This phase is followed by the characteristic thermophoretic motion, from which F_{hot} is gained. After turning the laser off, the fluorescent molecules start to diffuse back.

Chapter 4

Proteins and Plasma

In this chapter the background of the used biomaterial is presented. The binding of various proteins to different NPs is discussed in this dissertation (Chapter 5 and 6). Knowledge of the protein properties and its biological function is essential for experiments and interpretation of results. Additionally, experiments are performed in complex media such as plasma or serum. Biofluids are scattering media, which are crowded by macromolecules and hence strongly disturb FCS experiments by distortion of the confocal volume. The distinction between plasma and serum is explained. The dependence of the viscosity on the temperature and the composition of the medium is demonstrated for mixtures of phosphate buffered saline (PBS) and FBS. The impact of these solutions on FCS measurements is discussed.

4.1 Biomolecular Corona

When bare NPs are exposed to biological fluids, proteins and other biomolecules adsorb to them. The resulting layer(s) of biomaterial is called “protein corona” or “biomolecular corona” (Figure 4.1 a) [8–11]. The composition of the corona gives the NP its biological identity and therefore determines the fate of the NP inside a living system in dependence on its composition [77]. However, the corona is not static. It evolves with time and environmental changes when traveling through different compartments of the body. Certain proteins will be replaced with fresh ones from the new local environment, resulting in a change of the biological identity. The particle may then show characteristics of both the original milieu and the new one [9, 78]. Understanding of the evolution of the corona is mandatory regarding the general safety of NPs, but also for potential

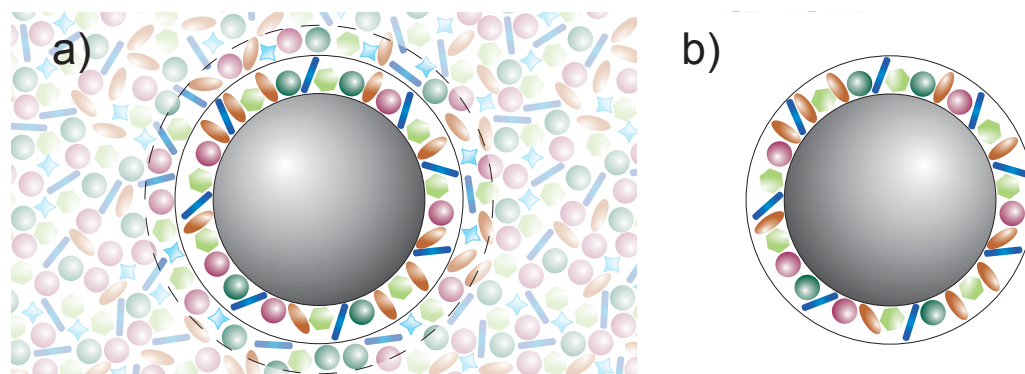


Figure 4.1: a) Inside an organism, NPs will almost invariably be surrounded by a mixture of biomolecules. These biomolecules adsorb fast and strongly onto the NP's surface. Due to very strong adsorption, the biomolecules might never come off again. This implies that the identity of the NP is effectively hidden by the covering biomolecules on its surface. The corona is divided into two sections. The hard corona (inner circle, dark colors) and the soft corona (outer circle, light colors). The hard corona is often considered to be irreversibly bound due to its slow exchange, while the loosely associated molecules of the soft corona exhibit dynamic exchange with its surroundings. b) NP with hard corona after removal of the surrounding protein solution. Removal can be performed by centrifugation as in publication P1 in Chapter 5. This way, the hard corona becomes analytically accessible.

therapeutic applications as drug carriers. Biomolecules within organisms, such as lipids, sugars or proteins, adsorb strongly to the NP's surface. In the beginning, abundant proteins bind that are slowly replaced by proteins with a higher affinity. The original NP and its physico-chemical properties are thereby effectively masked. These biophysical properties may differ significantly for the coated and the uncoated NP. Thus, the object whose eventual hazards need to be investigated, is not the original bare NP, but rather the complex consisting of NP and the involved biomolecules from the organism. The biomolecular corona itself can be divided into two parts: the hard and the soft corona (Figure 4.1 a). The molecules of the hard corona are in direct contact with the bare NP surface and remain there for a relevant time [79]. In comparison, the molecules of the soft corona are only loosely associated and exhibit a dynamic exchange with its environment. While the soft corona can be almost completely replaced, the hard corona is robust and long-lived in the presence of added full plasma. Depending on the time-scale of the experiment, the hard corona is also termed irreversible [21, 80]. Studies of the biomolecular corona often use techniques to separate the hard corona-NP complexes from solutions (Figure 4.1 b). Methods such as centrifugation, size exclusion

chromatography or magnetic isolation are applied for separation, followed by analysis by gel electrophoresis, liquid chromatography mass spectrometry or nuclear resonance spectroscopy [81, 82].

Interactions of the NP's corona with the biological machinery have to be considered in cell experiments. Significant differences in the uptake of NPs in cell medium with and without serum have been observed [83, 84]. The adhesion of protein-NP complexes to cells is strongly reduced compared to the effect for the bare NPs. The presence of the corona reduces the unspecific interactions between the pristine NP and the membrane of the cells. Specific corona-receptor interaction may be possible and trigger the biological recognition, if signaling molecules are present in the corona. Still the extent of cellular uptake depends on the detailed system. Already in the year 1962, the effect of protein adsorption to flat surfaces was discussed by L. Vroman [85, 86]. This concept is adapted to the exchange kinetics of NP's corona molecules. The "Vroman effect" postulates competitive protein adsorption on a surface. Although the total amount of adsorbed biomolecules stays roughly constant, the identities of the adsorbed proteins can change over time. The effect also describes the evolution of the protein corona from abundant, not weakly binding proteins to the subsequent replacement by less abundant but stronger binding molecules [87–89].

4.2 Plasma Proteins

In this work, the following representative proteins are considered. Although there are more than 3,500 proteins in human plasma present, only a few hundreds are usually part of the corona of NPs [90]. The selected proteins are numerous in plasma and have been detected in the corona of solid NPs or liposomes [89, 91–95].

4.2.1 Serum Albumin

Serum albumins are the most abundant protein in blood plasma and serum. For instance human serum albumin (HSA) makes up almost 55% of plasma proteins in humans ($35\text{--}50\text{ g l}^{-1}$). It is a single chain protein with a globular shape and a molecular weight of 67 kDa. In the liver, serum albumin (SA) is produced and secreted into circulation. The task of SA is the regulation of the oncotic pressure of plasma to keep the blood within circulation [90]. It sequesters and transports many metabolites within the body,

especially less soluble, and hydrophobic ones such as lipids, vitamins or hormones. For binding and transport, SA possesses three binding domains which are specific for metal ions, lipids and nucleotides, respectively [96]. In addition, SA is an important antioxidant and has enzymatic properties such as binding and activation of drug conjugates (e.g. ibuprofen) [97]. It also acts as a chaperone molecule promoting the folding of proteins [98]. In research, SA is often used as blocking agent to avoid nonspecific protein-surface interactions [96]. SA is used to avoid protein-protein interactions and is added as a stabilizer to solutions, for instance in cryopreservation. For modeling and simulations, SA offer a distribution of exposed residues that provide the opportunity to study regions with different degree of hydrophobicity.

4.2.2 Fibrinogen

Fibrinogen (Fib) is a heavy (340 kDa) rod-like molecule that plays a key role in coagulation. It is known as coagulation factor I and is converted to fibrin during coagulation. It can support both platelet-platelet and platelet-surface interactions by binding to the glycoprotein IIb-IIIa receptor [99]. Fib consists of three subunits, the so called α , β and γ chains. Its concentration in plasma varies from 1.7 to 4.5 mg ml⁻¹, corresponding to about 7% of the total serum proteins. Fib obtains a high surface affinity and usually displaces preadsorbed proteins [100]. Bound Fib might interact with the Mac-1 receptor, which would increase NP uptake by phagocytosis [101, 102].

4.2.3 Fibronectin

Another high-molecular weight protein of the extracellular matrix is fibronectin (FN). It usually exists as a dimer and has a molecular weight of 440 kDa. FN is abundant in body fluids as well as part of the insoluble extracellular matrix. This protein obtains binding sites for heparin, integrins or collagen. FN is important to cell adhesion, growth, migration and differentiation [103].

4.2.4 Transferrin

Transferrin (Tf) is a glycoprotein with a molecular weight of 80 kDa. The task of Tf is the transport of iron in the human body. At least 80% of the iron bound to circulating Tf is delivered to the bone marrow and incorporated into newly formed erythrocytes

as shown by radioactive tracer studies [104, 105]. The spleen and the liver, which is a basic depot for stored iron, are further major sites of iron delivery. At its homologous N-terminal and C-terminal iron-binding domains, Tf can bind up to two Fe^{3+} ions [106]. Only in the presence of an anion (usually carbonate), ferric iron couples to Tf with an association constant of about 10^{20} M^{-1} at pH 7.4 [107]. The anion acts as a bridging ligand between metal and protein [108, 109]. The iron binding to Tf is neglectable without the anion cofactor. Normally, about one-third of the iron-binding sites of Tf are occupied. Therefore, almost no iron occurs in circulation that is not bound to Tf. Through receptor-mediated endocytosis of Tf, iron is taken into vertebrate cells. Iron-loaded Tf binds to receptors on the outer face of the cell membrane with a very high affinity. The receptor binding seems to be mediated by the C-terminal domain [110]. Its concentration in blood is about 3 mg ml^{-1} , or 25 mM, respectively. Hence, cellular Tf receptors are ordinarily fully saturated. After adsorption to its receptor on the cell membrane, Tf is quickly internalized by invagination of clathrin-coated pits with formation of endocytic vesicles [111, 112]. In an acidic environment such as inside the endosome (pH = 5.5) [113, 114], the release of iron is favored [115]. The release of bound iron is induced by the reduction of bound Fe^{3+} to Fe^{2+} [116, 117]. Upon release, the metal-protein bond is loosened by protonation of the anion. After the release of iron, receptor bound transferrin (Tf) is transported to the cell surface. Here, Tf is released from its receptor and circulates again and undergoes further rounds of iron delivery [110–112, 118]. Due to overexpression of endogenous Tf receptors on various cancer cells, Tf has been used as a targeting agent to overcome the shortage of specificity of conventional therapeutic NPs or contrast media [119–122].

4.2.5 Apolipoprotein A1

Apolipoprotein A1 (ApoA1) is a lipid-binding protein that acts as a transporter for cholesterol in plasma. ApoA1 is produced mainly by the liver and the intestine as a preproprotein. After maturation, the protein is secreted into plasma as a lipid-poor/-free protein with a molecular weight of 28 kDa. ApoA1 is the main acceptor of cholesterol from artery wall cells, freeing them from excess fats [127]. Cholesterol, phospholipids, triglycerides and ApoA1 form precursors of high-density lipoproteins (HDLs) [128]. The major protein component of HDL is ApoA1 [129]. α -helices form amphipathic regions to which lipids can bind reversibly. A lack of ApoA1 is associated with atherosclerosis [130]. Moreover, a cardioprotective effect of HDL in humans is suspected [131]. The

	SA	Fib	Tf	FN	ApoA1
mass [kDa]	69	340	80	440	28
amino acids	585	2800	679	2355	243
average concentration in blood plasma [mg/ml]	40	3	3	0.3	1.3-1.6
isoelectric point	4.8	5.5	5.2-5.9	5.5-6.0	5.6
spherical R_h [nm]	3.3-3.6	9	3.6	9	3
size [nm]	8x8x3	6.7x11	4.2x10x7	15.5x8.8	3.6x6.3
shape	globular	rod-like	prolate ellipsoid	elongated	ellipsoid, horseshoe

Table 4.1: Overview of the properties of proteins used for NP binding studies. Molecular weight, number of amino acids, average concentration in plasma, isoelectric point, spherical hydrodynamic radius, geometrical size and shape. [100, 123–126]

role of lipoproteins for barrier crossing is under discussion [78, 132]. In Alzheimer’s Disease (AD) patients, ApoA1 binds to $A\beta$ and prevents the neurodegenerative impact of this protein [133]. In addition, a potential therapeutic benefit in cancer treatment has been highlighted [134, 135].

4.3 Amyloidogenic Proteins

Amyloidogenic proteins are related to serious diseases such as Alzheimer’s Disease (AD) or Parkinson’s Disease. The proteins involved aggregate into characteristic fibrils. This process is not only of interest due to medical reasons, it is also valuable for engineering new nanomaterials that are based on hierarchical self-assembly. In this thesis, we study the aggregation process of amyloid beta ($A\beta$) and characterize several species of α -synuclein (α -syn).

4.3.1 Amyloid β_{1-42}

$A\beta$ is a peptide that is present in the brain and is under suspicion to cause a common form of dementia: AD. The concentration of $A\beta$ in the cerebrospinal fluid (CSF) is in the nanomolar range ($\approx 500 \text{ ng l}^{-1}$) [136, 137]. It is a product of the normal cellular metabolism and thus $A\beta$ appears in the brain fluids of all humans. Therefore, it is assumed that $A\beta$ might be of physiological relevance in the central nervous system.

The list of suggested tasks ranges from ion channel modulation, kinase activation and regulation of the cholesterol transport to learning and memory [138]. In AD, the balance between generation and clearance of A β is disturbed. Either too much A β is released into the CSF or the removal does not work properly. Both lead to an increased level of A β in the CSF, later to the aggregation of A β and AD. So far, the only known natural source of A β is the amyloid precursor protein which is a transmembrane protein that is expressed in most cell types [138]. The amyloid precursor protein is cleaved by several secretases and the resulting product is A β . Depending on the cutting point, A β molecules with various length can be produced, ranging from 39-43 amino acids. In this work, the focus lies on A β_{1-42} due to its prominent role in the process of aggregation. Monomeric A β has a molecular weight of approx. 4.5 kDa and a hydrodynamic radius of 0.90 ± 0.05 nm [139]. An α -helical structure or random-coil structure was found for the monomer [138]. The A β monomer is assumed to evolve into a β -hairpin conformation in water that is stabilized by intramolecular H-bonds and antiparallel β -strands [140]. At physiological pH, A β adopts quickly β -sheet structure [141]. Assembled forms of synthetic A β are highly sensitive to preparation and incubation [142] and are therefore called metastable. Synthetic A β in aqueous solution also tends to self-aggregate [143, 144]. Factors that favor aggregation are the presence of detergents, a high ionic strength or the addition of salts to A β solutions [141].

4.3.2 α -synuclein

The presynaptic protein α -syn is related to Parkinson's Disease in a similar way as A β is to AD. Deposits of α -syn, so-called Lewy bodies, in the brain are the pathological hallmark of the disease. α -syn has a molecular weight of 14 kDa and is mainly found at the tips of neurons. It may be involved in the transport and regulation of dopamine, but the function of α -syn in healthy people is not well understood yet [145-147]. Interactions of α -syn with a variety of proteins and with lipid vesicles are known [148-151]. The latter leads to the assumption that α -syn may play a role in lipid metabolism [152, 153]. In the cytosol, α -syn exhibits a random-coil secondary structure in aqueous solution [154, 155]. The sequence of α -syn consists of three main regions: the N-terminal region, the NAC region and the C-terminal region. An amphipathic helical conformation in its N-terminal and the NAC region is induced upon the interaction with phospholipid membranes [156, 157]. The NAC region is mainly hydrophobic and seems to be essential for fibrillation [158].

4.4 Blood Plasma and Serum

In order to perform preliminary experiments under closer to physiological conditions, but before the more complex *in vivo* experiments, the used buffer is replaced by a biological fluid, such as blood plasma or serum. For instance, instead of a conventional buffer, plasma or plasma buffer mixtures are used to mimic the *in vivo* situation partially. In literature, the expressions “serum” and “plasma” are repeatedly used interchangeably, although these blood extracts are not the same from a physiological point of view.

Both fluids are prepared in dissimilar ways, using no or different chemical additives and therefore different biomolecules are inactivated or even precipitated from the final solution [159]. For the extraction of plasma, blood is treated with a substance to avoid coagulation. Anticoagulants used are sodium citrate, heparin or ethylenediaminetetraacetic acid (EDTA). A careful selection of the anticoagulant is necessary to ensure that the biological phenomena observed are representative. For instance, coagulation factors such as factor VIII or fibrinogen (Fib), stay active in citrate blood, but they are inactivated when EDTA is used [160, 161]. EDTA removes calcium or other divalent ions from the sample to avoid coagulation. In this way, enzymes that require calcium, are inactivated, e.g. ADAMTS13 (a disintegrin and metalloprotease with thrombospondin type 1 motifs 13) that regulates the length distribution of the protein von Willebrand factor [162]. This is essential for experiments or diagnostic tests, in which the activity of an enzyme is determined or even quantified [163]. Furthermore, plasma can be gained without any additives during plasmapheresis. In contrast, serum is produced by the centrifugation of coagulated blood. The supernatant is collected and contains all natural components of blood, except for the coagulation agents that were used during coagulation. Nevertheless, it is observed that the total protein content in serum is lower than in plasma [164]. Strongly simplified, serum can be defined as blood plasma without or only with low amounts of coagulation factors such as fibrin or Fib. Centrifugation is crucial for both extracts to get rid of all cells contained in solution. The difference in protein corona composition of NPs incubated in human serum and plasma was shown by Mirshafiee *et al.* [95]. An actual difference in the composition was found, indicating that plasma is the more realistic system for *in vitro* experiments mimicking the *in vivo* situation.

Instead of human plasma, fetal bovine serum (FBS), is often used to imitate the physiological situations. FBS plays a major role in cell culture as a part of medium to grow cells. Thus, it is a common product that is easily accessible in large amounts as a by-product of the industrial production of dairy products and meat. An advantage of FBS is that

it is possible to sterilize it by filtering, decreasing the risk of bacterial contaminations for experiments. For mimicking molecular effects such as molecular crowding and establishing new routines, FBS is a good alternative to human serum or plasma.

4.5 Viscosity of Mixtures of Fetal Bovine Serum and Phosphate Buffered Saline

There is a certain trend towards applying FCS in the area of medicine, e.g. to characterize drug nanocarriers, or clinical applications such as diagnostics [22, 165, 166]. Measurements in plasma, serum or mixtures of biofluids and buffer are often used to perform experiments under closer to physiological conditions. In Chapter 5 of this thesis, FBS is added to precoated NPs to study the reversibility of protein binding and in Chapter 6 the influence of biofluids from different species on the release profile of thermosensitive liposomes (TSLs) is investigated. It has been stated that FCS is suitable to measure in complex fluids such as plasma or serum, but there is no systematic study that considers all the various aspects that have to be taken into account when measuring in biofluids. Measuring in complex biofluids provides additional challenges in the evaluation of data. Scattering and hydrodynamic effects due to crowding have to be considered [167–169]. Crowding occurs when high concentrations of macromolecules are present and that this presence can alter the properties and interactions of biomolecules in solution. Properly determined values of the viscosity in literature are rare. Often important information on the underlying experiments are missing such as the ionic strength of the dilution buffer or the temperature at which the viscosity or density of a medium was determined. Although temperature-dependency of media and diffusion is known, it is not always considered properly in analysis. In order to ensure proper results from FCS measurements and analysis of experiments in mixtures of FBS and PBS, physical properties of these solutions, such as density and viscosity, are determined in a systematic way and at experimentally relevant temperatures: room temperature 22 °C and body temperature 37 °C. GFP is used as a test molecule, since no binding to serum components was observed in previous experiments. Crowding leads to an increase of the dynamic viscosity and a slowing down of the diffusion. This effect has to be considered in the analysis, especially for the conversion from diffusion constant D to the hydrodynamic size using the Stokes-Einstein equation (Equation 2.35), where the correct value for the viscosity of the surrounding medium $\eta(T)$ has to be used. The density of mixtures of FBS and PBS

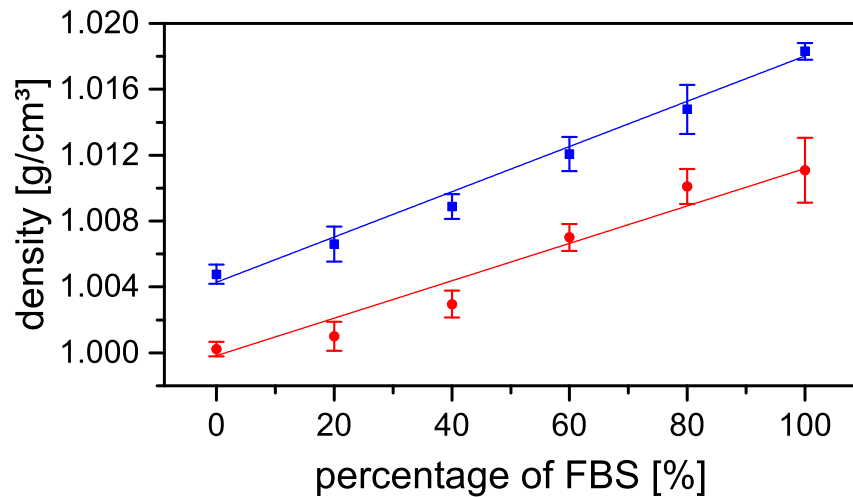


Figure 4.2: Density of mixtures of PBS and FBS ranging from 0 to 100% FBS at room temperature 22 °C (blue squares) and physiological temperature 37 °C (red circles). Data is the average of 30 measurements. Linear fits to guide the eye. Error bars represent the standard deviation.

was measured at 22 and 37 °C using a Gay-Lussac pycnometer (Figure 4.2). The density is an input parameter for viscosity measurements. The viscosity was determined with a capillary viscometer with a heating element (Anton Paar).

The dependence of the viscosity on temperature and the fraction of FBS is shown in Figure 4.3. These results are clearly contradictory to statements such as “Although the viscosity of plasma is variable and higher than that of PBS, which could alter the diffusion time, 1:1 or greater dilution is sufficient to normalize the viscosity to that of water” [165]. The suitability of estimations should be questioned carefully, and in case of doubt be rechecked, before use. Assuming a viscosity of water of $\eta(22\text{ °C}) = 0.955\text{ mPa s}$ and $\eta(37\text{ °C}) = 0.692\text{ mPa s}$, a deviation of up to 13-15% is observed for 40% FBS at the corresponding temperature. The impact of a crowded solution on the structure parameter was evaluated in a study of crowded vesicle solutions by Engelke et. al [170]. The conclusions of this paper are transferable to measurements in biofluids. The importance of control measurements and a well-defined calibration cannot be emphasized enough for FCS measurements in complex media [170, 171]. In an appropriate calibration measurement, the distortion of the focal volume due to scattering is independent and can thus be determined separately. A correct calibration can compensate for several artifacts, making FCS measurements in complex and scattering media reliable.

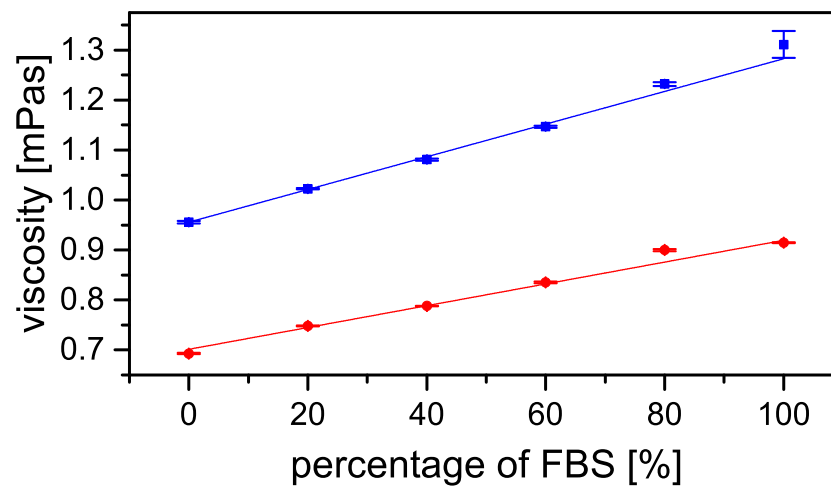


Figure 4.3: Viscosity of mixtures of PBS and FBS ranging from 0 to 100% FBS at room temperature 22 °C (red circles) and body temperature 37 °C (blue squares). Data is the average of at least 50 measurements. Linear fits to guide the eye. Error bars represent the standard deviation.

Chapter 5

Interaction of Proteins with Solid Nanoparticles

The objective of the work described in this chapter is to gain insights into the interactions of proteins and solid NPs from a fundamental point of view. Knowledge of these processes is relevant for understanding how NPs interact with living organisms. As outlined in Chapter 4, NPs acquire a biomolecular corona when they are in contact with biological fluids. The interaction with and the uptake by cells is dominated by the corona, for instance dictating the biocompatibility and efficacy of nanotherapeutics. In order to be able to elucidate how the biomolecular corona affects these reactions, one has to first understand the corona itself, in particular its kinetics, meaning the types of biomolecules that form it, their abundance and their residence times. To this end, four representative blood plasma proteins, that are presented in Section 4.1, and several types of NPs are chosen. The used NPs are characterized in the following section.

5.1 Solid Nanoparticles

Many different types of nanoparticles are available to address the diverse and evolving needs of research. Polymer, silica and further NPs are available with different surface chemistries and in a range of sizes. A NP is defined as a particle with a spherical size between 1 and 100 nm in diameter, in a broader definition NPs can have a size of up to 10,000 nm. Nano-sized objects behave in a very unique fashion in many respects, compared to their bulk form and therefore have to be characterized separately.

5.1.1 Silica

The application of silica NPs is widely spread in all areas of industry. Silica particles are inherently hydrophilic and negatively charged. NPs made of silica are very stable compared to polymer microspheres. These NPs are available with various chemical surface modifications that allow to tune their physico-chemical properties. Their mesoporous structure makes them suited to load drugs into them and use them as biomedical devices [172–174]. Silica NPs are supposed to have a large specific surface area. Small-diameter spheres present more surface area per unit mass, while larger spheres present more surface area per bead.

5.1.2 Polystyrene Latex

Polystyrene NPs are as widely distributed as silica. Due to their hydrophobicity, they strongly bind hydrophobic molecules such as proteins or nucleic acids. Thus, these NP can be easily coated with specific proteins by covalent binding, reducing the capacity to bind biomolecules non-specifically. Polystyrene NPs are available with various surface chemistries. In particular, particles with carboxyl (PSCOOH) surfaces are popular. PSCOOH particles are negatively charged, sensitive to low concentrations and multi-valent cations. These beads are made by the formation of many single chain polymers which may be likened to a ball of “wool”. Thus, the determination of the surface area is complicated and this area may be much greater that predicted. This is important for protein binding and charge calculations.

5.1.3 Further Nanoparticles

The following particles in suspension were kindly provides from the JRC Nanomaterials repository NanoMILE project.

Fe dex SPION

Superparamagnetic iron oxide nanoparticles (SPION) coated with dextran (Dextran-SPION) are widely applied for clinical magnetic resonance imaging of cancer tumors and have been utilized to detect metastases and to delineate primary tumors [175]. Moreover Dextran-SPION have been used for imaging inflammatory components of atherosclerosis [176]. These NPs are injected directly into circulation. Due to their common application

in medicine, there is a need to investigate their potential hazards and nanosafety. To determine protein corona assembly Dextran-SPION particles with a primary size of 20 nm were chosen (NanoMILE code: N4I121114b).

Titania

Titania (TiO_2) is especially known for its usage in food industry, its presence in sunscreen and its application in paint industries [177]. It is used as a catalyst or in self-cleaning surfaces [178]. Titania NPs are considered to be poorly soluble. NPs made out of titania are negatively charged and have a hydrophilic surface [124]. They are considered to be not harmful to the environment, making them a popular "negative control" in *in vitro* and *in vivo* experiments [179]. In the context of protein corona studies, an understanding of how the interaction of proteins with titania particles affects the harmlessness is necessary. Therefore, uncoated TiO_2 particles with a primary size of 70 nm were chosen (NanoMILE code: NIST-TiO₂-SRM1898-240214b).

Ceria

There is a wide range of applications of ceria (CeO_2) NPs. They are used as UV-absorbent, polishing agent for silicon wafers and as a fuel additive to decrease diesel particle emission [180, 181]. Moreover, ceria nanoparticles can store hydrogen [182]. With this diverse applicability, the need for understanding the biocompatibility and thus for the protein corona formation comes up. To this end, uncoated CeO_2 particles with a primary size of 33 nm were chosen (NanoMILE code: NM-212).

5.2 Understanding the Kinetics of Protein-Nanoparticle Corona Formation

The content of the work presented in this section is the subject of publication P1 [183]. The following text and figures are adapted from this publication, with only a few editorial changes. Theory and simulations in P1 were performed by O. Vilanova. P. M. Kelly contributed sodium dodecyl-sulphate polacrylamide gel electrophoresis (SDS-PAGE) and differential centrifugation sedimentation (DCS) to P1 [183]. The original article is attached in Appendix · P1.

5.2.1 Motivation

New types of NPs for various applications are developed every year as nanotechnology advances. The sheer number of already existing and newly developed NPs makes it impractical to investigate the interactions of each type of NP with biological fluids and to test completely if they are eventually harmful to humans or nature. The interaction of the NPs with cells is often mediated by the biomolecular corona and not directly by physico-chemical properties of the nanomaterial itself. The underlying molecular mechanisms that regulate corona formation and kinetics are still poorly understood. In order to overcome this limitation, an approach that combines theory and basic experiments is needed to develop mathematical models for the potential hazards caused by nano-sized particles. With this combination the large relevant time span ranging from 100 μ s to hours can be probed either by simulations or experiment, respectively. If there is a systematic understanding of the kinetics of protein-NP corona formation, it might be possible to predict eventual hazards and control the NP composition based on a hierarchy of equilibrium binding constants and some basic physical key parameters of the nanomaterial. Here, the aim is to understand the time evolution of the composition of the protein corona in a three-component simplified model plasma. The results of four experimental techniques, FCS, DCS, microscale thermophoresis (MST) and SDS-PAGE, are compared to two independent theoretical approaches, molecular dynamics simulations and non-Langmuir differential rate equation (NLDRE) theory. By using the experimental results for single protein solutions as an input and combining two theoretical approaches, it is possible to predict the kinetics of the protein corona.

5.2.2 Computational and Theoretical Approach

For molecular dynamics simulations, a coarse-grained model is implemented that adopts a description within the framework of the DLVO theory to qualify the protein-NP interaction. The theoretical approach is based on NLDREs. A combination of simulation and analytic theory is necessary to extrapolate the numerical results to physiologically relevant time scales (~ 1 h). The full simulations would take much longer than those achievable within a reasonable time. Details on the computational and theoretical approach can be found in the attached article in Appendix · P1 and its associated supplementary information [183].

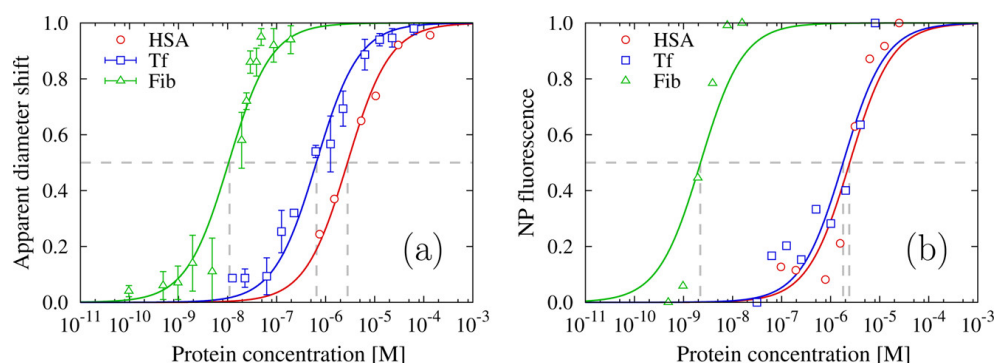


Figure 5.1: Experimental determination of binding affinity for silica NPs in monocomponent protein solutions of HSA (red), Fib (green), or Tf (blue), as a function of the molar concentration of proteins. For each set, the concentration at which the normalized data has the value 0.5 corresponds to the protein dissociation constant $K_D = K^{-1}$ (Table 5.1). (a) Normalized DCS apparent diameter of the NP coated by proteins with respect to the value with no proteins. (b) Normalized MST relative fluorescence F_{norm} after diffusion of fluorescently labeled NPs under thermal gradient. In both subfigures, symbols represent the experimental data, and lines are the best fits using the Equation 3.8. Molar concentration is expressed in $\text{M} = \text{mol l}^{-1}$. Reprinted with permission from [183]. Copyright 2016 American Chemical Society.

5.2.3 Equilibrium Binding Constants in Single-Protein Solutions

Due to the essential role of the binding affinities K , respectively its inverse $K_D = K^{-1}$, in the presented approach, their values are measured by two independent experimental techniques: DCS and MST. While MST probes the interaction of proteins and NPs directly in solution, for DCS the NPs are extracted from protein solutions after incubation [65, 184–186]. A combination of these two approaches ensures that reliable values for each of the proteins interacting with silica NPs are obtained. The results are shown in Figure 5.1. The fits were performed applying the law of mass action in the limit of low concentration of NPs ($[L]_{\text{tot}} \gg [R]_{\text{tot}}$) in terms of Equation 3.8. The sole free fitting parameter is K_D which marks the concentration for $Y = 0.5$. The values from both techniques agree on the order of magnitude, with the following hierarchy of dissociation constants: $K_D^{\text{Fib}} \ll K_D^{\text{Tf}} < K_D^{\text{HSA}}$. As shown in Table 5.1 the values for HSA coincide within the error bars and agree with previous literature [87, 187, 188]. The results for Tf and Fib are only of the same order of magnitude, however the MST measurements are biased more strongly by agglomerates of NPs than the DCS measurements [189]. The K_D values are used to determine the respective DLVO's Hamaker constants needed for the molecular dynamic simulations (see Equation S8 of the supporting information of [183]).

protein	K_D^{DCS} [μM]	K_D^{MST} [μM]
HSA	2.8 ± 0.2	2.4 ± 0.6
Tf	0.65 ± 0.08	1.8 ± 0.4
Fib	$(11 \pm 0.2) \cdot 10^{-3}$	$(2.2 \pm 0.9) \cdot 10^{-3}$

Table 5.1: Dissociation constants K_D determined with DCS and MST for HSA, Tf and Fib. Adapted with permission from [183]. Copyright 2016 American Chemical Society.

5.2.4 Competitive Adsorption in Two-Component Protein Solutions

Solutions containing two of the three named proteins are considered to test the competitive adsorption between different kinds of proteins. A sequential protocol in which we introduce one type of protein at a time into the initial NP suspension, enables a better comparison between experiments and simulations. Firstly, 100 $\mu\text{g}/\text{ml}$ silica NPs are incubated with different concentrations of HSA. After equilibration of the pre-coating step, 5 $\mu\text{g}/\text{ml}$ Fib are added to the solution and the adsorption kinetics of Fib onto the NP are studied. Simulations are performed before the experiments to check the predictive power of the approach.

Due to the hierarchy of the dissociation constants $K_D^{\text{Fib}} \ll K_D^{\text{HSA}}$, Fib is expected to displace the adsorbed HSA molecules on the surface of the NPs. As illustrated in Figure 5.2 a, the adsorption kinetics of Fib strongly depend on the initial concentration of HSA. The rate of adsorption of Fib clearly decreases for increasing concentration of HSA as shown by simulation. When the concentration of HSA changes from 0 to 10 mg/ml , the adsorbed amount of Fib on the NP decreases from $\simeq 90\%$ to $\simeq 35\%$ after 10 seconds of simulated time, respectively. Using the NLDRE theory to extrapolate the long-time behavior of the system, the following is predicted: Despite the much higher affinity of Fib to the silica surface, it would take more than 5 minutes for Fib to displace HSA and to have more than 50% of Fib adsorbed at 10 mg/ml HSA. Even after 30 minutes, the adsorption of Fib is still slower relative to pristine NPs and the saturation level is reached within the time frame of 100 minutes.

In order to validate the theoretical predictions, FCS experiments are performed following the same protocol as mentioned above. An excellent overall agreement of experimental results and theoretical predictions is obtained (Figure 5.2 a) and a change in the adsorption kinetics of Fib in the presence of competing proteins is verified. To further validate the quality of the theoretical predictions, the relative mass of proteins on the NP surface was determined using SDS-PAGE and densitometry (Figure 5.2 b). Again, the experi-

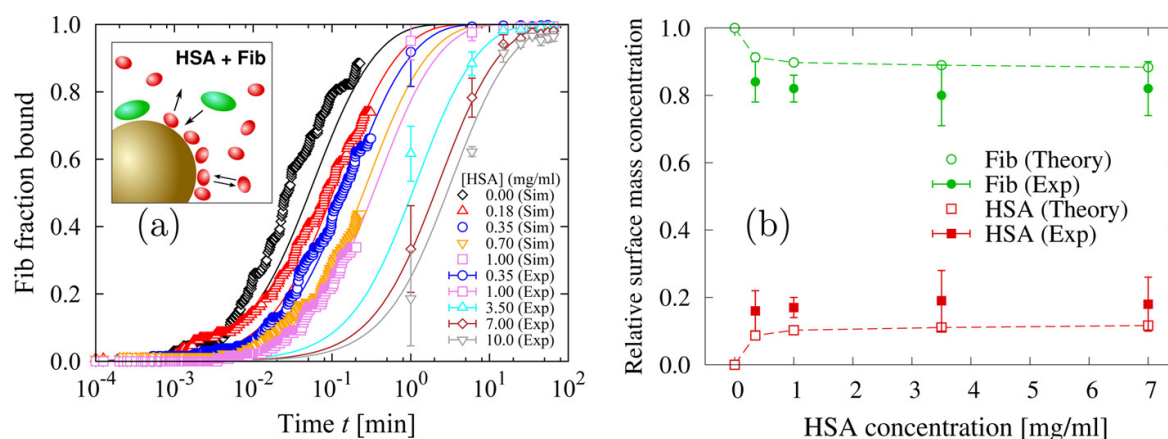


Figure 5.2: Two-component protein solution: Competitive adsorption of Fib onto silica NPs precoated with HSA at different concentrations. (a) Simulation results (open symbols without error bars) of the fraction bound of adsorbed Fib as a function of time are extrapolated to large time-scales, applying the NLDRE theory (lines), to enable us to compare our predictions with experimental data from FCS (symbols with error bars). The agreement is excellent. Concentrations are $5 \mu\text{g/ml}$ for Fib, $100 \mu\text{g/ml}$ for silica NPs, and for the lines from top to bottom, 0.00, 0.18, 0.35, 0.70, 1.00, 3.50, 7.00, and 10.00 mg/ml for HSA. Lines and symbols with matching colors correspond to the same HSA concentration. Inset: Schematic representation of Fib (green) displacing HSA (red) on the NP surface (golden). (b) Relative surface mass concentration of HSA (red) and Fib (green) after 120 min as a function of the HSA concentration in solution, as predicted from NLDRE theory (open symbols connected by a dashed line), and compared with data from SDS-PAGE (symbols with error bars). Reprinted with permission from [183]. Copyright 2016 American Chemical Society.

mental data follows the theoretical predictions with very good agreement, confirming the capability of the theory to predict the outcome for binary solutions. As a final test of the predictive power of the approach, simulations, theoretical evaluations and experiments are repeated using Tf instead of HSA during the precoating step. Experiments and theory match (Figure 5.3). This verifies the general applicability to other binary solutions.

5.2.5 Competitive Adsorption in Three-Component Protein Solutions and Memory Effect

For systematic extension of the approach to more complex solutions, the same procedure is used to study a ternary suspension of HSA, Tf and Fib. Therefore, a three steps exposure protocol is applied:

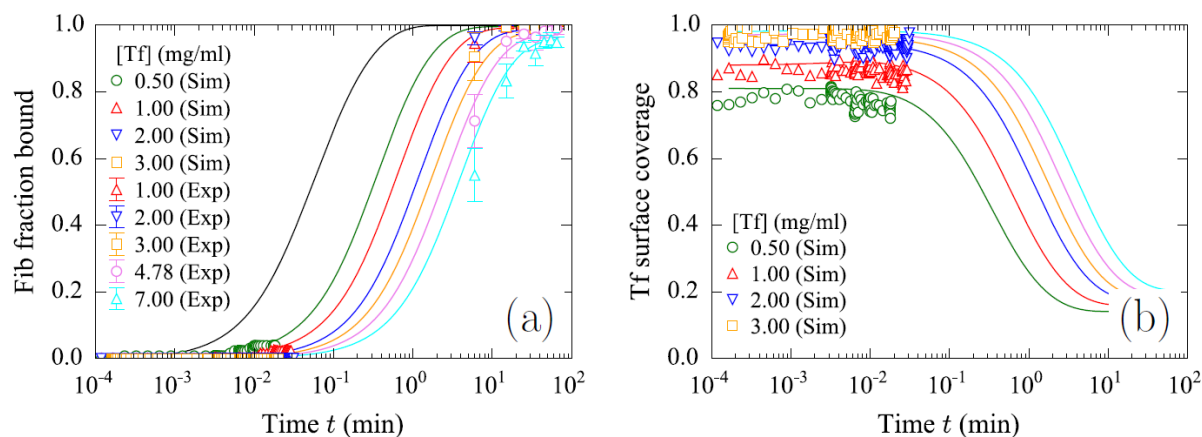


Figure 5.3: Competitive adsorption of Fib displacing a protein corona of Tf after incubation. a) As in Figure 5.2 but for Tf concentrations (for the lines from top to bottom) 0.00, 0.50, 1.00, 2.00, 3.00, 4.78, and 7.00 mg/ml. b) NP surface coverage of Tf from numerical simulations (open symbols) and non-Langmuir differential rate equation (NLDRE) theory (lines). Lines from bottom to top are for 0.50, 1.00, 2.00, 3.00, 4.78, and 7.00 mg/ml for Tf. Reprinted with permission from [183]. Copyright 2016 American Chemical Society.

1. Incubation of NPs in HSA
2. Addition of Tf, competition with HSA for NP surface is expected
3. Addition of Fib, competition with both present proteins for the corona

This process is visualized in Figure 5.4 a). Two cases of equal concentrations of HSA and Tf are considered in the following:

1. Low concentration case: 0.07 mg/ml of each protein, HSA and Tf
2. High concentration case: 3.50 mg/ml of each protein, HSA and Tf

The concentration of the silica NPs is fixed at 100 $\mu\text{g}/\text{ml}$ and the one of Fib at 5 $\mu\text{g}/\text{ml}$. Again, the single preincubation steps are run until equilibrium is reached and after the addition of Fib simulations are performed spanning $\simeq 0.1$ min. The long-time kinetics of Fib adsorption were extrapolated using the NLDRE theory. For the low concentration case, saturation of Fib is predicted to be reached ≈ 10 min (Figure 5.4 b), for the high protein case after roughly 50 min (Figure 5.4 c). FCS experiments confirm these predictions.

Comparing the results for ternary and binary solutions for the low concentration case, it is observed that for ternary solutions the adsorption of Fib is slightly slower than for

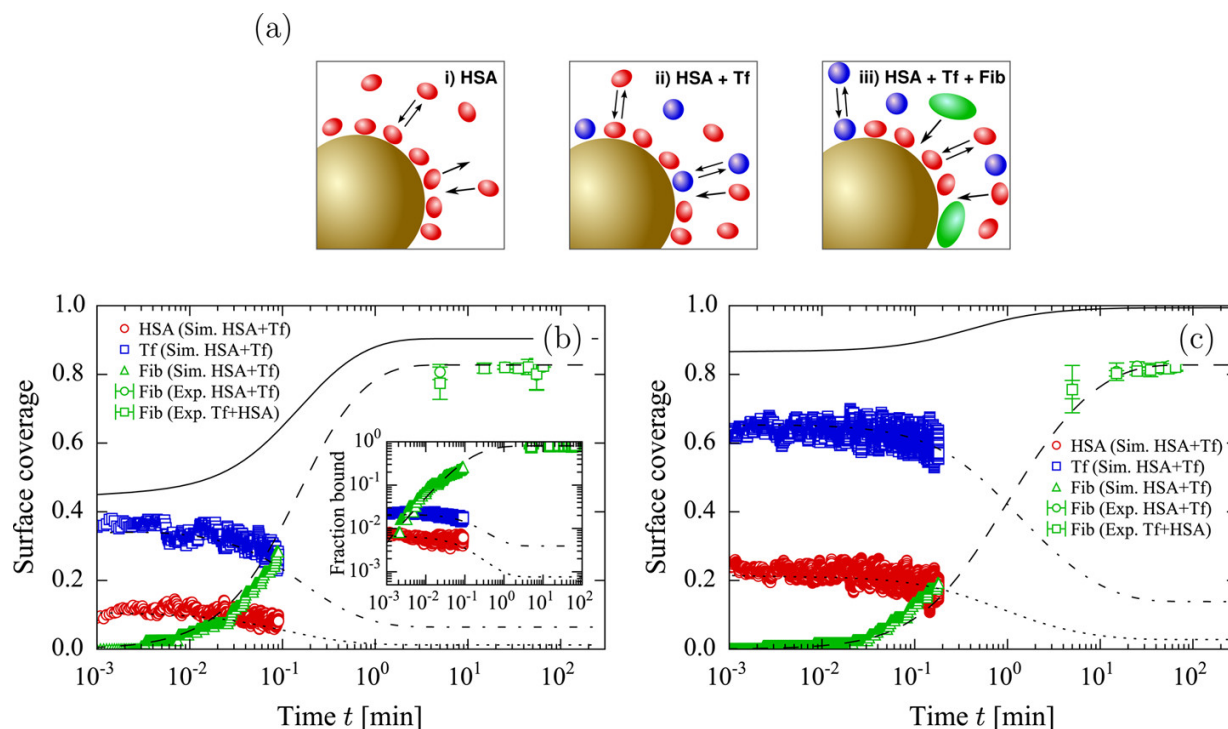


Figure 5.4: Three-component protein solution: Competitive adsorption of Fib on silica NPs precoated with HSA first and Tf next. (a) Schematic representation of the three-step adsorption protocol with Fib (green) displacing Tf (blue) and HSA (red) on the NP surface (golden). (b) Normalized surface coverage of HSA (red circles) and Tf (blue squares) for the low concentration case (both at 0.07 mg/ml), and Fib (green triangles, at 5 μg/ml) adsorbed on 100 μg/ml silica NPs as a function of time, calculated by simulations at short times ($t \leq 0.1$ min) and extrapolated to long time ($t \geq 200$ min) by the NLDRE theory (dotted line for HSA, dot-dashed line for Tf, dashed line for Fib, and solid line for the total surface coverage). The prediction for Fib compares well with the fraction bound of Fib measured by FCS (symbols with error bars) for $t \leq 3$ min. The two sets of experimental data refer to (circles) first precoating with HSA and next with Tf and to (squares) the vice versa order. The saturation value for the Fib surface coverage is reached for $t \approx 10$ min. Inset: Fraction bound of adsorbed proteins corresponding to the surface coverage in the main panel in double-logarithmic scale. (c) Same as in (b) but for HSA and Tf in the high concentration case (both at 3.5 μg/ml). Here, the saturation value for the Fib surface coverage is reached for $t = 50$ min. Reprinted with permission from [183]. Copyright 2016 American Chemical Society.

the binary case at a comparable total mass concentration. In the high concentration case, such an effect was not observed. A possible interpretation is that this is a consequence of the fact that the dissociation constants of HSA and Tf are comparable and both significantly higher than the one of Fib. As a result, the adsorption kinetics of Fib might be regulated only by the total mass concentration of the competing proteins. Within the error bar of simulation and experiment, no difference in the kinetics of Fib is observed, independent of whether NPs are incubated in the order HSA-Tf or *vice versa*. This observation supports the previous interpretation. Nevertheless, the experiments show an interesting phenomenon regarding the kinetics before the addition of Fib to the protein solution. A dependence on the order of incubation is observed. This effect is termed memory effect.

In order to quantify this phenomenon experimentally, two different incubation protocols are established. In protocol A, the silica NPs are incubated in 3.5 mg/ml HSA, then Tf is added at the same concentration for another hour. In protocol B the order of incubation is inverted with the same concentrations and times. The NPs are separated from the unbound proteins and their corona is analyzed using SDS-PAGE. The relative abundance of HSA and Tf is determined (Figure 5.5). The final amount of each protein depends on the protocol applied. In particular, the first incubated protein is always more abundant in the corona at the end of the procedure (Figure 5.5 b). The same qualitative result is obtained for low concentrations of proteins (0.07 mg/ml). This implies that the memory effect does not depend strongly on the initial concentration of proteins.

Possible mechanisms that induce the memory effect for the competition of HSA and Tf for the NP surface are discussed. For the computational model, the two different incubation protocols give the same corona after a transient time. Hence, the appearance of the memory effect implies that other interactions among proteins and NPs besides those included in the model exist. Under the assumption that the adsorption of proteins in the NP causes a change in the protein-protein interaction, a possible interpretation is that this difference is a result of a conformational variation of protein upon adsorption. More specifically, it is supposed that the change can be included in the model as a three-body interaction between proteins and NPs. This hypothesis proved to be sufficient to simulate the memory effect (Figure 5.5 c and d). As a result, the memory effect can be interpreted as a consequence of how the adsorption on the NP affects the interaction of the first-added protein with those adsorb at a later time, e.g., due to conformational changes, impeding the replacement of the first by the latter proteins.

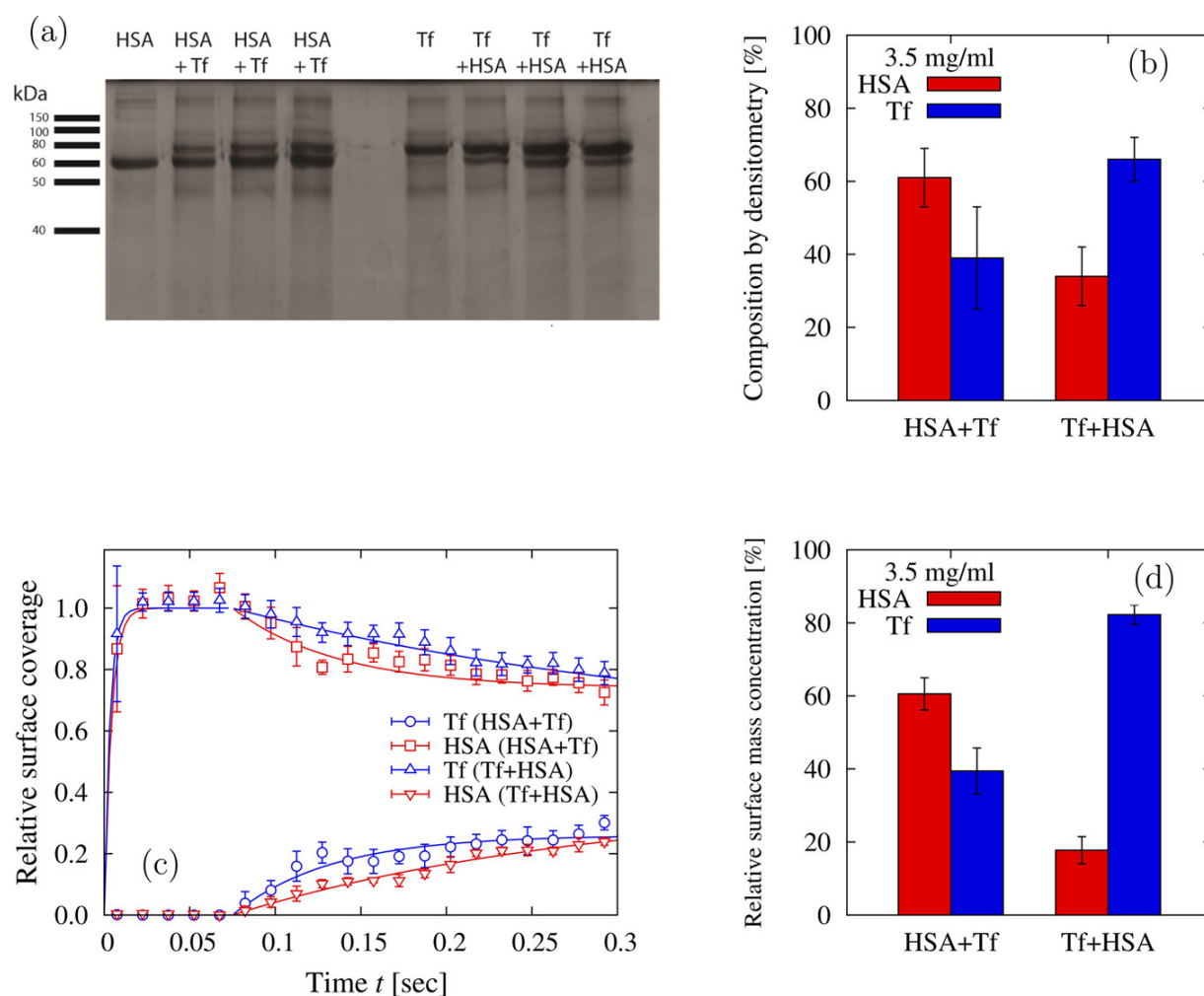


Figure 5.5: Memory effect in experiments and simulations for the high protein concentration case (a) SDS-PAGE gel analysis after incubating the NPs in HSA and Tf, in different orders: (from left to right, as indicated by labels) HSA alone; protocol A with HSA first and Tf second (three different samples); Tf alone; protocol B with Tf first and HSA second (three different samples). (b) Densitometry results for the percentage of protein corona composition after the gel analysis with NP incubation with HSA (red) and Tf (blue) following the same protocols as in panel a (as indicated by the labels on the bottom). The error bars are estimated as standard deviation among the three independent samples. Results are calculated after subtracting background noise. (c) Simulation results for the kinetics of the competitive protein adsorption of the model with three-body interaction between HSA, Tf, and NP: We show the relative protein adsorption on the NP of Tf (blue) and HSA (red) following the two protocols (protocol A: circle for Tf and squares for HSA, protocol B: triangles upward facing for Tf and triangles downward facing for HSA), as a function of time t . In both protocols, the incubation time is 0.075 s, and the quantities are normalized to the value of the main component at this time. (d) Relative surface mass concentration from simulations in panel c after $t = 0.3$ s, to compare with experimental results in panel b. Reprinted with permission from [183]. Copyright 2016 American Chemical Society.

5.2.6 Conclusions

A combination of simulations and theory with limited experimental information on single-protein solutions allowed for prediction of the composition of the corona in a ternary protein solution. When the environment changes, evidence of memory in the corona formation are found. The approach presented shows that it is possible to implement a concept toward the prediction of the kinetics of the corona and its composition in complex solution changing over time. This is especially important considering NPs that move around in the body. The key for understanding the modulation of the corona is the presented knowledge. Tuning the protein corona in a controlled way may be used to design specific NP properties such as better engineered drug delivery carriers.

5.3 Hierarchy of Protein Nanoparticle Binding Affinities

The content of the work presented in this section is the subject of manuscript M2. Experiments presented in manuscript M2 were performed by A. Das and T. Preiß. The following text and figures are adapted manuscript M2, with only a few editorial changes. The original manuscript is attached in Appendix · M2.

Differences in the interaction of proteins and NPs depend on the size, charge and stability of the NP as well as the size and charge of the proteins. Variation in adsorption affinities thus seems to be caused by the different protein structure and chemical nature of the NPs, resulting in diverging surface properties and consequently a hierarchy of binding proteins. In Section 5.2, an attempt to understand the corona composition in the presence of multiple kinds of proteins is presented. Experiments, simulations and theory are combined to investigate the corona kinetics of three blood plasma proteins. In this section, the experimental studies are extended to a range of NPs of comparable sizes, but different hydrophobicity. The protein-NP affinities in of four representative plasma proteins and six different kinds of NPs are explored:

- SA, Tf, Fib and FN
- silica, ceria, titania, PSCOOH, PSOSO₃H and Fe dex SPION.

Detailed portraits of the proteins and NPs can be found in Table 4.1 and Section 5.1, respectively. FCS is used to systematically study the binding of all possible combinations of the above mentioned proteins and NPs. The results are discussed in the protein-NP

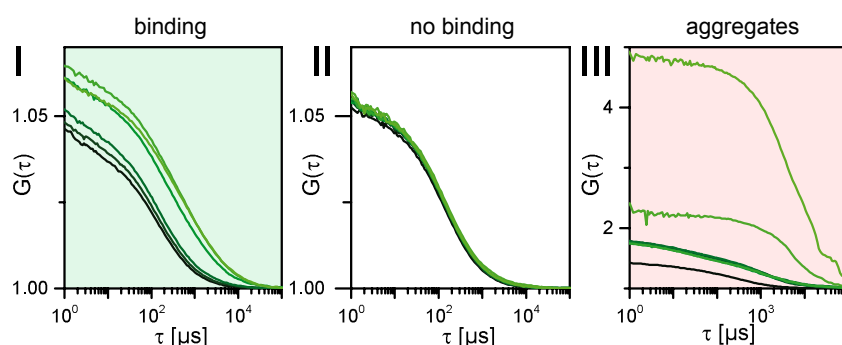


Figure 5.6: Typical evolution of the correlation curves of proteins after the addition of NPs. The kinetics fall into one of three categories: binding (I), weak or no binding (II), or aggregation (III).

interaction matrix. In the case of binding without aggregation, the binding curves in terms of the fraction of protein bound, as a function of increasing molar protein/NP-ratio, are measured. The determined binding curves are described by the law of mass action (Equation 3.7) allowing the determination of the adsorption area per protein. The binding affinities were compared to the off-kinetics of the corona proteins in the presence of competitive full serum proteins.

5.3.1 Systematic Measurement of Protein-Nanoparticle Combinations

All combinations of four representative blood proteins interacting with six kinds of NPs are studied. The change in the correlation function of the fluorescently labeled proteins after the addition of NPs is measured. Protein adsorption is found to fall into one of three categories: strongly binding (I), weakly binding or non-binding (II) and aggregating (III) (Figure 5.6).

In the first case, the amplitude of the FCS curves can increase with time, while the characteristic times shift slightly to larger values. Here, the proteins bind strongly to the NPs. The effective number of fluorescent objects decreases as proteins adsorb onto the NPs, while the correlation function develops a second slower component due to reduced diffusion of the bound proteins. Secondly, proteins may not bind to NPs or the interaction is so weak that binding is not detectable within the scope of the presented experiments. Here, the correlation curves do show no or little deviations from the curves of pure protein. The third case, frequently observed, is the appearance of extremely large amplitudes and broad tails of the correlation curves towards the longer time regime. In addition, the fluctuations of the raw fluorescence signal show abnormally high bursts.

Both observations indicate the presence of large aggregates of undefined size that diffuse sparsely and irregularly through the confocal volume with slow diffusion times. The evolution of the FCS correlation curves with time for all measured combinations of proteins and NPs is summarized in the interaction matrix (Figure 5.7).

Typical correlation functions at various time points from 0 to 60 minutes are presented. The observed kinetics are classified according to the criteria defined in Figure 5.7. The matrix demonstrates that after the interaction of proteins and NPs it is not always possible to preserve monodisperse systems. Instead, clear signatures of NP aggregation are observed. For instance, Fib gives rise to aggregates (Figure 5.7, second column). In contrast, bovine serum albumin (BSA) forms a stable coating on PSCOOH and PSOSO₃H, while it is weakly adsorbed on the remaining four NPs, although silica and polystyrene particles have similar size.

5.3.2 Theoretical Model of Protein Adsorption to Nanoparticles

Based on the theory presented in Chapter 3, the limits of weak and strong binding are discussed. The binding of protein P to nanoparticles NP is generally described as an adsorption process in analogy to the Langmuir adsorption model for adsorbates from liquids to a flat solid surface. In many studies, changes inferred to the NPs due to protein adsorption are measured. For instance, the measurement of the hydrodynamic diameter of the NP by FCS [66, 88, 190–193] or dynamic light scattering [194], or changes induced by proteins as measured in surface plasmon resonance [195], affinity capillary electrophoresis [196, 197] or fluorescence quenching [196, 198, 199]. In this chapter, the notation P/NP is used. Equation 3.8 turns into

$$\theta(P)_{NP} = \frac{[PS]}{[S]} = \frac{[P/NP]}{[P/NP] + K_D/NP} \quad (5.1)$$

where S is the total number of available binding sites in solution, $S = NP \cdot s$ with s being the number of binding sites per NP. K_D/NP describes the normalized equilibrium dissociation constant.

However, an important caveat needs to be addressed when this equation is used in experiments, where the protein is titrated against the NP. Applying Equation 5.1, it is assumed that the total concentration of protein added to NP solution is almost equal to the concentration of unbound protein P. In the case of strong binding, the free proteins are depleted, leading to strong deviations of Equation 5.1 from the non-approximated

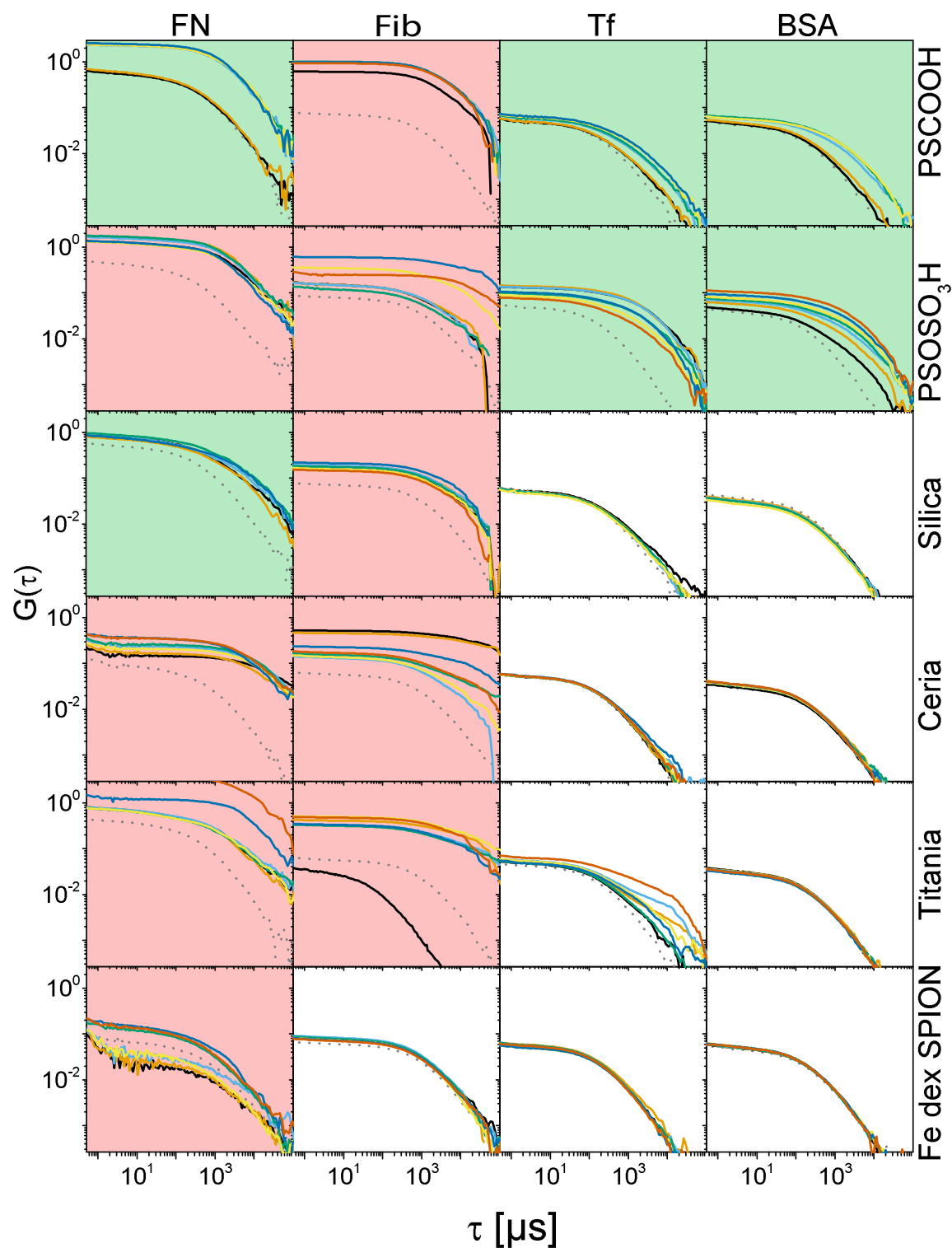


Figure 5.7: Matrix of FCS kinetics of all possible combinations of proteins and NPs showing the time dependent evolution of the FCS correlation: pure protein: dotted, 5 min after NP addition: black, 10 min: orange, 20 min: light blue, 30 min: green, 45 min: yellow, 60 min: dark blue. The data is highlighted according to the behavior: aggregation (red), strong binding (green) and weak or no binding (white).

law of mass action

$$\begin{aligned} \vartheta(P)_{NP} &= \frac{[PS]}{[PS] + [S_{\text{free}}]} \\ &= \frac{([s] + [P/NP] + K_D/NP) - \sqrt{([s] + [P/NP] + K_D/NP)^2 - 4[s][P/NP]}}{2[s]}. \end{aligned} \quad (5.2)$$

A comparison of the results for both equations is shown in Figure 5.8a). The deviations for strong binding ($K_D/NP < 100$) are visible. While for weak binding the Langmuir isotherm is applicable, it is not appropriate for the determination of K_D/NP in case of strong binding and leads to significant overestimation of the binding affinity.

As mentioned in Section 3.4, the amount of free and bound protein is determined. The concentration of the labeled protein is fixed, while the concentration of NP is varied. For this case, Equation 3.7 can be rewritten in the P/NP notation as

$$\begin{aligned} Y(P/NP)_P &= \frac{[PS]}{[PS] + [P_{\text{free}}]} \\ &= \frac{([s] + [P/NP] + K_D/NP) - \sqrt{([s] + [P/NP] + K_D/NP)^2 - 4[s][P/NP]}}{2[P/NP]}, \end{aligned} \quad (5.3)$$

that merges into the strong binding model of Milani *et al.* [21] for $K_D/NP \ll 1$, discussed in Section 3.3. Equation 5.3 is theoretically evaluated for various K_D/NP but fixed concentration of binding sites per NP, s , in Figure 5.8b). The transition to the strong binding model for decreasing K_D/NP is clearly visible. In short, the strong binding model assumes that proteins are strongly bound to NP in such a way that all proteins are adsorbed up to the point when all binding sites available on NP are occupied by proteins. The sharp discontinuity at this point is illustrated in Figure 5.8b) and gives the number of available binding sites per NP.

5.3.3 Determination of Protein Adsorption Area and Binding Affinity

If the fraction bound is plotted versus P/NP, the maximum number of molecules adsorbing in a monolayer per NP, i.e. the number of binding sites per NP, can be directly read from the graph. Knowledge of the number of binding sites per NP enables estimating the surface area available for each protein. For instance, the binding of FN to silica NPs

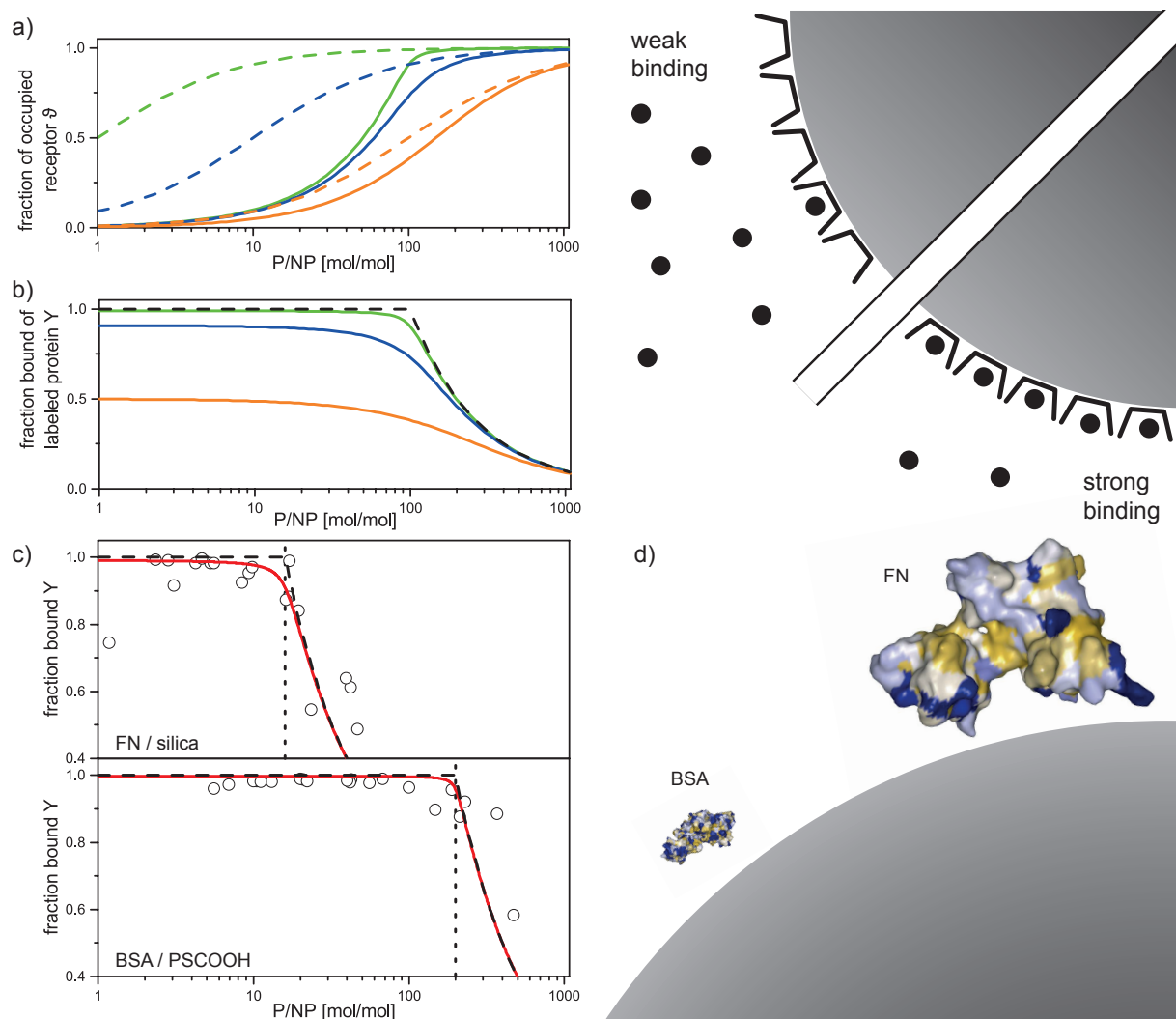


Figure 5.8: Theoretical analysis of protein-NP binding curves a) Analysis of the surface coverage of NPs. Fraction of NP coated according to the Langmuir adsorption model (dashed) and according to the exact solution of the law of mass action shown in Equation 5.2 (solid line). Data are plotted for different K_D/NP : 1 (green), 10 (blue) and 100 (orange) b) Fraction of protein bound to NPs according to the law of mass action for the case of strong binding (dashed lines) and for its exact solution. c) Adsorption measurements for FN/silica and BSA/PSCOOH. Solid red lines are fits according to Equation 5.3. Fits according to the strong binding model (Equation 3.17) are represented by the dashed black line. The number of binding sites per NP may be read off from the position of the kink (vertical dotted line). d) To-scale representation of the proteins BSA and FN and a NP with a diameter of 100 nm.

	FN	Tf	BSA
material NP	silica	PSOSO ₃ H	PSCOOH
s	16	300±100*	200
surface area per protein [nm ²]	1963	105	157
K_D/NP	0.15	0.31	0.41
desorption rate k_{off} [min ⁻¹]	2.7×10^{-3}	8.3×10^{-3}	8.8×10^{-3}

Table 5.2: Values determined from fitting in Figures 5.8 and 5.8c). A correlation between the desorption rate k_{off} and the normalized dissociation constant is K_D/NP indicated.
* from Milani *et al.* [21]

and of BSA to PSCOOH NPs are analyzed in Figure 5.8 c. Both NPs have a diameter of 100 nm. The red line is the best fit to Equation 3.7. For FN/silica $s = 16$ binding sites per NP and a normalized equilibrium constant $K_D/NP = 0.15$ is obtained, and for BSA/PSCOOH $s = 200$ and $K_D/NP = 0.41$ (Table 5.2). The average area available per protein is 1963 nm² for the first combination, and 157 nm² for the second one. The results of BSA/PSCOOH are in good agreement with former studies of Milani *et al.* [21]. There, the binding of Tf to PSOSO₃H NPs of the same size were evaluated. Considering that Tf is only slightly larger than BSA, it is consistent that the available surface area per protein is of the same order of magnitude. The data reflects the correct tendency that BSA has a smaller adsorption area than FN in accordance with the fact that the hydrodynamic radius is smaller by a factor of 3 compared to FN.

The results of the interaction matrix are only a first indicator of the binding behavior. In the case of weak or no binding, a systematic screening through a wide range of protein and NP concentrations is necessary to obtain a meaningful representation of the fraction bound versus P/NP. Three combinations are selected that showed no aggregation in the interaction matrix: BSA/PSCOOH, BSA/TiO₂ and BSA/CeO₂. The concentration of BSA ranges from 45 nM to 45 μM, while the NPs' ranges from 1 μg/ml to 1 mg/ml (Figure 5.9). In the case of binding of PSCOOH, the fraction bound is high at low protein concentration and high NP concentration and falls off with increasing protein and decreasing NP concentrations. For TiO₂ and CeO₂, only a very low fraction bound in all measured cases is observed. These measurements confirm that in both cases the proteins bind very weakly to NPs, which, in principle, was already shown in the interaction matrix, but has now been confirmed over a larger range of protein and NP concentrations.

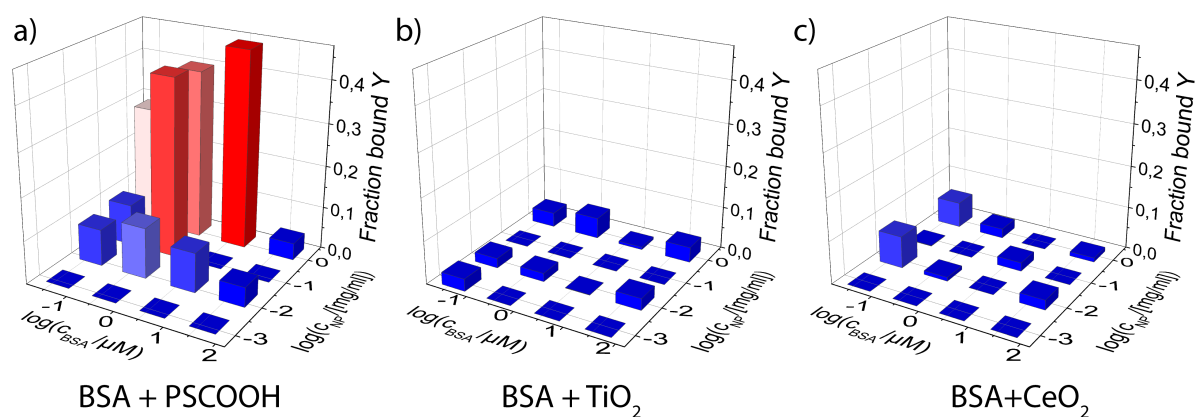


Figure 5.9: Fraction bound of BSA to a) PSCOOH NPs, b) TiO₂ NPs and c) CeO₂ NPs from zero (blue) to 50% (red) as a function the concentration of BSA and NPs. While PSCOOH shows relevant binding with BSA that depends on both, the concentration of protein and NP, TiO₂ and CeO₂ show very little to no binding.

5.3.4 Hierarchy of Desorption Kinetics

A relation of the binding affinities to the resistance to competitive binding is probed. To this end, NP with a layer of adsorbed labeled proteins are formed by incubation for at least one hour. The off-kinetics are measured after the addition of competitive serum proteins (10% FBS). The amount of free and bound protein is measured using FCS in the time course of 1 hour. This type of experiment is performed for those combinations that showed strong binding in the interaction matrix. The desorption kinetics follow an exponential decay (Figure 5.10). However, the majority of protein adsorbed is not fully removed within the time of our experiment, as indicated by considerable offsets in the time courses. This offset may be interpreted as the hard corona that seems to be irreversibly bound to the NP on the time scale of the reversibility experiments. The characteristic desorption rates k_{off} is determined. The desorption rate ($k_{off} = 1/t_{off}$) is calculated from these values. In general, the smaller proteins (BSA and Tf) are replaced more efficiently than larger proteins such as FN. Furthermore, the kinetics of the protein desorption depends on the NP type. For instance, BSA shows a faster desorption rate from PSCOOH than PSOSO₃H ($8.8 \times 10^{-3} \text{ min}^{-1}$ vs. $2.4 \times 10^{-3} \text{ min}^{-1}$). Most importantly, however, there seems to be a correlation between the desorption rate k_{off} and the experimentally determined normalized dissociation constant K_D/NP . Knowing that $k_{off} = K_D \cdot k_{on}$ and assuming that k_{on} is independent of protein and NP type, an increasing off-rate with increasing values for K_D/NP is expected. The values determined

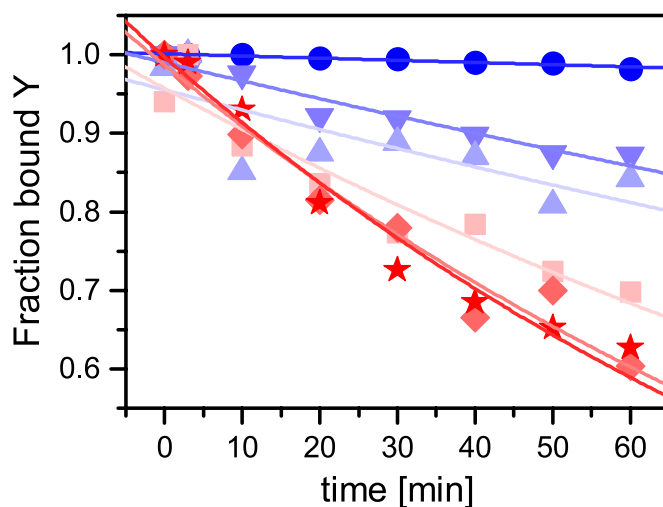


Figure 5.10: Desorption kinetics of protein coated NPs in FBS for various combinations of proteins and NPs. The characteristic desorption rates are determined by exponential fitting. The desorption rate k_{off} for BSA with PSCOOH (star) is $8.8 \times 10^{-3} \text{ min}^{-1}$, Tf with PSOSO₃H (diamonds) $8.3 \times 10^{-3} \text{ min}^{-1}$, Tf with PSCOOH (squares) $5.6 \times 10^{-3} \text{ min}^{-1}$, FN with silica (upwards triangles) $2.7 \times 10^{-3} \text{ min}^{-1}$, BSA with PSOSO₃H (downwards triangles) $2.4 \times 10^{-3} \text{ min}^{-1}$ and for FN with PSCOOH (circles) $3.0 \times 10^{-4} \text{ min}^{-1}$.

for BSA/PSCOOH, Tf/PSOSO₃H and FN/silica are in agreement with this expectation (Table 5.2). It is worth noting that the addition of serum to aggregates did not lead to a desorption or redispersion of the complexes.

5.3.5 Conclusion

This study is an attempt to find a systematic behavior of the interactions of representative blood proteins and NPs. The interactions may be classified as aggregation, strong binding, and weak or no binding. All three classes are identified in the interaction matrix. The data suggests that proteins that are large and act as natural coagulators, such as Fib and FN, are more susceptible to aggregation. These proteins are likely to shield NPs, reduce the overall charges of the NPs and promote cross-bridging between NPs by binding to other proteins. When proteins bind to NPs without disturbing their colloidal stability, binding isotherms in accordance with thermodynamic models of protein adsorption are observed. The importance of usage of the full law of mass action in the case of strong binding is stressed, since protein concentrations are readily depleted in the presence of strongly adsorbing NPs. In case of strong binding, K_D/NP , as well as the average area occupied by the adsorbed proteins, have been determined. These

characteristic parameters of the protein-NP interaction are meaningful values and have predictive power. For instance, it is shown that the protein adsorption area correlates with the hydrodynamic bulk size of the protein. The stability of the protein layers in the presence of competing serum and the desorption kinetics are evaluated. The desorption kinetics of proteins is directly related to the hierarchical order of K_D /NP. Competitive binding biomolecules are able to quickly detach protein layers, which are weakly bound, whereas some proteins are strongly bound. This reinforces the hypothesis that the NPs retain "memory" of the strong binding proteins, which they first encounter in their travel through different environments, as discussed in Section 5.2. Hence, the study of thermodynamic binding of each kind of protein allows for ranking of protein-NP affinities and represents a step towards a better understanding of protein-NP interaction in biological environment, for instance in serum or plasma. Systematic measurement of protein-NP interactions will be valuable to the biomedical community but requires the consideration of protein and NP concentrations especially in the case of strong binding. The dissemination of tabulated protein-NP data in publically accessible libraries, such as nanosafetycluster.eu, is beginning to emerge. There is hope that databases combined with theoretical modeling tools will enable the prediction of the protein corona on NPs and possibly first estimations on the impact of NP toxicity.

Chapter 6

Thermosensitive Liposomes as Drug Delivery Systems

The content of the work presented in this chapter is the subject of manuscript M3. TSLs and fluorescence spectroscopy (FS) measurements were provided by Barbara Kneidl. The following text and figures are adapted from the publication, with only a few editorial changes. The original manuscript is attached in Appendix · M3.

6.1 Motivation

A proper biophysical characterization of drug nanocarriers becomes more and more important due to strict rules concerning approval procedures for new medication. Quantitative assays allow finding potential for improvement of a drug delivery system and offer a tool for continuous validation in the development process and afterwards. In addition, possible obstacles that can arise during *in vivo* testing might be discovered in such assays beforehand.

The advantages of liposomes for drug delivery were already recognized in the 1970s [200–202]: they are biocompatible, biodegradable and show little or no antigenic or allergenic activity. Many FDA-approved and therapeutically applied NP-based drug delivery vehicles fall into this class, such as Doxil, DaunoXome or Marqibo [203–207]. In order to allow localized therapy and thus a reduction of side-effects, a controllable drug release mechanism is desirable. Such promising stimulus-responsive drug nanocarriers are TSLs. The release of TSLs is triggered by an increase in the temperature in the tumor area in response to local hyperthermia or focused high-intensity ultrasound [208–211].

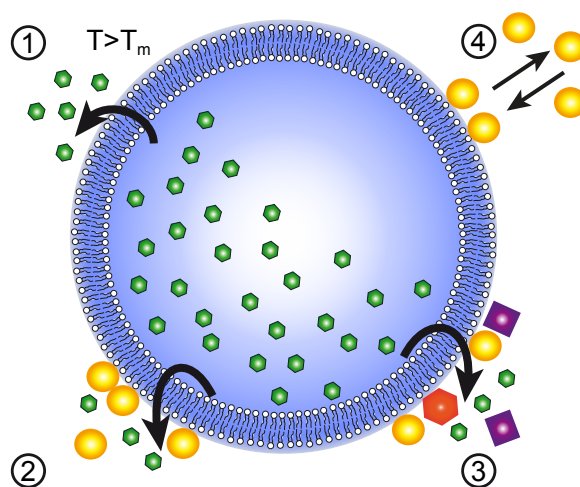


Figure 6.1: Illustration of the experimental setting and the processes studied: Release of dye (green hexagons) from liposomes in buffer (1), in the presence of a specific plasma protein (2, yellow spheres) and in the presence of whole plasma (3, mixed colors). The reversible binding of selected plasma proteins to DPPG₂-TSLs (4) was also studied.

The lipid composition of TSLs is designed to have a melting phase-transition temperature (T_m) a few degrees above a chosen target temperature. At this point, the structure of the lipid bilayer changes from a solid-gel phase to a liquid-crystalline phase. The permeability of the membrane for the encapsulated drug increases at temperatures in the vicinity of T_m , causing a release of the cargo by passive transfer along a concentration gradient [208]. In the following, we use TSLs composed of 1,2-dipalmitoyl-sn-glycero-3-phosphocholine (DPPC)/1,2-distearoyl-sn-glycero-3-phosphocholine (DSPC)/1,2-dipalmitoyl-sn-glycero-3-phosphodiglycerol (DPPG₂) (50/20/30 mol/mol) as proposed by Lindner *et al.* [212]. The phase transition of these TSLs proceeds above mammalian body temperature, here at $T_m \sim 43^\circ\text{C}$ [213, 214]. In comparison to the more generally used Lyso-PC containing TSL formulations, this mixture proved to be more stable in serum and showed prolonged circulation time in rodents and in cats [212, 214–216]. Therefore, DPPG₂-TSLs seem well applicable for *in vivo* use in clinical settings.

A profound impact on the T_m of DPPG₂-TSLs and the efficiency of drug release by the presence of plasma or serum have been noted in several studies [217, 218]. The opsonization and/or penetration of proteins into the lipid bilayer is assumed to destabilize the membrane. This is usually reflected by a shift of T_m to lower values [219, 220]. In the context of therapeutic planning and safety issues raised by uncontrolled release, investigation of these alterations in T_m is very important for the translatability of *in vitro*

studies into clinical practice. Furthermore, the development of a biomolecular corona can affect both the circulation time of a drug nanocarrier and its final destination. In practice, this effect equates with unwanted uptake by the liver or spleen.

Here, the impacts of plasma proteins on the T_m of DPPG₂-TSLs and the temperature-dependent release of cargo molecules are studied (Figure 6.1). A novel assay using fluorescein di- β -D-galactopyranoside (FDG) and FCS is presented. This assay is applied to determine the molar release ratio per TSLs in buffer, for four representative plasma proteins and physiological fluids of different species (rat, mouse, human, cow). In an additional set of experiments to look for a correlation of release profiles and protein properties, the binding isotherms of the four plasma proteins to DPPG₂-TSLs and their equilibrium binding constants are measured.

6.2 Evaluation of Basic Parameters of Thermosensitive Liposomes

6.2.1 Characterization of Thermosensitive Liposomes

The established method to assess the response of liposome formulations to external triggers, such as temperature or the addition of a detergent, is to measure changes in the fluorescence intensity of released carboxyfluorescein (CF) by fluorescence spectroscopy (FS) [221, 222]. It is assumed that the concentration of CF inside the liposome is so high that the fluorescent molecules are self-quenched, and that they dequench only after release from the liposome [223, 224].

For initial characterization of the TSLs, a similar liposome construct as in the standard FS assay is used. Inside the TSLs CF is encapsulated ($\lambda_{ex} = 488$ nm). The membrane is partially labeled with rhodamine ($\lambda_{ex} = 543$ nm). The two different fluorescent labels allow characterizing the behavior of DPPG₂-TSLs and the encapsulated dye in different media. This is of importance to ensure that there is no uncontrolled release due to changes of medium, e.g. while injection into blood stream, and in order to be able to quantify the release with precision later on. There is a good agreement of the results of size measurements by dynamic light scattering (DLS) and FCS in buffer (0.9% NaCl) for TSLs with the rhodamine membrane label ($D_{h,DLS} = 105$ nm vs. $D_{h,FCS} = 96.1 \pm 4.1$ nm). At the same time, the concentration of TSLs in a standard sample was evaluated to be 0.28 nM using an excitation of $\lambda_{ex} = 543$ nm. In contrast to DLS, FCS can be used to

cargo	100 mM CF	1 mM FDG	empty
membrane label	RhPE	-	-
phosphate concentration [nM]	41.5	38	45
z-potential [mV]	-28.5	-25.9	-30.5
DLS diameter [nm], z-average	105	114	105
PDI	0.068	0.134	0.083
FCS D_h [nm], ex. 488 nm	82.6 ± 5.4	-	-
FCS D_h [nm], ex. 543 nm	96.1 ± 4.1	-	-
FCS D_h [nm], ex. 488 nm in FBS	99.1 ± 4.1	-	-

Table 6.1: Characterization of different types of DPPG₂-TSLs by DLS and FCS measurements. FCS data are averages (\pm standard deviation) of three independently prepared samples. PDI, polydispersity index, D_h hydrodynamic diameter.

measure the size distribution of DPPG₂-TSLs not only in buffer but also in complex fluids such as FBS. FCS selectively detects the fluorescently labeled liposomes and thus avoids interfering signals by other components of the fluid [225]. Characterization under essentially physiological conditions is important to learn about the stability of DPPG₂-TSLs and possible obstacles to their use for drug delivery in living organisms. The size of TSLs was determined in FBS with FCS. For FCS measurements with $\lambda_{ex} = 488$ nm, TSL with CF as a payload are used to determine the size of the liposomes. The obtained hydrodynamic diameter (99.1 ± 4.1 nm) is in good agreement with the values determined in buffer (see Table 6.1). This confirms that FBS has no significant effect on DPPG₂-TSL size.

6.2.2 FCS-based FDG assay

After characterization, the release behavior of DPPG₂-TSL is studied from liposomes filled with CF. This requires that the released substance yields a clear signal that is not obscured by non-released substances or buffer components. The dye in the TSL should diffuse significantly more slowly than the released dye, permitting unambiguous discrimination between the two signals. Due to significant differences in the brightness of a single free dye molecule relative to that of a filled TSL, precise analysis of the dynamics of release is quite complex and does not provide single-molecule resolution. To overcome this limitation, a novel assay to measure the release from liposomes is developed. The underlying idea is to load into the TSL a dye that becomes fluorescent only after being released. Here, the only signal measured in the FCS experiments is that originating from

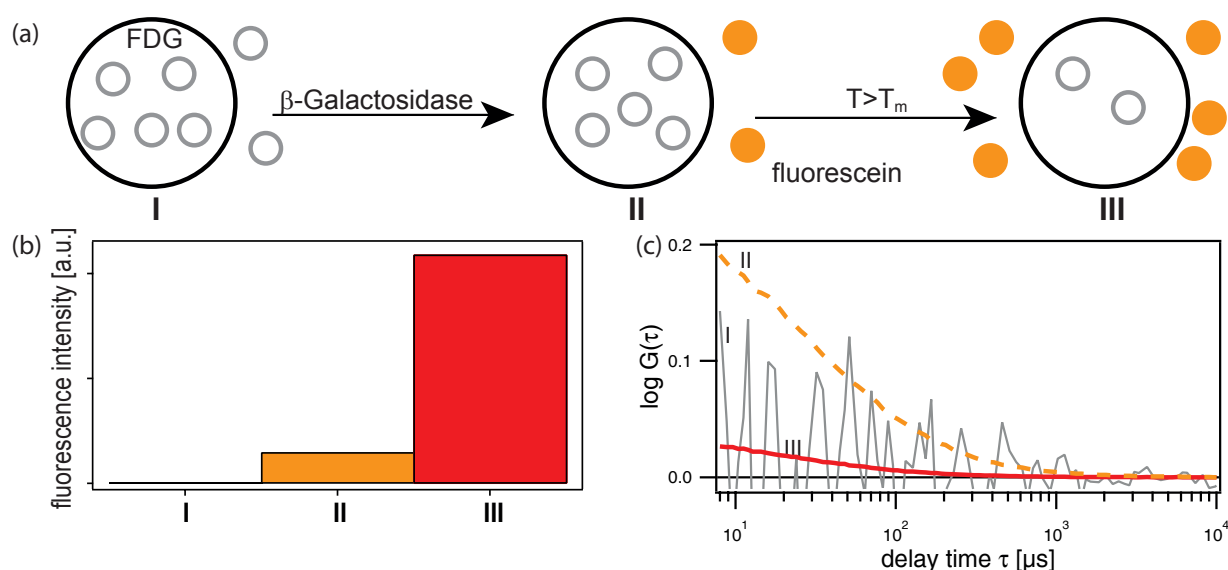


Figure 6.2: (a) Experimental set-up. FDG within the TSL is non-fluorescent. FDG that was not removed during purification of TSLs is also shown (I). β -gal hydrolyzes external FDG, generating the strongly fluorescent compound fluorescein (II), and subsequently allows one to monitor the temperature-dependent release of FDG from TSLs (III). (b) Count rates for scenarios I-III. In the absence of β -gal, the fluorescence is indistinguishable from background noise (I). For II a weak signal from the FDG that was not removed by purification is observed. For III a high signal is obtained due to the large amount of FDG that is released at $T > T_m$. (c) Corresponding fluorescence correlation curves. The correlation curve of I corresponds to background noise and is not analyzable.

the released dye (see Figure 6.2). As a result, the correlation curve is not compromised by the presence of fluorescent TSLs. In order to achieve this improvement in signal resolution, FCS is combined with the use of fluorescein di- β -D-galactopyranoside (FDG) as cargo load of the TSLs.

FDG is non-fluorescent, but becomes fluorescent when cleaved by β -gal following its release (Figure 6.3). The enzyme β -gal is membrane-impermeable. Consequently, no fluorescence signal will be detected as long as FDG is confined within the TSL (Figure 6.2 b), I). If β -gal is added to the solution, free FDG is hydrolyzed and the resulting fluorescence signal can be characterized using FCS. The levels of release are determined from this measurement (Figure 6.2 b), II and III). The versatile applications and its high sensitivity, even for concentrations in the pico- to nanomolar range, make FCS an ideal method for characterizing TSLs, their release behavior and their interaction with proteins.

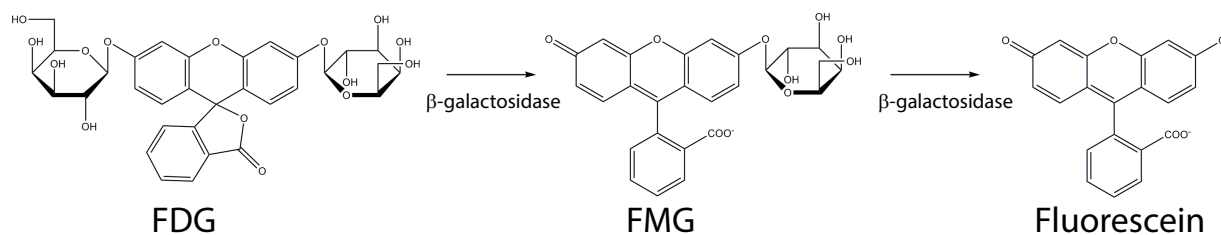


Figure 6.3: Sequential hydrolysis of non-fluorescent FDG to fluorescent fluorescein by β -gal.

6.2.3 Encapsulation and Purification Efficiency

DPPG₂-TSLs are loaded in highly concentrated FDG solution (1 mM). Subsequently, the remaining free dye is removed by filtration. The level of fluorescent dye associated with the purified TSLs is measured as a control. This measurement after purification yields a weak signal. It corresponds to a concentration of 3.36 nM of non-encapsulated FDG in the sample solution that contains 0.28 nM TSLs (Figure 6.2 II). Thus, for quantification of the absolute release in the succeeding experiments, this offset value has to be considered for correction. Otherwise, the magnitude of the induced release is seriously overestimated, especially at low temperatures.

In light of these observations, the encapsulation efficiency of the DPPG₂-TSLs is determined in two different ways. In both cases, the ratio of the experimental to the theoretical value is calculated. Firstly, the common definition of the cargo/lipid ratio in terms of molecular concentrations of each is applied. A value of $8.0 \pm 0.7\%$ is obtained. This value is in good agreement with the expected encapsulation efficiency of $\sim 6.1\%$ for DPPG₂-TSLs, according to Lindner *et al.* [212]. Nonetheless, this value seems surprisingly low. For this reason, an additional comparison of the measured amount of [fluorescein]/[TSL] to a theoretical estimate of this value is performed. Applying this definition, an encapsulation efficiency of $53.7 \pm 9.4\%$ is obtained. Intuitively, this value seems more likely. The different definitions of the encapsulation efficiency might lead to this difference. While the cargo/lipid ratio is appropriate for drugs that bind to the lipid membrane, the definition of drug/TSL is more suited for cargo that remains free in solution, such as FDG. In the supplementary data of M3, both calculations are presented in detail (Appendix · M3).

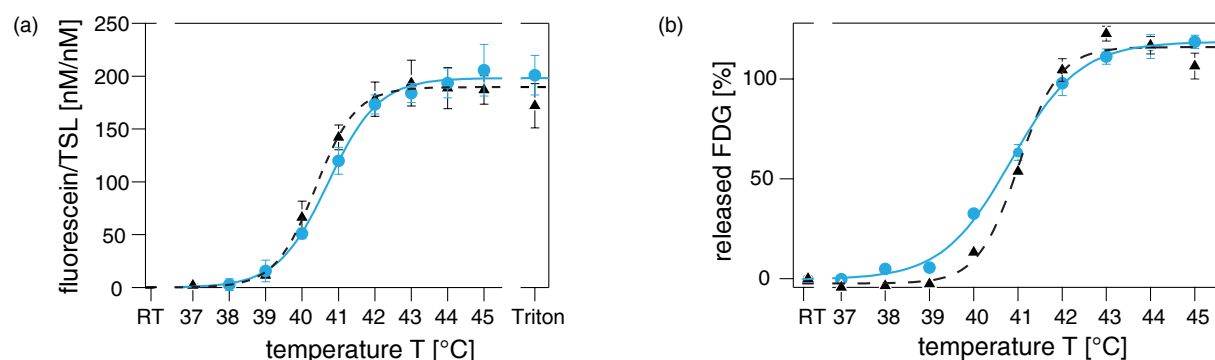


Figure 6.4: Temperature-dependent release of fluorescein from FDG-loaded DPPG₂-TSLs in HBS + 1 mM MgCl₂ (triangles, dashed line) and FBS (circles, line). (a) Molar ratio of fluorescein released per DPPG₂-TSL, measured using FCS. (b) Relative fluorescence intensity compared to total release determined by fluorescence spectroscopy (FS). Lines are sigmoidal fits.

6.3 Release from Thermosensitive Liposomes

Given that the offset concentration of FDG is known, it can be corrected with great precision. The FDG assay enables the study of the temperature-dependent release profiles of FDG from TSLs. DPPG₂-TSLs are expected to undergo a phase transition that disrupts the membrane integrity at temperatures around 43 °C. The disruption leads to the release of the cargo inside the TSLs, here FDG. The DPPG₂-TSL solution is heated to temperatures ranging from 37–45 °C to actively induce release. In order to provide constant measurement conditions, the liposome solution is then cooled down to 4 °C. After this step, β -gal is added and FCS measurements are performed at room temperature (22 °C). Addition of β -gal after cooling ensures that the enzyme is unable to cross the membrane and no FDG inside the TSL is hydrolyzed. The concentration of FDG in the surrounding medium is determined from the FCS data and is expressed relative to the concentration of TSLs in the sample solution, i.e. as [fluorescein]/[TSL] in the following.

6.3.1 Release in Buffer and FBS

The amounts of cargo released at various temperatures is determined with the approach. The results are displayed in Figure 6.4 a). No release is found up to 37 °C, with the first discharge of cargo being detected at 38 °C. The amount of FDG released then increases with increasing temperature, yielding an S-shaped curve that reaches saturation at

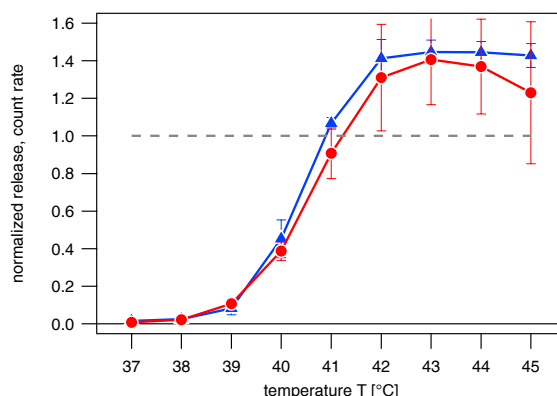


Figure 6.5: Release profile of TSL in buffer (blue) and FBS (red) determined by normalization of the measured count rate (fluorescence intensity) analogous to the analysis of FS measurements. Physically unrealistic release values above 100% are obtained using this approach for analysis.

around 43 °C. As a control, the release induced by the detergent Triton is measured. Triton completely disrupts the TSL membranes leading to the release of all encapsulated FDG molecules. Within the margin of error, the measured value is equal to the saturation value for the release at high temperatures. In conclusion, all FDG is released from the DPPG₂-TSL at temperatures above 43 °C.

The results of this novel assay are compared to conventional FS data to further validate the performance of the FCS-based assay. The relative change in fluorescence normalized with respect to the Triton value is shown in Figure 6.4 b). Both release profiles (Figure 6.4 a and b) follow the same trend of strongly increasing release around a critical temperature of 40-41 °C, saturation at temperature about 43 °C, and barely detectable release below 40 °C, indicating that the membrane is practically impermeable within the last temperature range. FCS data shows the molar ratio of FDG molecules released per TSL, while FS data show the total fluorescence intensity and hence the amount of FDG release relative to the total release caused by membrane disintegration upon addition of Triton. It is worth noting, that the data shown in Figure 6.4 b shifts below 0% and exceed 100%. This is an intrinsic artifact of the FS approach, which is due to impact of Triton on the brightness of the dye and therefore on the normalization. These values can be reproduced when performing the same analysis as for FS, using the count rates measured with FCS (Figure 6.5).

In FCS experiments, it is observed that the level of emission by the dye molecules is decreased compared to a solution without Triton (see Figure S5 in Appendix · M3).

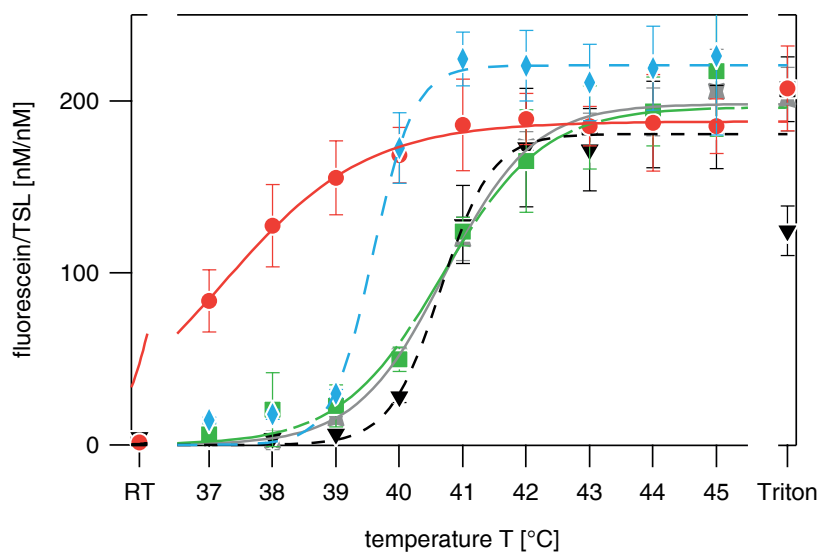


Figure 6.6: Impact of plasma on the temperature-dependent release profile: mouse plasma (red circles), rat plasma (green squares), human plasma (black inverted triangles), human plasma doped with Lyso-PC (blue diamonds) and fetal bovine serum (asterisks, gray trace). Lines are sigmoidal fits.

Due to this observation, it is assumed that methods that solely rely on the analysis of changes in fluorescence intensity in the presence of Triton, which is often used to determine the release behavior, are not optimally suited for highly precise measurements, at least not for fluorescein [221, 222]. The FCS approach presented may provide a more reliable alternative. Instead of solely depending on absolute brightness measurements, FCS measures absolute concentrations. This is especially useful for determinations of spurious release.

Subsequently, the temperature-dependent release profile is measured in the more physiologically relevant medium FBS. Here, the release curves are similar to those in buffer, irrespective of the measurement technique employed, proving that FBS does not influence the release behavior significantly (Figure 6.4, circles).

6.3.2 Release in Plasma of Various Species

Animal testing plays a key role in the further drug development for use in humans. In order to identify possible obstacles before *in vivo* testing, repetition of the above *in situ* experiments in the presence of plasma from various species is of interest. Here, the release profiles in mouse, rat and human plasma are compared to the results obtained

in FBS (Figure 6.6). Corresponding FS data are available in Figure S6 of the attached manuscript M3. The same general trend is observed for FBS, human and rat plasma. Strikingly, for mouse plasma a clear deviation from the other curves is observed. The release profile is characterized by a significant release even at 37 °C. This behavior was previously reported by Hossann *et al.* [214]. The increased Lyso-lipid content of mouse plasma might be a possible cause of this difference [226, 227].

In order to check this hypothesis, human plasma is supplemented with Lyso-PC until a level that is comparable to the one in mouse plasma is obtained. Upon addition of Lyso-PC, a slight shift of the release curve towards lower temperatures, relative to human plasma without Lyso-PC, is observed. Similarly, the onset of release in mouse plasma is shifted to lower temperatures relative to plasma from other mammals. However, the effect in mouse plasma is much more pronounced than in human plasma enriched in Lyso-PC, indicating that Lyso-PC might contribute to this phenomenon, but does not explain it entirely.

6.3.3 Release in Protein Solutions

Considering that plasma consists of numerous components, a multitude of molecules or molecular interactions could conceivably contribute to the observed differences in human and mouse plasma. In order to better understand these results, the impact of several prominent blood proteins on the temperature-dependent release is evaluated by using single-protein solutions as the external medium (Figure 6.7).

ApoA1 (7.1 μM), Fib (1.7 μM), SA (15.2 μM) and Tf (12.6 μM) are chosen. Detailed portraits of the used plasma proteins are presented in Section 4.2. Lower concentrations of ApoA1 and Fib are used because they have been observed to bind strongly to drug nanocarriers in other studies [91, 228, 229].

ApoA1 seems to impede the cargo release in comparison to the results in the absence of proteins. SA and Fib cause a more pronounced release at lower temperatures than in pure buffer. This shift of SA was described before. The partial penetration of the adsorbed protein is assumed to affect the integrity of the lipid membrane [230–232]. The change in the release profile that is induced by ApoA1 can be explained analogously. ApoA1 probably acts to seal the packing defects that form in the membrane, thereby reducing cargo release from DPPG₂-TSL. Relative to cargo loss in pure buffer, Tf seems to have only a minor influence.

In full plasma, the observed effects of the single proteins seem to largely compensate for

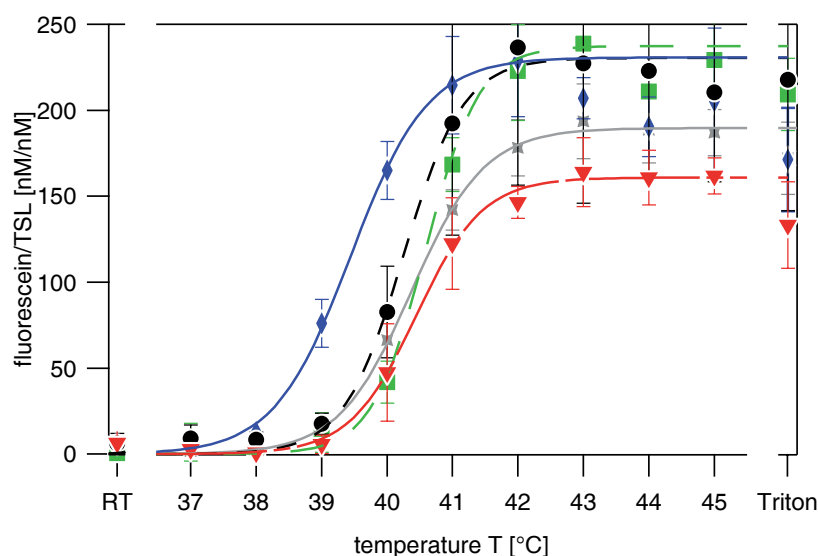


Figure 6.7: Temperature-dependent molar release in the presence of specific proteins from plasma: SA (blue diamonds), Tf (green squares), Fib (black circles) and ApoA1 (red triangles). For reference, the release profile in HBS + 1 mM MgCl₂ is shown in gray (asterisks). Lines are sigmoidal fits.

each other. They might contribute, however, to the differences observed between the kinetics of release in plasma of different species (Figure 6.6).

6.4 Binding of Proteins to Thermosensitive Liposomes and its Reversibility

In the next series of experiments, the binding of the four representative plasma proteins from the previous section is evaluated: SA, Fib, ApoA1 and Tf. The question of interest is, if there is a correlation of the release profile determined in Subsection 6.3.3 and the binding affinities of the named proteins. The dissociation constant K_D of fluorescently labeled proteins is determined using FCS, which is especially suited to study the binding behavior of strong binders, as shown before [21, 66, 166]. A fixed concentration of fluorescently labeled protein is measured to determine the concentration of free proteins in solution. Varying concentrations of unlabeled TSLs are added to the solution. After one hour of incubation, the fraction bound of the labeled protein is measured. In Figure 6.8 the normalized binding isotherms for various proteins to DPPG₂-TSL are shown. For analysis, Equation 3.8 is used instead of Equation 3.7, because the number of

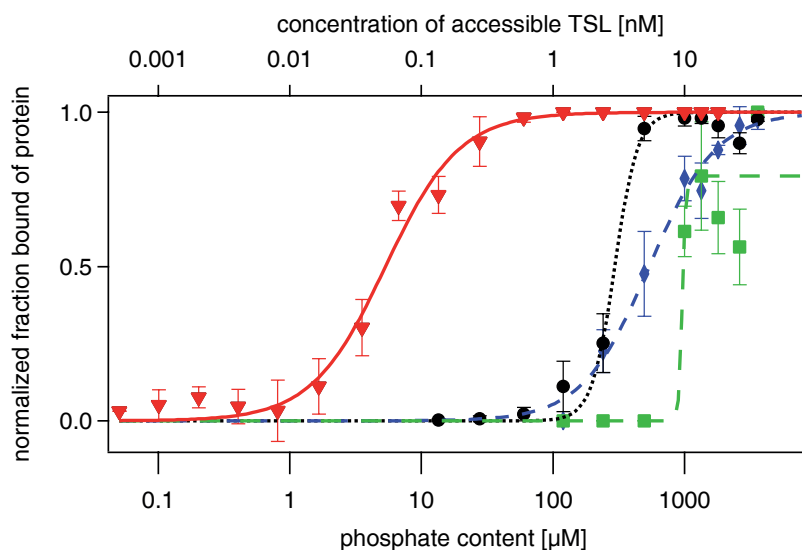


Figure 6.8: Normalized binding isotherms of labeled proteins to DPPG₂-TSL. The concentration of the TSLs is titrated against a fixed concentration of labeled protein: ApoA1 (red inverted triangles), Fib (black circles), SA (blue diamonds) and Tf (green squares).

protein	ApoA1	Fib	SA	Tf
K_D [nM]	0.053 ± 0.004	2.951 ± 0.174	5.393 ± 0.405	9.652 ± 0.001

Table 6.2: Dissociation constants K_D of the plasma proteins ApoA1, Fib, SA and Tf.

available ligands, i.e. binding sites on the DPPG₂-TSL, is much larger than the number of receptors, i.e. the mole fraction of the labeled protein as discussed in Section 3.4. Table 6.2 summarizes the results of the analysis. For ApoA1 strong binding is observed. The binding constant of ApoA1 is two orders of magnitude higher than those for the other proteins. This strong binding might be an explanation why ApoA1 is the only protein tested that reduced the efficiency of release (Figure 6.7). Efficient binding and blocking of packing defects might presumably leads to a reduction in release. The other three proteins showed weaker binding. Only SA strongly affects the release profile. It is suggested that SA increases the permeability of the liposome bilayer, which causes an enhanced release, while its weak binding prevents the high surface coverage that might well reduce this effect.

In order to clarify if the proteins used in these experiments are the ones that build a part of the protein corona on the DPPG₂-TSL, and that influence the release profile in plasma or serum, FBS is added to the protein-TSL complexes. Reversibility experiments provide a means to do this. The kinetics of the protein detachment are monitored for one hour.

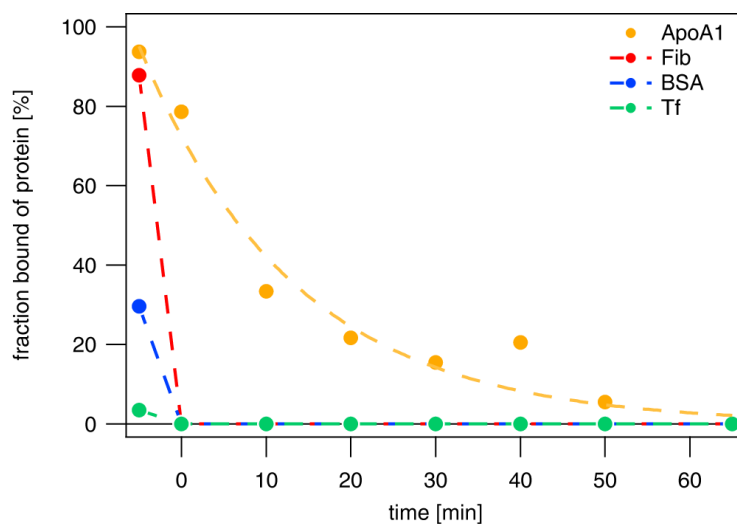


Figure 6.9: Example kinetics for different proteins after the addition of FBS: ApoA1 (orange), Fib (red), BSA (blue) and Tf (green). The last three proteins are replaced immediately after the addition of FBS, while the amount of adsorbed ApoA1 decreases slowly with time. After 1 hour, all ApoA1 is replaced as well. ApoA1 is fitted with an exponential fit.

It is observed that all four proteins come off the TSLs over the course of one hour (Figure 6.10). While SA, Fib and Tf are immediately displaced, ApoA1 is displaced slowly (Figure 6.9). A possible explanation for this observation might be that other biomolecules in FBS possess a much higher affinity for the liposome surface than the four tested proteins. Thus, the molecules from FBS replace the labeled proteins bound to the surface of the TSLs. The displacement of proteins from the DPPG₂-TSL in FBS explains why their impacts on the temperature-dependent release in the presence of FBS is not observed.

Interestingly, ApoA1 is removed slower from TSL than the other three proteins. This could be used as a natural coating for DPPG₂-TSL. For instance, higher concentrations of ApoA1 for incubation can be applied to fully cover the surface of the liposomes. Thus, it might be possible to increase circulation times as apolipoproteins are stated to prevent opsonization. This is in agreement with the slow replacement which was observed in the above reversibility experiments [227]. In addition, the selectivity of DPPG₂-TSL might be increased, leading to an improved targeting of the liposomes. Similar tests could be performed for other substances as well.

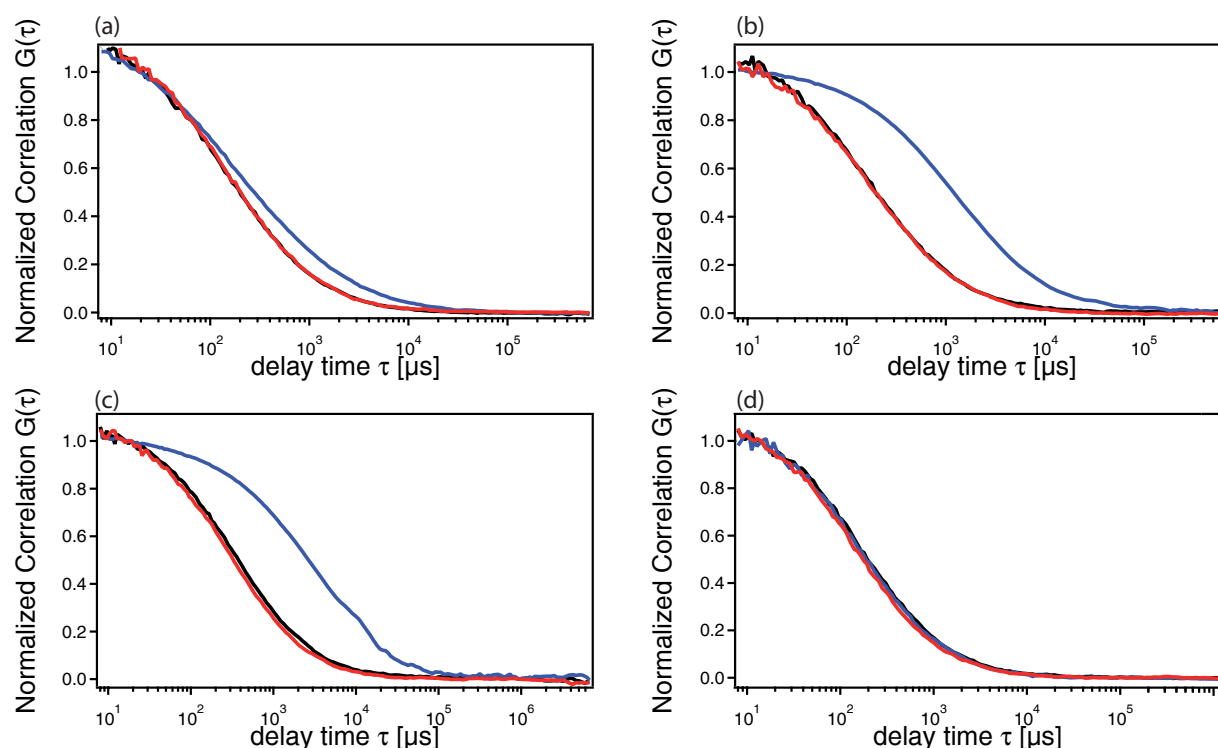


Figure 6.10: Normalized correlation curves of protein alone (black), protein and DPPG₂-TSL (blue) after one hour of incubation and after the addition of FBS and another hour of incubation (red). The signal of free proteins (black) shifts towards larger diffusion times after one hour of incubation with DPPG₂-TSL (blue) and back to the starting curve, after the addition of FBS and incubation for another hour (red). This means that the binding of all tested proteins is reversible. (a) BSA, (b) ApoA1, (c) Fib and (d) Tf.

6.5 Conclusion

A novel and highly sensitive assay for quantification of the temperature-dependent release of FDG-loaded TSLs based on FCS, is presented. The FCS approach is validated by comparing the measurements of the temperature release profile of FDG-loaded DPPG₂-TSL to standard fluorescein FS studies. With regard to determining spurious release at temperatures below T_m , the FCS-based assay proves to be superior. In order to ensure that TSL membranes remain sealed at room temperature, the assessment of low drug release is important. This is a prerequisite for controlling the dosage dispensed and avoiding non-specific delivery to healthy tissue. Furthermore, the approach based on FCS yields information on size and encapsulation efficiency, as well as interactions of liposomes with blood plasma proteins. For the first time, the binding of selected blood components to DPPG₂-TSL and the resulting shift in the critical release temperature

are determined. While Fib, ApoA1 and Tf bound to DPPG₂-TSL did not affect the temperature release profile, SA induced a noteworthy shift. The FCS data confirms that the temperature of release is shifted in the presence of mouse plasma towards lower values for T_m , but remains largely unaffected by rat and human plasma, as well as by FBS. There seems to be no systematic correlation between the binding affinity and the shift in the temperature of release. Nevertheless, binding of proteins to TSLs is very probably an essential precondition for any change in the intrinsic thermal properties upon contact with physiological fluids.

The presented approach is applicable to a broad field of possible interactions of liposomes with their environment. In the context of medical use of TSLs, for instance, such interactions can be specific proteolytic plasma cascades. The design of alternative membrane coatings based on combinations of plasma proteins will be facilitated by a better understanding of protein adsorption onto and desorption from TSLs and drug-delivery nanocarriers in general. Such synthetic coronas are biocompatible, and could possibly prevent further opsonization and increase the circulation time. To this end, quantitative biophysical assays for multiple protein-membrane interaction parameters will be instrumental for the realization of improved targeting strategies.

Chapter 7

Protein Self-assembly in Health and Disease

The content of this chapter is the subject of the publications P4 [49], M5 and P6 [233]. The following text and figures are adapted from these publications, with only a few editorial changes.

7.1 Background on Self-assembly

Self-assembly of proteins is relevant in terms of fundamental research in Biophysics, Biology, Pharmacology and Medicine. This process is often mentioned in the context of neurodegenerative diseases such as Parkinson's, Alzheimer's or Huntington's Disease. A hallmark of these afflictions is the appearance of protein deposits, so-called plaques in the brain. The protein that is the major building block of these deposits is characteristic for the particular disease. For instance, aggregates of α -syn are associated with Parkinson's Disease [235], $A\beta$ with Alzheimer's Disease (AD) [236] and polyglutamine with Huntington's Disease [237]. Although the proteins show no common features in their sequences length or native structure, the morphologies of their amyloid fibrils are remarkably similar [238, 239]. Understanding the underlying biophysical and molecular mechanisms in detail is key to the development of effective treatment. Self-assembly leads to the co-existence and interaction of several subspecies of different size and charge that have to be considered when proposing a mechanistic model. Namely, these highly heterogeneous species are monomers, oligomers, protofibrils and fibrils (Figure 7.1). At present, there is growing evidence that oligomers are the most toxic subspecies assumed

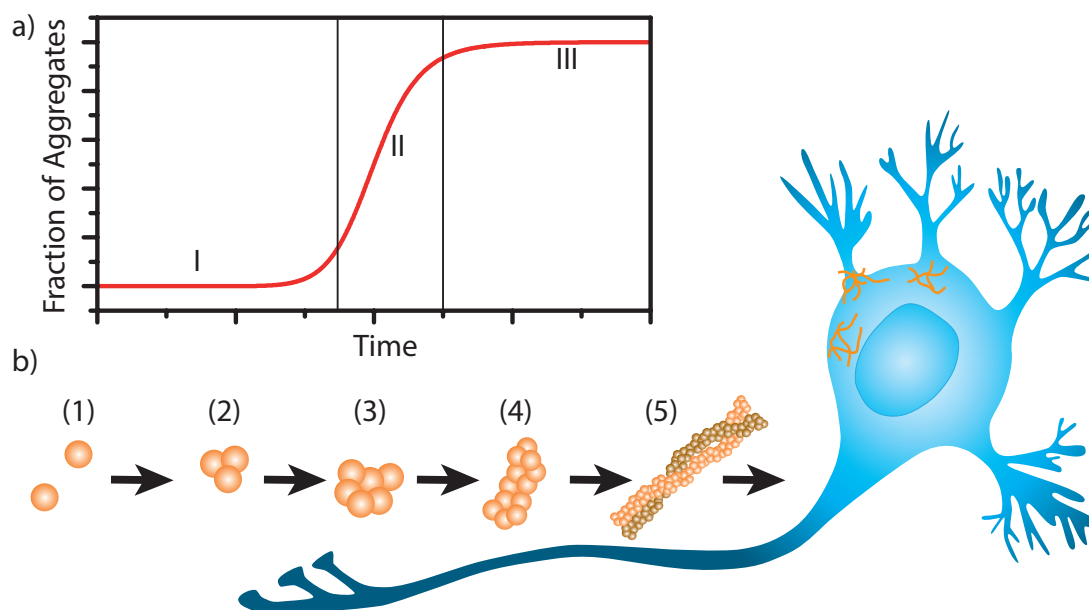


Figure 7.1: a) Characteristic curve of the macroscopic process during amyloid fibrillation. The aggregation process is typically divided into a lag phase (I), a growth or elongation phase (II) and a final plateau (III). b) Nucleated self-assembly process of amyloid aggregation. The formation of fibrils proceeds through a multistage process. Monomers (1) form low molecular weight aggregates (2), then higher molecular weight aggregates (3) in the nucleation phase, which has a characteristic lag time before the formation of protofibrils (4) and fibrils (5) dominates the kinetics. A secondary nucleation process leading to the formation of larger subspecies via fibril-catalyzed reactions has also been suggested (not shown) [234]. The final step is the deposit of plaques on neurons, the pathological hallmark of the mentioned amyloid diseases.

to be responsible for neuronal injury, although the specific forms that cause damage *in vivo* have not been identified yet [141, 144, 240]. It is hypothesized that a common pathway of agglomeration for all amyloidogenic proteins exists. Although several models are under discussion, they all have a common major feature on the macroscopic level and only differ in issues considering the microscopic level (Figure 7.1) [239, 241]. The known starting material in the process of protein agglomeration is the monomer. The following step is already under discussion, however. It is not clear, whether the protein starts the aggregation process in its native form or not. A nonspecific conformational change of the monomeric protein, often termed “misfolding”, might take place. This process, and the involved change of properties of the protein, might be the initial step that give the monomer a higher propensity to aggregate [242, 243]. The transition from

the monomeric state to small oligomers is assumed to be the critical step in many models. Oligomers are suspected to act as nuclei of fibrillation. They consist of 3-50 monomers and are often metastable. Early forms such as trimers, tetramers and octamers are also termed oligomers [141]. Compared to the rod-like shape of larger assemblies, they are often called spherical. Another class of intermediates in the process of self-assembly are protofibrils. These precursors of amyloid fibrils are flexible rod-like structures with a high β -sheet content. The final product of aggregation are fibrils with a highly ordered cross- β structure [238]. They are expected to be in a dynamic equilibrium with low-order oligomers and monomers. Fibrils are composed of several protofibrils which are twisted around each other to form a left-handed double helix [244]. They further grow from their ends by addition of monomers. Plaques are not considered in kinetic models although they are used as pathological markers for disease. They are composed of insoluble amyloid fibrils. For many amyloidogenic proteins, no correlation between their appearance and neurotoxicity has been found [234]. On the contrary, plaques remove and inactivate smaller, toxic aggregates by binding them [141].

The kinetics of the nucleated self-assembly reaction display a sigmoidal behavior on the macroscopic scale consisting of three phases (Figure 7.1 a) [138, 245]. A lag phase (I) is followed by a steep increase during the elongation or growth phase (II) ending in a final plateau (III). The elongation phase is short compared to the lag phase. This rapid process is followed by a saturation phase, where the aggregation curve plateaus [138, 141, 246]. No single microscopic process can be ascribed to a single phase, since the law of mass action does not allow a discontinuity in the reaction rates [247, 248]. Every process takes place at every phase, sometimes more pronounced, sometimes less. During the growth phase, the overall conversion rate of peptides and proteins into amyloids is greatest. An equilibrium of monomers and other species is reached in the final plateau. The largest uncertainties concern the processes in the lag phase. There is growing evidence that the lag phase is not solely a waiting time for the occurrence of nuclei. A collective waiting behavior of millions of nuclei is not in agreement with the law of mass action and may be possible only for single-molecule reactions [239]. Instead, multiple reactions proceed in parallel. The dominating processes are assumed to be the growth and proliferation of millions of initially formed primary nuclei. The formation of such primary nuclei is termed primary nucleation. This is in agreement with the simplified nucleation-dependent polymerization model for amyloid aggregation [138, 141, 245, 246]. More recent results indicate the presence of secondary nucleation

processes which appear more frequently in the growth phase [249, 250]. A catalytic effect of the surface of fibrils was observed for $A\beta$ and α -syn [234, 240, 251]. The breakage of fibrils might speed up the process of fibrillation by providing additional free fibril ends available for monomers to bind to.

The lag time can be shortened in experiments by seeding with preformed nuclei that fasten the aggregation process [138]. The current knowledge on amyloidogenic aggregation is still rather limited. The existence of distinct, parallel aggregation pathways depending on the surrounding conditions cannot be excluded [141]. The lack of a definite model proves that it is challenging to study protein aggregates and their kinetics because classical biophysical techniques, such as scattering, spectroscopic and calorimetric methods, are not well adapted for their study [233]. In particular, the concentrations of intermediate species are challenging to measure. Therefore, new experimental approaches are needed to overcome the limitations of the established techniques. In the following, two approaches to accomplish this, based on FCS and thermophoresis, respectively, are presented.

7.2 Quantification of Amyloid β_{1-42} Fibrillogenesis Using FCS

The content of this chapter is the subject of publications P4 [49] and M5. The following text and figures are adapted from the publications, with only a few editorial changes. The original publication and manuscript are attached in Appendix · P4 and M5.

Small aggregates (oligomers) of $A\beta$ are suspected to cause the neuronal injury leading to Alzheimer's Disease (AD). In this work, the aggregation process, especially the development of oligomers in the subcritical concentration regime is studied by FCS.

The experimental approach and pitfalls as well as analytical obstacles of peptide self-assembly are discussed in manuscript M5 in detail (Appendix · M5). Usage of FCS for the study of self-assembly needs careful and consistent sample preparation to ensure that the fitting methods produce results based on robust data. In the attached manuscript, the procedure for performing the measurements and the options for analysis are described in a general fashion.

7.2.1 Aggregation of $A\beta_{1-42}$ in sodium phosphate buffer

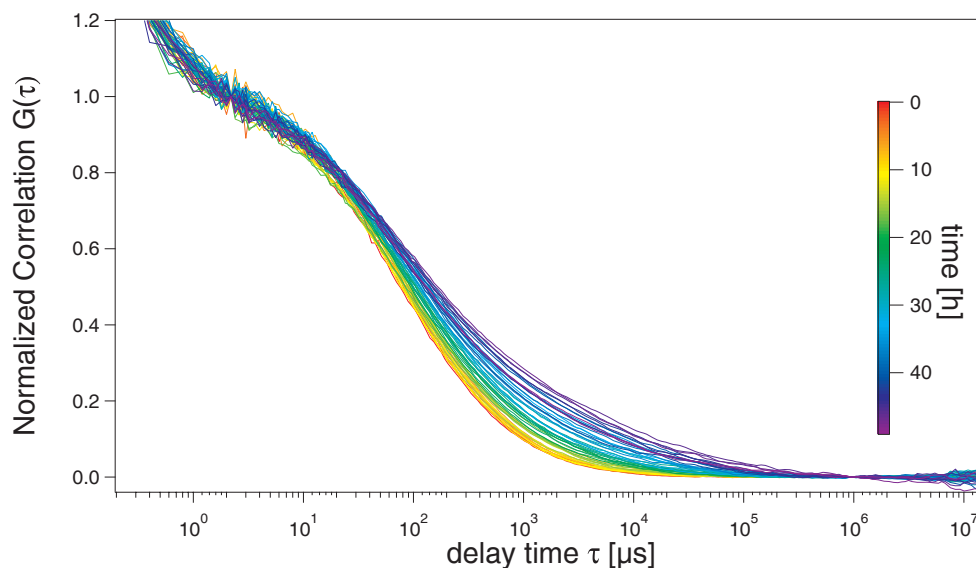


Figure 7.2: Normalized average correlation curves over 48 h for a sample containing 20 μM $A\beta_{1-42}$ (0.01% labeled). Over the course of the experiment the curves shift to the right and a buckling develops, suggesting an increase in the number of various species and particle sizes. Reprinted from [49] with permission from Elsevier.

The aggregation of $A\beta_{1-42}$ is studied at 10 and 20 μM in the presence of 0.01% labeled $A\beta_{1-42}$ in sodium phosphate buffer by FCS. Differences in the time before onset of oligomer formation may depend on preparation conditions, and/or additional stresses applied to the sample to speed up this process [141, 252–255]. Consistent preparation methods are used to minimize these effects. Measurements are taken systematically over 48 h. The evolution of an autocorrelation function over the time course of a typical experiment is shown in Figure 7.2. The development of the exemplary sample suggests that species of higher molecular weight appear over several hours, as indicated by a shift in the delay time to higher values.

7.2.2 Comparison of MEMFCS and GDM fitting

A one-component fit works only for the first few time points. Thereafter, it leads to unsatisfactory and physically unrealistic results. Thus, a more sophisticated approach for fitting is needed.

The established maximum entropy method for FCS data analysis (MEMFCS) is utilized

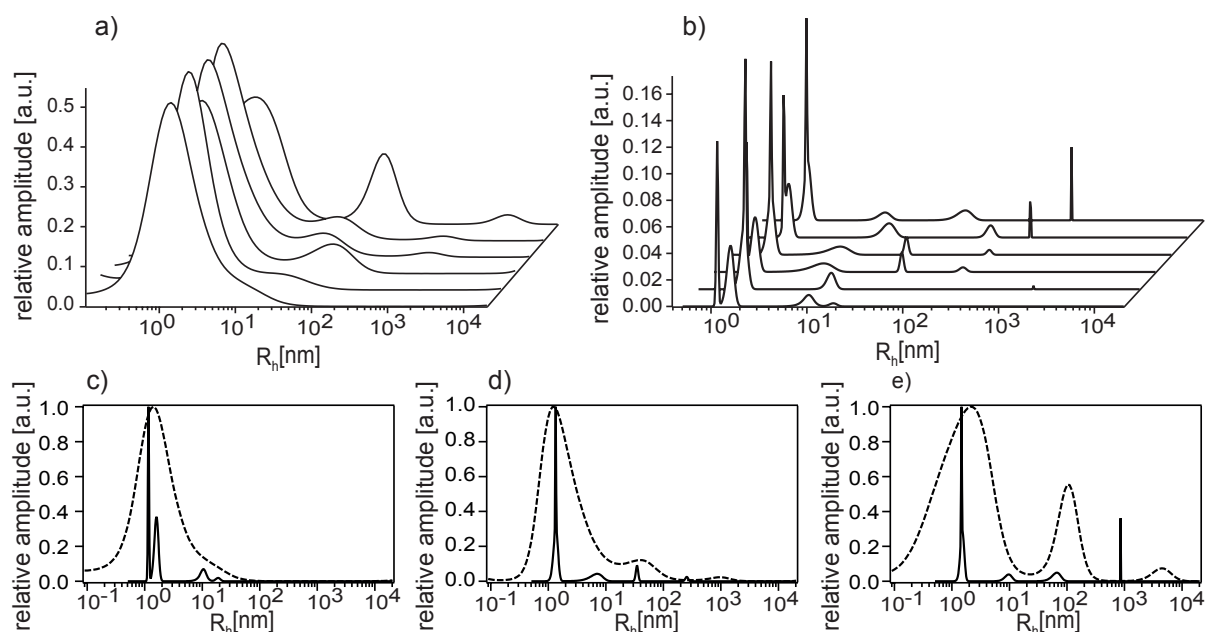


Figure 7.3: Size distribution determined with a) MEMFCS and b) 5GDM. Both fitting approaches provide similar trends, but the GDM fitting gives sharper and defined peaks, especially in the range of low molecular weight oligomers. Measurements taken at 0, 5, 16, 20, 40 and 48 h. c-e) Direct comparison of the results of MEMFCS (dashed) and 5GDM (solid line) for c) 0 h, d) 20 h and e) 48 h. Both fitting methods provide consistent results. Reprinted from [49] with permission from Elsevier.

to analyze the correlation curves at various time points throughout the experiment (Figure 7.3 a) [39, 256]. Analyzing the first measurement reveals a single peak with a hydrodynamic radius (R_h) maximum at 1.44 nm and a shoulder towards larger hydrodynamic radii. At the end of the experiment, three peaks are present, corresponding to the following spherical hydrodynamic radii: 2.09 nm, 101.17 nm and 4.5 μm . The broad peaks obtained with MEMFCS are likely to include size distribution data for several different species in solution (see Section 2.2.5).

Size distribution curves resulting from MEMFCS show Gaussian-type distribution characteristics. Thus, the experimental data was fit with a Gaussian distribution model (GDM) with a fixed number of peaks. This approach was inspired by initial work by Pal. *et al.*, who used this concept as an alternative to MEMFCS for microemulsion droplets [47]. The underlying idea is that a species is not monodisperse with a single value for its size or diffusion time τ_D , but rather a Gaussian distribution on a logarithmic time-scale with peak diffusion times τ_P . The work of Pal *et al.* is extended to using more than one single peak and to varying further fitting parameters. The fraction of each component

is determined using Equation 2.32. More details on the theoretical background are presented in Section 2.2.5. The validity of the GDM is verified by extensive testing of the well characterized dye Alexa488. Here, using one Gaussian peak worked successfully, while a higher number of distributions is rejected by the fitting algorithm correctly. For the analysis of $A\beta$ aggregation the usage of five peaks for the GDM analysis is chosen. This choice is a good balance between distinguishing the various species in solution (monomer, small oligomer, larger oligomer, protofibril and fibril) and not having so many free parameters that the outcome of the fits is physically unrealistic. Consistent results are obtained for the analysis of many curves using this approach. An inappropriate description of the system is observed for the usage of less than five peaks. In this case, the algorithm leads to results such as component sizes smaller than monomeric $A\beta$ together with very large particles at early time points. The results of the analysis with the 5GDM are presented in more detail in Figure 7.4.

Compared to MEMFCS, there is a larger number of more sharply defined peaks representing different levels of $A\beta_{1-42}$ aggregation. At early time points of the experiment, 5GDM fitting gives two peaks at 1.17 nm and 1.62 nm. If a weighted sum of these first two peaks is calculated using the relative amplitudes, a R_h of 1.44 nm is obtained. This value corresponds exactly to the one for the first peak determined with MEMFCS fitting. A direct comparison of the results of both fitting methods for selected time points (0, 20 and 40 h) is shown in Figures 7.3. 5GDM and MEMFCS are in good agreement and show the same trends for all three time points. However, significant differences for the determined size of the fibrils are observed at later times (48 h): $R_h = 4.5 \mu\text{m}$ for MEMFCS versus $R_h = 0.85 \mu\text{m}$ for GDM. These particle sizes are beyond the reasonable measurable range for FCS, and the values must be artifacts of the fitting procedure in both approaches.

7.2.3 Evaluation of the Four Fractions of $A\beta_{1-42}$ Aggregates

5GDM reveals a larger number of components within the system than MEMFCS, but each of these species represents a range of particle sizes. It is impossible to analyze the first two peaks separately, since they fuse and separate several times during the experiment (Figure 7.3 d and e). Thus, the percentages of these two peaks are pooled and treated as one. Consequently, a four level fraction model for $A\beta_{1-42}$ aggregation is obtained, although a five peak fitting algorithm is applied. An explanation for the fusion of the first two peaks might be a dynamic equilibrium that is assumed between

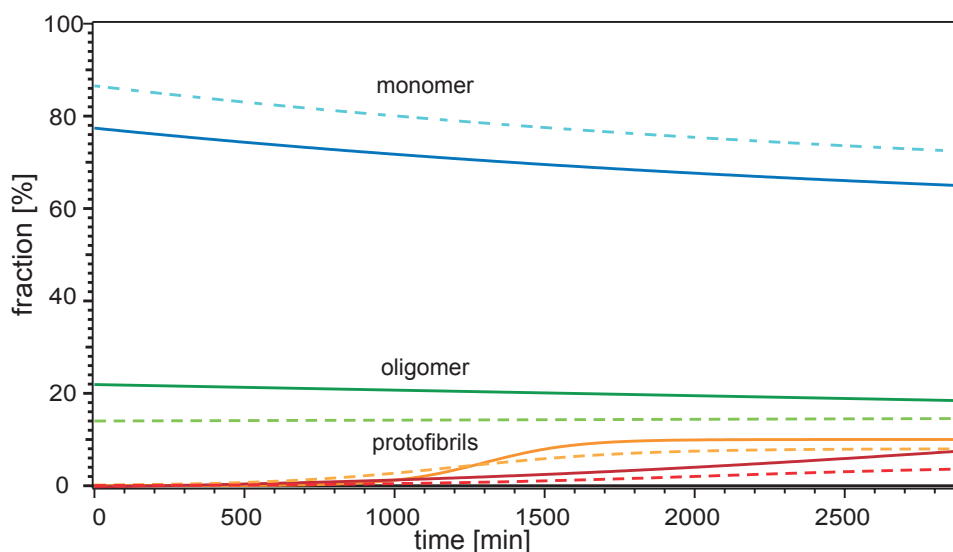


Figure 7.4: Development of the fractions of the four aggregate levels of $A\beta_{1-42}$ in sodium phosphate buffer, dashed lines represent $10\ \mu\text{M}$ samples, solid lines represent $20\ \mu\text{M}$ samples. The fractions were determined using 5GDM analysis. The proportion of small components/monomers (blue) decreases over time, while the amount of protofibrils (orange) and fibrils (red) increases after a certain lag time (16 h). The fraction of high molecular weight oligomers stays constant (green). The experiments are performed in triplicate to ensure reproducibility. Adapted from [49] with permission from Elsevier.

monomers and small oligomers [257, 258]. The following size ranges are defined based on the fitting:

1. small components including monomers and oligomers with low molecular weight
2. oligomers with higher molecular weight
3. protofibrils
4. fibrils

5GDM fitting and Equation 2.32 are used to determine the fractions of the various $A\beta$ species in solution. The averaged values of the development of the fractions with time are shown in Figure 7.4. In the lower concentration samples the rate of aggregation is slower, which is consistent with previous experiments [259]. After 48 h, the proportion of monomers and small oligomers (fraction 1) is higher in the lower concentration sample: 72.4% for $10\ \mu\text{M}$ versus 64.9% for $20\ \mu\text{M}$. The proportion of the fibrils behaves accordingly. For $10\ \mu\text{M}$, 3.6% are obtained, as opposed to 7.5% fibrils for $20\ \mu\text{M}$. The

amount of fraction 1 decreases as fibrillation proceeds, while the R_h of this component is fairly stable. Taken together, these results indicate a real decrease of the proportion of monomers/small oligomers in solution. The evolution of the first two peaks, which are summarized as fraction 1, is shown in Figure S1 of Publication P4 (Appendix · P4). Only some data points lie in the monomer range between 0.8 and 1 nm, and most of the data points lie between 1 and 2 nm [139]. This size range represents mixtures of monomers and small oligomers. For this reason, 5GDM is not able to differentiate between these two species reliably and hence these components are pooled in fraction 1. Nonetheless, a clear difference between fraction 1 and larger aggregates is determined. At the initial stage of the experiment, small components are the dominant species (Figure 7.4). The mixture of monomers and small oligomers are part of the starting material. Purely monomeric samples do not aggregate on a reasonable experimental time scale [139]. The proportion of high molecular weight oligomers (fraction 2) stays constant throughout the experiment (14% for 10 μM and 19% for 20 μM). The R_h increases slowly in size for this fraction, and is in the range of 10 nm. Due to these observations, it is assumed that an equilibrium between small components (fraction 1) and larger oligomers is established before the first measurement. At the beginning of the experiment, neither protofibrils nor fibrils are present in FCS data, but they appear after a lag time. This observation is consistent with a nucleation-dependent polymerization model [138]. Both species show a sigmoidal behavior with a mean lag time of ~ 16 h. A saturation level of 10% for 20 μM and 8% for 10 μM , is reached for the proportion of the protofibrils, while the amount of fibrils continues to increase until the end of the experiment. Fibril formation is confirmed additionally by transmission electron microscopy (see Figure S3 of Publication P4). The presence of fibrils is consistent with 5GDM analysis and the size values obtained for fibrils are in agreement with published studies [244, 246, 260].

7.2.4 Preliminary Experiments in Artificial CSF

In order to change over to physiological conditions, experiments are repeated in artificial CSF, which is a special buffer that mimics natural CSF. Immediately after mixing stock $A\beta$ with this buffer, large sedimenting particles are observed. During the following FCS measurement, this manifests as decreasing number of particles because of the loss of material to the large precipitating aggregates. The remaining monomers are now at a much lower concentration. Since their concentration is now below the concentration needed for the onset of fibrillation, no higher order oligomers are formed. The higher

ionic strength of artificial CSF accelerates the kinetics for $A\beta_{1-42}$ in the μM range [141]. An attempt to find a regime in which a broader distribution of particles sizes by an incremental decrease of the concentration of $A\beta$ to the nM range failed. Similar results are obtained for adding labeled $A\beta$ to pre-aggregated samples in artificial CSF. In these experiments, only single events in the count rate plots are observed, but these bursts correspond to fibrils rather than to oligomers. A systematic evaluation is not performed because these single events do not meet the requirements of the statistical basis needed for quantitative FCS analysis. These results are consistent with Nag *et al.* [139]. They suggested that $A\beta_{1-42}$ aggregation depends on physiological factors at low concentrations of $A\beta_{1-42}$. Furthermore, aggregates are expected to dissociate below a certain critical concentration because they are thermodynamically unstable. However, beyond the limitation of this special experimental system, there are no technical barriers to applying FCS and 5GDM analysis in artificial or real CSF or other complex biological fluids.

7.2.5 Conclusion

A novel fitting algorithm for FCS data capable of discriminating several different sized components in solution simultaneously, has been developed. The fibrillation of $A\beta_{1-42}$ was studied and four aggregates types were identified in solution: small components (including monomer and low molecular weight oligomers), high molecular weight oligomers, protofibrils and fibrils. Over 48 h, each component is observed for a range of protein concentrations. Clearly, the general features of the aggregating system are consistent using both methods, but the 5GDM provides a more detailed and potentially more realistic description of the aggregating system with a better resolution of the species with low molecular weight than MEMFCS. The presented analysis method may also be useful for monitoring the aggregation of other proteins or characterizing systems with a size distribution such as NPs and colloids [16].

7.3 Quantitative Study of α -synuclein Aggregates

In this chapter, FCS is used as a complementary technique in the context of thermophoresis of complex polymers and of advanced theoretical modeling of microscale thermophoresis (MST) with quantitative predictions for the protein α -synuclein (α -syn).

Thermophoresis, atomic force microscopy (AFM) and free flow electrophoresis experiments in P6 were performed by M. Wolff and A. K. Buell [233]. The original article is attached in Appendix · P6. The following text and figures are adapted from the publication P6, with only a few editorial changes within the framework of Creative Common License 4.0.

Although MST is an emerging technique with high potential in the field of quantification of binding of proteins in their native environment, the thermophoresis of such complex systems is not entirely understood yet. There is still a lack of a theory that allows the prediction of the value of the Soret coefficient S_T of any protein under a given set of conditions. The issue of quantitative measurements of thermophoresis of proteins or protein assemblies has only been investigated by a few studies so far [261, 262]. The presented approach includes a precise control of sample preparation, independent and quantitative determination of size, electrophoretic and thermophoretic mobility, as well as theoretical modeling. In short, the Soret coefficient S_T of polymers is assumed to be a combination of three main contributions:

$$S_T = \underbrace{S_T^{\text{CM}} + S_T^{\text{EL}}}_{\text{charge-dependent}} + S_T^{\text{NI}}. \quad (7.1)$$

For charged biopolymers, the capacitor effect (S_T^{CM}) and the Seebeck effect (S_T^{EL}) are of importance. At present, the nonionic contribution (S_T^{NI}) cannot be modeled completely. Likely, surface properties of the macromolecule undergoing thermophoresis are involved in this contribution, such as hydrophobicity [74]. The complete thermophoretic model is discussed in detail in publication P6 and its attached supplement [233].

7.3.1 Results

In order to examine the importance of electrostatic effects in protein thermophoresis, FCS and free flow electrophoresis are used together with thermophoretic measurements of the Soret coefficient of α -syn. The properties of α -syn are studied in its monomeric, oligomeric and fibrillar form. A minimally invasive labeling strategy was applied, in which only a few protein molecules are labeled within each aggregate. The diffusion constant and the hydrodynamic size of the various forms were determined with FCS (Figure 7.5 and Table 7.1). AFM is used as an additional control technique for the size

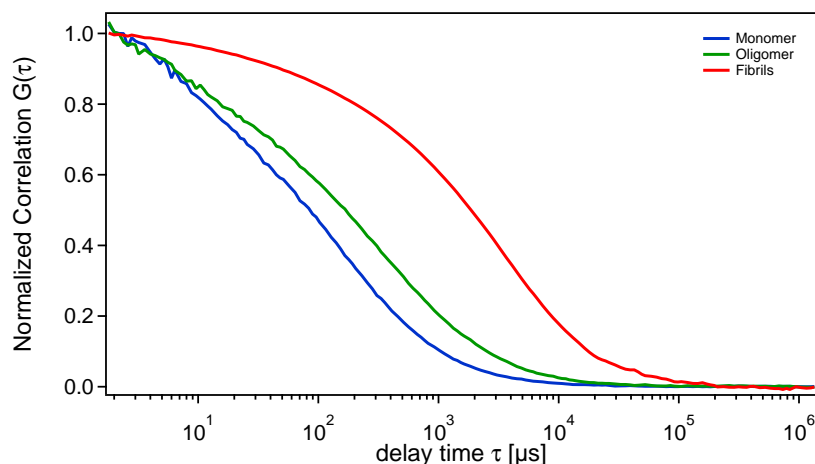


Figure 7.5: Normalized autocorrelation curves of monomeric (blue), oligomeric (green) and fibrillar (red) α -syn. Accurate determination of the diffusion constant and the (effective) hydrodynamic radii of the different species is possible using FCS and the Stokes-Einstein equation (Equation 2.35). The shift of the curves to the right towards longer diffusion times is an indicator for an increase in size. Reprinted with permission from [233].

form	D [$\mu\text{m}^2 \text{s}^{-1}$]	spherical R_h [nm]	el. mob. [$\mu\text{m s}^{-1} \text{V}^{-1} \text{cm}^{-1}$]	charge [-e]	charge [-e] (thermophoresis)
monomer	82 ± 3.4	2.8 ± 0.1	-2.06 ± 0.11	-10.9	-6.6
oligomer	35 ± 3.4	7.5 ± 0.7	-3.09 ± 0.46	-50.4	-22.1
fibril	4.1 ± 0.4	-	-2.91 ± 0.02	-(200-300)	-78

Table 7.1: Results of FCS and microfluidic free flow electrophoresis measurements. The data is averages of several independent experiments.

values. Microfluidic free flow electrophoresis enables the independent determination of electrophoretic mobility and an estimation of the effective charge [263].

Figure 7.5 clearly demonstrates the difference in the diffusive behavior of the different forms of α -syn. A shift to longer diffusion times with increasing size and molecular weight of the complex is observed. The hydrodynamic radii of the monomeric and the oligomeric form almost differ by a factor of three, while the values for the charges determined by free flow electrophoresis only differ by a factor of five, even though a typical oligomer is built by 30 monomers (Figure 7.6) [264]. For fibrils, a radius of 4 nm and an average length of 200 nm was obtained by AFM. The charge increases 20- to 30-fold compared to the monomer.

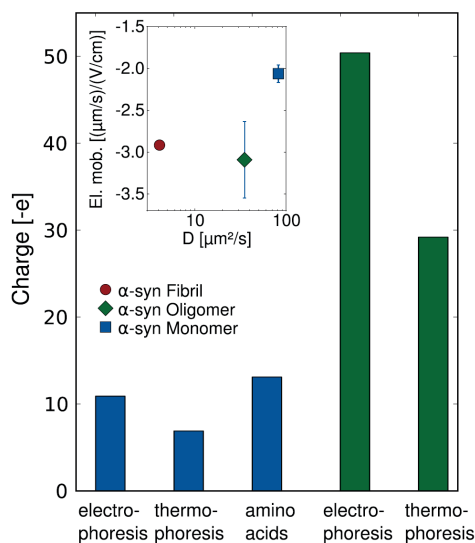


Figure 7.6: Charges determined with various approaches for different subspecies of α -syn. Inset: The diffusion properties of fluorescently labeled monomeric (red), oligomeric (green) and fibrillar (blue) α -syn, determined with FCS, in dependence on the free flow electrophoretic mobilities. Reprinted with permission from [233].

Knowledge of the electrostatic properties and the size of proteins may be used to predict the Soret coefficient. It is demonstrated that the current model describes the change of S_T caused by a change of the ionic environment. S_T depends on the salt concentration of the surrounding medium. The Soret coefficients were determined for all three species using thermophoresis. The Soret coefficient of different species of α -syn varies mainly due to their dependence on their size and charge. The values of the charges obtained by best fit of the thermophoretic model are in a plausible range, as shown in Table 7.1. Nevertheless, the charges determined by the complementary techniques free flow electrophoresis and thermophoresis vary significantly. This deviation might be caused by models that are still too simplified, uncertainties in S_T of salts or still additional unknown factors of the Soret coefficient.

In order to test if the change in thermophoretic behavior of fibrils in the presence of additional unlabeled monomeric α -syn is caused by an increase in size due to monomer incorporation, α -syn fibrils are measured with FCS before and after incubation with additional unlabeled monomers at 70°C. The structural rearrangements and/or desolvation that are required for this reaction are greatly accelerated by the increase in temperature [251, 265]. The increase in size of the fibrils is clearly visible in the corresponding correlation curves determined by FCS (Figure 7.7).

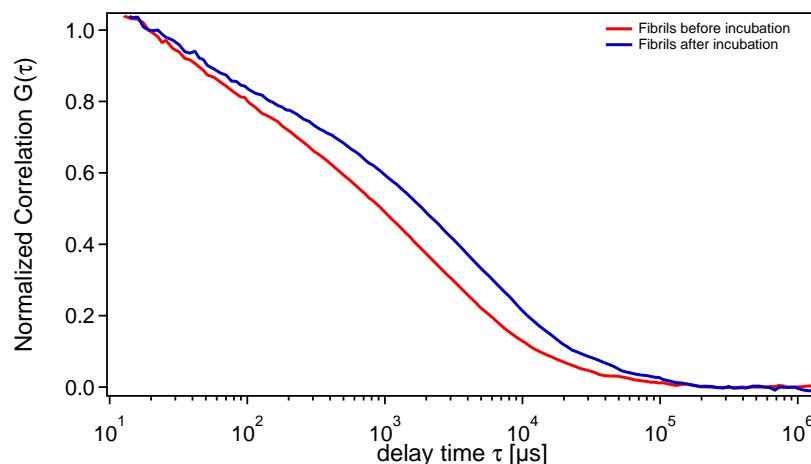


Figure 7.7: Normalized autocorrelation curves of fibrillar α -syn before and after incubation with $70 \mu\text{M}$ unlabeled monomeric protein at 70°C . The shift to the right towards longer diffusion times indicates an increase in size. The diffusion constant changes from $3.8 \pm 0.2 \cdot 10^{-12} \text{m}^2 \text{s}^{-1}$ to $2.4 \pm 0.2 \cdot 10^{-12} \text{m}^2 \text{s}^{-1}$. Adapted with permission from [233].

Additionally, FCS is used to measure the longtime stability of purified oligomers. A sample of oligomers is measured continuously for more than 60 h at room temperature (Figure 7.8). Only a very slight trend towards growing sizes is observed. This finding validates that oligomers are thermodynamically highly stable and display negligible kinetics of dissociation over days.

The established general principles regarding the thermophoresis of protein aggregates are applied for two exemplary binding studies to test the concept for ligand screening. Firstly, the interaction with a single domain nanobody is investigated. Secondly, the binding of the small biomolecule epigallocatechin gallate is studied. Both substances are potential drug candidates that are supposed to influence α -syn upon binding, so their binding affinities are determined. Details on these projects are shown in the attached publication P6 [233].

7.3.2 Conclusion

In the attached publication P6, a quantitative description of the thermophoretic behavior of different forms of the complex protein α -syn is provided. The determined Soret coefficients are in good agreement with the theoretical model based on charge effects. This is key towards a quantitative understanding of the thermophoresis of charged proteins in their various forms. Herein, electrostatic effects and the size of proteins play an

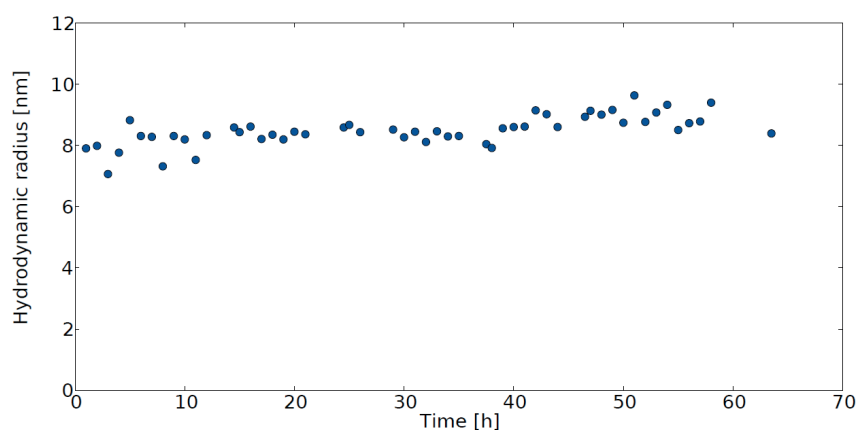


Figure 7.8: Time resolved size measurement of labeled α -syn oligomers over more than 60 h obtained with FCS at room temperature. The data is a confirmation of the high structural stability of these types of aggregates. Reprinted with permission from [233].

important role. For instance, oligomeric and fibrillar α -syn show similar electrophoretic properties, but very different thermophoretic ones. Complementary techniques such as FCS and AFM are relevant to promote new promising technological developments such as MST and to make progress in the corresponding theoretical model as demonstrated in this study. The approach presented may be applied to similar proteins, such as $A\beta$, to screen for new drugs. The low sample volume requirements and the rapidity of each measurement offer a potential for high throughput screening for diagnostics or theoretical development.

Chapter 8

Conclusion and Future Prospects

In the presented work, biophysical questions considering binding interactions with a background in pharmacology and medicine are addressed. Here, FCS proved to be a versatile method for the investigation of interactions of proteins and drug nanocarriers, the impact of the adsorbed proteins on the release and protein self-assembly.

The binding of proteins to solid NPs and liposomes was evaluated. An excellent agreement of the evolution of the protein corona on silica NP in experiments and the predictions by simulations and non-Langmuir differential rate equation (NLDRE) theory in a three-component model plasma were obtained. The combined simulation-theory approach uses only information determined from easily performable single protein-NP experiments. Evidence of “memory” in the evolution of the protein corona was found upon changes in the molecular composition of the environment, which confirms the assumption that the initial corona is not completely exchanged upon transition of biological compartments. This effect would have significant implications for medical applications and warrants further investigation. Building on this, a systematic study of single protein-NP interactions was performed using representative proteins and NPs. For strong binders, equilibrium binding constants and the average area occupied by a single protein were determined. Desorption rates of proteins from NPs were measured in the presence of FBS and linked to the hierarchical order of the protein-NP affinity.

All of this is key for comprehension of the modulation of the corona and its natural development inside the body. In the end, this allows understanding where a NP might end up and which proteins influence this location. Tuning the protein corona in a controlled way may be used to design specific NP properties and thus control the fate of NP in mammalian bodies. In this way, more advanced drug delivery carriers can be

created by stable binding of target molecules, such as Tf or ApoA1, on the NP surface. Hazardous NPs might be coated, so that they are eliminated quickly from the human body and cause less damage. Given the prominence of NPs already present in products of our every day life, such as in food, sunscreen and cosmetics, and any of a multitude of promising future uses of NPs yet to be discovered, knowledge and control of such coatings would be invaluable.

The discussed future prospects can be assigned equally well to TSLs, which are conceptualized for therapeutic application. The stability of TSLs was shown in different media. A novel assay based on FDG as a cargo load and FCS to determine the release from liposomes with high precision was established. To clarify whether the presence of proteins alters the behavior upon intentional release, the temperature-dependent release profiles of TSLs were measured in buffer, serum or plasma from different species, as well as in single-protein solutions. A correlation between the release behavior and the binding affinities of the four selected proteins was not observed. The FCS data confirmed a shift towards lower values of T_m in the presence of mouse plasma. Evaluation of such *in situ* information is important to avoid obstacles and serious misinterpretation of results during *in vivo* animal testing. The presented approach is applicable to a broad field of possible interactions of all kinds of liposomes with their environment. TSLs themselves offer the chance to become a valuable tool in controlled drug delivery. When filled with a contrast agent, TSLs can be used together with magnetic resonance imaging for guided drug delivery, allowing online monitoring of the release and hence controlling of the released drug concentrations. This would be a unique characteristic of the combination of TSLs and magnetic resonance imaging guided drug delivery in medicine.

The problematic of amyloidogenic proteins such as α -syn and $A\beta$ is both an interesting biophysical question with a wide impact as well as an inspiration to the development of novel approaches and existing methods. In this thesis, the self-assembly of $A\beta$, with focus on the toxic intermediate species was studied. To this end, an alternative algorithm to MEMFCS for the analysis of polydisperse samples was successfully implemented: the GDM. A protocol for the evaluation of self-assembling proteins for FCS was established. In the context of α -syn studies, FCS served as a complementary technique to take thermophoresis to the next level. Together, both methods hold the potential to contribute a little bit to understanding the biophysical mechanisms of self-assembly and in both cases the non-invasiveness of FCS and MST is crucial in order to measure processes that would easily be disturbed by changes to the environment. Potential therapeutical candidates

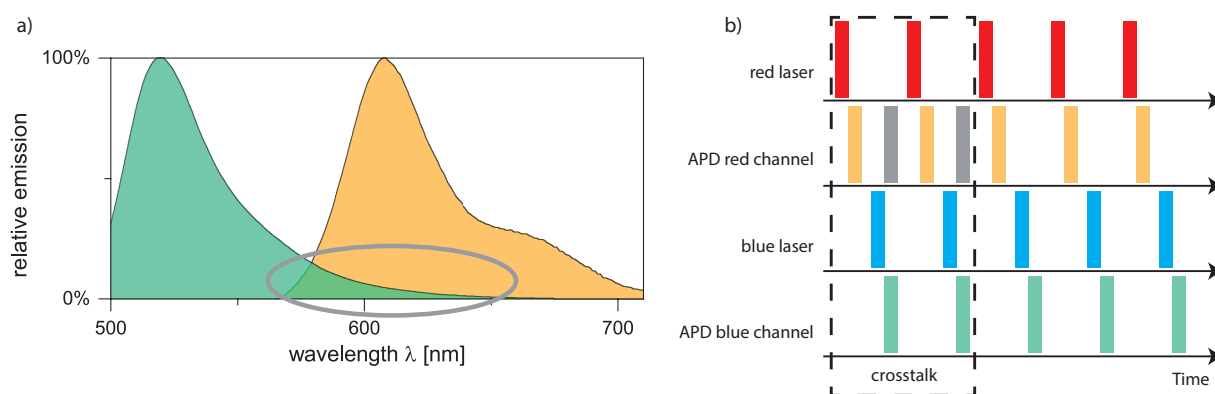


Figure 8.1: PIE-FCCS. a) Crosstalk of two dyes. The emission spectra of the blue and the red dye overlap. Spectrum of blue dye shown in green, of red dye shown in orange. The signal tail of the blue dye, distorts the real signal of the red dye. b) The excitation lasers are interleaved in a way that the fluorescence emission caused by one pulse is finished, before the next light pulse arrives. An unambiguous assignment of excitation pulse and emission is possible, allowing elimination of the spectral crosstalk. For instance, the crosstalk in the red detection channel caused by excitation is shown in gray. This signal can be excluded from further analysis.

could be screened by FCS or thermophoresis, and any change in the behavior of the self-assembly of $A\beta$, α -syn or other amyloidogenic proteins would be instantly visible *in vitro*. This could help reduce the need for animal testing and at the same time identify promising drugs that should be studied as to their *in vivo* applicability.

Although conventional FCS proved useful in these studies, it faces some limitations. For instance, the FCS-approach works well in case of strong binding, but comes to its limits for weak interactions such as the ones shown in the interaction matrix in Section 5.3. FCS measurements, as presented in this work, rely on a size/mass difference of the binding partners. Interactions of receptor-ligand combinations that possess similar hydrodynamic sizes are difficult to detect in this setting. Such processes include the binding of proteins to nanoparticles with a size of only 10 – 20 nm, but also protein-protein interactions during early self-assembly.

In order to overcome limitations of standard FCS to study binding interactions, further developments of FCS may be applied: pulsed-interleaved excitation (PIE)-fluorescence cross correlation spectroscopy (FCCS). PIE-FCCS was introduced in 2005 to extend the capabilities of FCS and FCCS [266].

For cross correlation, multiple excitation sources are used to excite differently fluorescently labeled ligand and receptor. Thus, the two particle types can be separated by the

color of the emitted light and the simultaneous appearance (colocalization) of both colors, and therefore the presence of both molecules, is an indicator for binding. The cross correlation of both is a measure of the fraction of built complexes. A disadvantage of using a conventional FCCS set-up with continuous laser is spectral crosstalk (Figure 8.1 a). For instance, photons which are detected in the red channel after blue excitation are either emitted from a blue fluorophore or red fluorophore which is directly excited by the blue light. This effect then leads to an increased amplitude in the cross correlation, overestimating the intensity of binding. One way to overcome this limitation is to interleave the excitation sources, as in PIE, allowing the detected fluorescence emission to be assigned to the light pulse that generated it (Figure 8.1 b, gray). In PIE, this is put into practice by alternating the different light sources with sufficient delay so that all emitted photons from one laser pulse are detected before the next pulse of a different color arrives. In this way, the signals are not only separated spectrally but also temporally. Only photons in the blue channel are correlated after a blue excitation pulse and photons in the red channel only after red excitation. In this way, spectral crosstalk as mentioned above, and thus biased interaction activities, are eliminated and the contrast in the longer wavelength channel can be increased (Figure 8.1 b) [267].

PIE-FCCS enables measuring of weak interactions with high sensitivity that are not accessible to conventional FCS. This approach might be a useful extension for more detailed studies of the memory effect, the hierarchy of protein-NP interactions or the protein-TSL binding discussed in Chapters 5 and 6, respectively. Additionally, this technique provides a means to characterize interactions of receptor-ligand combinations that possess similar hydrodynamic sizes, leading to only a small change in the diffusion properties upon binding. In particular, this is useful to consider interactions of proteins with each other such as SA and Tf, but it also enables studying the first steps of protein self-assembly with a higher resolution. This way, a better understanding of the nucleation processes of amyloidogenic proteins might be obtainable, helping in pharmacological development. Given the immense stability of the fibrillar proteins resulting from these self-assembly processes in amyloidogenic diseases, there is also great interest in understanding and being able to replicate these processes to build other fibril materials. Already hybrid membranes of β -lactoglobulin amyloid fibrils and activated carbon are used to remove heavy metal and radioactive waste from water [26]. Of course, in order to truly be able to control these self-assembly processes, knowledge and understanding of the initial nucleation steps, that cannot be resolved by conventional FCS, are extremely crucial.

PIE-FCCS should be capable of sheeding a light onto these processes and thus enlarge our understanding and reproduction capabilities thereof.

Taken together, these findings will contribute to a better understanding of biophysical binding interactions and consequently will contribute to better engineered drug delivery vehicles made from solid NPs or liposomes. The presented platform technologies have the potential for further development and might contribute to the combat of amyloidogenic diseases by providing a means to efficiently screen for novel medication. Research nowadays is becoming increasingly interdisciplinary, and thus it should come as no surprise that physics, in the form of FCS and sophisticated evaluation algorithms, can add a valuable contribution to things that in the past would have been considered purely medical questions, and might have been impossible or at least significantly more challenging to answer.

Publications and Manuscripts

Associated Publications and Manuscripts

All publications are fully reprinted with permission.

- P1 O. Vilanova*, **J. J. Mittag***, P. M. Kelly*, S. Milani, K. A. Dawson, J. O. Rädler and G. Franzese. Understanding the Kinetics of Protein-Nanoparticle Corona Formation *ACS Nano*, 2016. *shared first authorship
- M2 **J. J. Mittag***, T. Preiß*, A. Das*, S. Milani, J. O. Rädler. Hierarchy of Protein Nanoparticle Binding Affinities. *to be submitted to The Journal of Physical Chemistry C*. *shared first authorship
- M3 **J. J. Mittag**, B. Kneidl, T. Preiß, G. Winter, S. Wuttke, M. Hossann, H. Engelke and J. O. Rädler. Impact of Plasma Protein Binding on Cargo Release by Thermosensitive Liposomes Probed by Fluorescence Correlation Spectroscopy. *under revision, European Journal of Pharmaceutics and Biopharmaceutics*, 2017.
- P4 **J. J. Mittag**, S. Milani, D. M. Walsh, J. O. Rädler, J. J. McManus. Simultaneous Measurement of a Range of Particle Sizes During Abeta Fibrillogenesis Quantified Using Fluorescence Correlation Spectroscopy. *Biochemical and Biophysical Research Communications*, 2014.
- M5 **J. J. Mittag**, J. O. Rädler and J. J. McManus. Peptide Self-assembly Measured by Fluorescence Correlation Spectroscopy. *accepted, Methods in Molecular Biology*, 2017.
- P6 M. Wolff, **J. J. Mittag**, T. W. Herling, E. De Genst, C. M. Dobson, T. P. J. Knowles, D. Braun and A. K. Buell. Quantitative Thermophoretic Study of Disease-related Protein Aggregates. *Scientific Reports*, 2016.

Further Publication

C. Aponte-Santamaria , S. Lippok, **J. J. Mittag**, T. Obser, R. Schneppenheim, C. Baldauf, F. Gräter, U. Budde, J. O. Rädler. Mutation G1629E Increases von Willebrand Factor Cleavage via a Cooperative Destabilization Mechanism. *Biophysical Journal*, 2017.

P1 · Understanding the Kinetics of Protein-Nanoparticle Corona Formation

O. Vilanova*, J. J. Mittag*, P. M. Kelly*, S. Milani, K. A. Dawson,
J. O. Rädler and G. Franzese

ACS Nano, 2016.

*shared first authorship

Understanding the Kinetics of Protein–Nanoparticle Corona Formation

Oriol Vilanova,^{*,†,‡,⊥} Judith J. Mittag,^{¶,⊥} Philip M. Kelly,^{§,||,⊥} Silvia Milani,[¶] Kenneth A. Dawson,^{§,||} Joachim O. Rädler,[¶] and Giancarlo Franzese^{†,‡,⊥}

[†]Secció de Física Estadística i Interdisciplinària—Departament de Física de la Matèria Condensada, Facultat de Física, Universitat de Barcelona, Martí i Franquès 1, Barcelona 08028, Spain

[‡]Institut de Nanociència i Nanotecnologia, Universitat de Barcelona, Av. Joan XXIII S/N, Barcelona 08028, Spain

[¶]Faculty of Physics, Center for Nanoscience, Ludwig-Maximilians-Universität, Geschwister-Scholl-Platz 1, Munich 80539, Germany

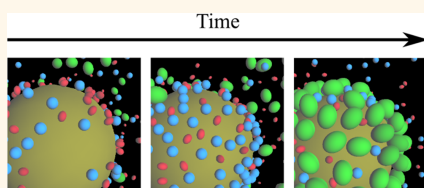
[§]Center for BioNano Interactions, School of Chemistry and Chemical Biology and ^{||}Conway Institute for Biomolecular and Biomedical Research, University College Dublin, Belfield, Dublin 4, Ireland

Supporting Information

ABSTRACT: When a pristine nanoparticle (NP) encounters a biological fluid, biomolecules spontaneously form adsorption layers around the NP, called “protein corona”. The corona composition depends on the time-dependent environmental conditions and determines the NP’s fate within living organisms. Understanding how the corona evolves is fundamental in nanotoxicology as well as medical applications. However, the process of corona formation is challenging due to the large number of molecules involved and to the large span of relevant time scales ranging from 100 μ s, hard to probe in experiments, to hours, out of reach of all-atoms simulations. Here we combine experiments, simulations, and theory to study (i) the corona kinetics (over 10^{-3} – 10^3 s) and (ii) its final composition for silica NPs in a model plasma made of three blood proteins (human serum albumin, transferrin, and fibrinogen). When computer simulations are calibrated by experimental protein–NP binding affinities measured in single-protein solutions, the theoretical model correctly reproduces competitive protein replacement as proven by independent experiments. When we change the order of administration of the three proteins, we observe a *memory* effect in the final corona composition that we can explain within our model. Our combined experimental and computational approach is a step toward the development of systematic prediction and control of protein–NP corona composition based on a hierarchy of equilibrium protein binding constants.

KEYWORDS: protein–nanoparticle interactions, competitive protein adsorption, protein corona, FCS, DCS, SDS-PAGE, microscale thermophoresis, molecular simulation

The interaction of NPs with biological media is key in the transport of NPs across the cell membrane. When NPs are exposed to fluids that contain proteins and other biomolecules, part of those biomolecules are immediately adsorbed forming the so-called “protein corona”. This corona is believed to depend on the different biological environments crossed by the NP as well as on the current surroundings.^{1,2} Therefore, layers of adsorbed proteins that are formed while the NPs move from a biological milieu to another evolve as the concentration of protein and the media composition change.³ Nowadays it is generally accepted that part of the proteins in the corona can remain for a relevant time on the NP surface (hard corona),⁴ possibly preventing the adsorption of other molecules. Other proteins, instead, dynamically exchange with those in solution (soft corona).^{5,6} Nevertheless, our knowledge



Kinetics of protein adsorption onto NPs. Red: Albumin, blue: Transferrin, green: Fibrinogen.

about the dynamic exchange of the corona in response to changes in the composition of the milieu is still very limited. Due to the relevant role that the evolution of the corona plays in the way that NPs interact with biological systems, *e.g.*, in their targeting of specific cellular receptors,⁷ it is crucial for any possible biological application⁸ to understand how the processes of protein adsorption and exchange occur in the corona.⁹ Hence, there is a need for an accurate modeling of the kinetics of the protein corona in order to decipher the biological identity of the NPs.

Received: July 25, 2016

Accepted: November 9, 2016

Published: November 9, 2016

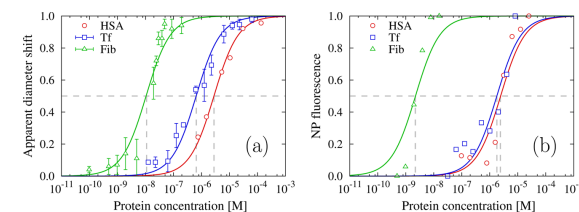


Figure 1. Experimental characterization of NPs in monocomponent protein solutions of HSA, Fib, or Tf, as a function of protein molar concentration along binding isotherms. For each set, the concentration at which the normalized data has the value 0.5 corresponds to the protein binding affinity K_D (Table 1). (a) Normalized DCS apparent diameter, eq 3, of the NP coated by proteins with respect to the value with no proteins. (b) Normalized MST relative fluorescence F_{norm} , eq 4, after diffusion of fluorescently labeled NPs under thermal gradient. In both panels, symbols are the experimental data, and lines are the best fits with eq 1. Molar concentration is expressed in $M = \text{mol/L}$.

Coarse-grained (CG) molecular simulations have proven to be a powerful tool for the study of NPs interacting with biological systems at the macromolecular scale.^{10,11} Recently Vilaseca *et al.* developed a computational approach to simulate the adsorption of proteins on flat surfaces.¹² These theoretical results suggest that the corona composition, after exposure to a multicomponent system, undergoes a relaxation scenario. In particular, fast-diffusing but weakly adsorbing proteins reach the surface first, but are replaced by strong-binding proteins next.

The mechanism of formation of the corona of the NP can be separated into two main stages: (i) the bare NP enters the biological environment and comes in contact with biomolecules that first adsorb forming the initial corona; and (ii) the corona composition starts to evolve due to competition between proteins. An atomistic description of such a complex mechanism of formation and evolution of the protein corona is at the moment computationally unfeasible and, more importantly, avoidable. Here we show that by combining experiments, computer simulations, and theory, we are able to develop an approach that allows us to predict the corona composition in a variety of cases. We present results for a three-component model plasma, and we describe how the approach can be extended in a systematic way to more complex protein solutions.

We consider a solution composed of different combinations of the following representative blood plasma proteins: human serum albumin (HSA), transferrin (Tf), and human fibrinogen (Fib). These proteins are very numerous in plasma and are present in the corona of silica (SiO_2) NPs.¹³ HSA is the most abundant protein in plasma, representing almost 55% of its composition.¹⁴ It is a globular protein, with a small mass of 67 kDa, that regulates the osmotic pressure of plasma. Tf has a concentration in plasma of 3 mg/mL, with a mass of about 80 kDa. This protein transports iron through the body and maintains the iron homeostasis. Fib is a rod-like protein with a large mass of 340 kDa and has a key role in coagulation. Its concentration in plasma varies from 1.7 to 4.5 mg/mL.

We measure the affinity of each protein for the silica NPs using two independent approaches, namely differential centrifugal sedimentation (DCS) and microscale thermophoresis (MST). While the DCS characterization^{9,15–17} is performed by extracting the NPs from the solution, with MST we probe the interactions of NPs with proteins directly in solution. Using a combination of these two experimental techniques, we obtain reliable binding constants for each of the individual proteins interacting with silica NPs. Next, we use the

measured NP affinities—and other known parameters—of the proteins to define a CG model that includes protein–NP and protein–protein interactions, up to three-body contributions. Yet the model is simple enough to allow us to perform molecular dynamics (MD) simulations for NPs in binary and ternary protein solutions up to 10 s. This time scale is out of reach of atomistic simulations and approaches the lower limit of the experimental time resolution. However, the relevant time scale for the experiments and the biological applications is as long as hours. Therefore, we develop an original theoretical approach, based on the non-Langmuir differential rate equation (NLDRE), to extrapolate the adsorption kinetics over hours. We test our theoretical predictions about the adsorption kinetics by using fluorescence correlation spectroscopy (FCS). With this technique, we label one protein species at a time and follow its binding on NPs precoated with other proteins. This allows us to monitor the adsorption kinetics and the displacement from a precoated corona by competitive binding. Finally, we verify our theoretical predictions about the relative composition of the hard corona using sodium dodecyl-sulfate polyacrylamide gel electrophoresis (SDS-PAGE).

RESULTS AND DISCUSSION

Binding Affinities Measurements in Single-Protein Solutions. We prepare solutions of HSA, Tf, and Fib with silica NPs and measure by DCS the change in the sedimentation time with respect to conditions with no proteins (eq 3 and Figure 1a). By MST, we measure the normalized relative fluorescence F_{norm} of fluorescently labeled NPs in a monocomponent protein solution under a thermal gradient (eq 4 and Figure 1b). We fit both quantities (Figure 1) with the law of mass action, eq S1 in Supporting Information (SI), in the limit of low NP concentration, whose solution Γ_{eq} is the normalized surface coverage, as a function of the protein concentration C_p :

$$\Gamma_{eq}(C_p) = \frac{C_p}{K_D + C_p} \quad (1)$$

where K_D for each of the three proteins separately (Table 1) is the only fitting parameter of the experimental data and marks the concentration at which $\Gamma_{eq} = 0.5$. The estimates from the two techniques agree in order of magnitude, with $K_D^{Fib} \ll K_D^{Tf} < K_D^{HSA}$. Hence we establish a hierarchy of the tendency to adsorb on the NP surface, that for Fib is much larger than for Tf and for Tf larger than for HSA.

Table 1. Binding Affinity $K_D \equiv k^{off}/k^{on}$ Determined With DCS (center column) and MST (right column) for the Three Proteins Used in This Work^a

protein	K_D [μ M] (DCS)	K_D [μ M] (MST)
HSA	2.8 ± 0.2	2.4 ± 0.6
Tf	0.65 ± 0.08	1.8 ± 0.4
Fib	$(11 \pm 2) \times 10^{-3}$	$(2.2 \pm 0.9) \times 10^{-3}$

^aThe values for HSA coincide within the error bars and are consistent with previous literature.^{24–26} Those for Tf and Fib agree only in order of magnitude, however the MST measurements are possibly biased by agglomerates of NPs²⁷ and are based on less data and with larger noise (Figure 1) than the DCS measures. K_D is expressed in μ M = 10^{-6} M.

The CG Model. Our goal is to unveil the molecular mechanisms that regulate the corona formation, and simulations are potentially helpful to this aim. However, a direct comparison with experiments is unfeasible with all-atoms simulations. Hence, we resort to a model where we coarse-grain many degrees of freedom, and in this way, we step up the size and duration of our MD simulations, approaching the experimental scale.

In our CG approach, we introduce effective potentials for protein–NP and protein–protein (two-body and three-body interactions) with implicit solvent. For the protein–NP effective interaction, we adopt a description within the framework of the well-established DLVO theory for colloidal dispersions (Figure 2a and eq S8 in SI).^{18,19}

For the two-body protein–protein effective interaction, we follow Vilaseca *et al.*¹² and consider an interaction potential that encodes two different conformations for each protein (eq S9 in SI and Figure 2b). This model, adopted to describe the competition among proteins near a surface, compares well with the experimental data without preassumptions about the adsorption mechanisms or the adsorption rates.

At high concentrations of protein, we introduce a three-body correction to the protein–protein interactions. We find that this term is essential to get simulation results consistent with the experimental data. This effective three-body interaction (eq S10 in SI) is due to correlations between pairs of proteins near the surface of the NP and could arise from conformational changes of surface-adsorbed proteins.

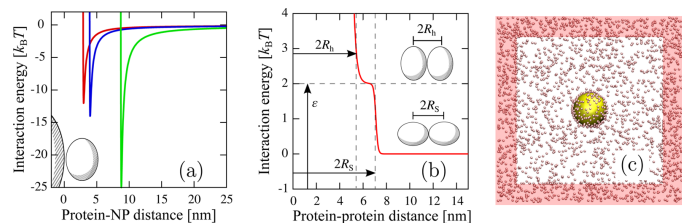


Figure 2. Schematic representation of the CG model. (a) The protein–NP interaction potential (continuous line, eq S8 in SI) as a function of the distance between the surface of the silica NP (sketched as a portion of a large sphere on the left) and the center of the protein (red line for HSA, blue for Tf, and green for Fib). For sake of clarity, in the panel we sketch only the HSA as an ellipsoid (on the right). (b) The protein–protein interaction potential (continuous line, eq S9 in SI) as a function of the distance between the centers of two HSA proteins. The dashed horizontal line marks the characteristic interaction energy ϵ . Inset: sketch of two possible HSA conformations defining the characteristic distances R_h and R_s (both marked by dashed vertical lines in the main panel). (c) Snapshot of the simulation box showing the NP (golden sphere in the center) surrounded by the protein solution (small spheres). The highlighted red zone corresponds to the buffer region, which we use to maintain the protein concentration constant as in the experimental setup.

Table 2. Parameters for the CG Model of Proteins^a

	HSA	Tf	Fib
R_h [nm]	2.7^{28}	3.72^{16}	8.5^{29}
R_s [nm]	3.6^{30}	3.72^5	$11.0^{30,31}$
ϵ [$k_B T$]	2^{12}	2^{12}	2^{12}
M [kDa]	67	80	340
ϕ [mV]	-15^{32}	$-10^{33,34}$	-20^{31}
A_H [$k_B T$]	9.75	8.4	7
N_{max}	550	450	120

^a R_h and R_s are the two characteristic length-scales of a protein in each conformation: R_h is obtained from the maximum surface concentration of each protein, and R_s is the hydrodynamic radius. ϵ is the repulsion energy between two adsorbed proteins at the shorter diameter distance in eq S9 in SI. M is the mass of the protein (as specified by Sigma-Aldrich), ϕ is the zeta-potential in PBS, A_H is the Hamaker constant, calibrated as explained in the text, for the DLVO interaction potential with silica NP in eq S8 in SI. N_{max} is the maximum number of adsorbed molecules forming a full monolayer on the NP, as computed by simulations. We indicate the adopted units near the parameters and the used references, if applicable, near their values.

The model's parameters (Tables 2 and S1 in SI) are all known but the DLVO's Hamaker constant A_H in eq S8 in SI. We estimate A_H (Figure S3 in SI) based on our knowledge of the binding affinities K_D^{Fib} , K_D^{Tf} , and K_D^{HSA} given by the eq 1 derived from the fit of the experimental data.

Competitive Protein Adsorption in Two-Component Protein Solutions. In order to test the competitive adsorption between different kinds of proteins, we consider solutions containing two among the three proteins, HSA, Tf, and Fib. To allow a better comparison between simulations and experiments, we follow a sequential protocol in which we introduce one kind of protein at a time into the initial NP suspension.

First, we perform simulations of silica NPs suspensions, at a concentration of 100μ g/mL, with HSA at different concentrations, chosen within the range of accessible experimental values. After equilibrating the precoating, we add to the solution Fib at 5μ g/mL concentration and study the adsorption kinetics of Fib (Figure 3).

Because $K_D^{Fib} \ll K_D^{HSA}$, we expect that Fib will displace the adsorbed HSA proteins. However, we find a strong dependence of the Fib adsorption kinetics on the concentration of HSA.

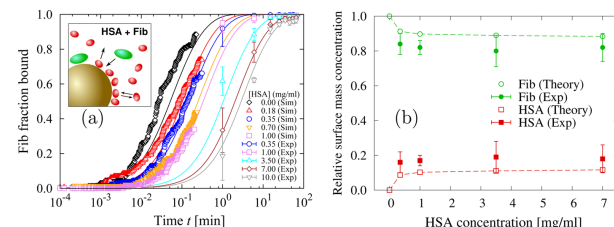


Figure 3. Two-component protein solution: Competitive adsorption of Fib on silica NPs precoated with HSA at different concentrations. (a) Simulation results (open symbols without error bars) of the fraction bound of adsorbed Fib as a function of time are extrapolated to large time-scales, using the NLDRE theory (lines), to allow us to compare our predictions with our experimental data (symbols with error bars). The agreement is excellent. Concentrations are 5μ g/mL for Fib, 100μ g/mL for silica NPs, and for the lines from top to bottom, 0.00, 0.18, 0.35, 0.70, 1.00, 3.50, 7.00, and 10.00 mg/mL for HSA. Lines and symbols with matching colors correspond to the same HSA concentration. Inset: Schematic representation of Fib (green) displacing HSA (red) on the NP surface (golden). (b) Relative surface mass concentration of HSA (red) and Fib (green) after 120 min as a function of the HSA concentration in solution, as predicted from NLDRE theory (open symbols connected by a dashed line), and compared with data from SDS-PAGE (symbols with error bars).

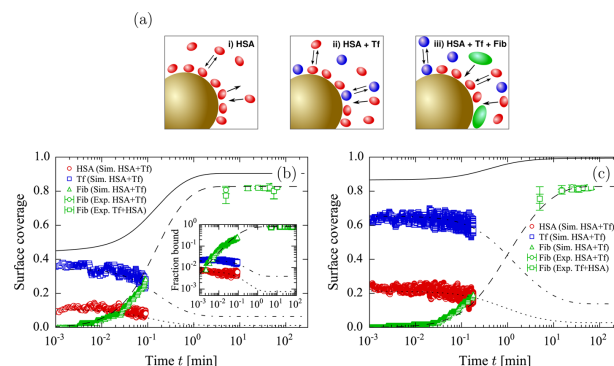


Figure 4. Three-component protein solution: Competitive adsorption of Fib on silica NPs precoated with HSA first and Tf next for 2 h. (a) Schematic representation of the three-steps adsorption protocol with Fib (green) displacing Tf (blue) and HSA (red) on the NP surface (golden). (b) Normalized surface coverage, eq 1, of HSA (red circles, at concentration 0.07 mg/mL), Tf (blue squares, at 0.07 mg/mL), and Fib (green triangles, at 5μ g/mL) adsorbed on 100μ g/mL silica NPs as a function of time, calculated by simulations at short times ($t \leq 0.1$ min, Figure S6 in SI) and extrapolated to long time ($t \geq 200$ min) by the NLDRE theory (dotted line for HSA, dot-dashed line for Tf, dashed line for Fib, and solid line for the total surface coverage). In simulations we precoat the NPs first with HSA, until equilibrium, and next with Tf, until equilibrium, before adding Fib at $t = 0$. The prediction for Fib compares well with the fraction bound of Fib measured by FCS (symbols with error bars) for $t \geq 3$ min. The two sets of experimental data refer to (circles) first precoating with HSA for 1 h and next with Tf for 2 h and to (squares) first Tf (1 h) and next HSA (2 h). The saturation value for the Fib surface coverage is reached for $t \approx 10$ min. Inset: Fraction bound, eq 6, of adsorbed proteins corresponding to the surface coverage in the main panel in double-logarithmic scale. (c) Same as in panel b but for HSA and Tf at 3.5 mg/mL concentrations. In this case, the saturation value for the Fib surface coverage is reached for $t \approx 50$ min.

The simulations clearly show that the rate of adsorption of Fib decreases for increasing concentration of HSA in solution. In particular, after 10 s of simulated time, we find that the Fib adsorbed on the NP decreases from $\approx 90\%$ to $\approx 35\%$ when the HSA concentration changes from 0 to 10 mg/mL, respectively.

To better understand this effect with the numerical approach, simulations much longer than those achievable within a reasonable time would be necessary. However, we develop an analytic theory that allows us to extrapolate our numerical results to physiologically relevant time scales (~ 1 h). Our NLDRE theory is based on the law of mass action and differs

from the standard Langmuir theory of adsorption because we do not assume constant adsorption rates. The essential parameters of our theory are the binding affinities and the adsorption/desorption rates of the molecules, that we assume to be dependent on each protein surface coverage and the concentration of NPs and proteins. As explained in SI, these parameters can be fitted from adsorption data at an early stage.

We use the NLDRE theory to extrapolate the long-time behavior of the system (Figure 3) and predict that at the highest HSA concentration (10 mg/mL), it would take more than 5 min for Fib to displace HSA and to have more than 50%

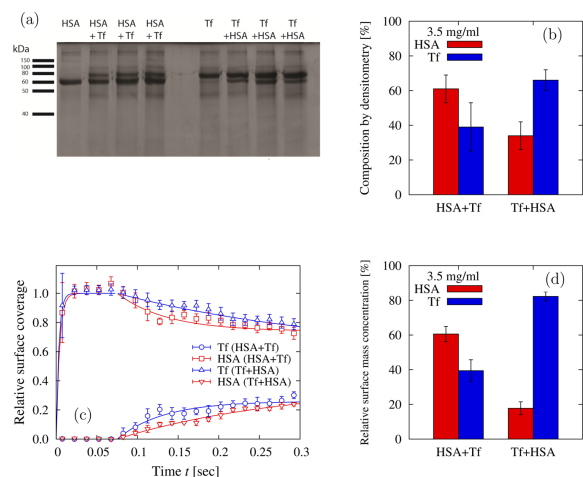


Figure 5. Memory effect in experiments and simulations when we invert the NP incubation order of HSA and Tf both at 3.5 mg/mL concentration. (a) SDS-PAGE gel analysis after incubating the NP in HSA and Tf, in different orders: (from left to right, as indicated by labels) HSA alone; protocol A with HSA first and Tf second (three different samples); Tf alone; protocol B with Tf first and HSA second (three different samples). (b) Densitometry results for the percent of protein corona composition after the gel analysis with NP incubation with HSA (red) and Tf (blue) following the same protocols as in panel a (as indicated by the labels on the bottom). The error bars are estimated as statistical deviation among the three independent samples in panel a. Results are calculated after subtracting background noise. (c) Simulation results for the kinetics of the competitive protein adsorption of the model with three-body interaction between HSA, Tf, and NP (eq S10 in SI): We show the relative protein adsorption on the NP of Tf (blue) and HSA (red), both at 3.5 mg/mL concentration, following the two protocols (protocol A: circle for HSA, protocol B: triangles up for Tf and triangles down for HSA), as a function of time t . In both protocols, the incubation time is $t_{inc} = 0.075$ s, and the quantities are normalized to the value of the main component at t_{inc} . (d) Relative surface mass concentration from simulations in panel c after $t = 0.3$ s, to compare with experimental results in panel b.

of Fib adsorbed, despite the much higher tendency of Fib to adsorb on the NP surface. Our theory predicts that after 30 min, the Fib adsorption kinetics on NPs precoated with HSA at 10 mg/mL concentration is still relatively slower compared to pristine NPs (Figure 3) and that the saturation level is reached within the time frame of 100 min (Figure 3b).

In order to test our theoretical predictions, we perform experiments following the same protocol as in the simulations, *i.e.*, adding Fib at 5 $\mu\text{g/mL}$ concentration to silica NPs (at 100 $\mu\text{g/mL}$) precoated with HSA at different concentrations. We study the adsorption kinetics by estimating the Fib fraction bound with FCS. The fraction bound is defined in eq 6. We verify that the Fib adsorption kinetics change due to the presence of competing proteins on the corona with an overall excellent agreement with our theoretical predictions (Figure 3a).

We repeat the experiment with different HSA incubation times, remove the adsorbed proteins from the NP surface, separate them using SDS-PAGE technique (Figure S4 in SI), and finally estimate the relative mass of each protein on the NP surface by densitometry (Figure 3b). We find that the experimental data follow our theory with very good agreement, confirming the predictive capability of the theory for binary solutions.

Furthermore, we test that the theory can be applied to other binary solutions. In particular, we repeat simulations, theoretical

calculations, and experiments using Tf instead of HSA during the precoating step and then adding Fib in solution. Again, we find that our theory for binary solutions, based on short-time simulations, allows us to make predictions about the adsorption kinetics in excellent agreement with the experiments (Figure S5 in SI).

Competitive Protein Adsorption in Three-Component Protein Solutions. To verify if our approach can be extended in a systematic way to more complex protein solutions, we apply the same procedure to a ternary suspension with HSA, Tf, and Fib. In this case, we follow a three steps exposure protocol: (i) we first incubate NPs in HSA, (ii) we add Tf in solution expecting competition with HSA for the NP surface, and (iii) we finally add Fib that will compete with both Tf and HSA for the corona (Figure 4a).

As for the binary solution, we run short-time simulations for a selected number of cases. Specifically, we consider equal concentrations for HSA and Tf. We first simulate the precoating of silica NPs (at 100 $\mu\text{g/mL}$) with HSA at 0.07 mg/mL until the system is equilibrated. Then we run the simulation adding Tf (at 0.07 mg/mL) until a stable corona of HSA and Tf is formed. Then we add Fib (at 5 $\mu\text{g/mL}$) and perform a simulation for ≈ 0.1 min. Finally, we calculate the long-time behavior of the Fib adsorption using our NLDRE theory. We predict that the corona kinetics reaches the saturation of Fib in ≈ 10 min (Figure 4b).

As in the case of the two-component solution, we test the theoretical prediction by FCS experiments. In particular, we measure the Fib fraction bound after incubating the NPs for 1 h with HSA and, later, for another hour with Tf, both at 0.07 mg/mL concentration (Figure 4a). The comparison of the experimental data with the theoretical prediction is, also for this ternary solution, very good (Figure 4b).

We find a similar good agreement between the experiments (Figure 4c) and the theoretical predictions when we consider the case of NPs sequentially precoated with HSA and Tf at higher concentrations (3.5 mg/mL each). In this case the theory predicts a large slowing down of the protein corona kinetics with respect to the case at lower HSA and Tf concentration, with a saturation of Fib only after ≈ 50 min (Figure 4c). Experiments confirm this prediction.

We observe that the competition with HSA and Tf makes the Fib adsorption slightly slower than the competition with solely HSA at a comparable total mass concentration. For example, for HSA and Tf at 0.07 mg/mL, the time needed for reaching 50% of Fib fraction bound is $t \approx 0.2$ min (Figure 4b), while for HSA at 0.18 mg/mL, it is $t \approx 0.1$ min (Figure 3). However, the time difference between the two cases is negligible when we compare the Fib adsorption kinetics for HSA and Tf at 3.5 mg/mL (Figure 4c) and for HSA at 7.0 mg/mL (Figure 3). This could be interpreted as a consequence of the fact that the binding affinities of HSA and Tf are comparable and both much higher than that of Fib, hence the Fib kinetics is regulated only by the total mass concentration of the competing proteins.

Furthermore, we find, both in simulations and experiments, that within the error bar, there is no difference in Fib kinetics if we incubate first with HSA and then add Tf or *vice versa* (Figure S7 in SI). However, our experiments show that the kinetics *before* the addition of Fib displays a *memory* effect if we change the incubation order, as we discuss in the next section.

Memory Effects in Competitive Protein Adsorption of HSA and Tf. After a preliminary screening showing differences in the kinetics when we invert the incubation sequence of HSA and Tf, we investigate experimentally the memory effect considering two different incubation protocols. In protocol A, we first incubate the silica NP for 1 h with HSA at 3.5 mg/mL, then we add Tf at the same concentration (3.5 mg/mL) for another hour. In protocol B, we invert the order of incubation, first Tf and next HSA, with the same concentrations and times. After each protocol, we wash the NP to remove unbound proteins, and next we remove the attached proteins and electrochemically separate them inside a gel matrix (SDS-PAGE gel analysis, Figure 5a). Finally, after visualization, we quantify the relative abundance of each protein.

We find that the final amount of each protein depends on the protocol. Specifically, the first incubated protein is always more abundant in the corona at the end of the process (Figure 5b). We repeat the experiments for HSA and Tf at smaller concentration, 0.07 mg/mL (Figure S8 in SI), and find the same qualitative result, suggesting that the memory effect does not depend strongly on the initial protein concentrations. On the other hand, by adding Fib after each incubation protocol, we do not find any strong effect on the Fib adsorption (Figure S7 in SI), *i.e.*, the memory effect occurs in our samples before the addition of Fib.

Based on these experimental evidence, we focus on investigating the possible mechanism causing the memory effect for the competitive adsorption between HSA and Tf. In particular, we compare the experiments with the results from

our computational model. We observe that for the model defined by eqs S8 and S9 in SI, the two different incubation protocols lead to the same corona after a transient time (Figure S9 in SI). Therefore, the memory effect implies the existence of other interactions among proteins and NP beside those described by eqs S8 and S9 in SI. Hence we hypothesize that the protein adsorption on the NP induces a change in the protein-protein interaction. This change can be interpreted as a consequence of a protein conformational variation upon adsorption. Specifically, we assume that the change can be modeled by a three-body interaction between the proteins and the NP (eq S10 in SI).

We find that our hypothesis is sufficient to simulate the memory effect (Figure 5c,d). Hence the memory effect can be interpreted as a consequence of how the adsorption on the NP changes the interaction of the first-incubated protein with those adsorbed at a later time, *e.g.*, due to conformational variations, hampering the replacement of the first by the latter proteins.

CONCLUSIONS

We study by experiments, simulations and theory the kinetics of the protein corona forming on 100 nm silica NPs suspended in a ternary solution made of HSA, Tf, and Fib. With the goal of developing a predictive computational model based on a limited knowledge of the protein-NP interactions, we first evaluate the NP binding affinities of each of these three proteins in monocomponent solutions by DCS and MST. We use the estimates of $K_D^{\text{Fib}} \ll K_D^{\text{Tf}} < K_D^{\text{HSA}}$ as parameters in a CG model for the protein-NP interactions and perform $\approx 10^5$ numerical simulations of the model for the competitive protein adsorption on silica NP in binary solutions. To extrapolate the Fib kinetics at physiologically relevant time scales (~ 1 h) and compare with FCS and SDS-PAGE techniques, we develop a NLDRE theory predicting a strong slowing down of Fib adsorption on HSA-precoated NPs compared to pristine NPs. While pristine NPs are covered with more than 50% of the Fib in solution within seconds, it takes more than 5 min when the NPs has been incubated with HSA at 10 mg/mL concentration. All our results show that the Fib kinetics slows down when the NPs are incubated with a higher HSA concentration. Therefore, the kinetic slowdown would become even more relevant for HSA concentrations as high as in human plasma (from 35 to 50 mg/mL). The analysis of the Fib adsorption kinetics on NPs after Tf incubation shows a similar slowdown and a similar good agreement between our theoretical predictions and the experiments. We expect a stronger kinetic effect when the competing proteins have similar affinities. For example, our preliminary results for Fibrinogen competing with Fibronectin show a kinetic effect lasting for tens of hours, a time-scale relevant for the evolution of the protein corona in NP uptake scenarios.

To test further the predictive power of our computational model, we perform $\approx 10^5$ numerical simulations of a three step exposure protocol, first incubating the NPs with HSA, then with Tf, and finally adding Fib. Next we extrapolate the results up to hours with the NLDRE theory. For this ternary solution, we predict a Fib adsorption kinetics that slows down with the total mass concentration of the two competing proteins in a fashion comparable to the case of the binary solutions. We understand this similarity as a consequence of the fact that both HSA and Tf have a binding affinity orders of magnitude higher than K_D^{Fib} . In this sense the relevant parameter determining the Fib adsorption slowdown is the total mass concentration of the

competing proteins and not their relative amount. Also in this case, we test the theoretical predictions by comparing with FCS and SDS-PAGE techniques, and we find a very good agreement for the Fib kinetics, independent of the incubation order.

Nevertheless, a detailed experimental analysis of the kinetics before the addition of Fib shows a *memory* effect when we invert the order of precoating between HSA and Tf. The protein incubated first is always more abundant in the final corona. We realize that for reproducing this experimental feature, it is sufficient to add to our computational model a three-body interaction among the proteins and the NP. This additional term mimics the effect that the protein adsorption on the NP has on the protein–protein interaction. We interpret this mechanism as a consequence of possible irreversible degeneration of proteins at the NP surface.

In conclusion, by combining simulations and theory with limited experimental information on single-protein solutions, we are able to predict the protein corona composition in a ternary solution. We find evidence of *memory* in the corona formation when the environment changes, and we propose a mechanism that can account for this effect. Our results show that it is possible to develop an approach toward the prediction of the protein corona kinetics and composition in complex milieu that are changing with time. This is particularly relevant in those cases, e.g., in which a NP is traveling through the body. This knowledge is key for understanding how to modulate the protein corona. As a matter of fact, tuning the protein corona could be exploited to design specific NP properties. It can help to better engineer drug delivery carriers or a generation of biocomplexes for nanotherapeutics. It may allow the development of patient-optimized NPs, making use of the fact that the protein corona will change when the NP is incubated in blood plasma extracted from patients with different diseases.

MATERIALS AND METHODS

Experimental Approach. Silica NPs (nominal diameter 100 nm) were purchased from Polysciences Inc. (cat no. 24041). FITC-labeled silica NPs were purchased from Kisker Biotech (cat no. PSI-G0.1). NPs were characterized by DLS to determine their size (Figure S10 in SI) and z-potential before use. Proteins (Fib, Tf, BSA) labeled with Alexa488 were purchased from Invitrogen (Life Technology) and treated as recommended from the supplier. Unlabeled Fib, holo-Tf, and HSA were purchased from Sigma-Aldrich.

Differential Centrifugation Sedimentation. DCS measures the sedimentation time of objects. It is then possible to calculate their diameter by assuming a value of the density of these objects (eq 2).¹⁵ When proteins or other molecules bind to the surface of NPs, they not only change their overall size but also the net density of the object. This causes a change in the sedimentation properties of the NP. It is convenient, from an experimental perspective, to assume a density of the core material and observe the change in apparent diameter as a function of protein concentration. The term apparent diameter is used as the size reported does not reflect the true size of the NP–protein complex, but it actually reflects the combination of changes in both the size and density which occur after the formation of the protein corona. The diameter is computed as

$$D \equiv \left[\frac{18\eta \ln(r_f/r_0)}{(\rho_{NP} - \rho_f)\omega^2 t_s} \right]^{1/2} \quad (2)$$

where D is the particle diameter (cm), η is the fluid viscosity (poise), r_0 and r_f are the initial and the final radius of rotation (cm), ρ_{NP} is the particle density (g/mL), ρ_f is the fluid density (g/mL), ω is the rotational velocity (rad/s), and t_s is the time required to sediment from r_0 to r_f (s).

Prior to DCS analysis, silica NPs were incubated in different concentrations of single protein solutions for 1 h at room temperature. After this, the solution was injected neat into the spinning DCS disk. The particles then sediment through a sucrose gradient at $30^\circ\text{C} \pm 4^\circ\text{C}$. Due to the different sedimentation rates of the free protein and the NPs, it is assumed that, upon injection, the NPs would be immediately separated from the surrounding protein as they pass through the disk. This gives the opportunity for proteins to desorb as the particles are no longer in equilibrium with their surroundings. The typical measurement time for these particles was on the order of 1–2 min.

After data acquisition, the changes in sedimentation can be rationalized by considering the object as more complex and modeling the sedimentation using a core–shell model (eq 3). This assumes that the object formed of a core of known size and density and a shell of protein of known density and variable thickness, with apparent diameter:

$$D_a^2 \equiv \frac{D_c^3 \rho_c + (D_T^3 - D_c^3) \rho_T - D_T^3 \rho_f}{D_T(\rho_c - \rho_f)} \quad (3)$$

where D_a is the apparent diameter of the NPs, D_c and ρ_c are the NP core diameter and density, respectively, D_T is the total diameter of the core and the shell, and ρ_s and ρ_f are the shell and fluid densities, respectively. This equation describes a NP with a shell composed of species with a single density.¹⁵

In all cases the particles are assumed to be spherical and the layers homogeneous and discrete. For most cases, a progressive increase in shell thickness causes a nonlinear change in the sedimentation properties. However, we observe (Figure S1d in SI) that the reported shifts can be rationalized using eq 3: For this system and suitably small shifts (<12 nm), a linear approximation between the surface coverage of the NP and the protein concentration is acceptable. Hence, the apparent diameter, in this case, can be used to directly reflect the shell thickness of proteins. Assuming that the maximum saturation point of the curves is indicative of full surface coverage, the shell thickness can be normalized to represent a surface coverage percentage.

DCS is not biased by agglomerates, as it measures the time each particle takes to sediment. The time separation between the large agglomerates, that sediment first, and the individual particles, that sediment later, guarantees that even in the case of agglomeration, the single particle population can be monitored. In particular, by monitoring the main population peak in DCS, it is possible to follow the adsorption of protein (Figure S1a–c in SI), even with colloidal instability present, most obvious around the 50% coverage for Fib (Figure S1c in SI).

Microscale Thermophoresis. MST is a technique for binding studies and allows us to determine the binding affinities of the proteins to the NPs. In a standard assay, the binder (NP) is fluorescently labeled and kept at constant concentration, while the ligand (protein) is not. These conditions are very useful for proteins with low binding affinities or for measurements in complex fluids like plasma. As described in refs 20 and 21, we measure how the binding induces changes of the fluorescent signal in a thermal gradient by determining the relative fluorescence:

$$F_{\text{norm}} \equiv \frac{F_{\text{hot}}}{F_{\text{cold}}} \quad (4)$$

where F_{hot} is the fluorescence after thermodiffusion and F_{cold} is the initial fluorescence. By fitting F_{norm} as a function of the protein concentration using a Hill equation (eq 1), we estimate the binding affinity. However, when there is NP aggregation, the technique averages agglomerates and single particles data, introducing noise in the affinity constants estimate.

MST measurements were performed on a Monolith NT 0.15 (NanoTemper, Germany) using 40% of blue LED (488 nm) and 1 V IR-laser power. Laser on and off times were set at 35 s and 5 s, respectively. Standard treated capillaries from NanoTemper were used. FITC-labeled silica NPs were used at a constant concentration of

0.313 mg/mL, while for the protein of interest, a 1:1 dilution series was prepared.

Fluorescence Correlation Spectroscopy. FCS is a highly sensitive fluorescence technique that allows for the determination of the number and the size of particles simultaneously in solution. By diffusing into and out of the confocal volume, labeled particles, i.e., proteins, create fluctuations in the fluorescence intensity. The fluorescence signal is temporally correlated for the analysis. A two component fit to the time–correlation function $G(\tau)$ is used to determine quantitatively the amplitude and the diffusion time of the fast freely diffusing proteins τ_{protein} and the slower bound proteins $\tau_{\text{protein-NP}}$. We follow the procedure described by Rusu *et al.*²² and Milani *et al.*⁵ using a two component fitting formula:

$$G(\tau) = \frac{1}{N} \left((1-y) \left(\frac{1}{1 + \frac{\tau}{\tau_{01}}} \right) \left(\frac{1}{1 + \frac{\tau}{S^2 \tau_{01}}} \right)^{1/2} + y \left(\frac{1}{1 + \frac{\tau}{\tau_{02}}} \right) \left(\frac{1}{1 + \frac{\tau}{S^2 \tau_{02}}} \right)^{1/2} \right) \quad (5)$$

From these results, we can determine the fraction bound of proteins on the NP surface⁵ that is

$$f_b \equiv 1 - \frac{N_{\text{free}}}{N_0} \quad (6)$$

where N_0 is the initial protein number from a fit in a monocomponent solution and $N_{\text{free}} \leq N_0$ is the amount of unbound protein after incubation with NPs.

FCS measurements were performed on a LSM10 microscope equipped with a ConfoCor2 unit (Carl Zeiss Jena, Germany), an argon laser (488 nm), and an apochromatic 40 \times water-immersion objective with a NA of 1.2 (Carl Zeiss Jena, Germany). Fluorescence emission was separated from excitation light by using the corresponding band-pass filter S25/25 nm. All measurements were performed at room temperature (22 $^\circ\text{C}$) using NUNC eight-well slides (Thermo Scientific) and a sample volume of at least 200 μL . To avoid unwanted adsorption of proteins to the walls, the chambers were precoated with 5 mg/mL BSA for 1 h. Afterward the chambers were rinsed with Milli-Q to remove unbound BSA.

SDS-PAGE. SDS-PAGE is a method by which proteins in a complex mixture can be separated based on their molecular weight. This technique has been applied previously to study the proteins which make up the biomolecular corona.^{13,23} Briefly the proteins adsorbed on the NPs are removed from their surface, denatured, and loaded on a gel, whereby they are separated by applying an electric field. The protein bands can subsequently be visualized by staining the proteins with Coomassie Brilliant Blue dye.

Silica NPs (100 $\mu\text{g/mL}$, 0.5 mL) were incubated in different HSA concentrations (0.35–7 mg/mL) for 1 h at room temperature. After that, Fib was added to a final concentration of 5 $\mu\text{g/mL}$. The NPs were incubated with Fib for varying lengths of time (0–120 min), and the times reported correspond to the incubation time with Fib before hard corona preparation. The hard corona samples were prepared by removing the excess proteins from the sample, achieved through 4 successive cycles of centrifugation (20000 $\times g$, 10 min) and resuspension in PBS. The final NP pellet was suspended in 10 μL PBS with an additional 5 μL loading buffer. The samples were subsequently boiled for 5 min before loading on a 6–4% discontinuous Tris-glycine gel.

The samples were run for 1 h at 130 V. The gels were then extracted and fixed in 40% EtOH, 10% acetic acid for 1 h. Following this, the gel was placed in 0.025% w/w Coomassie Brilliant Blue dispersed in 10% EtOH and 10% acetic acid. The gel was left overnight to stain before imaging.

Computational and Theoretical Approach. For our computational and theoretical calculations we used a computer cluster with dedicated Graphical Processing Units (GPUs):

- CPU processors: 4 \times PCs with an INTEL i7-870 and 6 GB RAM, 1 \times PC with an INTEL i7-3770 and 8 GB RAM.
- GPU processors: 4 \times NVIDIA GTX 460, 2 \times NVIDIA GTX 660, 1 \times NVIDIA GTX 760, 1 \times NVIDIA Tesla C2075.

All machines were running under GNU/Linux Ubuntu 12.04. The programming codes were compiled using CUDA-C version 5.0 and GCC 4.6.

MD Simulations. We performed MD simulations of the CG model at constant volume and constant temperature, using a Langevin thermostat. We fixed the simulation box size based on the NP concentration, having one single NP in our volume (Figure 2c).

We kept a constant concentration of proteins in solution, regardless of the number of proteins adsorbed on the NP surface, adopting a method that mimics the experimental buffer. Specifically, we divided the system in two regions: the inner region, containing the NP with all the proteins concentrations fixed to the experimental values, and the outer region, which is used as a reservoir to control the concentration of proteins in the inner region. The outer region is not considered for the calculation of the observable quantities.

We compute the adsorption kinetics by counting the number of adsorbed proteins at every time-step. A protein is considered to be adsorbed when the minimum surface-to-surface distance between the protein and the NP is <0.5 times the specific protein's radius.

Rescaling of Numerical Time Scale to Real Time Scale. Our CG calculations give us qualitative information about the kinetics, and only after the comparison with the experiments, we can extract the correct time scales and make our predictions quantitative. To match the time scales of simulations, numerical NLDRE solutions and experiments in, e.g., Figure 3, we fit the experimental results with the NLDRE solution of eq S4 in SI, assuming $k_{\text{off}}^{\text{Fib}} \approx 0$ and adjusting the value of $k_{\text{off}}^{\text{Fib}}$. This assumption is justified by the large affinity of Fib to the NP. Furthermore, in eq S4 in SI also $k_{\text{off}}^{\text{HSA}}$ and $k_{\text{off}}^{\text{BSA}}$ are free parameters. Because we verify that the specific values of these two parameters do not affect the behavior of the Fib fraction bound, we assume $k_{\text{off}}^{\text{HSA}} = k_{\text{off}}^{\text{BSA}}$. This procedure allows us to calculate the value of the Fib fraction bound at early stages, not available from experiments, within the NLDRE formalism with eq S3 in SI and match it with our computational results. Therefore, on the one hand, we match the NLDRE curve with the experimental fraction bound and, on the other hand, the NLDRE curve with the computational fraction bound. In this way we are able to calculate the scaling factor C_i (Table S1) in $t_{\text{real}} = C_i \times t_{\text{sim}}$ where t_{sim} is the simulation time and t_{real} is the time in real units. We observe that this procedure leads to the same scaling factor C_i for data in Figures 3 and 4.

ASSOCIATED CONTENT

Supporting Information

The Supporting Information is available free of charge on the ACS Publications website at DOI: 10.1021/acsnano.6b04858.

Additional experimental data, theoretical results and methodological developments (PDF)

AUTHOR INFORMATION

Corresponding Author

*E-mail: ovilanova@fnf.ub.edu.

ORCID

Oriol Vilanova: 0000-0003-1242-2377

Giancarlo Franzese: 0000-0003-3006-2766

Author Contributions

¹O.V., J.M., and P.K. contributed equally to this work.

Notes

The authors declare no competing financial interest.

ACKNOWLEDGMENTS

All the authors acknowledge the support of the EU FP7 NanoTransKinetics project grant NMP4-SL-2011-266737. P.M.K. acknowledges the Irish Research Council for funding under the Embark scheme (RS/2011/106). O.V. and G.F. acknowledge the support of Spanish MEC grant FIS2012-31025.

REFERENCES

- (1) Monopoli, M. P.; Åberg, C.; Salvati, A.; Dawson, K. A. Biomolecular Coronas Provide the Biological Identity of Nanosized Materials. *Nat. Nanotechnol.* **2012**, *7*, 779–786.
- (2) Lundqvist, M.; Stigler, J.; Cedervall, T.; Berggård, T.; Planagan, M. B.; Lynch, I.; Elia, G.; Dawson, K. A. The Evolution of the Protein Corona Around Nanoparticles: A Test Study. *ACS Nano* **2011**, *5*, 7503–7509.
- (3) Corbo, C.; Molinaro, R.; Parodi, A.; Toledano Furman, N. E.; Salvatore, F.; Tasciotti, E. The Impact of Nanoparticle Protein Corona on Cytotoxicity, Immunotoxicity and Target Drug Delivery. *Nanomedicine* **2016**, *11*, 81–100.
- (4) Casals, E.; Pfaller, T.; Duschl, A.; Oostingh, G. J.; Punter, V. Time Evolution of the Nanoparticle Protein Corona. *ACS Nano* **2010**, *4*, 3623–3632.
- (5) Milani, S.; Bombelli, F. B.; Pitek, A. S.; Dawson, K. A.; Rädler, J.; Baldelli Bombelli, F. Reversible Versus Irreversible Binding of Transferrin to Polystyrene Nanoparticles: Soft and Hard Corona. *ACS Nano* **2012**, *6*, 2532–2541.
- (6) Dell'Orco, D.; Lundqvist, M.; Oslakovic, C.; Cedervall, T.; Linse, S. Modeling the Time Evolution of the Nanoparticle-Protein Corona in a Body Fluid. *PLoS One* **2010**, *5*, e10949.
- (7) De Simone, A.; Spadaccini, R.; Temussi, P. A.; Fraternali, F. Toward the Understanding of MNEI Sweetness from Hydration Map Surfaces. *Biophys. J.* **2006**, *90*, 3052–3061.
- (8) Habash, M.; Reid, G. Microbial Biofilms: Their Development and Significance for Medical Device-Related Infections. *J. Clin. Pharmacol.* **1999**, *39*, 887–898.
- (9) Salvati, A.; Pitek, A. S.; Monopoli, M. P.; Prapainop, K.; Bombelli, F. B.; Hristov, D. R.; Kelly, P. M.; Åberg, C.; Mahon, E.; Dawson, K. A. Transferrin-Functionalized Nanoparticles Lose Their Targeting Capabilities When a Biomolecule Corona Adsorbs on the Surface. *Nat. Nanotechnol.* **2013**, *8*, 137–143.
- (10) Tavanti, F.; Pedone, A.; Menziani, M. C. Competitive Binding of Proteins to Gold Nanoparticles Disclosed by Molecular Dynamics Simulations. *J. Phys. Chem. C* **2015**, *119*, 22172–22180.
- (11) Ding, H.; Ma, Y. Design Strategy of Surface Decoration for Efficient Delivery of Nanoparticles by Computer Simulation. *Sci. Rep.* **2016**, *6*, 26783.
- (12) Vilaseca, P.; Dawson, K. A.; Franzese, G. Understanding and Modulating the Competitive Surface-Adsorption of Proteins Through Coarse-Grained Molecular Dynamics Simulations. *Soft Matter* **2013**, *9*, 6978–6985.
- (13) Monopoli, M. P.; Walczyk, D.; Campbell, A.; Elia, G.; Lynch, I.; Baldelli Bombelli, F.; Dawson, K. A. Physical-Chemical Aspects of Protein Corona: Relevance to *in Vitro* and *in Vivo* Biological Impacts of Nanoparticles. *J. Am. Chem. Soc.* **2011**, *133*, 2525–2534.
- (14) Anderson, N. L. The Human Plasma Proteome: History, Character, and Diagnostic Prospects. *Mol. Cell. Proteomics* **2002**, *1*, 845–867.
- (15) Walczyk, D.; Bombelli, F. B.; Monopoli, M. P.; Lynch, I.; Dawson, K. A. What the Cell “sees” in Bionanoscience. *J. Am. Chem. Soc.* **2010**, *132*, 5761–5768.
- (16) Pitek, A. S.; O'Connell, D.; Mahon, E.; Monopoli, M. P.; Baldelli Bombelli, F.; Dawson, K. A. Transferrin Coated Nanoparticles: Study of the Bionano Interface in Human Plasma. *PLoS One* **2012**, *7*, e40685.
- (17) Krpetić, Z.; Davidson, A. M.; Volk, M.; Lévy, R.; Brust, M.; Cooper, D. L. High-Resolution Sizing of Monolayer-Protected Gold Clusters by Differential Centrifugal Sedimentation. *ACS Nano* **2013**, *7*, 8881–8890.
- (18) Derjaguin, B.; Landau, L. Theory of the Stability of Strongly Charged Lyophobic Sols and of the Adhesion of Strongly Charged Particles in Solutions of Electrolytes. *Prog. Surf. Sci.* **1993**, *43*, 30–59.
- (19) Verwey, E.; Overbeek, J.; van Nes, K. *Theory of the Stability of Lyophobic Colloids: The Interaction of Sol Particles Having an Electric Double Layer*; Elsevier Publishing Company: Amsterdam, The Netherlands, 1948.
- (20) Seidel, S. A. I.; Dijkman, P. M.; Lea, W. A.; van den Bogaart, G.; Jerabek-Willemsen, M.; Lazic, A.; Joseph, J. S.; Srinivasan, P.; Baaske, P.; Simeonov, A.; Katritch, I.; Melo, F. A.; Ladbury, J. E.; Schreiber, G.; Watts, A.; Braun, D.; Duhr, S. Microscale Thermophoresis Quantifies Biomolecular Interactions Under Previously Challenging Conditions. *Methods* **2013**, *59*, 301–315.
- (21) Lippok, S.; Seidel, S. A. I.; Duhr, S.; Uhland, K.; Holthoff, H.-P.; Jenne, D.; Braun, D. Direct Detection of Antibody Concentration and Affinity in Human Serum Using Microscale Thermophoresis. *Anal. Chem.* **2012**, *84*, 3523–3530.
- (22) Rusu, L.; Gambhir, A.; McLaughlin, S.; Rädler, J. Fluorescence Correlation Spectroscopy Studies of Peptide and Protein Binding to Phospholipid Vesicles. *Biophys. J.* **2004**, *87*, 1044–1053.
- (23) Cedervall, T.; Lynch, I.; Lindman, S.; Berggård, T.; Thulin, E.; Nilsson, H.; Dawson, K. A.; Linse, S. Understanding the Nanoparticle-Protein Corona Using Methods to Quantify Exchange Rates and Affinities of Proteins for Nanoparticles. *Proc. Natl. Acad. Sci. U. S. A.* **2007**, *104*, 2050–2055.
- (24) Lindman, S.; Lynch, I.; Thulin, E.; Nilsson, H.; Dawson, K. A.; Linse, S. Systematic Investigation of the Thermodynamics of HSA Adsorption to N-Isopropylacrylamide/N-Tert-Butylacrylamide Copolymer Nanoparticles. Effects of Particle Size and Hydrophobicity. *Nano Lett.* **2007**, *7*, 914–920.
- (25) Baier, G.; Costa, C.; Zeller, A.; Baumann, D.; Sayer, C.; Araujo, P. H. H.; Malländer, V.; Musyanovych, A.; Landfester, K. BSA Adsorption on Differently Charged Polystyrene Nanoparticles Using Isothermal Titration Calorimetry and the Influence on Cellular Uptake. *Macromol. Biosci.* **2011**, *11*, 628–638.
- (26) Brewer, S. H.; Glomm, W. R.; Johnson, M. C.; Knag, M. K.; Franzen, S. Probing BSA Binding to Citrate-Coated Gold Nanoparticles and Surfaces. *Langmuir* **2005**, *21*, 9303–9307.
- (27) Jecklin, M. C.; Schauer, S.; Dumelin, C. E.; Zenobi, R. Label-Free Determination of Protein-Ligand Binding Constants Using Mass Spectrometry and Validation Using Surface Plasmon Resonance and Isothermal Titration Calorimetry. *J. Mol. Recognit.* **2009**, *22*, 319–329.
- (28) Mura-Galelli, M. J.; Voegel, J. C.; Behr, S.; Bres, E. F.; SchAAF, P. Adsorption/desorption of Human Serum Albumin on Hydroxyapatite: A Critical Analysis of the Langmuir Model. *Proc. Natl. Acad. Sci. U. S. A.* **1991**, *88*, 5557–5561.
- (29) Adamczyk, Z.; Barbasz, J.; Cieśl, M. Mechanisms of Fibrinogen Adsorption at Solid Substrates. *Langmuir* **2011**, *27*, 6868–6878.
- (30) Armstrong, J. K.; Wenby, R. B.; Meiselman, H. J.; Fisher, T. C. The Hydrodynamic Radii of Macromolecules and Their Effect on Red Blood Cell Aggregation. *Biophys. J.* **2004**, *87*, 4259–4270.
- (31) Adamczyk, Z.; Nattich, M.; Wasilewska, M.; Sadowska, M. Deposition of Colloid Particles on Protein Layers: Fibrinogen on Mica. *J. Colloid Interface Sci.* **2011**, *356*, 454–464.
- (32) Macritchie, F. Proteins at Interfaces. *Adv. Protein Chem.* **1978**, *32*, 283–326.
- (33) Tousi, S. H.; Saberi, M. R.; Chamani, J. Influence of PH on the Interaction Between Human Serum Albumin and Serum Transferrin with Cyclophosphamide: Spectroscopic, Zeta Potential and Molecular Dynamic Investigation. *Rom. J. Biochem.* **2011**, *48*, 135–175.
- (34) Yajima, H.; Sakajiri, T.; Kikuchi, T.; Morita, M.; Ishii, T. Molecular Modeling of Human Serum Transferrin for Rationalizing the Changes in Its Physicochemical Properties Induced by Iron Binding. Implication of the Mechanism of Binding to Its Receptor. *J. Protein Chem.* **2000**, *19*, 215–223.

Supporting Information to: Understanding the Kinetics of Protein-Nanoparticle Corona Formation

Oriol Vilanova,^{*,†,‡} Judith J. Mittag,[¶] Philip M. Kelly,^{§,||} Silvia Milani,[¶] Kenneth A. Dawson,^{§,||} Joachim O. Rädler,[¶] and Giancarlo Franzese^{†,‡}

[†]*Secció de Física Estadística i Interdisciplinària-Departament de Física de la Matèria Condensada, Facultat de Física Universitat de Barcelona, Martí i Franquès 1, 08028, Barcelona, Spain*

[‡]*Institut de Nanociència i Nanotecnologia, Universitat de Barcelona, Av. Joan XXIII S/N, 08028 Barcelona, Spain*

[¶]*Faculty of Physics, Center for Nanoscience, Ludwig-Maximilians-Universität, Geschwister-Scholl-Platz 1, 80539 Munich, Germany*

[§]*Centre for BioNano Interactions, School of Chemistry and Chemical Biology, University College Dublin, Belfield, Dublin 4, Ireland*

^{||}*Conway Institute for Biomolecular and Biomedical Research, University College Dublin, Belfield, Dublin 4, Ireland*

E-mail: ovilanova@ffn.ub.edu

Analysis of DCS data

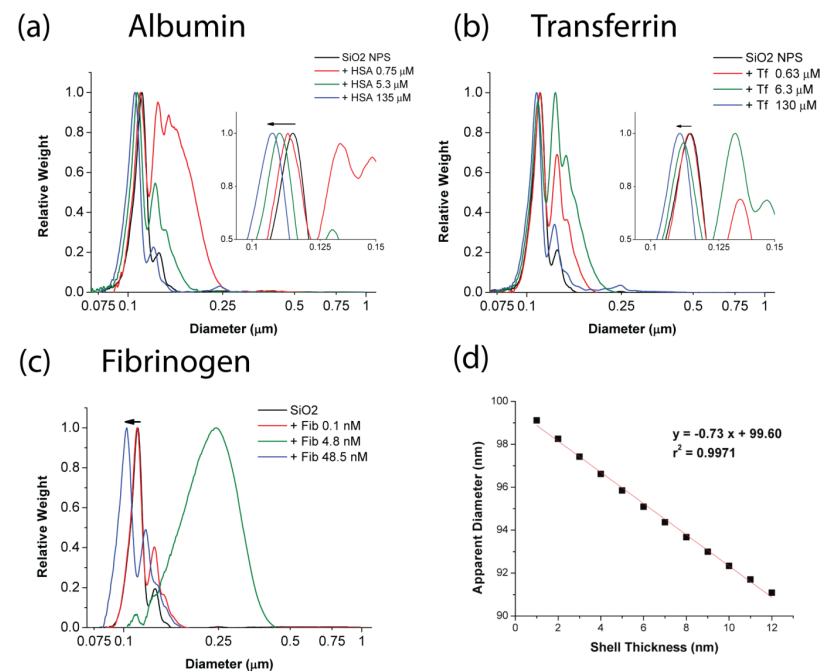


Figure S1: DCS measurements for silica NPs incubated in protein solutions. The main peak (insets) is used to monitor the surface coverage in all cases for low (red line), medium (green line) and high protein concentrations (blue line) and for silica NP without protein (black line), for (a) HSA, (b) Tf, (c) Fib. (d) Apparent diameter as function of the shell thickness for the core shell modeling (Eq. (3)) of 100 nm silica NP ($\rho=2.2$ g/ml) coated in a shell of protein ($\rho=1.05$ g/ml) sedimenting through a solution with average density $\rho_f=1.064$ g/ml.

Non-Langmuir Differential Rate Equations (NLDRE) Theory

The law of mass action describes the adsorption process of a protein onto a binding site of a NP by the differential equation:

$$\frac{d}{dt}\Gamma = k^{\text{on}}(C_0 - C_S\Gamma)(1 - \Gamma) - k^{\text{off}}\Gamma \quad (\text{S1})$$

where t is the time since the addition of NPs to the system, $\Gamma \equiv N_{\text{ads}}/N_{\text{max}}$ is the normalized surface coverage of proteins, N_{ads} is the number of adsorbed proteins and N_{max} is the maximum number of binding sites on the NP surface, k^{on} and k^{off} are the rates of adsorption and desorption, respectively, C_0 is the concentration of proteins in solution and C_S is the concentration of binding sites on the NP surface.

The classical Langmuir model assumes that the rates k^{on} , k^{off} and the binding affinity $K_D \equiv k^{\text{off}}/k^{\text{on}}$ are constants. We find that, with this very strong assumption, we are unable to fit our data. Therefore, we make the plausible assumption that the rates depend on the surface coverage:

$$\begin{aligned} k^{\text{on}}(\Gamma) &= k_{\emptyset}^{\text{on}}(1 - \alpha\Gamma) \\ k^{\text{off}}(\Gamma) &= k_{\emptyset}^{\text{off}}(1 - \beta\Gamma). \end{aligned} \quad (\text{S2})$$

Here, the parameters $k_{\emptyset}^{\text{on}}$ and $k_{\emptyset}^{\text{off}}$ are the rates of adsorption at null surface coverage and can be fitted from kinetic data; α and β are fitting parameters for the binding isotherm of a protein and take into account, in an effective way, the protein-protein interactions between adsorbing proteins.

The equilibrium surface coverage Γ_{eq} is obtained at very long times for $d\Gamma/dt = 0$. This quantity can be related to the experimental values of the fraction bound f , Eq. (S3), with the following relation:

$$\Gamma_{\text{eq}} = \frac{fC_0}{C_S}. \quad (\text{S3})$$

The problem of protein solutions with more than one kind of protein is more complex. For instance, we consider the case in which the NP is initially incubated in a solution containing

one kind of protein (e.g., HSA), with the further addition of another kind of protein (e.g., Fib) that competes with the previously adsorbed protein for the surface binding sites. In this case, the adsorption processes of each protein need to be described separately. This translates into a set of coupled non-linear differential equations for the surface coverage of each kind of protein on the NP surface:

$$\begin{aligned} \frac{d\Gamma_{\text{Fib}}}{dt} &= k_{\text{Fib}}^{\text{on}}C_{\text{Fib}}(\Gamma_{\text{Fib}})(1 - \Gamma_{\text{Fib}} - \Gamma_{\text{HSA}}) - k_{\text{Fib}}^{\text{off}}\Gamma_{\text{Fib}} \\ \frac{d\Gamma_{\text{HSA}}}{dt} &= k_{\text{HSA}}^{\text{on}}C_{\text{HSA}}(\Gamma_{\text{HSA}})(1 - \Gamma_{\text{Fib}} - \Gamma_{\text{HSA}}) - k_{\text{HSA}}^{\text{off}}\Gamma_{\text{HSA}} \end{aligned} \quad (\text{S4})$$

where t is the time since the addition of the second protein (Fib). In Eq. (S4) all the symbols are equivalent to those in Eq. (S1) with C_{HSA} and C_{Fib} being the protein concentrations of HSA and Fib, respectively, and with indices for k^{on} , k^{off} and Γ indicating the protein to which they are related. The initial conditions of this system are defined to be:

$$\begin{aligned} \Gamma_{\text{Fib}}(0) &= 0 \\ \Gamma_{\text{HSA}}(0) &= \Gamma_{\text{HSA}}^{\text{prec}} \end{aligned} \quad (\text{S5})$$

where $\Gamma_{\text{HSA}}^{\text{prec}}$ is the equilibrium surface coverage of proteins at the end of the preliminary incubation step.

Again, assuming that the rates of adsorption are functions of the surface coverage of each protein, we introduce the cross-interactions between different kinds of proteins:

$$\begin{aligned} k_{\text{HSA}}^{\text{on}}(\Gamma_{\text{HSA}}, \Gamma_{\text{Fib}}) &= k_{\emptyset, \text{HSA}}^{\text{on}}(1 - \alpha_{\text{HSA, HSA}}\Gamma_{\text{HSA}} - \alpha_{\text{HSA, Fib}}\Gamma_{\text{Fib}}) \\ k_{\text{HSA}}^{\text{off}}(\Gamma_{\text{HSA}}, \Gamma_{\text{Fib}}) &= k_{\emptyset, \text{HSA}}^{\text{off}}(1 - \beta_{\text{HSA, HSA}}\Gamma_{\text{HSA}} - \beta_{\text{HSA, Fib}}\Gamma_{\text{Fib}}) \\ k_{\text{Fib}}^{\text{on}}(\Gamma_{\text{HSA}}, \Gamma_{\text{Fib}}) &= k_{\emptyset, \text{Fib}}^{\text{on}}(1 - \alpha_{\text{Fib, HSA}}\Gamma_{\text{HSA}} - \alpha_{\text{Fib, Fib}}\Gamma_{\text{Fib}}) \\ k_{\text{Fib}}^{\text{off}}(\Gamma_{\text{HSA}}, \Gamma_{\text{Fib}}) &= k_{\emptyset, \text{Fib}}^{\text{off}}(1 - \beta_{\text{Fib, HSA}}\Gamma_{\text{HSA}} - \beta_{\text{Fib, Fib}}\Gamma_{\text{Fib}}) \end{aligned} \quad (\text{S6})$$

where the indices for $k_{\emptyset}^{\text{on}}$ and $k_{\emptyset}^{\text{off}}$ indicate the protein to which they are related.

We set the parameters $\alpha_{\text{HSA, HSA}}$, $\alpha_{\text{Fib, Fib}}$, $\beta_{\text{HSA, HSA}}$ and $\beta_{\text{Fib, Fib}}$ equal the those for the one-

component systems, Eq. (S2), and we make the following hypothesis for the cross-interaction parameters:

$$\begin{aligned}\alpha_{\text{HSA,Fib}} &= \alpha_{\text{Fib,HSA}} = \frac{1}{2}(\alpha_{\text{HSA,HSA}} + \alpha_{\text{Fib,Fib}}) \\ \beta_{\text{HSA,Fib}} &= \beta_{\text{Fib,HSA}} = \frac{1}{2}(\beta_{\text{HSA,HSA}} + \beta_{\text{Fib,Fib}}).\end{aligned}\tag{S7}$$

The computational model

Effective potentials: Protein-NP interaction

The functional form of the protein-NP interaction (Fig. 2a) is defined as

$$\begin{aligned}U_{\text{DLVO}}(d) &\equiv U_{\text{DLVO}}^{\text{LJ}}(d) + U_{\text{DLVO}}^{\text{Elec}}(d) \\ \text{with } U_{\text{DLVO}}^{\text{LJ}}(d) &\equiv \frac{A_{\text{H}}}{2520} \frac{2R_h R_{\text{NP}}}{R_h + R_{\text{NP}}} \left[\frac{\sigma}{d} \right]^6 \frac{1}{d} - \frac{A_{\text{H}}}{12} \frac{2R_h R_{\text{NP}}}{R_h + R_{\text{NP}}} \frac{1}{d} \\ \text{and } U_{\text{DLVO}}^{\text{Elec}}(d) &\equiv \frac{64\pi k_B T \gamma_{\text{prot}} \gamma_{\text{NP}} \rho_{\infty}}{\kappa^2} \frac{R_h R_{\text{NP}}}{R_h + R_{\text{NP}}} e^{-\kappa d}\end{aligned}\tag{S8}$$

where A_{H} is an energy related to the Hamaker constants of the NP and the protein, R_{NP} is the NP radius, R_h is the shortest characteristic length-scales of the folded protein, $\sigma \simeq 0.5$ nm is the minimum approach distance between the NP and the protein,^{1,2} and $d \equiv r - R_{\text{NP}} - R_h \geq \sigma$, is the separation distance between the surfaces of the NP and the center of the protein. The parameters of the electrostatic part $U_{\text{DLVO}}^{\text{Elec}}$ are the thermal energy $k_B T$, the reduced surface potential defined as $\gamma_{\alpha} \equiv \tanh[ze\phi_{\alpha}/4k_B T]$ where α is an index that correspond to one of the proteins or the NP, ϕ_{α} the zeta-potential (Table S3), $\kappa^{-1} = 0.304/\sqrt{I(\text{M})}$ ³ is the Debye-Hückel screening length, ze and ρ_{∞} are the valence in electron charges e and the concentration of ions in solution, respectively.^{4,5} Table 2 and table S1 summarize the set of parameters derived from the experiments and used in our simulations.

Table S1: Other parameters for the coarse-grained model

PBS Ionic strength (pH 7.5)	24 mM
Valence of ions in solution	$ze = 1e$
Inverse Debye-Hückel length	$\kappa = 0.508 \text{ nm}^{-1}$
Temperature	$T = 24 \text{ }^\circ\text{C}$ ($k_B T = 25.6 \text{ meV}$)
SiO ₂ NP ϕ	-24 mV ⁶
$\varepsilon_{\text{HSA,HSA}}$	-0.2 $k_B T$
$\varepsilon_{\text{Tf,Tf}}$	-2.5 $k_B T$
$\varepsilon_{\text{Fib,Fib}}$	0.0 $k_B T$
$\varepsilon_{\alpha,\beta}$ with $\alpha \neq \beta$ and $\alpha, \beta = \text{HSA,Tf,Fib}$	0.0 $k_B T$
d_3	60 nm
C_t	$7.5 \times 10^3 \text{ sec/sec}$
t_{inc}	0.075 sec
K_D^{HSA}	2.7 μM
K_D^{Tf}	1.2 μM
K_D^{Fib}	0 M

Table S2: Parameters for the NLDRE

$k_{\emptyset}^{\text{on}}(\text{HSA})$	$1.5 \times 10^7 \text{ sec}^{-1}\text{M}^{-1}$
$k_{\emptyset}^{\text{on}}(\text{Tf})$	$1.5 \times 10^7 \text{ sec}^{-1}\text{M}^{-1}$
$k_{\emptyset}^{\text{on}}(\text{Fib})$	$1.5 \times 10^7 \text{ sec}^{-1}\text{M}^{-1}$
$k_{\emptyset}^{\text{off}}(\text{HSA})$	5.0 sec^{-1}
$k_{\emptyset}^{\text{off}}(\text{Tf})$	0.5 sec^{-1}
$k_{\emptyset}^{\text{off}}(\text{Fib})$	0.0 sec^{-1}
$\alpha_{\text{HSA-HSA}}$	-0.5
$\alpha_{\text{Tf-Tf}}$	-0.98
$\alpha_{\text{Fib-Fib}}$	0.0
$\beta_{\text{HSA-HSA}}$	10
$\beta_{\text{Tf-Tf}}$	50
$\beta_{\text{Fib-Fib}}$	0.1

Effective potentials: Protein-protein interaction, 2-body contribution

The protein-protein 2-body interaction potential (Fig. 2b) is defined as⁷

$$\begin{aligned}
 U_2(r_{ij}) &\equiv U_2^h(r_{ij}) + U_2^s(r_{ij}) \\
 \text{with } U_2^h(r_{ij}) &\equiv \varepsilon \left[\frac{R_{h,i} + R_{h,j}}{r_{ij}} \right]^{24} \\
 \text{and } U_2^s(r_{ij}) &\equiv \varepsilon \frac{1}{1 + \exp \left[30 \frac{r_{ij} - (R_{s,i} + R_{s,j})}{R_{h,i} + R_{h,j}} \right]}
 \end{aligned} \tag{S9}$$

where $r_{ij} = |\vec{r}_i - \vec{r}_j|$ is the distance between the centers of two proteins i and j , and ε is a characteristic interaction energy between the two proteins. We describe the proteins as ellipsoids with a larger diameter $2R_s$ and a smaller diameter $2R_h$, that mimic their asymmetric shapes. The smaller radius R_h is calculated from experimental data on the highest surface adsorption concentration of the protein on a flat surface.⁸ The larger radius R_s is given by the hydrodynamic radius computed from the experimental measure of the diffusion coefficient D of each protein, which can be obtained by the Stokes-Einstein law (Table 2). We assume that the parameters R_s are constant within the investigated range of protein concentrations. We verify this hypothesis by computing D_{Fib} for Fib in solution with HSA at increasing concentrations (Fig. S2).

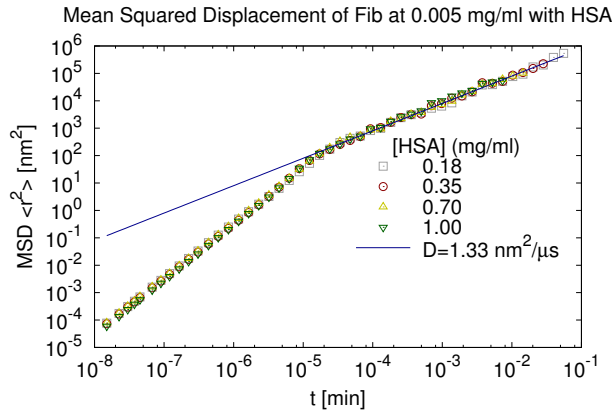


Figure S2: Mean squared displacement (MSD) $\langle r^2 \rangle$ of Fib at 0.005 mg/ml in solution with HSA at different concentrations, from 0.18 to 1.00 mg/ml. The fitting of the long-time diffusive regime gives a diffusion coefficient $D_{\text{Fib}} = 1.33 \text{ nm}^2/\mu\text{s}$ independent on HSA concentration.

Effective potentials: Protein-protein interaction, 3-body contribution

We define the protein-protein 3-body interaction potential as

$$U_3(\vec{r}_i, \vec{r}_j, \vec{r}_{\text{NP}}) = \varepsilon_{i,j} \exp\left[-\frac{\sqrt{d_i d_j}}{d_3}\right] \exp\left[-\frac{(r_{ij} - \delta_{i,j})^2}{2\omega_{i,j}^2}\right] \quad (\text{S10})$$

where \vec{r}_i is the position vector of protein i , \vec{r}_{NP} is the position vector of the NP, $d_i \equiv |\vec{r}_i - \vec{r}_{\text{NP}}| - R_{h,i} - R_{\text{NP}}$ is the relative distance of the center of a protein to the NP surface, R_{NP} is the NP radius, $R_{h,i}$ is the smaller radius of the protein i , $r_{ij} \equiv |\vec{r}_i - \vec{r}_j|$ is the protein-protein relative distance, $\varepsilon_{i,j}$ is a characteristic energy, d_3 is the range of this interaction from the NP surface, $\delta_{i,j} \equiv R_{h,i} + R_{h,j}$ is the smaller protein-protein distance and $\omega_{i,j} \equiv \delta_{i,j}/4$ is a cutoff range. The parameters of this interaction depend on the types of proteins i and j and are given in Table S1.

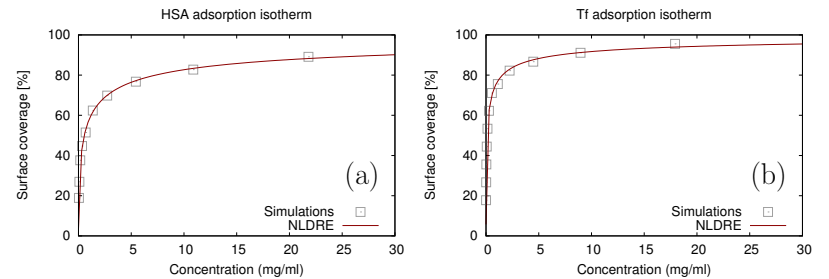


Figure S3: The adsorption isotherms for (a) HSA and (b) Tf with calibrated values $A_{\text{H}}^{\text{HSA}} = 9.75 k_{\text{B}}T$ and $A_{\text{H}}^{\text{Tf}} = 8.4 k_{\text{B}}T$. We estimate N_{max} from the fitting of the surface coverage percentage $100N_{\text{ads}}/N_{\text{max}}$ with Eq. (S1) (Table 2).

Estimate of free parameters A_{H} and N_{max}

For each protein we make an initial guess for A_{H} and simulate the adsorption in a mono-component solution at $C_{\text{P}} = K_{\text{D}}$ and at larger protein concentrations. We fit the resulting adsorption isotherm to the large-time solution of Eq. (S1), fixing K_{D} and leaving N_{max} as free parameter. We compare N_{max} with the number $N_{\text{ads}}(K_{\text{D}})$ of adsorbed proteins at concentration K_{D} and fine-tune A_{H} , in successive iterations, until we find $N_{\text{max}} = 2N_{\text{ads}}(K_{\text{D}})$ corresponding to $\Gamma_{\text{eq}}(K_{\text{D}}) = 0.5$ (Fig. S3). The resulting fitting parameters are reported in Table 2.

HSA - Fib competition. Gel analysis

Hard Corona 30 mins

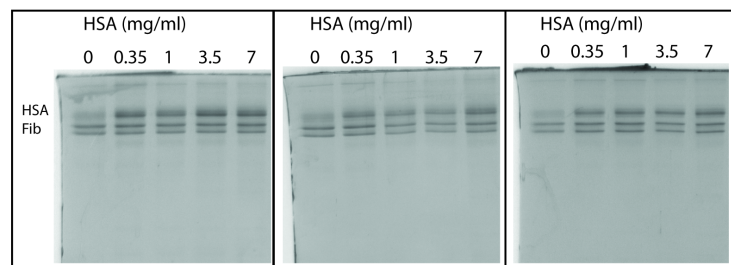


Figure S4: Gel samples showing the competitive adsorption of Fib displacing a protein corona made of HSA after incubation for 30, 60, 120 minutes, for different concentration of HSA, from 0 to 7 mg/ml, as indicated near each gel sample. Labels “HSA” and “Fib” on the left of the gels indicate the gel signatures of HSA and Fib, respectively.

Transferrin - Fibrinogen competition

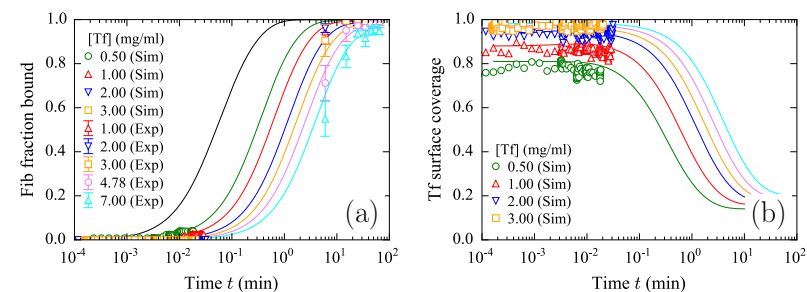


Figure S5: Competitive adsorption of Fib displacing a protein corona of Tf after incubation. **a)** As in Fig. 3 but for Tf concentrations (for the lines from top to bottom) 0.00, 0.50, 1.00, 2.00, 3.00, 4.78, and 7.00 mg/ml. **b)** NP Surface coverage of Tf from numerical simulations (open symbols) and NLDRE theory (lines). Lines from bottom to top are for 0.50, 1.00, 2.00, 3.00, 4.78, and 7.00 mg/ml for Tf.

HSA-Tf-Fib competition and memory effects

(Fig. S6, S7 and S8)

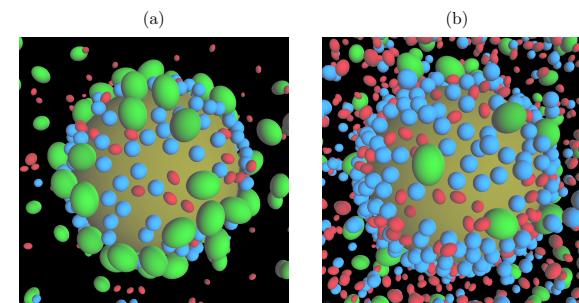


Figure S6: a) Snapshot of a simulation corresponding to Fig. 4b at $t = 0.1$ min. b) Same as in a) but for Fig. 4c.

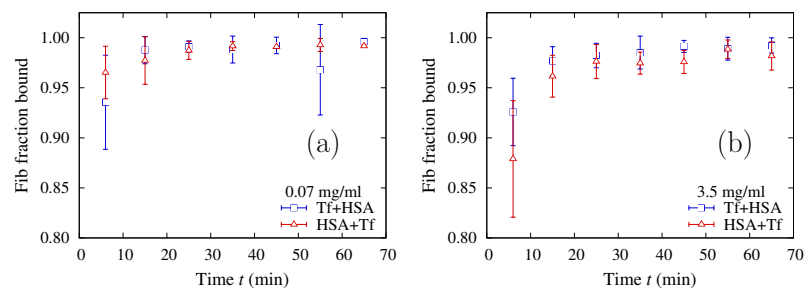


Figure S7: **a)** FCS experiment results of the kinetics analysis of Fib at $5 \mu\text{g/ml}$ adsorbed on $100 \mu\text{g/ml}$ silica NPs incubated following the protocol *A* (red triangles: incubation first in HSA at 0.07 mg/ml for 1 hour and next in Tf at 0.07 mg/ml for another hour), compared with the case in which we follow the protocol *B* (blue squares: incubation first Tf and next HSA, with same concentrations and times). **b)** Same as in panel a but for HSA and Tf at 3.5 mg/ml HSA. Within the error bar there is no difference in Fib kinetics between the different orders of protein addition.

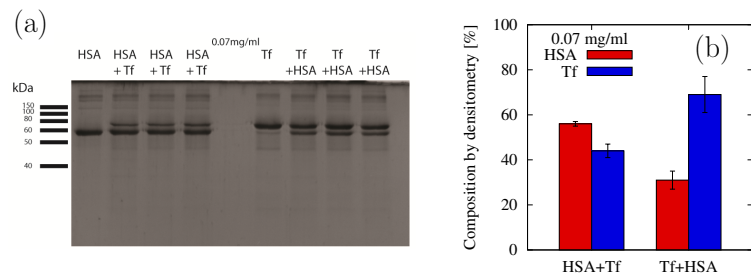


Figure S8: Same as in Fig. 5a,b but for HSA and Tf both at 0.07 mg/ml concentration. **a)** SDS-PAGE gel analysis. **b)** Densitometry results.

Simulations of different incubation protocols without three-body interaction contribution

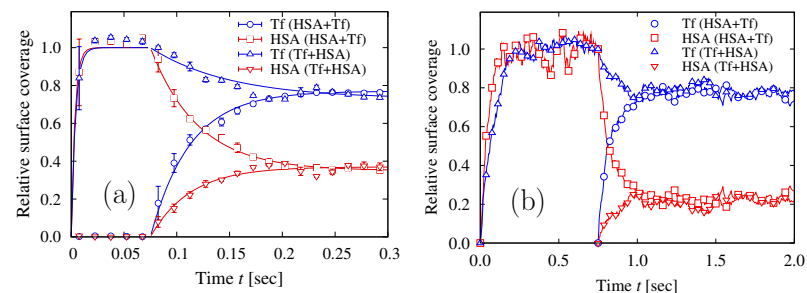


Figure S9: Simulation results of HSA and Tf competitive adsorption without the three-body contribution to the protein-protein interaction (Eq. (S10)). **a)** As in Fig. 5c with HSA and Tf at 3.5 mg/ml . In this case, both incubation protocols lead to the same relative protein adsorption, independent on the incubation order, after a short transient time ($\Delta t \simeq 0.15 \text{ sec}$). **b)** Simulation results for HSA and Tf concentrations at 0.07 mg/ml . Under these conditions, the incubation time needed to equilibrate the system before adding the next protein is longer compared to systems at higher concentrations ($t_{\text{inc}} = 0.75 \text{ sec}$).

Fluorescence Correlation Spectroscopy basics

The FCS technique analyzes the fluctuations in the intensity of the measured particle fluorescence. The fluorescence signal $F(t)$ at time t is hardware processed into the normalized autocorrelation function

$$G(\tau) \equiv 1 + \frac{\langle F(t)F(t+\tau) \rangle}{\langle F(t) \rangle^2}, \quad (\text{S11})$$

where angular brackets denote the average over time t . Indicating with $S \equiv z_0/w_0$ the structure parameter of the laser beam, where z_0 is the half axes and w_0 the radius of the beam, and assuming an ideal three dimensional Gaussian shape for the confocal volume, the autocorrelation curve for N freely diffusing identical molecules (single component solution) is described by

$$G(\tau) = \frac{1}{N} \left(1 + \frac{\tau}{\tau_D}\right)^{-1} \left(1 + \frac{\tau}{S^2 \tau_D}\right)^{-1/2} + 1, \quad (\text{S12})$$

where τ is the correlation time and τ_D is the translational diffusion time of the molecule. In a multicomponent system, the measured autocorrelation function is a weighted sum of the autocorrelation functions of its components.

The translational diffusion time is defined as the average dwell time of a molecule with diffusion constant D in the confocal volume:

$$\tau_D \equiv \frac{\omega_0^2}{4D}. \quad (\text{S13})$$

For all experiments, we average 10 independent measurements (30s each) and use a 10 nM dye solution with known diffusion coefficient (Alexa488 $D = 435 \mu\text{m}^2/\text{s}$) to determine the structure parameter S and to calibrate the instrument.

NP characterization

Table S3: Size and Z-Potential of silica NPs used in this study as measured by DLS and DCS.

	Diameter (nm)	PDI	Z-Potential (mV)	Conductivity (MS/cm ²)
DLS	123±1	0.030±0.003	-24±2	-1.8±0.2
DCS	114.4±0.1	-	-	-

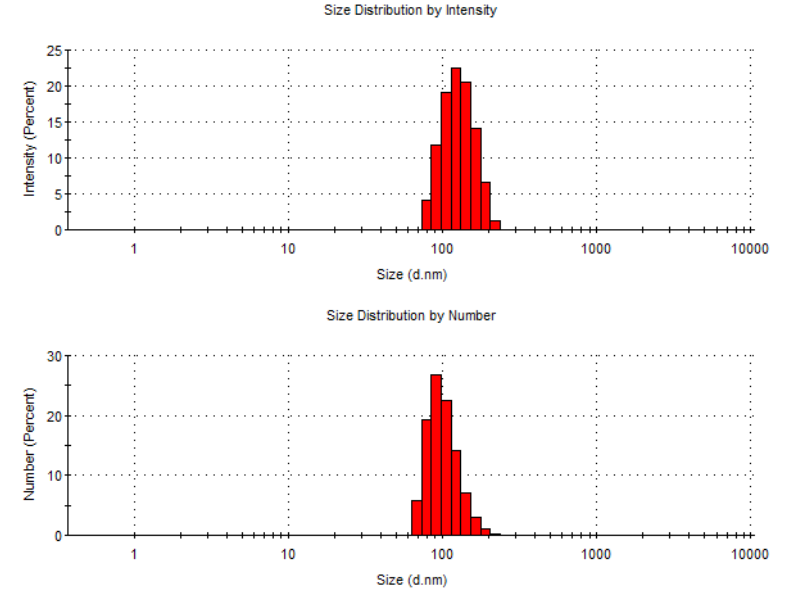


Figure S10: **Nanoparticle Characterization.** Size distribution of SiO₂ nanoparticles used for this study as measured by DLS. Both Intensity (upper) and number weighted distributions (lower) are shown. Measurements represent stock particles dispersed in water.

References

1. Ryan, J. N.; Gschwend, P. M. Effects of Ionic Strength and Flow Rate on Colloid Release: Relating Kinetics to Intersurface Potential Energy. *J. Colloid Interface Sci.* **1994**, *164*,

21–34.

2. Ruckenstein, E.; Prieve, C. D. Adsorption and Desorption of Particles and Their Chromatographic Separation. *AIChE J.* **1976**, *22*, 276–283.
3. Israelachvili, J. N. *Intermolecular and Surface Forces: Revised Third Edition*; Elsevier Science, 2011.
4. Everaers, R.; Ejtehadi, M. Interaction Potentials for Soft and Hard Ellipsoids. *Phys. Rev. E* **2003**, *67*, 041710.
5. Bhattacharjee, S.; Elimelech, M.; Borkovec, M. DLVO Interaction Between Colloidal Particles: Beyond Derjaguin's Approximation. *Croat. Chem. Acta* **1998**, *71*, 883–903.
6. Monopoli, M. P.; Walczyk, D.; Campbell, A.; Elia, G.; Lynch, I.; Bombelli, F. B.; Dawson, K. A. Physical-Chemical Aspects of Protein Corona: Relevance to *in Vitro* and *in Vivo* Biological Impacts of Nanoparticles. *J. Am. Chem. Soc.* **2011**, *133*, 2525–2534.
7. Vilaseca, P.; Dawson, K. A.; Franzese, G. Understanding and Modulating the Competitive Surface-Adsorption of Proteins Through Coarse-Grained Molecular Dynamics Simulations. *Soft Matter* **2013**, *9*, 6978–6985.
8. Höök, F.; Vörös, J.; Rodahl, M.; Kurrat, R.; Böni, P.; Ramsden, J.; Textor, M.; Spencer, N.; Tengvall, P.; Gold, J.; Kasemo, B. A Comparative Study of Protein Adsorption on Titanium Oxide Surfaces Using *in Situ* Ellipsometry, Optical Waveguide Light-mode Spectroscopy, and Quartz Crystal Microbalance/dissipation. *Colloids Surfaces B Biointerfaces* **2002**, *24*, 155–170.

M2 · Hierarchy of Protein Nanoparticle Binding Affinities

J. J. Mittag*, T. Preiß*, A. Das*, S. Milani, J. O. Rädler.

to be submitted to The Journal of Physical Chemistry C.

*shared first authorship

Hierarchy of protein nanoparticle binding affinities

Judith J. Mittag[#], Tobias Preiß[#], Anuradha Das[#], Silvia Milani, Joachim O. Rädler *

Faculty of Physics & Center for Nanoscience, Ludwig-Maximilians-Universität, Geschwister-Scholl-Platz 1, 80539 Munich, Germany

*Corresponding author: raedler@lmu.de

[#] These authors have contributed equally

KEYWORDS. Fluorescence correlation spectroscopy, protein corona, protein nanoparticle interaction, binding, off-kinetics

ABSTRACT. Protein adsorption and desorption from nanoparticles (NPs) governs the fate of nanoparticles interacting with living cells. Proteins may bind weakly or strongly and hence will show different tendency to remain bound when facing competitive binding with abundant blood proteins depending upon the protein itself as well as the type of NP. Here, we explore protein-NP affinities in case of four representative plasma proteins and six different kinds of NPs. Using fluorescence correlation spectroscopy (FCS) we systematically study the interactions between all combinations of proteins and NPs. In the case of binding without aggregation the fraction of protein bound is determined as a function of increasing molar protein/NP-ratio. The binding

isotherms are described in terms of adsorption models based on the law of mass action and discussed in the limits of weak and strong binding. We show that the adsorption layers of strong binders, such as fibronectin, bovine serum albumin and transferrin, are displaced by competitive binding of full blood serum proteins with off-kinetics following the order of the measured equilibrium affinities. Hence, measurement of thermodynamic binding constants brings forth some degree of predictability of protein-NP corona formation and competitive displacement under exposure to serum conditions.

INTRODUCTION. Nanoparticles (NPs) are of importance for their diverse utility in technology and biomedical applications owing to their wide range of tunable optical, mechanical as well as physicochemical properties¹⁻³. In particular due to the virtue of small size, NPs are effective in accessing living systems. The *in vivo* application of NPs, however, demands careful analysis of the immediate and distant interaction of the NPs with biomolecules and insights into their impact on human health and environment. Upon entering the body, NPs are exposed to a great number of biological components. Some of them, particularly proteins, are adsorbed on the NPs depending upon its surface property. This adsorbed layer of protein on the NPs surface is termed protein corona⁴⁻⁷. When the binding of protein to the NP is irreversible or of long duration it is called “hard corona”. On the other hand, when the protein layer is reversibly bound to the NP surface, i.e. it comes off quickly in dilute solutions or in the presence of other biomolecules, it is referred to as “soft corona”⁸⁻¹¹. The protein corona has significant biological impact since the behavior of a NP now depends on the corona rather than the NP surface alone^{4,6}. Proteins in the corona can both enhance and inhibit biological responses to NPs, and therefore intimately affect

the fate of the NP. It has been proposed that proteins bound tightly in the corona might provide a map of the pathway that a particle takes as it crosses various biological compartments^{6, 12-13}. Adsorption patterns have been regarded as an adsorption sequence where the most abundant proteins with lower affinity are displaced by less abundant proteins with higher affinity to the investigated surface. This displacement is known as “Vroman-effect”¹⁴⁻¹⁶. The adsorption and competitive binding of proteins to nanoparticles have been in the focus of various theoretical studies using protein structure data and molecular dynamics (MD) to predict the composition of the NP protein corona¹⁷⁻²¹.

The formation of a protein corona has been studied in experiment by numerous methods including surface plasmon resonance²², ITC⁸, DCS²³, thermophoresis²⁴, AFM²⁵ and fluorescence correlation spectroscopy (FCS)^{9, 26-31}. FCS stands out among those techniques as binding of particular fluorescently labeled protein can also be measured in the presence of other abundant proteins or full blood plasma^{26, 28, 32}. Secondly, FCS allows for measurement of the fraction of protein bound to NPs and hence can determine binding isotherms quantitatively. Recently, we used FCS to study the formation of layers of proteins on NPs. There, we found that the measured fraction of proteins bound to the NP is in quantitative agreement with a “strong binding model” that assumes that the first layer of proteins is strongly bound and not or only very slowly exchanging⁹. The interaction of protein with the NPs differs depending on the size, charge, stability of the NP as well as the size and charge of the proteins^{6, 33-34}. Variation in adsorption affinities thus seems to be caused by the different protein structure and chemical nature of the nanoparticles, resulting in diverging surface properties and consequently a hierarchy of binding proteins. In an attempt to understand the corona composition in the presence of multiple kinds of proteins, we combined experiments, simulations, and theory to investigate the corona kinetics of

three blood proteins (human serum albumin, transferrin, and fibrinogen)²⁹. In the present work, we extend the experimental studies to serum proteins having different molecular weight, similar isoelectric point and different abundance in plasma, and nanoparticles having comparable sizes, but different hydrophobicity. The proteins used are fibronectin (FN), fibrinogen (FG), transferrin (Tf) and bovine serum albumin (BSA). The molecular weight along with their isoelectric point and hydrodynamic radius is listed in Table 1³⁵⁻³⁷. BSA is a globular protein which is a major constituent of the cow blood plasma. It binds effectively with chemical agents and is widely used as a blocking agent³⁸. The blood glycoprotein Tf with its oblate spheroid shape is primarily associated with binding to and transportation of iron³⁹⁻⁴⁰. BSA and Tf are comparatively smaller in size than FN and FG. FG and FN are large and complex glycoproteins that help in blood coagulation⁴¹. The NPs chosen are: silica (silicon dioxide, SiO₂), ceria (cerium oxide, CeO₂), titania (titanium dioxide, TiO₂), carboxylated polystyrene (PSCOOH), sulphonated polystyrene (PSO₃H) and iron dextrane SPION (Fe dex SPION). All particles studied here were previously characterized in the context of concerted activities with EU funded research consortia.

In this article, we study all combinations of the above mentioned proteins and nanoparticles using FCS. Protein adsorption is found to fall into one of three categories: strongly binding, weakly binding or non-binding and aggregating. In case of binding and non-aggregating proteins, the fraction of bound protein as a function of the molar protein/NP-ratio is measured. We demonstrate that the measured isotherms are described by the law of mass-action allowing for attribution of equilibrium constants and adsorption area per protein. While binding constants of order follow Langmuir isotherm behavior, we emphasize that in case of strong binding ($K_D/NP < 100$) depletion of free protein needs to be considered to reproduce strong binding

isotherms. The binding affinities were compared to the off-kinetics of the corona proteins in the presence of competitive full serum proteins.

RESULTS AND DISCUSSION. In order to examine protein binding to NPs, different types of NPs were incubated in a solution of proteins and characterized *in situ* by means of FCS autocorrelation functions. Four of the most abundant serum proteins with significant differences in their size and shape were chosen as model systems for the investigation.

Fluorescence correlation spectroscopy study of protein adsorption to NPs

We use FCS to measure the fraction of bound proteins. Herein labeled proteins and unlabeled NPs are used. Figure 1a shows a schematic drawing of a FCS experiment where unlabeled NPs and labeled proteins diffuse in a solution illuminated by a focus laser beam. Labeled molecules diffusing through the detection volume provoke a fluctuating fluorescent signal. The characteristic time dependence of the fluctuations are described by the normalized time correlation function $G(\tau)$. For identical fluorescent particles undergoing Brownian motion $G(\tau)$ is given by the following equation⁴²

$$G(\tau) = \frac{1}{N} \left(1 + \frac{\tau}{\tau_D}\right)^{-1} \left(1 + \frac{\tau}{S^2\tau_D}\right)^{-\frac{1}{2}} + 1 \quad (\text{Equation 1})$$

where S is the structural parameter of the laser focus, N the average number of fluorescent molecules in the focal volume, τ_D the characteristic diffusion time of the fluorescently labeled molecules. Adding unlabeled NPs to a solution of labeled proteins alters the diffusion of those proteins that are adsorbed onto the NPs. In this case, we obtain a two-component system and the

measured autocorrelation function is the weighted sum of the autocorrelation functions of each component:

$$G(\tau) = A_1 G_{protein}(\tau) + A_2 G_{NP}(\tau) \quad (\text{Equation 2})$$

Figure 1b schematically depicts a time autocorrelation function showing two characteristic diffusion times. A two-component fit to $G(\tau)$ allows for determination of the amplitude A_2 of the slow (bound proteins) and A_1 of fast component (free proteins) in the system (see vertical lines in red and blue in Figure 1b). The fraction of protein bound to the NP surface is quantified by a two-component fit to the time autocorrelation function of the FCS signal (see supplementary material, Figure S1). Here, in order to improve the robustness of the fitting, the diffusion constant of the labeled protein is previously determined in a separate experiment and then used as a fixed parameter in two-component fits.

Measurement of protein – nanoparticle combinations

In the following section, we study all combinations of four prototypical proteins interacting with six kinds of NPs. We use FCS and measure the time correlation function of the fluorescently labeled proteins after addition of NPs. We find three different scenarios for the evolution of the fluorescence autocorrelation signal as prototypically shown in Figure 1c, I-III. Firstly, the amplitude of the FCS signal can increase with time after NP addition, while the characteristic times shift slightly to larger values. In this case, the proteins bind to NPs. The effective number of fluorescent objects decreases as proteins adsorb to NPs, while the correlation function develops a second slower component due to the reduced diffusion of proteins bound to NPs. Secondly, proteins may not bind to NPs or the interaction is so weak that binding is not detectable with FCS. Here, the correlation curves do show none or little deviations from the

correlation curves of the pure protein. The third case, frequently observed, is that the correlation curves exhibit extremely large amplitudes and broad tails towards the longer time regime. In addition, the fluctuations of the raw fluorescence signal show abnormally high bursts. Both facts indicate the presence of large aggregates of undefined sizes that diffuse sparsely and irregularly through the confocal volume with slow diffusion times.

The evolution of the FCS correlation function with time for all measured combinations of proteins and NPs is shown in Figure 2. According to the criteria shown in Figure 1c we made a rough categorization of the observed binding behavior. Typical correlation functions at various time intervals from 0 to 60 minutes are shown in matrix- like representation for all proteins and NPs (Figure 2). The overview demonstrates that after addition of protein it is not always possible to preserve monodisperse systems. Instead clear signatures of NP aggregation are observed, that are likely induced by protein adsorption. For example FG gives rise to aggregates. On the other hand some proteins have a low affinity for a few surfaces. An example of the wide variation in affinity with respect to the surface adsorption of proteins to NP is found in the binding patterns of BSA for silica and polystyrene NPs, although these particles have similar size. Albumin forms a stable coating on PSCOOH and PSOSO₃H, while it is weakly adsorbed on SiO₂ particles. The varying degree of surface coverage of the NP for serum albumin may be attributed to hydrophobicity. The hydrophobicity of metal oxides leads to non-adhesion for other small proteins such as Tf and BSA. Smaller proteins own a lesser amount of interaction sites which leads to lesser adsorption.⁴³

Theoretical model of protein adsorption to NPs

The binding of protein P to nanoparticles NP is generally described as an adsorption process in analogy to the Langmuir adsorption model for adsorbates from liquids to a flat solid surface. Adsorption is considered as a reversible reaction of a protein P with a free binding site S on the NP surface.



where S denotes the total number of binding sites presented on NPs, P the protein concentration and PS the concentration of occupied binding sites. In this case, the fraction of occupied binding sites to the total concentration of binding sites, S, i.e. the fraction of NPs coated, is:

$$\theta(P)_{NP} = \frac{[PS]}{[S]} = \frac{[P]}{[P] + K_D} \quad (\text{Equation 4}).$$

Where $K_D = ([P] \cdot [S])/[PS]$ denotes the equilibrium dissociation constant. Equation 4 is generally used to determine the dissociation constant from experimental adsorption isotherms^{30-32, 44-45}. In these experiments protein is titrated against a fixed concentration of NPs. Changes inferred to the NPs due to protein adsorption are measured. For instance, the measurement of the hydrodynamic diameter of the NP by FCS^{28, 30-32, 44-45} or dynamic light scattering²⁷, or changes induced by proteins as measured in surface plasmon resonance⁴⁶, affinity capillary electrophoresis⁴⁷⁻⁴⁸ or fluorescence quenching^{47, 49-50}. However, an important caveat needs to be addressed when Equation 4 is used in these kinds of titration experiments. It is generally assumed that the total concentration of protein added to the NP solution is almost equal to the concentration of unbound protein, P, which enters Equation 4. However, if the binding affinity of protein to NPs is strong, free proteins P are depleted as schematically depicted in Figure 3a. In the later case that proteins are strongly bound, $P_{free} \ll P_{total}$, the rigorous solution of the mass action Equation 3 has to be used⁵¹:

$$\vartheta(P)_{NP} = \frac{[PS]}{[PS]+[S_{free}]} = \frac{([s]+[\frac{P}{NP}]+K_D/NP) - \sqrt{([s]+[\frac{P}{NP}]+K_D/NP)^2 - 4[s][\frac{P}{NP}]}}{2[s]} \quad (\text{Equation 5})$$

Here, the ratio of protein to NP concentration, P/NP has been introduced and becomes the relevant variable. Likewise the total number of binding sites is replaced by the number of binding sites per NP, $s = S/NP$. Note that the exact form of Equation 5 turns into Equation 4 in the limit of weak adsorption ($K_D/NP \gg 1$). To illustrate this point, Figure 3a demonstrates theoretical isotherms $\vartheta(P)_{NP}$ for both, the exact law of mass action (full lines) and the approximate Langmuir-type (dashed lines). It appears that the deviations for strong binding (values of $K_D/NP < 100$) are clearly visible. While for weak binding the Langmuir isotherm is applicable, it is not appropriate for the determination of K_D/NP in case of strong binding and leads to a significant overestimation of the binding affinity.

In the present study, we do not measure the fraction of coated NP surface but rather determine the amount of free and bound protein, since it is the protein that is fluorescently labeled in the FCS study. To this end, we remodel Equation 3 and solve for the fraction of bound protein

$$Y(P/NP)_{protein} = \frac{[PS]}{[P]} \text{ as a function of the molar P/NP-ratio.}$$

In order to illustrate the dependence of isotherms as measured in our experiments, we have plotted the theoretical fraction bound $Y(P, NP)_{protein}$ versus P/NP-ratio for various K_D/NP but fixed concentration of binding sites per NP, s , i.e. constant NP size (see Figure 3b). Note that in the limit of low values of K_D/NP the exact expression of the law of mass action,

$$Y(P/NP)_{protein} = \frac{[PS]}{[PS]+P_{free}} = \frac{([s]+[\frac{P}{NP}]+K_D/NP) - \sqrt{([s]+[\frac{P}{NP}]+K_D/NP)^2 - 4[s][\frac{P}{NP}]}}{2[\frac{P}{NP}]} \quad (\text{Equation 6}),$$

merges into the strong binding model. In the strong binding model of Milani *et al.*⁹, it is assumed that proteins are strongly bound to NP in such a way that all proteins are bound up to the point when all binding sites are occupied by proteins. The sharp discontinuity at this point in the $Y(P/NP)_{protein}$ curve is illustrated in Figure 3b. Secondly, it is noteworthy that Equation 6 describes the most general case, when the amount of available binding sites S_{free} , is not assumed to equal the total amount of interaction sites S . However, if the free concentration of binding sites on the NPs is approximately equal to the total concentration, $S \approx S_{free}$, Equation 6 reduces to

$$Y(NP)_{protein} = \frac{[s]}{[s]+K_D/NP} \quad (\text{Equation 7}).$$

Equation 7 corresponds to experiments, where NPs with many binding sites are added to a protein solution and the fraction of bound protein is measured. For low protein concentration, $Y(P/NP)_{protein}$ becomes quasi independent of the protein concentration as can be seen by the plateau regime in Figure 3b. However, if the free concentration of binding sites

Measurement of the protein adsorption area and binding affinity

In order to analyze binding isotherms it is convenient to plot the fraction bound versus the P/NP ratio, since the maximum number of molecules adsorbing in a monolayer per NP, i.e. the number of binding sites per NP, s , can be directly read from the presentation. Knowing the number of binding sites per NP in turn enables us to estimate the surface area available for each protein. As an example Figure 3c shows measurements of the fraction of FN bound to silica NPs and BSA to PSCOOH. The red line exhibits the best fit to Equation 5. In this case we obtain $s=16$ binding sites per 100nm NP and a normalized equilibrium constant of $K_D/NP=0.15$. In comparison BSA adsorbing to PSCOOH beads of same size shows a number of binding sites per NP, $s=200$ and

$K_D/NP=0.41$ (Table 1). In this table, the average area occupied by a single protein is calculated from s and compared to the hydrodynamic radius of the protein as obtained from the FCS diffusion times. The data reflect the correct tendency that BSA has a smaller protein adsorption area than FN in accordance with the fact that the hydrodynamic radius is smaller by a factor of 3 compared to FN. Furthermore the literature values of the molecular weight of the protein are given.

Our theoretical considerations showed that the fraction of bound protein is a function of both the protein as well as NP concentration. To demonstrate this fact, we measured the fraction bound through a wide range of protein and NP concentrations for three model systems that showed no aggregation in the interaction matrix. Figure 4 shows $Y(P)_{protein}$ for BSA/PSCOOH, BSA/TiO₂ and BSA/CeO₂, within a range of 45 nM to 45 μ M of BSA and within a range of 1 μ g/ml to 1 mg/ml NP concentration. In case of BSA/PSCOOH we observe, as expected from Equation 6, that the fraction bound is high at low protein concentration and high NP concentration and falls off with increasing protein and decreasing NP concentrations. For TiO₂ and CeO₂ NPs, we observed only a very low fraction bound in all measured cases. These measurements confirm that in both cases the proteins are very weakly binding to NPs, which in principle was already shown in Figure 2, but has now been confirmed over a larger range of protein and NP concentrations.

Hierarchy in desorption kinetics

Next we ask the question whether the binding affinity correlates with the resistance to competitive binding. To this end we form NP decorated with a labeled protein adsorption layer and measure the off-kinetics after exposure of the NPs to serum proteins. The particles are incubated for at least one hour in a suitable concentration of the selected protein, which allows a

monolayer to form. These protein coated particles are then exposed to 10% fetal bovine serum. The schematic diagram in Figure 5a illustrates the process of desorption due to competitive binding in serum. The amount of free and bound protein is measured using FCS. Figure 5 shows the resulting time courses of the fraction of bound protein for various protein-NP combinations that exhibited strong binding. The data show desorption kinetics with exponential decay rates. However, the majority of protein adsorbed is not fully removed as seen from considerable offsets in the time courses (Note that the fraction bound axis terminates at ~ 0.6 in Figure 5b). This offset may be interpreted as the hard corona that seems to be irreversible bound to the NP on the time scale of our experiments. The characteristic desorption-times are determined by exponential fits with offset and the corresponding kinetic off-rates, k_{off} , listed in Table 1. In general, it was observed that smaller proteins (BSA and Tf) are replaced more efficiently than larger proteins (FN) in the presence of serum. Also, the kinetics of protein desorption depends on the NP type. For instance, BSA has a higher kinetic off-rate in presence of PSCOOH than PSOSO₃H ($8.8 \cdot 10^{-3}$ versus $2.4 \cdot 10^{-3} \text{ min}^{-1}$). Most importantly, however, there seems to be a correlation between the off-rate k_{off} and the measured normalized dissociation constant K_D/NP . Knowing that $k_{off} = K_D \cdot k_{on}$ and assuming that k_{on} is independent of protein and NP type, we expect an increasing off-rate with increasing dissociation constant. The values listed in the last rows of Table 1 are in agreement with this expected dependency. The raw data of the evolution of autocorrelation function of two representative P-NP interactions with serum can be found in Figure S1. It is noteworthy that the addition of serum to aggregates of NPs and proteins were carried out but no desorption or redispersion effect has been observed.

CONCLUSION. In this article, we studied the interaction between selected proteins and NPs in an attempt to systematically cover the formation of protein corona. Primarily, three categories of protein-NP interaction have been noticed– strong binding, weak or no binding and aggregation. The data suggests that proteins that are large and natural coagulators, such as FG and FN, are more susceptible to aggregation. These proteins are likely to shield NPs, reduce the overall charges of NPs and promote cross-bridging between NPs by binding to other proteins. When proteins bind to NPs without disturbing their colloidal stability, we measured binding isotherms in accordance with thermodynamic models of protein adsorption. We discussed the importance of using the full mass action description since protein concentrations are readily depleted in the presence of strongly adsorbing NPs. In this case equilibrium binding constants as well as the average area occupied by the adsorbed proteins have been determined. These characteristic determinants of the protein-NP interaction are meaningful values and have predictive power. For example we showed that the protein adsorption area correlates with the hydrodynamic bulk size of the protein. We also tested for stability of the protein layers in presence of serum and showed that desorption kinetics of proteins is directly linked to the hierarchical order of the protein-NP dissociation constants. Competitive binding proteins are able to quickly detach protein layers, which are weakly bound, whereas some proteins are strongly bound. This shows that the NPs retain “memory” of the strong binding proteins, which first encounter in their travel through body compartments. A fact that was recently confirmed by theoretical modeling²⁹. Hence, the study of thermodynamic binding of each protein component allows for ranking of protein-NP affinities and can be used towards a better understanding of the protein-NP interaction in biological environment such as blood serum or plasma. Systematic measurement of protein-NP interactions will be valuable to the community but requires the consideration of protein as well

as NP concentrations especially in case of strong binding. The dissemination of tabulated protein-NP data in publically accessible libraries, such as nanosafetycluster.eu, is beginning to emerge. There is hope that databases combined with theoretical modeling tools will enable predictive capability for the composition of protein corona on NPs and possibly pre-estimate impact of NP toxicity.

MATERIALS. All proteins (BSA, Tf, FN, FG) were purchased from Invitrogen (Life Technology). BSA, Tf and FN were labeled with Alexa-488 whereas FG was labeled with Alexa-647. Silica, polystyrene carboxylated (PSCOOH) and polystyrene sulphonated (PSOSO₃H) beads with a diameter of 100nm were purchased from Polysciences Inc. (Warrington, USA). Further nanoparticles were obtained from the FP7 EU grants NanoMILE: TiO₂ [NIST SRM1898 (500nm), CeO₂ [JRC NM212] (300nm) and Fe dextrane SPION [N411121114] (20nm). Nanoparticles were checked for their sizes by DLS experiments (see Figure S2 in supplementary material). An initial stock solution of 5mg/ml was prepared in PBS or PB (Sigma) and later diluted as required in the corresponding medium.

CeO₂ and TiO₂ are larger size and this may be due to aggregation. However, the aggregated and precipitated NPs do not contribute to the fluorescence signal as we have used labeled proteins.

METHODS. FCS measurements were carried out on a LSM10 microscope fitted with a ConfoCor2 unit (Carl Zeiss Jena, Germany). We used two kinds of excitation – an argon ion laser of 488nm (TF, BSA and FN) and HeNe2 of 633nm (FG). All measurements were

performed with water immersion with an objective of 40X. A bandpass filter 525/25nm was used to separate the fluorescence emission from excitation light. Experiments were performed at room temperature regulated at 22°C. 384 well plates were used for measurements (Greiner bio one). The wells were precoated by pluronic acid in MilliQ for one hour and washed carefully with MilliQ later to wash off excess pluronic acid.

FIGURES

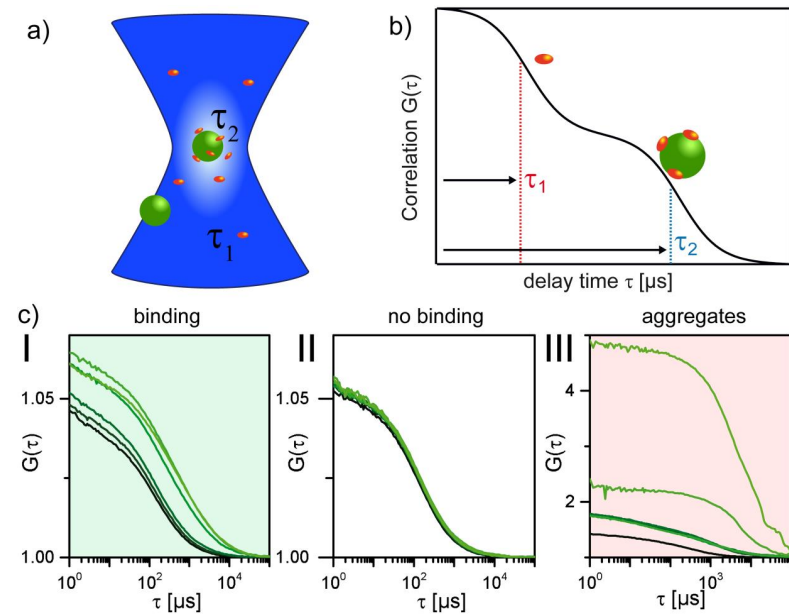


Figure 1. Protein-NP binding measurements using fluorescence correlation spectroscopy
a) Schematic drawing of labeled proteins binding to unlabeled nanoparticles detected by fluorescence in the laser focus volume. **b)** Time autocorrelation function of freely diffusing proteins and proteins adsorbed to NPs. In binding equilibrium the time correlation exhibits a free fraction with diffusion time τ_1 and a fraction bound with diffusion time τ_2 . **c)** Typical evolution of the time correlation functions of the proteins after addition of NPs. The interactions fall into one of three categories corresponding to binding (I), no binding (II) or aggregation (III).

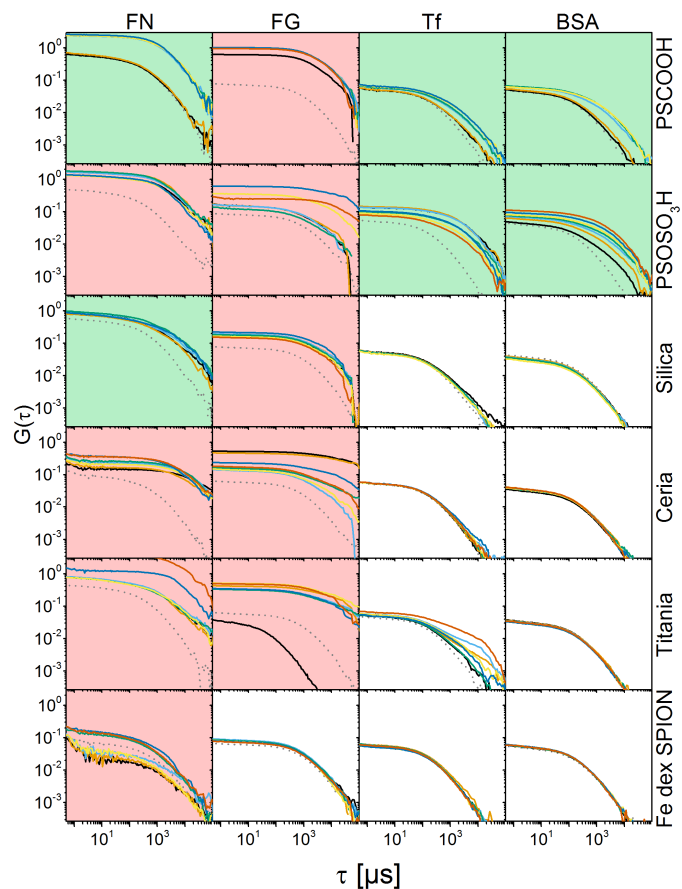


Figure 2. Matrix of FCS kinetics from all possible combinations of NP and proteins showing the time dependent evolution of the FCS autocorrelation (pure protein = dotted, after 5 min after NP addition = black, 10 min = orange, 20 min = light blue, 30 min=green, 45 min= yellow, 60 min = dark blue). Data are highlighted according to the behavior: aggregation: red, strong binding: green and weak binding or no binding: white.

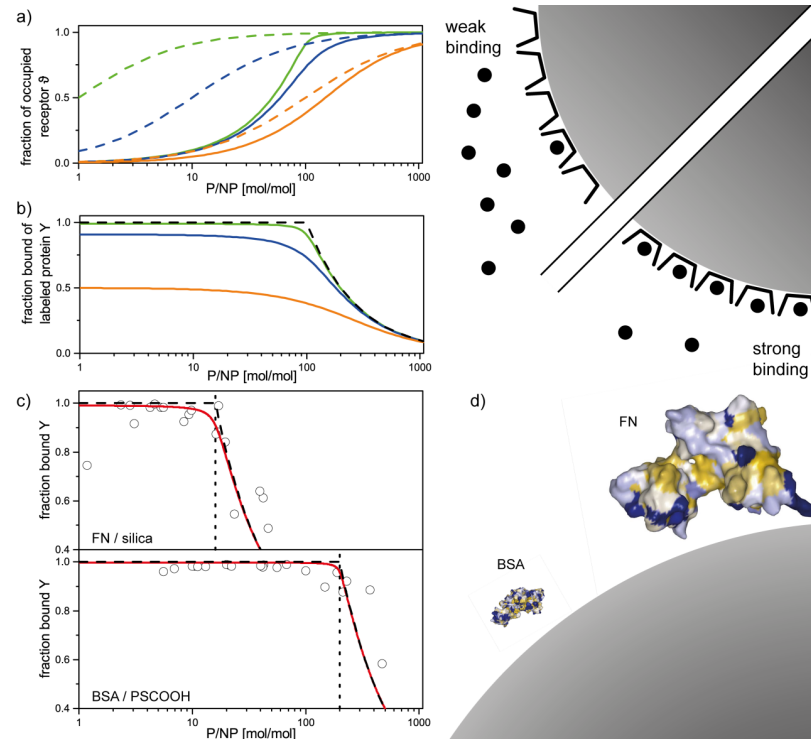


Figure 3. Theoretical analysis of protein-NP binding isotherms: **a)** Fraction of NP coated according to Langmuir adsorption model (dashed) and according to the exact solution of the law of mass action (solid line). Data are plotted for various K_D/NP values: 1 (green), 10 (blue) and 100 (orange). **b)** Fraction of protein bound to NPs according to the strong binding model (black dashed line) and according to the exact solution of the law of mass action (solid line). **c)** Adsorption isotherms measured for FN/silica and BSA/PSCOOH. Solid red lines represent fitting according to Equation 6 and dashed black lines according to the strong binding model. The position of full monolayer coverage (vertical dotted line) yields the number of binding sites per NP. **d)** To-scale representation of the proteins BSA and FN and the NP with diameter 100 nm.

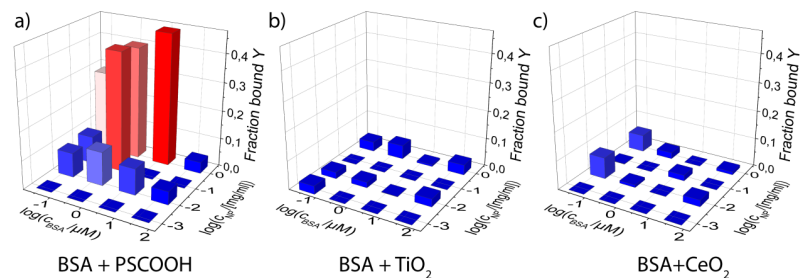


Figure 4. Fraction of bound of BSA to **a)** PSCOOH NPs, **b)** TiO₂ NPs and **c)** CeO₂ NPs from zero (blue) to 50% (red) as a function of BSA concentration and NP concentration. While PSCOOH NPs show relevant binding with BSA that is depended of both, concentration of protein and NP, TiO₂ and CeO₂ NPs show very little to no binding.

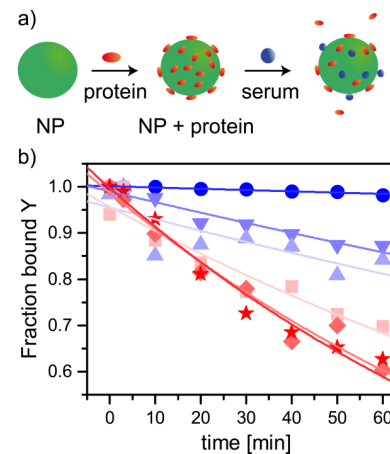


Figure 5. a) Schematic drawing of adsorption of labeled protein and following desorption by serum. **b)** Desorption kinetics of protein coated NPs in serum are shown for various combinations of protein and NPs. The solid lines were obtained with a single exponential fit, yielding desorption-time values. The characteristic desorption-rates k_{off} are as follows: $8.8 \cdot 10^{-3} \text{ min}^{-1}$ for BSA with PSCOOH (stars); $8.3 \cdot 10^{-3} \text{ min}^{-1}$ for Tf with PSOSO₃H (diamonds); $5.6 \cdot 10^{-3} \text{ min}^{-1}$ for Tf with PSCOOH (squares); $2.7 \cdot 10^{-3} \text{ min}^{-1}$ for FN with silica (upwards triangles); $2.4 \cdot 10^{-3} \text{ min}^{-1}$ for BSA with PSOSO₃H (downwards triangles); $3.0 \cdot 10^{-4} \text{ min}^{-1}$ for FN with PSCOOH (circles).

TABLES.

Table 1

Properties of proteins

	FN	FG	Tf	BSA
Molecular weight[kDa]	440	340	77	67
Hydrodynamic radius [nm]	9.0±0.7	8.5±0.9	3.6±0.1	3.3±0.1
Isoelectric point	5.6-6.1	5.8	5.6	5.4
Type of NP	silica	-	PSOSO ₃ H	PSCOOH
Number of sites per NP	16	-	300±100 ^{a)}	200
surface area per protein [nm ²]	1963	-	105	157
K _D /NP	0.15	-	0.31	0.41
k _{off} [min ⁻¹]	2.7·10 ⁻³		8.3·10 ⁻³	8.8·10 ⁻³

^{a)} from Milani *et al.*⁹

SUPPORTING INFORMATION. Autocorrelation function of desorption kinetics of proteins coated NP in 10% serum and stability of NPs in different media are shown (Figures S1 and S2). This material is available free of charge via the internet at <http://pubs.acs.org>.

ACKNOWLEDGMENT

Financial support from the FP7 EU grants NanoMILE and NanoTransKinetics, and the Excellence Cluster 'Nanosystems Initiative Munich (NIM)' is gratefully acknowledged.

ABBREVIATIONS

BSA, bovine serum albumin; CeO₂, cerium oxide; FCS, fluorescence correlation spectroscopy; FG, fibrinogen; FN, fibronectin; NP, nanoparticle; PSCOOH, carboxylated polystyrene; PSOSO₃H, sulphonated polystyrene; SiO₂, silicon dioxide; Tf, transferrin; TiO₂, titanium dioxide; CeO₂, Ceria

SYNOPSIS

In this work, we investigated binding of selected proteins and NPs in all possible combinations using fluorescence correlation spectroscopy. We found three categories of interactions, namely-binding, weak/no binding and aggregation. In case of binding we measured the fraction of bound protein vs. the protein/NP molar ratio and described these isotherms by the law of mass action allowing for attribution of equilibrium constants and adsorption area per protein. The normalized dissociation constant are shown to correlate with measured desorption rates, when protein coated NP are placed in serum protein. The data indicate that there is some degree of predictability in binding behavior of protein-NP mixtures based on the size of the protein and protein binding affinity to the NP.

REFERENCES

- Parhi, P.; Mohanty, C.; Sahoo, S. K., Nanotechnology-Based Combinational Drug Delivery: An Emerging Approach for Cancer Therapy. *Drug Discov Today* **2012**, *17*, 1044-52.
- Kumar, A.; Forbes, B.; Mudway, I.; Bicer, E. M.; Dailey, L. A., What Are the Biological and Therapeutic Implications of Biomolecule Corona Formation on the Surface of Inhaled Nanomedicines? *Nanomedicine* **2015**, *10*, 343-345.
- Zarschler, K.; Rocks, L.; Licciardello, N.; Boselli, L.; Polo, E.; Garcia, K. P.; De Cola, L.; Stephan, H.; Dawson, K. A., Ultrasmall Inorganic Nanoparticles: State-of-the-Art and Perspectives for Biomedical Applications. *Nanomedicine* **2016**, *12*, 1663-701.
- Monopoli, M. P.; Aberg, C.; Salvati, A.; Dawson, K. A., Biomolecular Coronas Provide the Biological Identity of Nanosized Materials. *Nat Nano* **2012**, *7*, 779-786.
- Klein, J., Probing the Interactions of Proteins and Nanoparticles. *Proc. Natl. Acad. Sci. U. S. A.* **2007**, *104*, 2029-30.
- Lundqvist, M.; Stigler, J.; Elia, G.; Lynch, I.; Cedervall, T.; Dawson, K. A., Nanoparticle Size and Surface Properties Determine the Protein Corona with Possible Implications for Biological Impacts. *Proceedings of the National Academy of Sciences of the United States of America* **2008**, *105*, 14265-14270.
- Lundqvist, M.; Stigler, J.; Cedervall, T.; Berggård, T.; Flanagan, M. B.; Lynch, I.; Elia, G.; Dawson, K., The Evolution of the Protein Corona around Nanoparticles: A Test Study. *ACS Nano* **2011**, *5*, 7503-7509.
- Cedervall, T.; Lynch, I.; Lindman, S.; Berggård, T.; Thulin, E.; Nilsson, H.; Dawson, K. A.; Linse, S., Understanding the Nanoparticle-Protein Corona Using Methods to Quantify Exchange Rates and Affinities of Proteins for Nanoparticles. *Proceedings of the National Academy of Sciences* **2007**, *104*, 2050-2055.
- Milani, S.; Baldelli Bombelli, F.; Pitek, A. S.; Dawson, K. A.; Rädler, J., Reversible Versus Irreversible Binding of Transferrin to Polystyrene Nanoparticles: Soft and Hard Corona. *ACS Nano* **2012**, *6*, 2532-2541.
- Casals, E.; Pfaller, T.; Duschl, A.; Oostingh, G. J.; Puntès, V., Time Evolution of the Nanoparticle Protein Corona. *ACS Nano* **2010**, *4*, 3623-3632.
- Corbo, C.; Molinaro, R.; Parodi, A.; Toledano Furman, N. E.; Salvatore, F.; Tasciotti, E., The Impact of Nanoparticle Protein Corona on Cytotoxicity, Immunotoxicity and Target Drug Delivery. *Nanomedicine (Lond)* **2016**, *11*, 81-100.
- Ruge, C. A.; Schaefer, U. F.; Herrmann, J.; Kirch, J.; Canadas, O.; Echaide, M.; Perez-Gil, J.; Casals, C.; Muller, R.; Lehr, C. M., The Interplay of Lung Surfactant Proteins and Lipids Assimilates the Macrophage Clearance of Nanoparticles. *PLoS One* **2012**, *7*, e40775.
- Wohlfart, S.; Gelperina, S.; Kreuter, J., Transport of Drugs across the Blood-Brain Barrier by Nanoparticles. *Journal of Controlled Release* **2012**, *161*, 264-273.
- Vroman, L.; Adams, A. L., Identification of Rapid Changes at Plasma-Solid Interfaces. *Journal of Biomedical Materials Research* **1969**, *3*, 43-67.
- Hirsh, S. L.; McKenzie, D. R.; Nosworthy, N. J.; Denman, J. A.; Sezerman, O. U.; Bilek, M. M. M., The Vroman Effect: Competitive Protein Exchange with Dynamic Multilayer Protein Aggregates. *Colloids and Surfaces B: Biointerfaces* **2013**, *103*, 395-404.
- LeDuc, C. A.; Vroman, L.; Leonard, E. F., A Mathematical Model for the Vroman Effect. *Industrial & Engineering Chemistry Research* **1995**, *34*, 3488-3495.
- Darabi Sahneh, F.; Scoglio, C.; Riviere, J., Dynamics of Nanoparticle-Protein Corona Complex Formation: Analytical Results from Population Balance Equations. *PLoS One* **2013**, *8*, e64690.
- Dell'Orco, D.; Lundqvist, M.; Oslakovic, C.; Cedervall, T.; Linse, S., Modeling the Time Evolution of the Nanoparticle-Protein Corona in a Body Fluid. *PLoS One* **2010**, *5*, e10949.
- Lopez, H.; Lobaskin, V., Coarse-Grained Model of Adsorption of Blood Plasma Proteins onto Nanoparticles. *The Journal of Chemical Physics* **2015**, *143*, 243138.
- Liu, R.; Jiang, W.; Walkey, C. D.; Chan, W. C. W.; Cohen, Y., Prediction of Nanoparticles-Cell Association Based on Corona Proteins and Physicochemical Properties. *Nanoscale* **2015**, *7*, 9664-9675.
- Albanese, A.; Walkey, C. D.; Olsen, J. B.; Guo, H.; Emili, A.; Chan, W. C. W., Secreted Biomolecules Alter the Biological Identity and Cellular Interactions of Nanoparticles. *ACS Nano* **2014**, *8*, 5515-5526.
- Patra, A.; Ding, T.; Engudar, G.; Wang, Y.; Dykas, M. M.; Liedberg, B.; Kah, J. C.; Venkatesan, T.; Drum, C. L., Component-Specific Analysis of Plasma Protein Corona Formation on Gold Nanoparticles Using Multiplexed Surface Plasmon Resonance. *Small* **2016**, *12*, 1174-82.
- Walczyk, D.; Bombelli, F. B.; Monopoli, M. P.; Lynch, I.; Dawson, K. A., What the Cell "Sees" in Bionanoscience. *Journal of the American Chemical Society* **2010**, *132*, 5761-5768.
- Wolff, M.; Mittag, J. J.; Herling, T. W.; Genst, E. D.; Dobson, C. M.; Knowles, T. P. J.; Braun, D.; Buell, A. K., Quantitative Thermophoretic Study of Disease-Related Protein Aggregates. *Scientific Reports* **2016**, *6*, 22829.
- Lee, Y. K.; Choi, E.-J.; Webster, T. J.; Kim, S.-H.; Khang, D., Effect of the Protein Corona on Nanoparticles for Modulating Cytotoxicity and Immunotoxicity. *International Journal of Nanomedicine* **2015**, *10*, 97-113.
- Engelke, H.; Dorn, I.; Radler, J. O., Diffusion and Molecular Binding in Crowded Vesicle Solutions Measured by Fluorescence Correlation Spectroscopy. *Soft Matter* **2009**, *5*, 4283-4289.
- Liedl, T.; Keller, S.; Simmel, F. C.; Radler, J. O.; Parak, W. J., Fluorescent Nanocrystals as Colloidal Probes in Complex Fluids Measured by Fluorescence Correlation Spectroscopy. *Small* **2005**, *1*, 997-1003.
- Rusu, L.; Gambhir, A.; McLaughlin, S.; Radler, J., Fluorescence Correlation Spectroscopy Studies of Peptide and Protein Binding to Phospholipid Vesicles. *Biophysical Journal* **2004**, *87*, 1044-53.
- Vilanova, O.; Mittag, J. J.; Kelly, P. M.; Milani, S.; Dawson, K. A.; Rädler, J. O.; Franzese, G., Understanding the Kinetics of Protein-Nanoparticle Corona Formation. *ACS Nano* **2016**, *10*, 10842-10850.
- Maffre, P.; Brandholt, S.; Nienhaus, K.; Shang, L.; Parak, W. J.; Nienhaus, G. U., Effects of Surface Functionalization on the Adsorption of Human Serum Albumin onto Nanoparticles – a Fluorescence Correlation Spectroscopy Study. *Beilstein J. Nanotechnol.* **2014**, *5*, 2036-2047.
- Rocker, C.; Potzl, M.; Zhang, F.; Parak, W. J.; Nienhaus, G. U., A Quantitative Fluorescence Study of Protein Monolayer Formation on Colloidal Nanoparticles. *Nat. Nano* **2009**, *4*, 577-580.
- Nienhaus, G. U.; Maffre, P.; Nienhaus, K., Studying the Protein Corona on Nanoparticles by Fcs. *Methods Enzymol* **2013**, *519*, 115-37.

33. Pino, P. d.; Pelaz, B.; Zhang, Q.; Maffre, P.; Nienhaus, G. U.; Parak, W. J., Protein Corona Formation around Nanoparticles - from the Past to the Future. *Materials Horizons* **2014**, *1*, 301-313.
34. Fleischer, C. C.; Payne, C. K., Nanoparticle–Cell Interactions: Molecular Structure of the Protein Corona and Cellular Outcomes. *Accounts of Chemical Research* **2014**, *47*, 2651-2659.
35. Boughton, B. J.; Simpson, A. W., The Biochemical and Functional Heterogeneity of Circulating Human Plasma Fibronectin. *Biochem. Biophys. Res. Commun.* **1984**, *119*, 1174-80.
36. Shi, Q.; Zhou, Y.; Sun, Y., Influence of Ph and Ionic Strength on the Steric Mass-Action Model Parameters around the Isoelectric Point of Protein. *Biotechnol. Prog.* **2005**, *21*, 516-523.
37. De, M.; Rana, S.; Akpınar, H.; Miranda, O. R.; Arvizo, R. R.; Bunz, U. H. F.; Rotello, V. M., Sensing of Proteins in Human Serum Using Conjugates of Nanoparticles and Green Fluorescent Protein. *Nat. Chem.* **2009**, *1*, 461-465.
38. Taylor, S.; Smith, S.; Windle, B.; Guiseppi-Elie, A., Impact of Surface Chemistry and Blocking Strategies on DNA Microarrays. *Nucleic Acids Research* **2003**, *31*, e87-e87.
39. Ponka, P.; Beaumont, C.; Richardson, D. R., Function and Regulation of Transferrin and Ferritin. *Semin Hematol* **1998**, *35*, 35-54.
40. Martel, P.; Kim, S. M.; Powell, B. M., Physical Characteristics of Human Transferrin from Small Angle Neutron Scattering. *Biophysical journal* **1980**, *31*, 371-80.
41. Mosesson, M. W., Fibrinogen and Fibrin Structure and Functions. *J Thromb Haemost* **2005**, *3*, 1894-904.
42. Hess, S. T.; Webb, W. W., Focal Volume Optics and Experimental Artifacts in Confocal Fluorescence Correlation Spectroscopy. *Biophysical journal* **2002**, *83*, 2300-17.
43. Jeon, S. I.; Andrade, J. D., Protein—Surface Interactions in the Presence of Polyethylene Oxide. *J. Colloid Interface Sci.* **1991**, *142*, 159-166.
44. Jiang, X.; Weise, S.; Hafner, M.; Rocker, C.; Zhang, F.; Parak, W. J.; Nienhaus, G. U., Quantitative Analysis of the Protein Corona on Fept Nanoparticles Formed by Transferrin Binding. *J. R. Soc. Interface* **2010**, *7 Suppl 1*, S5-S13.
45. Huhn, J.; Fedeli, C.; Zhang, Q.; Masood, A.; Del Pino, P.; Khashab, N. M.; Papini, E.; Parak, W. J., Dissociation Coefficients of Protein Adsorption to Nanoparticles as Quantitative Metrics for Description of the Protein Corona: A Comparison of Experimental Techniques and Methodological Relevance. *Int. J. Biochem Cell Biol.* **2016**, *75*, 148-61.
46. Canoa, P.; Simón-Vázquez, R.; Popplewell, J.; González-Fernández, Á., A Quantitative Binding Study of Fibrinogen and Human Serum Albumin to Metal Oxide Nanoparticles by Surface Plasmon Resonance. *Biosens. Bioelectron.* **2015**, *74*, 376-383.
47. Boulos, S. P.; Davis, T. A.; Yang, J. A.; Lohse, S. E.; Alkilany, A. M.; Holland, L. A.; Murphy, C. J., Nanoparticle–Protein Interactions: A Thermodynamic and Kinetic Study of the Adsorption of Bovine Serum Albumin to Gold Nanoparticle Surfaces. *Langmuir* **2013**, *29*, 14984-14996.
48. Li, N.; Zeng, S.; He, L.; Zhong, W., Probing Nanoparticle–Protein Interaction by Capillary Electrophoresis. *Anal. Chem.* **2010**, *82*, 7460-7466.
49. Zhang, H.; Wu, P.; Zhu, Z.; Wang, Y., Interaction of Gamma-Fe(2)O(3) Nanoparticles with Fibrinogen. *Spectrochim. Acta Mol. Biomol. Spectrosc.* **2015**, *151*, 40-7.
50. Cai, H.; Yao, P., Gold Nanoparticles with Different Amino Acid Surfaces: Serum Albumin Adsorption, Intracellular Uptake and Cytotoxicity. *Colloids Surf. B Biointerfaces* **2014**, *123*, 900-6.

51. Swillens, S., Interpretation of Binding Curves Obtained with High Receptor Concentrations: Practical Aid for Computer Analysis. *Molecular Pharmacology* **1995**, *47*, 1197-1203.

Supplementary Information

Of

Hierarchy of protein binding to nanoparticles

Judith J. Mittag[#], Anuradha Das[#], Tobias Preiß, Silvia Milani, Joachim O. Rädler *

Faculty of Physics & Center for Nanoscience, Ludwig-Maximilians-Universität, Geschwister-

Scholl-Platz 1, 80539 Munich, Germany

*Corresponding author: raedler@lmu.de

[#]These authors have contributed equally

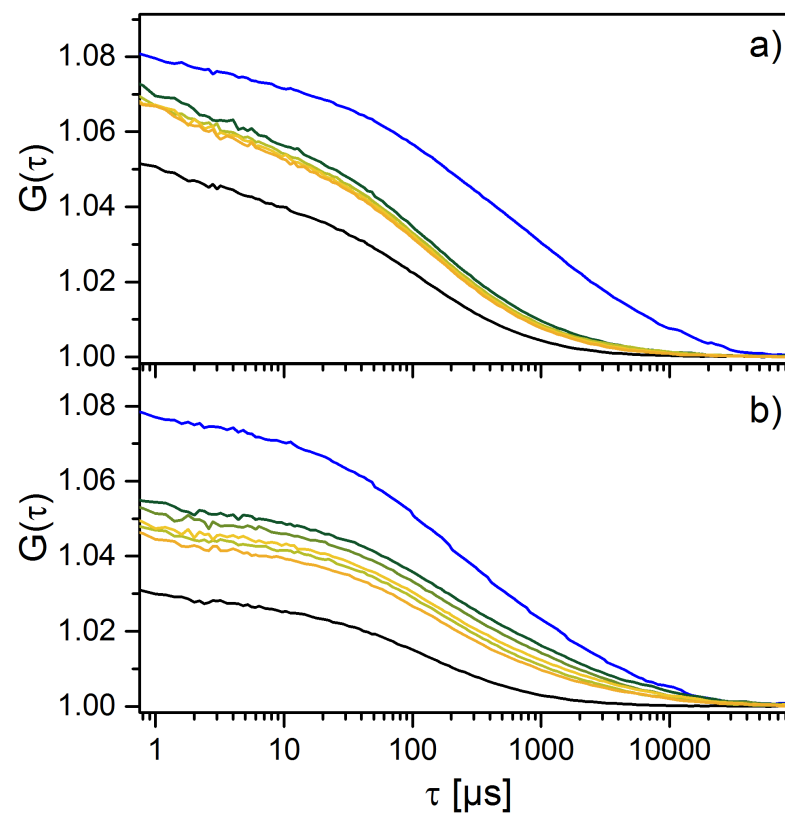


Figure S1. Different proteins have different off-rates on exposure to serum. The strength of binding also depends on NPs used. Here, autocorrelation function (ACF) of desorption kinetics of protein (BSA and Tf) coated nanoparticles (PSOSO₃H, PSCOOH) in 10% serum are shown: **a)** BSA and PSOSO₃H, **b)** Tf and PSCOOH. Black lines are the ACF of pure proteins, red lines represent ACF of coated NPs in PB, and solid lines are in presence of serum at different times. The different times are at 10, 20, 30, 40, and 50 minutes (green to yellow).

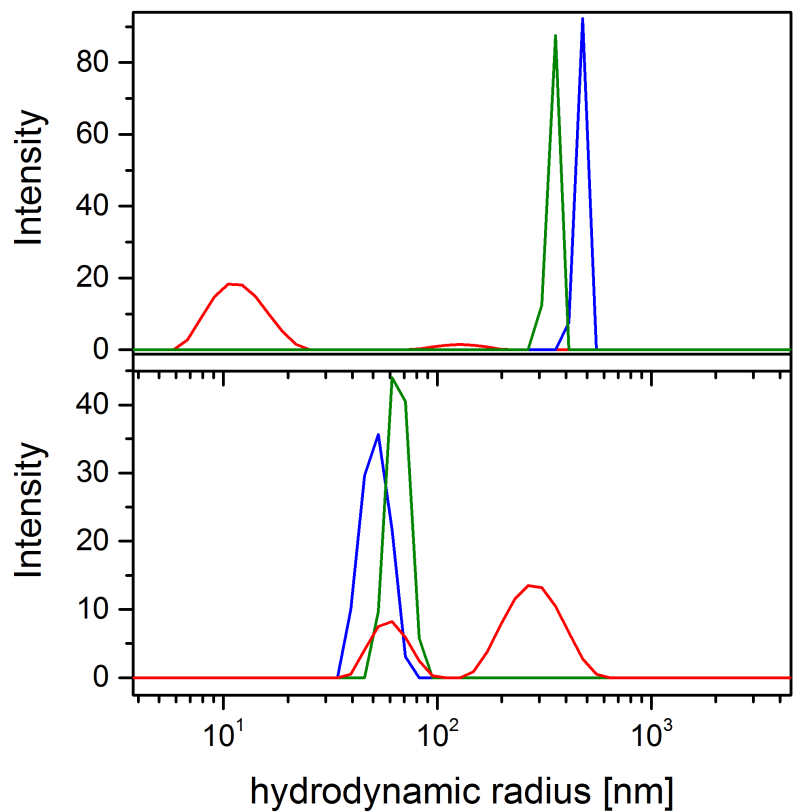


Figure S2. Various NPs are found to be stable in various media. This figure shows some representative DLS data for the stability of NPs in different media.

The sizes of the NPs are checked for all the NPs. DLS figures for Fe dex SPION (red), titania (blue) and ceria (green) are shown in the upper panel. The first was found to be stable in PB whereas later two in PBS.

Silica was found to be most stable in PB (blue) as seen in the lower panel of the figure. Silica in water (green) and PBS (red) are also shown in the same panel.

M3 · Impact of Plasma Protein Binding on Cargo Release by Thermosensitive Liposomes Probed by Fluorescence Correlation Spectroscopy

J. J. Mittag, B. Kneidl, T. Preiß, G. Winter, S. Wuttke, M. Hossann, H. Engelke and J. O. Rädler.

under revision, European Journal of Pharmaceutics and Biopharmaceutics, 2017.

Impact of plasma protein binding on cargo release by thermosensitive liposomes probed by fluorescence correlation spectroscopy

Judith J. Mittag^a, Barbara Kneidl^{b,c}, Tobias Preiß^b,
Martin Hossann^d, Gerhard Winter^e, Stefan Wuttke^e, Hanna Engelke^{e,*} and Joachim O. Rädler^{a,*}

^a Department of Physics and Center for NanoScience (CeNS), Ludwig-Maximilians-Universität, Geschwister-Scholl-Platz 1, 80539 München, Germany

^b Department of Internal Medicine III, University Hospital Munich, Ludwig-Maximilians-Universität, München, Germany

^c Department of Pharmacy, Pharmaceutical Technology and Biopharmaceutics, Ludwig-Maximilians-Universität, München, Germany

^d Thermosome GmbH, Am Klopferspitz 19, 82152 Planegg/Martinsried, Germany

^e Department of Chemistry and Center for NanoScience (CeNS), Ludwig-Maximilians-Universität, Butenandtstraße 5-13(E), 81377 München, Germany

*Corresponding author: hanna.engelke@cup.lmu.de, raedler@lmu.de

Keywords: thermosensitive liposomes, drug delivery, drug release, fluorescence correlation spectroscopy, plasma, protein adsorption

Abbreviations:

ApoA1, apolipoprotein; β -Gal, β -galactosidase; CF, carboxyfluorescein; DLS, dynamic light scattering; DPPC, 1,2-dipalmitoyl-*sn*-glycero-3-phosphocholine; DPPG₂, 1,2-dipalmitoyl-*sn*-glycero-3-phosphodiglycerol; DSPC, 1,2-distearoyl-*sn*-glycero-3-phosphocholine; FBS, fetal bovine serum; F(C)S, fluorescence (correlation) spectroscopy; FDG, fluorescein di- β -D-galactopyranoside; Fib, fibrinogen; Lyso-PC, 1-acyl-*sn*-glycero-3-phosphocholine; SA, serum albumin; T_m , temperature of the transition from the solid gel to the liquid disordered phase; TSL, thermosensitive liposome; Tf, transferrin

Abstract

Thermosensitive liposomes (TSLs) whose phase-transition temperature (T_m) lies slightly above body temperature are ideal candidates for controlled drug release via local hyperthermia. Recent studies, however, have revealed disruptive shifts in the transition temperature in mouse plasma, which are attributed to undefined interactions with blood proteins. Here, we study the effects of four major plasma proteins – serum albumin (SA), transferrin (Tf), apolipoprotein A1 (ApoA1) and fibrinogen (Fib) – on the temperature-dependent release of fluorescein di- β -D-galactopyranoside (FDG) from TSLs. The amount of fluorescein released was quantified by fluorescence correlation spectroscopy (FCS) after hydrolysis of FDG with β -galactosidase (β -Gal). This approach is more sensitive and thus superior to previous release assays, as it is impervious to the confounding effects of Triton on conventional fluorescence measurements. The assay determines the molar release ratio, i.e. the number of molecules released per liposome. We show that shifts in the T_m of release do not reflect protein affinities for the liposomes derived from adsorption isotherms. We confirm a remarkable shift in induced release towards lower temperatures in the presence of mouse plasma. In contrast, exposure to rat or human plasma, or fetal bovine serum (FBS), has no effect on the release profile.

Introduction

In the 1970s, Gregory Gregoriadis first proposed the use of liposomes for drug delivery [1–3]. Liposomes have many obvious advantages in this context: they are biocompatible, biodegradable and show little or no antigenic or allergenic activity. These features largely explain why the majority of FDA-approved and therapeutically applied nanoparticle-based delivery vehicles falls into the category of liposomal or lipid-based formulations, such as Doxil, DaunoXome or Marqibo [4–8]. A potential limitation of these products is the absence of a controllable drug release mechanism, which would enable localized therapy and thus reduce side-effects. Therefore, the next step in the development of lipid-based delivery platforms was the implementation of stimulus-responsive drug delivery. Thermosensitive liposomes (TSLs) are the most promising triggered systems, with one formulation (Thermodox) having successfully undergone clinical phase I studies in humans [9,10]. TSLs allow for temperature-controlled drug release in response to local hyperthermia or focused high-intensity ultrasound [11–14].

TSLs are composed of a lipid mixture that is designed to have a melting phase-transition temperature (T_m) a few degrees above a chosen target temperature. At this point, the structure of the lipid bilayer changes from a solid-gel phase to a liquid-crystalline phase. This change increases the permeability of the membrane for the encapsulated drug at temperatures in the vicinity of T_m , leading to the release of the drug by passive transfer along a concentration gradient [11]. In the present study, we use TSLs composed of DPPC/DSPC/DPPG₂ (50/20/30 mol/mol) (DPPG₂-TSL) as proposed by Lindner *et al.* [15]. The phase transition takes place at $T_m \sim 42^\circ\text{C}$, i.e., above mammalian body temperature [16,17]. This mixture proved to be more stable in serum than the more generally used Lyso-PC-containing TSL formulations [18] and showed a prolonged circulation time in rodents [15,19] and cats [20]. Hence, DPPG₂-TSLs seem well suited for *in-vivo* applications in clinical settings.

Recent release studies have noted that body fluids such as plasma or serum can have a profound effect on the transition temperature of liposomes and the efficiency of drug release [21,22]. It is thought that protein opsonization and/or penetration of proteins into the lipid bilayer are responsible for these changes, which usually shift T_m to lower values by destabilizing the membrane. (**Figure 1A**) [23,24]. In light of the therapeutic implications and safety issues raised by uncontrolled release, investigation of these alterations in T_m is extremely important for the translatability of *in-vitro* studies into clinical practice. In addition, the formation of a protein corona can affect both the circulation time of a drug carrier and its final destination, e.g., resulting in many cases in unwanted uptake by the liver or spleen.

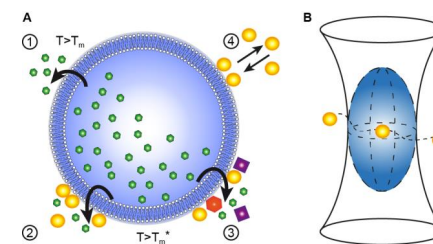


Figure 1: **A** Pictogram that illustrates the experimental setting and the processes studied: Release of dye (green hexagons) from liposomes in buffer (1), in the presence of a specific plasma protein (2, yellow spheres) and in the presence of whole plasma (3, mixed colors). The

reversible binding of selected plasma proteins to DPPG₂-TSL (4) was also studied. **B** The confocal volume in an FCS experiment: Fluorescently labeled particles diffuse through the confocal volume, leading to fluctuations in the fluorescence intensity (not drawn to scale), from which several physical parameters of interest, such as particle concentration and size, can be determined.

The standard way to determine the temperature response of a TSL formulation is to measure changes in the fluorescence intensity of released carboxyfluorescein (CF) by fluorescence spectroscopy (FS) [25,26]. This assay is based on the assumption that the concentration of CF inside the liposome is so high that the fluorescent molecules are self-quenched, and dequench only after release from the liposome [27,28].

In our assay for the quantification of release, we instead combine fluorescence correlation spectroscopy (FCS) with the use of fluorescein di- β -D-galactopyranoside (FDG). FDG is non-fluorescent, and formation of the fluorescein emitter requires the membrane-impermeable enzyme β -galactosidase (β -Gal). Thus, as long as FDG is confined within the liposomes, no signal will be detected (**Figure 2B, I**). If β -Gal is added to the dispersion, free FDG is cleaved and the resulting fluorescence can be characterized, and the levels of release measured, with high sensitivity by FCS (**Figure 2B, II and III**). This technique is an established method that allows one to determine not only concentrations of fluorescent particles in the pico- to nanomolar range (10^{-12} - 10^{-9} M, **Figure S1**), but also their diffusion coefficients, hydrodynamic radii and binding or cleavage interactions [29-34] – even in complex media like plasma or serum [35,36]. Diffusion of the fluorescently labeled particles through the confocal volume induces fluctuations in the fluorescence signal (**Figure 1B**). A model fit to the time correlation of the signal yields the physical characteristics mentioned above. Its flexibility makes FCS an ideal method for characterizing TSLs, their release behavior and their interaction with proteins.

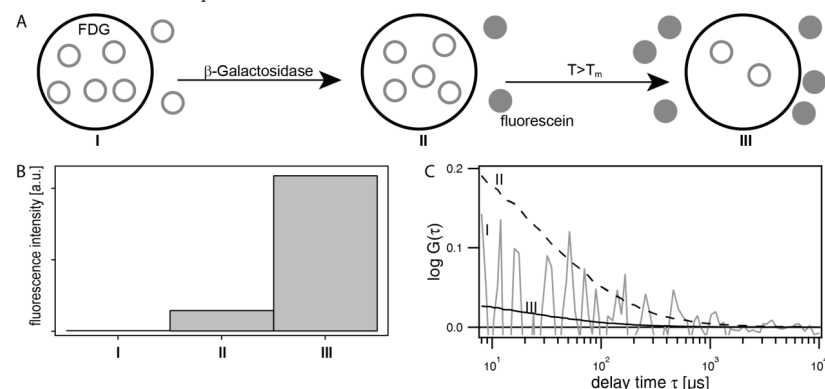


Figure 2: **A** Experimental set-up. FDG within the TSL is non-fluorescent. FDG that was not removed during purification of TSLs is also shown (I). β -Galactosidase hydrolyzes external FDG, generating the strongly fluorescent compound fluorescein (II), and subsequently allows one to monitor the temperature-dependent release of FDG from TSLs (III). **B** Count rates for scenarios I-III. In the absence of β -Gal, the fluorescence is indistinguishable from background noise (I). For II a weak signal from the FDG that was not removed by purification is observed. For III a high signal is obtained due to the large amount of FDG that is released at $T > T_m$. **C** Corresponding fluorescence correlation curves.

However, the potential of FCS for measurements of physicochemical parameters of TSLs and the quantification of drug release has not yet been fully exploited. Earlier publications focused on single features such as the interaction of proteins and liposomes [35,37] or the leakage or release of dyes from liposomes [38-41], but so far no study has attempted to characterize both of these processes simultaneously. However, understanding the interaction of liposomes with their protein environment and quantifying levels of unwanted release of drug molecules are vital prerequisites for the successful pharmaceutical development of targeted, liposome-based drug-delivery systems.

Here we study the effects of plasma proteins on the phase-transition temperature $T_m^{(*)}$ of DPPG₂-TSLs and the temperature-dependent release of cargo molecules. We use FDG encapsulated in DPPG₂-TSLs combined with FCS to quantify the molar release ratio of FDG per DPPG₂-TSL for four representative plasma proteins. In a second set of experiments we use FCS to measure the binding isotherms of the four plasma proteins to DPPG₂-TSL and determine their equilibrium binding constants. We show that FCS is capable of quantifying the release profile in buffer and allows for measurements in blood plasma. The FCS data confirm that the temperature of release is shifted in the presence of mouse plasma, but remains largely unaffected by rat and human plasma and by fetal bovine serum (FBS).

Materials and Methods

Chemicals

All lipids were obtained from Corden Pharma Switzerland LLC. The phospholipid DPPG₂ was synthesized as described before [42]. FDG and β -Gal were supplied by AAT Bioquest and Merck Millipore, respectively.

FBS (Gibco, Life Technologies), human plasma (from a volunteer donor) and animal plasma (Sera Laboratories) were aliquoted, stored at -20°C and thawed in a water bath at 37°C before use. For calibration of the FCS assay, Alexa 488 and Alexa 543 (Invitrogen, Life Technologies) and eGFP were used. All other chemicals and proteins were purchased from Sigma Aldrich GmbH, Carl Roth GmbH, Invitrogen or YoProteins. Proteins were dissolved in PBS as recommended by the suppliers and further diluted as required with HEPES-buffered saline (HBS, 20 mM HEPES, 150 mM NaCl, pH 7.4) supplemented with 1 mM MgCl_2 .

Preparation and characterization of TSLs

DPPG₂-TSLs were prepared and characterized by DLS as described in detail elsewhere [16,17]. In brief, the hydrodynamic diameter (z-average), size vs. intensity distribution plot and zeta-potential were determined by DLS using a Zetasizer Nano ZS (Malvern Instruments, Worcestershire, UK). The instrument was calibrated with a Nanosphere™ size standard (125 nm, Thermo Fisher Scientific, Waltham, MA, USA). Phospholipid composition was determined by phosphate analysis [42].

Fluorescence spectroscopy

Fluorescence intensity was measured with a Cary Eclipse fluorescence spectrometer (Varian Inc., Palo Alto, CA, USA) at room temperature (excitation/emission: 493/513 nm) and analyzed as described before [18]. The extent of cargo release was determined using the formula: $\text{Release } [\%] = (I(T) - I_0) / (I_{\text{end}} - I_0) * 100$, where $I(T)$ is the fluorescence intensity at the temperature T and I_0 is the background signal at room temperature. I_{end} is the signal obtained after treatment of a sample with 10% Triton X-100, which disrupts the liposomes, resulting in complete release of their contents.

To determine the temperature dependence of FDG release, the TSL stock solution was first diluted 1:50 (vol/vol) with 0.9% NaCl (=VL). A 100- μ l sample of VL was further diluted 1:10 (vol/vol) with FBS or HBS + 1 mM MgCl₂ (pH 7.4), and 20 μ l-aliquots of this solution were incubated at temperatures ranging from 37-45°C for 5 min in a thermocycler. Then ice-cold Tris solution (pH 7.4, 1 ml) was added to stop the reaction. A mixture of 100 μ l of VL and 100 μ l of 10% Triton that had been incubated for 15 min at 45°C and then diluted with 900 μ l of 0.9% NaCl served as the positive control (=TL). FDG release was measured by FS after adding to 20 μ l TL to 1 ml Tris. Prior to measurement, 100 μ l β -Gal (5.12 U/ml) was added to each sample and incubated for 30 min at room temperature in the dark.

Fluorescence Correlation Spectroscopy

Measurements were performed on an Axiovert 100 microscope equipped with a ConfoCor2 unit (Carl Zeiss Jena, Germany), an argon laser (488 nm), a helium-neon laser (543 nm) and an apochromatic 40x water-immersion objective with NA of 1.2 (Carl Zeiss Jena, Germany). Fluorescence emission was separated from excitation light by using the appropriate band-pass filters (500-530 nm and 560-615 nm, respectively). All measurements were performed at room temperature (22°C). NUNC 8-well slides (Thermo Scientific) and sample volumes of 200 μ l were used for release measurements.

In order to monitor the temperature-dependent release of FDG from liposomes the TSL stock solution was diluted 1:150 (vol/vol) with the appropriate medium (buffer, plasma, or protein solution), and 20 μ l-samples were incubated at defined temperatures between 37°C and 45°C for 5 min in a thermocycler (Eppendorf). The reaction was stopped by adding 175 μ l HBS + 1 mM MgCl₂ and 5 μ l β -Gal (51.2U/ml) that had been stored on ice. The samples were then incubated for 30 min at room temperature in the dark prior to analysis by FCS. As the positive control (complete release), a solution containing 20 μ l of diluted TSL and 20 μ l 10% Triton X100 was incubated for 15 min at 45°C, then 155 μ l of ice-cold HBS + 1 mM MgCl₂ and 5 μ l β -Gal (51.2 U/ml) were added and the samples were incubated for 30 min at room temperature in the dark.

Analysis of FCS data

The one-component fitting function

$$G(\tau) = 1 + \frac{1}{N} \left(1 + \frac{\tau}{\tau_D}\right)^{-1} \left(1 + \frac{\tau}{S^2 \tau_D}\right)^{-1/2}$$

is used to fit the correlation data from the FCS measurements for samples containing only one fluorescent species. The fit parameters N and τ_D are variables, and the structure parameter S was determined from the calibration with a solution containing eGFP in FBS or Alexa dye in HBS + 1 mM MgCl₂. Corrections for expansion of the confocal volume in the presence of Triton or FBS were applied (see **SI**). The finite size correction was used for size analysis of TSLs [43].

The hydrodynamic radius R_h of a spherical molecule can be determined with the Stokes-Einstein equation (see **SI**). Fitting of a sigmoidal function to the temperature-dependent release allows one to estimate the phase transition temperature T_m^* .

Measurements of protein binding by FCS

Measurement chambers (Sensoplate plus, 384-well plate, Greiner Bio-One) were precoated with 5 mg/ml BSA for 1 h to avoid unwanted adsorption of proteins to the walls. Afterwards the chambers were rinsed with MilliQ water to remove unbound BSA.

The samples were measured and analyzed essentially as described previously [37,44]. First we measured samples of the proteins labeled with Alexa 488 in the absence of DPPG₂-TSLs, in order to determine the size (τ_{D1}) and number (N_0) of particles present. Then the DPPG₂-TSLs were added and the samples were measured after 1 h of incubation. To determine the fraction of bound protein, we used a two-component fit (see **SI**). The diffusion time of the free protein was fixed to the value τ_{D1} . The diffusion time of the protein bound to TSLs τ_{D2} was treated as a free parameter. The fraction bound was then determined using the equation

$$fraction\ bound = 1 - \frac{N_{unbound}}{N_0} = 1 - \frac{N \cdot F_1}{N_0}$$

where N is the total number of particles in the confocal volume after the addition of TSLs, F_1 is the fraction of unbound fast diffusing protein in solution and N_0 is the initial number of proteins in the sample.

The K_D values were determined with fitting to a Hill-equation, and the reversibility of the binding was tested by adding FBS to the protein-TSL solutions and incubating for a further hour prior to measurement.

Statistical analysis

The data are expressed as the mean \pm standard deviation of at least three independent experiments.

Results and Discussion

Characterization of the TSLs

In order to ensure that there is no uncontrolled release due to changes of medium and in order to be able to quantify the release with precision later on, we first characterized the behavior of DPPG₂-TSLs containing the encapsulated dye in different media.

DPPG₂-TSLs were prepared with various payloads and with or without a membrane label depending on the experiment, and standard parameters such as z-potential, phosphate content and size were determined for each condition (see **Table 1**). The results of the size measurements by DLS and FCS in buffer (0.9% NaCl) show good agreement for TSLs with the rhodamine membrane label ($D_{h, DLS} = 105$ nm vs. $D_{h, FCS} = 96.1 \pm 4.1$ nm). At the same time, we evaluated the concentration of TSLs in a standard sample to be 0.28 nM using an excitation of $\lambda_{ex} = 543$ nm. In contrast to DLS, FCS can be used to measure the size distribution of DPPG₂-TSLs not only in buffer but also in complex fluids such as FBS. FCS selectively detects the fluorescently labeled DPPG₂-TSL and thus avoids interfering signals by other components of the fluid [45]. Characterization under essentially physiological conditions is important, given that we wish to learn about the stability of DPPG₂-TSLs and possible obstacles to their use for drug delivery in living organisms. Therefore, we chose FCS to measure the DPPG₂-TSL size in FBS. For FCS measurements with $\lambda_{ex} = 488$ nm we use TSL with CF as a payload to determine the size of the liposomes. We obtain a hydrodynamic diameter (99.1 ± 4.1 nm) that is in good agreement with the values determined in buffer (see **Table 1**). This confirms that FBS has no significant effect on DPPG₂-TSL size.

After characterization of the DPPG₂-TSLs, we sought to measure release from the liposomes with high precision by FCS. This requires that the released substance – here, CF – yields a clear signal that is not obscured by non-released substances or buffer components. The simplest way to perform such an experiment is to load the carrier – in our case the TSL – with the cargo CF. The dye in the TSL should diffuse significantly more slowly than the released dye, permitting unambiguous discrimination between the two signals. Due to significant differences in the brightness of a single free dye molecule relative to that of a filled TSL,

precise analysis of the dynamics of release is quite complex and does not provide single-molecule resolution. To overcome this limitation, we developed a novel assay to measure release from TSLs. The underlying idea is to load into the TSL a dye that becomes fluorescent only after being released. Here, the only signal measured in the FCS experiments is that originating from the released dye (see **Figure 2**). As a result, the correlation curve is not compromised by the presence of fluorescent TSLs. To achieve this improvement in signal resolution, we chose FDG as the cargo, as it only becomes fluorescent when cleaved by β -Gal following its release (**Figure S2**).

Cargo	100 mM CF	1 mM FDG	Empty
Membrane label	RhPE	-	-
Phosphate concentration [mM]	41.5	38	45
Z-potential [mV]	-28.5	-25.9	-30.5
DLS diameter [nm]	105	114	105
z-average			
PDI	0.068	0.134	0.083
FCS D_h [nm], ex. 488 nm	82.6 \pm 5.4	-	-
FCS D_h [nm], ex. 543 nm	96.1 \pm 4.1	-	-
FCS D_h [nm], ex. 488 nm in FBS	99.1 \pm 4.1	-	-

Table 1: Characterization of different types of DPPG₂-TSL by DLS and FCS measurements. FCS data are averages (\pm standard deviation) of three independently prepared samples. PDI, polydispersity index; D_h , hydrodynamic diameter.

Encapsulation and purification efficiency

Loading of DPPG₂-TSL is performed in highly concentrated FDG solution (1 mM). Subsequently, the excess dye was removed by filtration through Sephadex columns. As a control we measured the level of fluorescent dye associated with the purified TSLs. This measurement after purification yields a weak signal of FDG corresponding to a concentration of 3.36 nM of non-encapsulated FDG in the sample solution, which contains 0.28 nM TSLs (**Figure 2, II**). Hence, in order to quantify the absolute release in the following experiments, this offset value has to be applied as a correction. Otherwise, adventitious release, at low temperatures in particular, leads to serious overestimates of the magnitude of induced release.

We determined the encapsulation efficiency of the TSL in two different ways. In both cases, we calculated the ratio of the experimental to the theoretical value. Firstly, we used the common definition of the cargo/lipid ratio in terms of the molar concentrations of each. We obtain a value of $8.0 \pm 0.7\%$. This value seems surprisingly low. So we decided to compare the measured amount of [fluorescein]/[TSL] to a theoretical estimate of this value. Using this approach, we obtain an encapsulation efficiency of $53.7 \pm 9.4\%$. Intuitively, this value seems more likely. Both calculations are presented in detail in the **SI**. The difference arises from the different definitions of the encapsulation efficiency. While the cargo/lipid ratio is suited for drugs that bind to the lipid membrane, the definition of drug/TSL is more appropriate for cargo that remains free in solution, such as FDG.

Measurements of release in buffer and plasma

With knowledge of the offset concentration of FDG, it can be corrected with great precision, allowing us to study the concentration of the temperature-dependent release of FDG.

At temperatures around 42°C, TSLs are expected to undergo a phase transition that disrupts membrane integrity, which should result in release of the loaded FDG. In order to actively

induce release, the DPPG₂-TSL solution was heated to temperatures ranging from 37-45°C. To provide constant measurement conditions, the liposome solution was then cooled down to 4°C. After cooling, β -Gal was added and FCS was performed at room temperature (22°C). Addition of β -Gal after cooling ensures that the enzyme is unable to cross the membrane and no FDG inside the TSL is hydrolyzed. The concentration of FDG in the external medium was determined from the FCS curve and is expressed relative to the concentration of TSL in the dispersion, i.e. as [fluorescein]/[TSL] in the following.

With this assay we measured the amounts of cargo released at various temperatures, as displayed in **Figure 3A** (raw data in **Figure S3 and S4**). We find no release up to 37°C, and release is first detected at 38°C. The amount of FDG released then increases with increasing temperature, yielding an S-shaped curve that reaches saturation at around 43°C. As a control, we measured the release induced by Triton, which completely disrupts the TSL membranes leading to release of all FDG molecules. Within the margin of error, the measured value is equal to the saturation value for release at high temperatures. Hence, we can conclude that all FDG is released from the liposomes at temperatures above 43°C.

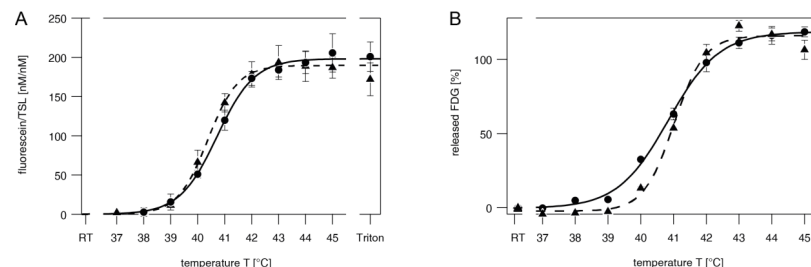


Figure 3: Temperature-dependent release of fluorescein from FDG-loaded DPPG₂-TSLs in HBS + 1 mM MgCl₂ (triangles, dashed line) and FBS (circles, line). A Molar ratio of fluorescein released per DPPG₂-TSL measured using FCS. B Relative fluorescence intensity compared to total release determined by fluorescence spectroscopy (FS).

To further evaluate the performance of the FCS-based assay, we compare the results with conventional FS data. **Figure 3B** shows the relative change in fluorescence normalized with respect to the Triton value. Both release profiles (**Figures 3A and B**) follow the same trend of strongly increasing release around a critical temperature of 40-41°C, saturation at temperature about 43°C, and barely detectable release below 40°C, indicating that the membrane is practically impermeable within this last temperature range. FCS data determine the molar ratio of FDG molecules released per liposome, while FS data show the total fluorescence intensity and hence the amount of FDG release relative to the total release caused by membrane disintegration upon addition of Triton. Note that the data shown in **Figure 3B** exceed 100% and shift below 0%. This is an intrinsic artefact of the FS approach, which is due to impact of Triton on the brightness of the dye and therefore on the normalization. We can reproduce these values when we perform the same analysis as for FS using the count rates measured with FCS (**Figure S4**). In FCS experiments, we observed that the level of emission by the dye molecules was decreased compared to a solution without Triton (see **Figure S5**). Due to this observation, we assume that methods that solely rely on the analysis of changes in fluorescence intensity in the presence of Triton, which is often used to determine release behavior [25,26], are not optimally suited for highly precise measurements, at least not for fluorescein. The FCS method employed here may provide a more reliable alternative, since it measures absolute concentrations and does not depend solely on absolute brightness measurements. This is especially useful for determinations of spurious release.

Next, we measured temperature-dependent release in the more physiologically relevant medium FBS. Here, the release curves are similar to those in buffer, irrespective of the measurement technique employed, showing that FBS does not influence temperature-dependent release significantly (**Figure 3**, circles).

In further drug development for use in humans, animal testing plays an important role. Therefore, we measured the release in the presence of mouse, rat and human plasma and compared it to the data for FBS (**Figure 4**). Corresponding FS data are shown in **Figure S6**. For FBS, human and rat plasma we observe the same general trend. Strikingly, for mouse plasma we observe a marked deviation from the other curves, characterized by significant release even at 37°C. This behavior was previously reported by Hossann *et al.* [18]. One possible cause is the increased lyso-lipid content of mouse plasma [46,47].

To test this hypothesis, we supplemented human plasma with Lyso-PC to generate a level that is comparable to that of mouse plasma. Upon addition of Lyso-PC, we observe a slight shift of the release curve towards lower temperatures, relative to human plasma without Lyso-PC. Similarly, the onset of release in mouse plasma is shifted to lower temperatures relative to plasma from other mammals. However, the effect in mouse plasma is much more pronounced than in human plasma enriched in Lyso-PC, indicating that Lyso-PC might contribute to this phenomenon, but does not explain it entirely.

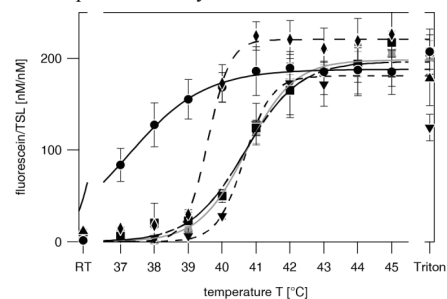


Figure 4: Effect of plasma on the temperature-dependent release profile: mouse plasma (circles), rat plasma (squares), human plasma (inverted triangles), human plasma doped with Lyso-PC (diamonds) and fetal bovine serum (asterisks, gray trace).

Release measurements in monodisperse protein solutions

Given that plasma consists of many components, a multitude of molecules or molecular interactions could conceivably contribute to this difference in human and mouse plasma. To better understand these observations, we evaluated the effect of several prominent blood proteins on release by using single-protein solutions as the external medium (**Figure 5**).

We chose to test the plasma proteins serum albumin (SA), transferrin (Tf), apolipoprotein A1 (ApoA1) and fibrinogen (Fib). The release of FDG from DPPG₂-TSLs was evaluated in 15.2 μ M SA, 12.6 μ M Tf, 1.7 μ M Fib and 7.1 μ M ApoA1. We decided to use lower concentrations of Fib and ApoA1 because they have been observed to bind strongly to drug nanocarriers in other studies [48–50].

Compared to the results in the absence of proteins, SA and Fib cause more pronounced release at lower temperatures, while ApoA1 seems to impede release (see **Figure 5**). The shift in the release of SA was described before. It is assumed that the adsorbed protein affects the integrity of the membrane by partial penetration [51–53]. A similar explanation can account

for the change in release behavior induced by ApoA1. ApoA1 probably acts to seal the packing defects that form in the membrane, thereby reducing cargo release from DPPG₂-TSL. Tf seems to have only a minor influence on release relative to cargo loss in pure buffer.

In plasma the observed effects of the single proteins seem to largely compensate for each other. However, they might contribute to the differences observed between the kinetics of release in plasma of different species (**Figure 4**).

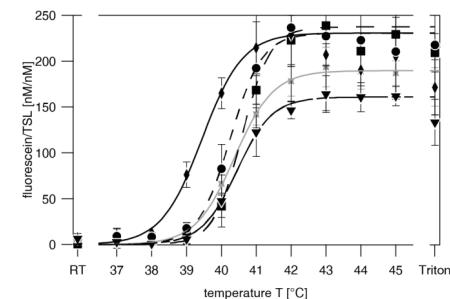


Figure 5: Temperature-dependent molar release in the presence of specific proteins from plasma: SA (diamonds), transferrin (squares), fibrinogen (circles) and apolipoprotein A1 (triangles). For reference, the release profile in HBS + 1 mM MgCl₂ is shown in gray (asterisks).

Binding of proteins to TSLs

Next, we evaluated the binding behavior of these plasma proteins to check whether there is any relationship between the effects of the proteins on release and their affinities for the TSLs. FCS allows us to determine the dissociation constant K_D for binding of fluorescently Alexa 488-labeled proteins, and is therefore well suited to the study of binding behavior, especially for strong binders, as shown before [37,44,54] (**Figure S8**). The results of titration series of DPPG₂-TSL for the various proteins are shown in **Figure 6**. For analysis we used a Hill-equation instead of the law of mass action, because the number of available ligands, i.e. binding sites on the DPPG₂-TSL, is much larger than the number of receptors, i.e. the mole fraction of the labeled protein, in agreement with Rusu *et al.* [37]. The results of the analysis are summarized in **Table 2**. For ApoA1 we observe strong binding, with a binding constant two orders of magnitude higher than those for the other proteins. This strong binding may explain why ApoA1 was the only protein tested that reduced the efficiency of release. A reduction in release can presumably be achieved by efficient binding and blocking of packing defects. Of the three other proteins with weaker binding constants, only serum albumin strongly affects release. As described above, SA is suggested to increase the permeability of the liposome bilayer, which leads to enhanced release, while its weak binding prevents the high surface coverage that might well reduce this effect.

To test the reversibility of binding, we added FBS to the TSL-protein mixtures after incubation and monitored the kinetics of protein detachment (**Figures S9 and S10**). Reversibility experiments provide a means to exclude or identify the proteins that are mainly responsible for the changes in release kinetics in plasma. All four tested proteins desorbed from the liposomes after addition of FBS. SA, Fib and Tf were immediately displaced, while ApoA1 detached from the liposomes over the course of 1 h (**Figure S10**). One explanation for this effect might be that other biomolecules in FBS have a much higher affinity for the

liposomes than the tested proteins, and therefore replace the labeled proteins on the surface of the liposomes. Alternatively, molecules that bind more strongly to the DPPG₂-TSLs than do the test proteins (other than ApoA1) may be present in the FBS solution and thus displace them from the liposomes. A combination of the two effects is also possible. The detachment of the proteins from the DPPG₂-TSL in FBS explains why we did not observe their impacts on temperature-dependent release in the presence of FBS.

Interestingly, ApoA1 was removed slower from the DPPG₂-TSL than the other proteins. By using higher concentrations of ApoA1 for incubation, this could be employed as a natural coating for the TSL. In this way, it might be possible to increase circulation times as apolipoproteins are stated to prevent opsonization [47] and improve targeting of DPPG₂-TSL by increasing their selectivity. Similar tests could be performed for other substances as well.

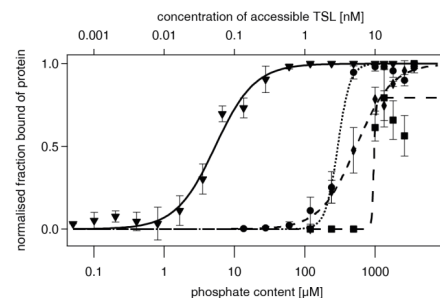


Figure 6: Binding isotherms of Alexa 488-labeled proteins to DPPG₂-TSL (normalized data). The concentration of the labeled proteins was kept constant while the concentration of TSL was varied; ApoA1 (inverted triangles), fibrinogen (circles), SA (diamonds) and transferrin (squares).

protein	Apolipoprotein A1	Fibrinogen	Serum albumin	Transferrin
K_D [nM]	0.053±0.004	2.951±0.174	5.393±0.405	9.652±0.001
$ \Delta T_m^* $ [°C]	0.01±0.12	0.12±0.11	0.92±0.09	0.21±0.11

Table 2: Dissociation constants K_D and $|\Delta T_m^*|$ of the tested plasma proteins ApoA1, Fib, SA and Tf. $|\Delta T_m^*|$ is the absolute difference between the T_m^* determined in protein solution and in pure buffer.

Conclusion

We have used a novel and highly sensitive assay based on FCS to quantify the temperature-dependent release of the contents of dye-loaded TSL. We validated the FCS approach by measuring the temperature release profile of FDG-loaded DPPG₂-TSL and comparing it to standard fluorescein FS studies. The FCS-based assay is superior with regard to determining spurious release at temperatures lower than the T_m . Assessment of low drug release is important to ensure that TSL membranes remain sealed at room temperature, which is a prerequisite both for controlling the dosage dispensed and avoiding non-specific delivery to healthy tissue. In addition, the FCS-based approach yields information on size and encapsulation efficiency, as well as interactions of TSLs with blood proteins. Here we have been able to monitor, for the first time, the binding of standard blood components to DPPG₂-TSL as well as the resulting shift in the critical release temperature. Surprisingly, only one of

the tested proteins (SA) induced such a shift, while others (Fib, ApoA1, Tf) bound but did not affect the temperature profile of release. Likewise plasma derived from human and rat, and whole bovine serum, had no effect in the temperature profile, in stark contrast to mouse plasma. Hence there seems to be no systematic relationship between binding affinity and shift in the temperature of release, yet protein binding is very probably an essential prerequisite for any change in the intrinsic thermal properties of TSL upon contact with body fluids. The assay is applicable to a broad field of possible interactions of liposomes with their environment such as interactions with specific proteolytic plasma cascades, to screen for the suitability of TSLs for medical use. A better understanding of protein adsorption to TSL and drug-delivery liposomes in general will facilitate the design of alternative membrane coatings based on combinations of plasma proteins. Such synthetic coronas are biocompatible, and could possibly prevent further opsonization and increase circulation time. To this end, quantitative biophysical assays for multiple protein-membrane interaction parameters will be instrumental for the elaboration of improved targeting strategies.

Acknowledgements: TP, JJM, JOR acknowledge Nanosystems Initiative Munich. JJM and TP were funded by the European Union Seventh Framework Programme (FP/2007-2013) under NMP4-2010-266737 (NanoTransKinetics).

Conflict of interest: MH holds shares in Thermosome GmbH, Planegg/Martinsried, Germany. All other authors declare no conflict of interest.

Appendix A: Supplementary information

References

- [1] G. Gregoriadis, B.E. Ryman, Liposomes as carriers of enzymes or drugs: a new approach to the treatment of storage diseases., *Biochem. J.* 124 (1971) 58.
- [2] G. Gregoriadis, Drug entrapment in liposomes., *FEBS Lett.* 36 (1973) 292–296.
- [3] Y. Perrie, Gregory Gregoriadis: Introducing liposomes to drug delivery., *J. Drug Target.* 16 (2008) 518–519.
- [4] D.D. Lasic, Doxorubicin in sterically stabilized liposomes, *Nature.* 380 (1996) 561–562.
- [5] D.D. Lasic, D. Needham, The “stealth” liposome: A prototypical biomaterial, *Chem. Rev.* 95 (1995) 2601–2628.
- [6] M. Slingerland, H. Guchelaar, H. Gelderblom, Liposomal drug formulations in cancer therapy : 15 years along the road, *Drug Discov. Today.* 17 (2012) 160–166.
- [7] A.H. Sarris, F. Hagemester, J. Romaguera, M.A. Rodriguez, P. McLaughlin, A.M. Tsimberidou, et al., Liposomal vincristine in relapsed non-Hodgkin’s lymphomas : Early results of an ongoing phase II trial, *Ann. Oncol.* 11 (2000) 69–72.
- [8] M.A. Rodriguez, R. Pytlik, T. Kozak, M. Chanabhai, R. Gascoyne, B. Lu, et al., Vincristine sulfate liposomes injection (Marqibo) in heavily pretreated patients with refractory aggressive non-Hodgkin lymphoma, *Cancer.* 115 (2009) 3475–3482.
- [9] B.J. Wood, R.T. Poon, J.K. Locklin, M.R. Dreher, K.K. Ng, M. Eugeni, et al., Phase I Study of Heat-Deployed Liposomal Doxorubicin during Radiofrequency Ablation for Hepatic Malignancies, *J Vasc Interv Radiol.* 23 (2012) 248–255.
- [10] T.M. Zagar, Z. Vujaskovic, S. Formenti, H. Rugo, F. Muggia, B.O. Connor, et al., Two phase I dose-escalation / pharmacokinetics studies of low temperature liposomal doxorubicin (LTLD) and mild local hyperthermia in heavily pretreated patients with local regionally recurrent breast cancer, *Int J Hyperth.* 6736 (2014) 285–294.
- [11] B. Kneidl, M. Peller, G. Winter, L.H. Lindner, M. Hossann, Thermosensitive liposomal drug delivery systems: state of the art review., *Int. J. Nanomedicine.* 9 (2014) 4387–4398.

- [12] A.A. Manzoor, L.H. Lindner, C.D. Landon, J. Park, A.J. Simnick, M.R. Dreher, et al., Overcoming limitations in nanoparticle drug delivery : Triggered, intravascular release to improve drug penetration into tumors, *Cancer Res.* 72 (2012) 5566–5576.
- [13] M. De Smet, E. Heijman, S. Langereis, N.M. Hijnen, H. Grull, Magnetic resonance imaging of high intensity focused ultrasound mediated drug delivery from temperature-sensitive liposomes: An in vivo proof-of-concept study, *J. Control. Release.* 150 (2011) 102–110.
- [14] A.H. Negussie, P.S. Yarmolenko, A. Partanen, A. Ranjan, G. Jacobs, D. Woods, et al., Formulation and characterisation of magnetic resonance imageable thermally sensitive liposomes for use with magnetic resonance-guided high intensity focused ultrasound, *Int. J. Hyperth.* 27 (2011) 140–155.
- [15] L.H. Lindner, M.E. Eichhorn, H. Eibl, N. Teichert, M. Schmitt-Sody, R.D. Issels, et al., Novel temperature-sensitive liposomes with prolonged circulation time, *Clin. Cancer Res.* 10 (2004) 2168–2178.
- [16] M. Hossann, M. Wiggenhorn, A. Schwerdt, K. Wachholz, N. Teichert, H. Eibl, et al., In vitro stability and content release properties of phosphatidylglycerol containing thermosensitive liposomes, *Biochim. Biophys. Acta - Biomembr.* 1768 (2007) 2491–2499.
- [17] M. Hossann, T. Wang, M. Wiggenhorn, R. Schmidt, A. Zengerle, G. Winter, et al., Size of thermosensitive liposomes influences content release, *J. Control. Release.* 147 (2010) 436–443.
- [18] M. Hossann, Z. Syunyaeva, R. Schmidt, A. Zengerle, H. Eibl, R.D. Issels, et al., Proteins and cholesterol lipid vesicles are mediators of drug release from thermosensitive liposomes., *J. Control. Release.* 162 (2012) 400–406.
- [19] S. Limmer, J. Hahn, R. Schmidt, K. Wachholz, A. Zengerle, K. Lechner, et al., Gemcitabine treatment of rat soft tissue sarcoma with phosphatidylglycerol-based thermosensitive liposomes, *Pharm. Res.* 31 (2014) 2276–2286.
- [20] K. Zimmermann, M. Hossann, J. Hirschberger, K. Troedson, M. Peller, M. Schneider, et al., A pilot trial of doxorubicin containing phosphatidylglycerol based thermosensitive liposomes in spontaneous feline soft tissue sarcoma, *Int. J. Hyperth.* (2016).
- [21] R.L. Juliano, F. Bonté, Interactions of liposomes with serum proteins, *Chem. Phys. Lipids.* 40 (1986) 359–372.
- [22] M.H. Gaber, K. Hong, S.K. Huang, D. Papahadjopoulos, Thermosensitive sterically stabilized liposomes: Formulation and in vitro studies on mechanism of doxorubicin release by bovine serum and human plasma, *Pharm. Res.* 12 (1995) 1407–1416.
- [23] T. Hosokawa, M. Sami, Y. Kato, E. Hayakawa, Alteration in the temperature-dependent content release property of thermosensitive liposomes in plasma., *Chem. Pharm. Bull. (Tokyo).* 51 (2003) 1227–1232.
- [24] T.M. Allen, L.G. Cleland, Serum-induced leakage of liposome contents, *Biochim. Biophys. Acta.* 597 (1980) 418–426.
- [25] J.N. Weinstein, S. Yoshikami, P. Henkart, R. Blumenthal, W.A. Hagis, Liposome-cell interaction: Transfer and intracellular release of a trapped fluorescent marker, *Science (80-)*. 2 (1977) 489–492.
- [26] J. Barbet, P. Machy, A. Truneh, L.E.E.D. Leserman, Weak acid-induced release of liposome-encapsulated carboxyfluorescein, *Biochim. Biophys. Acta.* 772 (1984) 347–356.
- [27] M. Ausborn, H. Schreier, G. Brezesinski, H. Fabian, H.W. Meyer, P. Nuhn, The protective effect of free and membrane-bound cryoprotectants during freezing and freeze-drying of liposomes, *J. Control. Release.* 30 (1994) 105–116.
- [28] J.H. Crowe, L.M. Crowe, Factors affecting the stability of dry liposomes., *Biochim. Biophys. Acta.* 939 (1988) 327–34.
- [29] P. Schwille, E. Hausteil, Fluorescence correlation spectroscopy. An introduction to its concepts and applications, *Biophys. Textb. Online.* (2001) 1–33.
- [30] J.A. Fitzpatrick, B.F. Lillemeier, Fluorescence correlation spectroscopy: linking molecular dynamics to biological function in vitro and in situ, *Curr Opin Struct Biol.* 21 (2011) 650–660.
- [31] R. Rigler, E. Elson, Fluorescence correlation spectroscopy: theory and applications, Springer, Berlin ; New York, 2001.
- [32] D. Magde, E.L. Elson, W.W. Webb, Fluorescence correlation spectroscopy. II. An experimental realization, *Biopolymers.* 13 (1974) 29–61.
- [33] D. Magde, W.W. Webb, E.L. Elson, Fluorescence correlation spectroscopy. III. Uniform translation and laminar flow, *Biopolymers.* 17 (1978) 361–376.
- [34] E.L. Elson, D. Magde, Fluorescence correlation spectroscopy. I. Conceptual basis and theory, *Biopolymers.* 13 (1974) 1–27.
- [35] H. Engelke, I. Dorn, J.O. Rädler, Diffusion and molecular binding in crowded vesicle solutions measured by fluorescence correlation spectroscopy, *Soft Matter.* 5 (2009) 4283–4289.
- [36] S. Lippok, M. Radtke, T. Obser, L. Kleemeier, R. Schneppenheim, U. Budde, et al., Shear-induced unfolding and enzymatic cleavage of full-length VWF multimers, *Biophys. J.* 110 (2016) 545–554.
- [37] L. Rusu, A. Gambhir, S. McLaughlin, J. Rädler, Fluorescence correlation spectroscopy studies of peptide and protein binding to phospholipid vesicles., *Biophys. J.* 87 (2004) 1044–1053.
- [38] K. Kristensen, J.R. Henriksen, T.L. Andresen, Quantification of leakage from large unilamellar lipid vesicles by fluorescence correlation spectroscopy, *Biochim. Biophys. Acta - Biomembr.* 1838 (2014) 2994–3002.
- [39] A. Blicher, K. Wodzinska, M. Fidorra, M. Winterhalter, T. Heimburg, The temperature dependence of lipid membrane permeability, its quantized nature, and the influence of anesthetics, *Biophys. J.* 96 (2009) 4581–4591.
- [40] A. Pashkovskaya, E. Kotova, Y. Zorlu, F. Dumoulin, V. Ahsen, I. Agapov, et al., Light-triggered liposomal release: Membrane permeabilization by photodynamic action, *Langmuir.* 26 (2010) 5725–5733.
- [41] A.I. Sorochkina, S.I. Kovalchuk, E.O. Omarova, A.A. Sobko, E.A. Kotova, Y.N. Antonenko, Peptide-induced membrane leakage by lysine derivatives of gramicidin A in liposomes, planar bilayers, and erythrocytes., *Biochim. Biophys. Acta.* 1828 (2013) 2428–2435.
- [42] H. Eibl, Synthesis of glycerophospholipids., *Chem. Phys. Lipids.* 26 (1980) 405–429.
- [43] B. Wu, Y. Chen, J.D. Mu, Fluorescence Correlation Spectroscopy of Finite-Sized Particles, 94 (2008) 2800–2808.
- [44] S. Milani, F.B. Bombelli, A.S. Pitek, K. Dawson, J. Rädler, Reversible versus irreversible binding of transferrin to polystyrene nanoparticles: soft and hard corona, *ACS Nano.* 6 (2012) 2532–2541.
- [45] J. Wolfram, K. Suri, Y. Yang, J. Shen, C. Celia, M. Fresta, et al., Shrinkage of pegylated and non-pegylated liposomes in serum, *Colloids Surfaces B Biointerfaces.* 114 (2014) 294–300.
- [46] A. Raynor, P. Jantschkeff, T. Ross, M. Schlesinger, M. Wilde, S. Haasis, et al., Saturated and mono-unsaturated lysophosphatidylcholine metabolism in tumour cells: a potential therapeutic target for preventing metastases, *Lipids Health Dis.* 14 (2015) 69–84.
- [47] G. Caracciolo, Liposome-protein corona in a physiological environment: Challenges and opportunities for targeted delivery of nanomedicines., *Nanomedicine.* 11 (2015) 543–557.

- [48] A.L. Capriotti, G. Caracciolo, C. Cavaliere, P. Foglia, D. Pozzi, R. Samperi, et al., Do plasma proteins distinguish between liposomes of varying charge density?, *J. Proteomics*. 75 (2012) 1924–1932.
- [49] M.P. Monopoli, D. Walczyk, A. Campbell, G. Elia, I. Lynch, F.B. Bombelli, et al., Physical-chemical aspects of protein corona: relevance to in vitro and in vivo biological impacts of nanoparticles., *J. Am. Chem. Soc.* 133 (2011) 2525–3254.
- [50] M. Lundqvist, J. Stigler, G. Elia, I. Lynch, T. Cedervall, K. Dawson, Nanoparticle size and surface properties determine the protein corona with possible implications for biological impacts., *Proc. Natl. Acad. Sci. U. S. A.* 105 (2008) 14265–14270. doi:10.1073/pnas.0805135105.
- [51] H. Khandelia, J.H. Ipsen, O.G. Mouritsen, The impact of peptides on lipid membranes, *Biochim. Biophys. Acta - Biomembr.* 1778 (2008) 1528–1536.
- [52] I. Zlatanov, A. Popova, Penetration of lysozyme and cytochrome C in lipid bilayer: fluorescent study., *J. Membr. Biol.* 242 (2011) 95–103.
- [53] J. Sabín, G. Prieto, J.M. Ruso, P. V Messina, F.J. Salgado, M. Nogueira, et al., Interactions between DMPC liposomes and the serum blood proteins HSA and IgG., *J. Phys. Chem. B.* 113 (2009) 1655–1661.
- [54] H. Engelke, S. Lippok, I. Dorn, R.R. Netz, J.O. Rädler, FVIII binding to PS membranes differs in the activated and non-activated form and can be shielded by annexin A5., *J. Phys. Chem. B.* 115 (2011) 12963–70.

Supplementary information

Impact of plasma protein binding on cargo release by thermosensitive liposomes probed by fluorescence correlation spectroscopy

Judith J. Mittag^a, Barbara Kneidl^{b,c}, Tobias Preiß^a,
Martin Hossann^d, Gerhard Winter^e, Stefan Wuttke^e, Hanna Engelke^{e,*} and Joachim O. Rädler^{a,*}

^a Department of Physics and Center for NanoScience (CeNS), Ludwig-Maximilians-Universität, Geschwister-Scholl-Platz 1, 80539 München, Germany

^b Department of Internal Medicine III, University Hospital Munich, Ludwig-Maximilians-Universität, München, Germany

^c Department of Pharmacy, Pharmaceutical Technology and Biopharmaceutics, Ludwig-Maximilians-Universität, München, Germany.

^d Thermosome GmbH, Am Klopferspitz 19, 82152 Planegg/Martinsried, Germany

^e Department of Chemistry and Center for NanoScience (CeNS), Ludwig-Maximilians-Universität, Butenandtstraße 5-13(E), 81377 München, Germany

*Corresponding author: hanna.engelke@cup.lmu.de, raedler@lmu.de

Basics of Fluorescence Correlation Spectroscopy Analysis

The normalised correlation function $G(\tau)$ is defined as

$$G(\tau) = \frac{\langle F(t)F(t+\tau) \rangle}{\langle F(t) \rangle^2} \quad (\text{Equation S1}),$$

where angular brackets denote the average over time t , $F(t)$ the fluorescence signal at time t and $F(t + \tau)$ the fluorescence signal at time $t + \tau$.

It is assumed that the confocal volume has an ideal three dimensional Gaussian shape. The ratio of the half axes z_0 to the radius of the laser beam w_0 is called structure parameter ω and is a measure for the size of the confocal volume. Physically relevant information can be extracted from the correlation curve by fitting a model to the experimental data. The autocorrelation curve for a single component freely diffusing in a 3D Gaussian element can be described by:

$$G(\tau) = \frac{1}{N} \left(\frac{1}{1+\tau/\tau_D} \right) \left(\frac{1}{1+\omega^2\tau/\tau_D} \right)^{\frac{1}{2}} + 1 \quad (\text{Equation S2})$$

where N is the number of particles inside the confocal volume, τ_D is the translational diffusion time of the species, τ is the correlation time and ω the structure parameter.

The translational diffusion time τ_D describes the average dwell time of a molecule with diffusion constant D in the confocal volume.

$$\tau_D = \frac{\omega_0^2}{4D} \quad (\text{Equation S3}).$$

For samples containing more than one component, the following equation is applicable

$$G(\tau) = \frac{\sum q_i^2 N_i^2 g_i(\tau)}{(\sum q_i N_i)^2} = \sum A_i g_i(\tau) = \frac{1}{B} \sum f_i g_i(\tau) \quad (\text{Equation S4})$$

With N_i being the number of particles inside the confocal volume and q_i represents the brightness of the i^{th} component. B is a normalization factor, f_i represents the fraction of the i^{th} component and g_i is

its time-dependent correlation function. This notation of the correlation functions makes it possible to differentiate between diffusing species with different diffusion behavior. Here, we use this approach to determine binding of small fluorescently labeled proteins to larger TSLs.

We did observe no difference in the overall intensity of a measurement without TSLs and one at a liposome concentration, where binding takes place. Therefore, we neglect possible quenching of the dye upon binding and use $q_i = q$ for both components.

For samples containing two components of different size a two component fit is used

$$G(\tau) = \frac{1}{N} \left[F_1 \left(\frac{1}{1+\tau/\tau_{D1}} \right) \left(\frac{1}{1+\omega^2\tau/\tau_{D1}} \right)^{\frac{1}{2}} + (1-F_1) \left(\frac{1}{1+\tau/\tau_{D2}} \right) \left(\frac{1}{1+\omega^2\tau/\tau_{D2}} \right)^{\frac{1}{2}} \right] + 1$$

(Equation S5)

Where τ_{D1} and τ_{D2} are the diffusion times of the two components and F_1 is the fraction of the first component. Here, we fix τ_{D1} to the value of the freely diffusing protein, so F_1 represents the fraction of unbound fast diffusing protein in solution. F_2 represents the fraction of slow diffusing liposomes with proteins bound to them with a diffusion time τ_{D2} .

To take optical dark states of the dye into account, a function that describes the triplet can be integrated into the fitting equation

$$G_{\text{Triplet}}(\tau) = \left(1 + \frac{T}{1-T} \exp\left(-\frac{\tau}{\tau_T}\right) \right) \quad (\text{Equation S6})$$

τ_T is the triplet state relaxation time and T the fraction of fluorophores in dark state.

The total correlation curve then becomes a product of the triplet function and the model $G(\tau)$

$$G_{\text{total}}(\tau) = G_{\text{Triplet}}(\tau) * G(\tau) \quad (\text{Equation S7})$$

The hydrodynamic radius R_h of a spherical molecule can be determined with the Stokes-Einstein-equation

$$R_h = \frac{k_B T}{6\pi\eta D} \quad (\text{Equation S8})$$

where $D = \omega_0^2/4\tau_D$ is the diffusion constant, ω_0 the radius of the confocal volume in the xy-plane, k_B is the Boltzman constant, T is the temperature in [K] and the viscosity of the surrounding medium η .

Determination of the linear regime of FCS

A titration series of FDG+ β -Galactosidase was performed to determine the linear regime of the FCS to obtain stable FCS results. Concentration of FDG+ β -Galactosidase for all experiments falls on the linear regime for FCS concentration measurements. This range was determined to be approximately 1-900 nM.

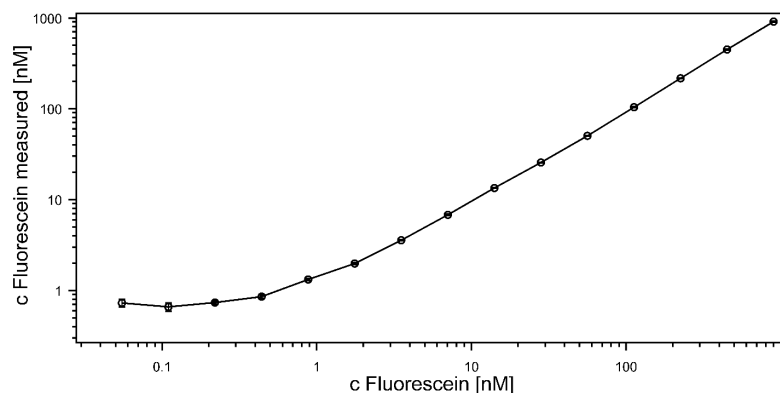


Figure S1: Titration series of FDG+ β -Galactosidase in HN-buffer + 1mM MgCl₂ to determine the linear range of FCS measurements (error bars are smaller than the symbols)

Correction of the FCS data

In comparison to our reference Alexa488 in water, we observe a slowdown of the diffusion times of the released FDG in the presence of unlabeled proteins or Triton.

Firstly, we checked if this due to an expansion of the confocal volume by the addition of these components or due to interactions with FDG. A sample using Alexa488 with and without Triton showed that the structure parameter is increased, leading to a relative increase in the confocal volume of 17-25%. This is equivalent to a correction factor B for the confocal volume of 1.17-1.25.

To correct for this effect in the determination of absolute concentration values in [M] we used the following correction:

$$B = \frac{V_{real}}{V_{calibration}} \quad (\text{Equation S9})$$

$$C_{corrected} = \frac{N}{N_A V_{calibration}} * B \quad (\text{Equation S10})$$

where $c_{corrected}$ is the concentration in [M], N is the number of the particles obtained from Equation S2, N_A is the Avogadro constant, $V_{calibration}$ is the determined confocal volume from a calibration measurement using Alexa488, V_{real} is the expanded confocal volume and B is the correction factor.

The same procedure of concentration correction is applied to all samples containing unlabeled proteins or/and Triton.

Fundamental concept of the FDG-TSL

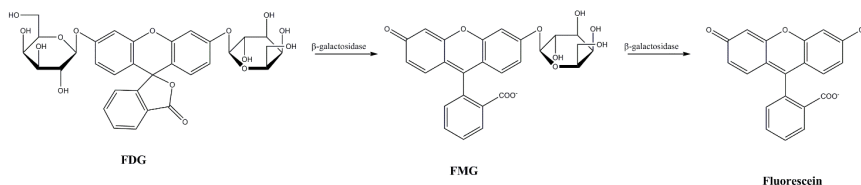


Figure S2: Sequential hydrolysis of FDG by β -Galactosidase

FDG (Fluorescein Di-galactoside) is a fluorescent substrate for the detection of β -Galactosidase. Non-fluorescent FDG is sequentially hydrolyzed by the enzyme β -Galactosidase. Firstly, FDG is turned into fluorescein monogalactoside (FMG) and then in a second step to strongly fluorescent fluorescein.

This assay is standardly used to detect even smallest amounts of β -Galactosidase as an indicator for LacZ gene expression. We use this concept the other way around, to prove the presence of tiny amounts of released FDG into a solution containing sufficient amounts of β -Galactosidase.

The liposomes are filled with 1mM FDG: The release of FDG by heating is verified by the addition of β -Galactosidase after stopping the release by cooling using ice-cold buffer. FDG is then turned into fluorescein. This concept allows us to measure released FDG/fluorescein on a single molecule level, obtaining a FCS-signal that is not influenced by partly filled liposomes.

Determination of the concentration of TSL in a standard sample

Six independent samples of DPPG₂-TSL with CF (24-24C) inside were prepared to have the same phosphate content as the TSL that were used for release measurements (26-16). For dilution 0.9% NaCl was used to be sure that no release is caused by different osmolarity inside and outside of the TSL. The measurements were performed at $\lambda_{ex} = 543$ nm to solely excite the membrane label (Rhodamine PE). This way bias caused by non-encapsulated free dye can be excluded/avoided.

0.3255 nM
 0.3120 nM
 0.2558 nM
 0.2977 nM
 0.2401 nM
 0.2685 nM
 0.2833 nM \pm 0.0307 nM

Estimation of the encapsulation efficiency for FDG-TSL

I. Determination via drug per liposome

We know the diameter of a liposome and the thickness of the lipid bilayer and can calculate the volume of a liposome using these values:

Diameter of a liposome (DLS): $d=114\text{nm} \rightarrow$ radius $r = 57\text{nm} - 5\text{nm}$ (thickness of lipid bilayer) = 52nm

Volume inside of a liposome = $\frac{4}{3} \pi r^3 = 5.88977 * 10^{-22} \text{ m}^3 = 5.88977 * 10^{-19} \text{ l}$

A solution containing 1mM FDG is used to hydrate the lipid film. If the same concentration is present inside the TSL, we expect for 100% encapsulation of 1mM FDG a number of molecules per liposome that is equal to:

$\text{FDG /TSL} = 1 * 10^{-3} \text{ mol/l} * 5.88977 * 10^{-19} \text{ l} * N_A = 354.69025 = 355$

$N_A =$ Avogadro constant

The measured value of FDG/TSL (Triton value) is: $190.6597 \pm 16.2715 = 191 \pm 16$

From that we estimate, the encapsulation efficiency to be
 Encapsulation efficiency = (measured FDG/TSL)/(theoretical FDG/TSL) * 100% = (191±16)/355 * 100% = 53.7±9.4%

II. Determination via drug/lipid

loading: drug/lipid = 1mM FDG/50mM lipid= 0.02

Measured drug concentration in sample: 54.1±4.6nM

Lipid concentration in sample: 33.333µM

Measured drug/lipid: 0.0016±0.00014

Encapsulation efficiency = (measured/loading)*100 = 8.0±0.7%

This value is in good agreement with the expected encapsulation efficiency of ~ 6.1% according to Lindner et al.[4].

Determination of Release using FDG-TSL

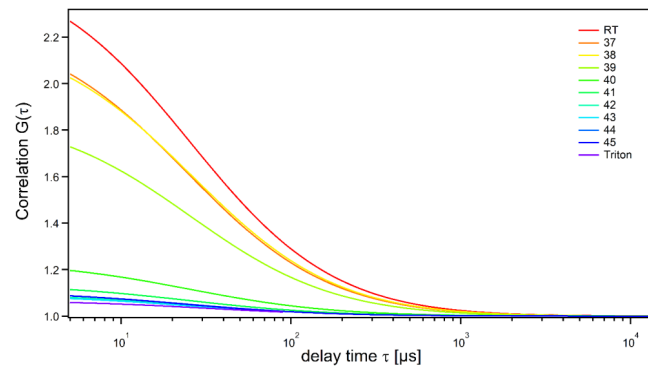


Figure S3: Correlation curves for different temperatures of FDG-TSL. The amplitude decreases with increasing temperature representing the increase in the concentration of released FDG.

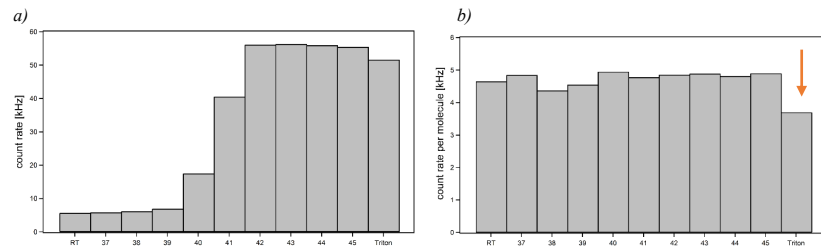


Figure S4: a) Corresponding count rate plot. The increase of signal with release is easily observable. The decrease in count rate for the Triton sample is clearly visible. Error bars are not shown, since they are smaller than the line thickness used. b) Corresponding count rate per molecule plot. The lower value of the count rate per molecule for the Triton sample is clearly visible, indicating an effect of Triton on the dye properties/brightness. This supports our assumption that an analysis completely relying on the total count rate can only provide a trend, but no single molecule precision.

Effect of Triton on the Release – Fluorescence intensity dependency in analysis

We are able to reproduce the same effect in release as in FS data (release >100%), if we use the count rate of the FCS measurements for analysis (b). The values above 100% might be the result of the effect of Triton on the brightness of the molecule (see sections below & above).

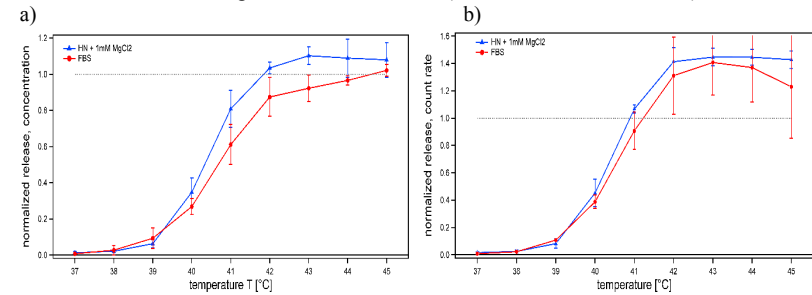


Figure S5: Release of FDG-TSL measured with FCS. A) The percentage release was determined by normalization of the measured concentration analogous to the FS measurements. b) The percentage release was determined by normalization of the measured count rate (fluorescence intensity) analogous to the FS measurements.

Release in different media measured by FS

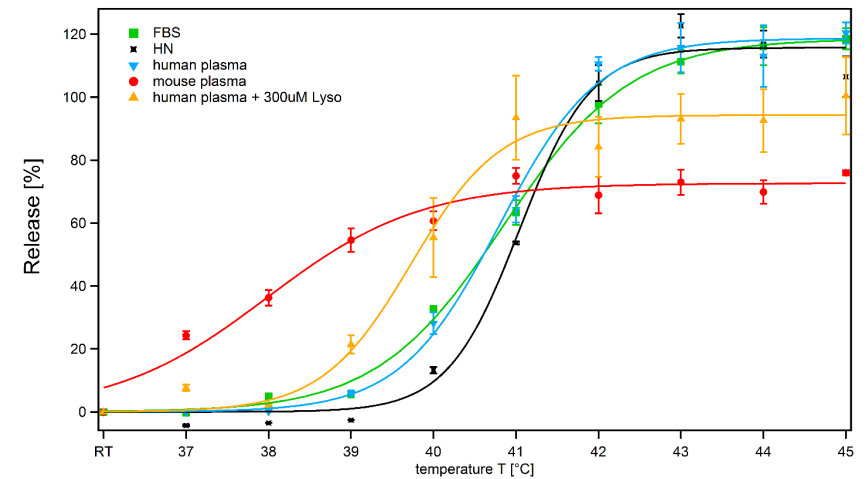


Figure S6: Percentage release of FDG-TSL determined in various media using FS. Data are averages of 3 individually prepared samples and their standard deviation.

Time-dependent release at different temperatures in FBS measured by FS

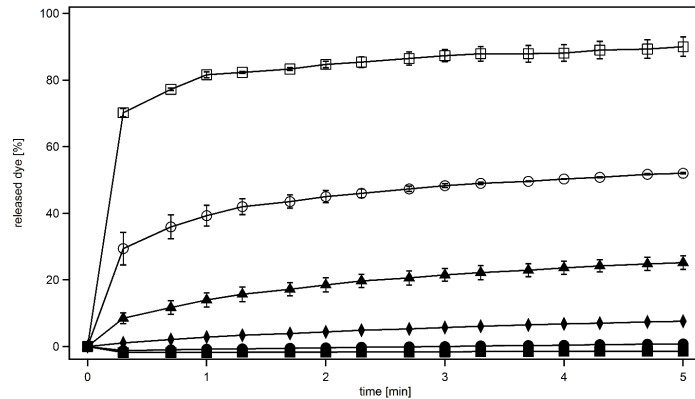


Figure S7: Time-dependent release in FBS measured with FS for 37°C (filled squares), 38°C (filled circles), 39°C (diamond), 40°C (triangle), 41°C (circle) and 42°C (square)

Binding studies

We investigated the equilibration time of the system after the addition of the DPPG₂-TSL to the labeled protein solution. We found that Fib binds at room temperature and reaches a plateau level of the fraction bound of around 80% after 15 minutes. ApoA1 binds strongly at room temperature and reaches a fraction bound of nearly 100% after 15 minutes. In comparison, BSA binds more slowly than Fib and reaches a plateau level of 28% after 40 minutes at room temperature. For the tested concentration of Tf we do not observe an analysable change in the data compared to the reference measurements without unlabelled TSL. From these data we conclude that an incubation time of 1h is enough for the system to equilibrate.

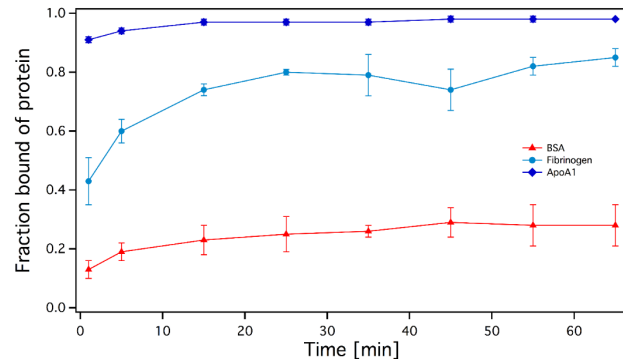


Figure S8: Kinetics of fraction of protein that is bound to DPPG₂-TSL. Fraction of Fib bound to TSL (light blue). For these measurements 7 µg/ml (20.6nM) of labelled Fib was used. Fraction of BSA bound to TSL (red). For these measurements 10 µg/ml (152nM) of labelled BSA was used. Fraction of ApoA1 bound to TSL (dark blue). For these measurements ~1 µg/ml (35.7nM) labelled ApoA1 was used.

Examples for binding of unlabelled proteins and its reversibility are shown in Figure S9. Firstly, the labelled protein is alone in solution (red). Then DPPG₂-TSL were added and incubated and after 1h measured. For binding a clear shift of the normalised correlation curves to the right is visible (blue). FBS was added and after another hour of incubation a last measurement was performed. These curves (black) are overlapping with the mono-protein solutions indicating that the binding of the labeled proteins to DPPG₂-TSL is reversed. A time series of the reversibility is shown in Figure S10.

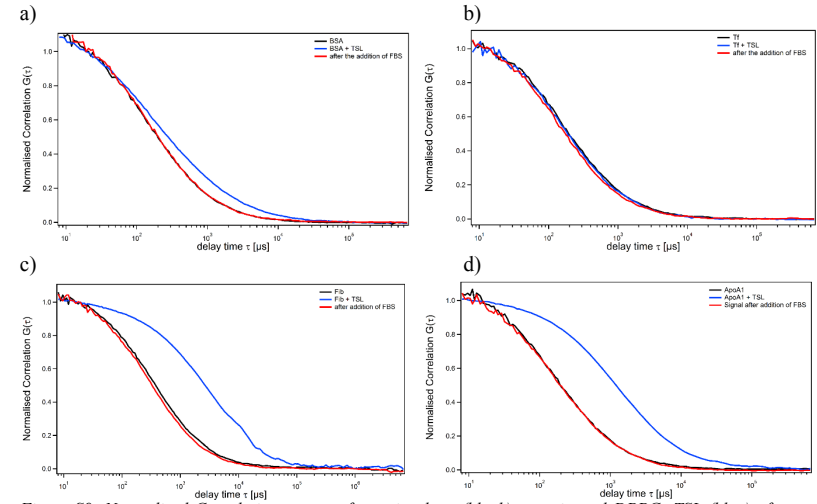


Figure S9: Normalised Correlation curves of protein alone (black), protein and DPPG₂-TSL (blue) after one hour of incubation and after the addition of FBS and another hour of incubation (red). The signal of free proteins (black) shifts towards larger diffusion times after one hour of incubation with DPPG₂-TSL (blue) and back to the starting curve, after the addition of FBS and incubation for another hour (red). This means the binding of all tested proteins is reversible.

a) BSA, b) Tf, c) Fib and d) ApoA1

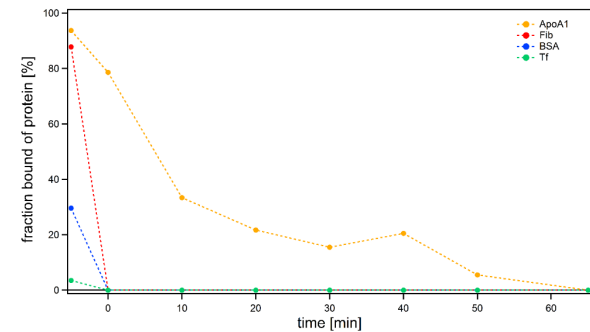


Figure S10: Kinetics for different proteins after the addition of FBS: Apo A1 (orange), Fibrinogen (red), BSA (blue) and Transferrin (green). The last three proteins are replaced immediately after the addition of FBS, while the amount of bound ApoA1 decreases slowly with time. After 1h all ApoA1 is replaced as well.

Supporting References

- [1] Medical Physiology: Principles for Clinical Medicine, Rodney A. Rhoades, David R. Bell, Chapter 9 p.171, 3rd Revised edition

- [2] U. Windberger, A. Bartholovitsch, R. Plasenzotti, K.J. Korak, G. Heinze, Whole blood viscosity, plasma viscosity and erythrocyte aggregation in nine mammalian species : reference values and comparison of data, *Exp. Physiol.* 88 (2003) 431–440.

- [3] H. Engelke, I. Dorn and J. O. Rädler, Diffusion and Molecular Binding in Crowded Vesicle Solutions Measured by Fluorescence Correlation Spectroscopy, *Soft Matter*, 5 (2009), 4283-4289

- [4] L.H. Lindner, M.E. Eichhorn, H. Eibl, N. Teichert, M. Schmitt-Sody, R.D. Issels, et al., Novel Temperature-Sensitive Liposomes with Prolonged Circulation Time, *Clin. Cancer Res.* 10 (2004) 2168–2178.

P4 · Simultaneous Measurement of a Range of Particle Sizes During Abeta Fibrillogenesis Quantified Using Fluorescence Correlation Spectroscopy

J. J. Mittag, S. Milani, D. M. Walsh, J. O. Rädler, J. J. McManus.

Biochemical and Biophysical Research Communications, 2014.



Simultaneous measurement of a range of particle sizes during $A\beta_{1-42}$ fibrillogenesis quantified using fluorescence correlation spectroscopy

Judith J. Mittag^a, Silvia Milani^a, Dominic M. Walsh^b, Joachim O. Rädler^a, Jennifer J. McManus^{c,*}

^a Ludwig-Maximilians-Universität, Fakultät für Physik & CeNS, Geschwister-Scholl-Platz 1, 80539 München, Germany

^b Laboratory for Neurodegenerative Research, Center for Neurologic Diseases, Brigham & Women's Hospital, Harvard Institutes of Medicine, Boston, MA 02115, USA

^c Department of Chemistry, National University of Ireland Maynooth, Maynooth, Co. Kildare, Ireland



ARTICLE INFO

Article history:

Received 7 April 2014
 Available online 24 April 2014

Keywords:

Fluorescence correlation spectroscopy
 Amyloid beta
 Aggregation
 Oligomerization
 Alzheimer's disease
 Protein folding disease

ABSTRACT

Low molecular weight oligomers of amyloid beta ($A\beta$) are important drivers of Alzheimer's disease. A decrease in $A\beta$ monomer levels in human cerebrospinal fluid (CSF) is observed in Alzheimer's patients and is a robust biomarker of the disease. It has been suggested that the decrease in monomer levels in CSF is due to the formation of $A\beta$ oligomers. A robust technique capable of identifying $A\beta$ oligomers in CSF is therefore desirable. We have used fluorescence correlation spectroscopy and a five Gaussian distribution model (5GDM) to monitor the aggregation of $A\beta_{1-42}$ in sodium phosphate buffer and in artificial cerebrospinal fluid (ACSF). In buffer, several different sized components (monomer, oligomers, protofibrils and fibrils) can be identified simultaneously using 5GDM. In ACSF, the faster kinetics of fibrillogenesis leads to the formation of fibrils on very short timescales. This analysis method can also be used to monitor the aggregation of other proteins, nanoparticles or colloids, even in complex biological fluids.

© 2014 Elsevier Inc. All rights reserved.

1. Introduction

The accumulation of fibrils formed from the amyloid beta-protein ($A\beta$) is a defining pathological hallmark of Alzheimer's disease (AD) [1]. However, recent evidence suggests that low molecular weight (M_w) diffusible aggregates of $A\beta$ (commonly referred to as $A\beta$ oligomers) are more important drivers of AD than the $A\beta$ fibrils found in amyloid deposits [2–4]. Several studies have shown that small protein aggregates are cytotoxic and contribute to synaptic dysfunction [5–10]. In nature, there are at least 20 different $A\beta$ isoforms all of which have the same common core of about 30 residues, but differ in the length of their N- and C-termini [11]. Within this family of peptides, primary sequences terminating at Ala42 are particularly associated with AD [12].

A lowering of $A\beta_{1-42}$ monomer levels in human cerebrospinal fluid (CSF) has been widely validated as a robust biomarker for the diagnosis of AD [13], including in pre-symptomatic individuals

that subsequently developed AD [14,15]. Mechanistically, the progressive accumulation of both soluble and insoluble $A\beta$ aggregates has been postulated to explain the decline in $A\beta_{1-42}$ monomer observed in CSF. Consequently, it is believed that measurement of $A\beta$ oligomer levels in CSF could offer an even more sensitive indicator than current biomarkers [13]. Despite intense efforts there are currently no validated, reliable and sensitive means to detect $A\beta$ oligomers in CSF. The oligomerization and subsequent formation of protein fibrils of $A\beta$ is a complex interplay of many peptides and mechanisms and is not yet fully understood [16–20]. However, the majority of studies find that the mechanism for fibrillogenesis is consistent with a nucleation-dependent polymerization model [5,18,21] as illustrated in Fig. 1(A). More recent work has suggested that a second nucleation step occurs [22].

The major difficulty in monitoring the progression of $A\beta$ fibrillogenesis is the range of particles sizes present. Even at the early stages of fibrillogenesis $A\beta$ will exist as monomer, heterogenous oligomers, protofibrils and fibrils. Few techniques can measure and track the components of such a heterogenous mixture of different sized species simultaneously. Several methods have been used to map the progression of peptide aggregation, from monomer to fibril, including, high performance liquid chromatography, gel electrophoresis, atomic force microscopy, transmission electron microscopy (TEM), Thioflavin T assays, dynamic light scattering and others [16]. Monomeric $A\beta$ has a hydrodynamic radius (R_h)

Abbreviations: $A\beta$, amyloid β -protein; $A\beta_{1-42}$, $A\beta$ spanning residues from Asp1 to Ala42; AD, Alzheimer's disease; CSF, cerebrospinal fluid; 5GDM, five Gaussian distribution model; FCS, fluorescence correlation spectroscopy; MEMFCS, maximum entropy method for FCS data analysis; M_w , molecular weight.

* Corresponding author.

E-mail addresses: judith.mittag@physik.lmu.de (J.J. Mittag), silvia.milani@physik.lmu.de (S. Milani), dwalsh3@partners.org (D.M. Walsh), raedler@lmu.de (J.O. Rädler), jennifer.mcmanus@nuim.ie (J.J. McManus).

<http://dx.doi.org/10.1016/j.bbrc.2014.04.088>
 0006-291X/© 2014 Elsevier Inc. All rights reserved.

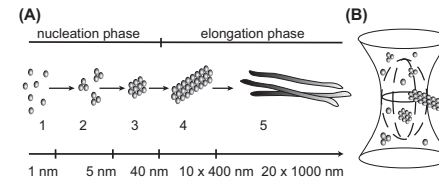


Fig. 1. (A) The standard nucleation-dependent polymerization (single nucleation) model for amyloid aggregation: formation of fibrils proceeds through a multistage process. Monomers (1) form low molecular weight aggregates (2), then higher molecular weight aggregates (3) in the nucleation stage, which has a characteristic lag time before the formation of protofibrils (4) and fibrils (5). A secondary nucleation step leading to the formation of oligomers via a fibril-catalyzed process has also been suggested [22] (not shown). (B) The conical volume for FCS measurements: fluorescently labeled monomers and peptides diffuse into and out of the conical volume leading to fluctuations in the fluorescence signal.

of 0.9 ± 0.1 nm [23], while oligomeric and fibril forms range in size from several nanometers to several microns [16–19].

It is challenging to quantitatively measure the sizes of different oligomers, which co-exist with $A\beta$ monomer, protofibrils and fibrils during a typical measurement. Fluorescence correlation spectroscopy (FCS) can be used to differentiate multiple components in a polydisperse solution and has already been used to study the aggregation of other amyloidogenic proteins. Notably, the aggregation of polyglutamine in cells [24], α -synuclein aggregation [25] and its binding to vesicles [26] have been studied. In relation to $A\beta$, FCS has been used to establish an in vitro saturation concentration of $A\beta_{1-40}$ [27], to test the interaction with aggregation inhibitors [28] and membranes [29,30], to study the depletion of oligomers under physiological conditions [23] and to determine the size distribution of $A\beta_{1-40}$ aggregates in solution [27,31,32]. Garai et al. [27] used a maximum entropy fitting method (MEM-FCS), which allowed multiple aggregating species within the system to be analyzed. While this is an improvement over standard fitting methods, it did not distinguish clearly between the oligomeric species in solution. Therefore, a need for a fitting procedure which can distinguish more clearly the different sized forms of $A\beta$ during fibrillogenesis exists.

Here, we have approached this problem by defining several sizes ranges (up to five) as Gaussian profiles (5GDM) and using these to fit the FCS autocorrelation function. This allows each pre-defined component to be fit to the data simultaneously, allowing more of the different sized components in the aggregating system to be determined at any particular time point during the experiment. The size distributions obtained using 5GDM analysis are compared to those obtained using MEMFCS. To our knowledge no previous work has used such a high number of Gaussian-shaped peaks and the same free variables for analysis of FCS data for polydisperse systems. This approach is not specific to $A\beta$, and we expect that it will be readily applied to study of other aggregating or amyloidogenic proteins.

2. Material and methods

2.1. Sample preparation

Synthetic $A\beta_{1-42}$ was purchased from W. M. Keck Biotechnology Facility at Yale University and Hilyte Fluor488™ labeled $A\beta_{1-42}$ was purchased from Anaspec Inc., Fremont (CA). The latter was dissolved in 1% NH_4OH and diluted to a final concentration of 1 mg/ml in 10 mM sodium phosphate buffer [33]. $A\beta_{1-42}$ was dissolved in 0.1% NH_4OH and then diluted with 100 mM Tris buffer at

1 mM, aliquoted and stored at -20 °C. Once thawed, peptide solutions were centrifuged at 100,000g and 4 °C for 1 h in a Beckman Optima Max XP ultracentrifuge (Indianapolis, IN) to remove pre-existing fibrils. The upper 75% of the supernatant was collected and the concentration of $A\beta_{1-42}$ determined by absorbance at 275 nm. Thereafter the supernatant was further diluted to the desired concentrations using 10 mM sodium phosphate buffer or artificial CSF (119 mM NaCl, 26.2 mM $NaHCO_3$, 2.5 mM KCl, 1 mM NaH_2PO_4 , 1.3 mM $MgSO_4 \cdot 7H_2O$, 11 mM D-(+)-Glucose and 2.5 mM $CaCl_2 \cdot 2H_2O$, pH adjusted to 7.3–7.4).

2.2. FCS experiments

FCS measurements were performed on a LSM10 microscope equipped with a ConfoCor2 unit (Carl Zeiss Jena, Germany), a 488 nm Argon laser and an apochromatic 40x water-immersion objective with a NA of 1.2. Fluorescence emission was separated from laser light using a bandpass filter (505–550 nm). Calibration was performed with Alexa 488 to determine the dimensions of the observation volume. Samples were filled in NUNC 8-Well-Plates (Thermo Scientific), which were coated with 15 μ g/ml poly-L-lysine (Biochrom AG). All measurements were performed at room temperature. Autocorrelation functions obtained from FCS measurements were analyzed as described in Supplementary information.

3. Results and discussion

3.1. Aggregation of $A\beta_{1-42}$ in sodium phosphate buffer

The aggregation of $A\beta_{1-42}$ was measured at 10 and 20 μ M in the presence of 0.01% labeled $A\beta_{1-42}$ in 10 mM sodium phosphate buffer, pH 7.4 by FCS. Variability in the time before onset of oligomer formation can depend on preparation conditions [16], and/or additional stresses applied to the sample to speed up the process [25,34–36]. Measurements were taken systematically over 48 h using consistent preparation methods to minimize these effects. Fig. 2 shows the evolution of an autocorrelation function over the time course of a typical experiment. This sample, at 20 μ M, indicates that higher M_w species appear over several hours, indicated by a shift in the delay time to higher values.

3.2. Comparison of MEMFCS and 5GDM fitting

Beyond the first few measurements, a one-component fit (SI Eq. (2)) leads to unsatisfactory and physically unrealistic results (not shown). Thus, a more sophisticated fitting method is required.

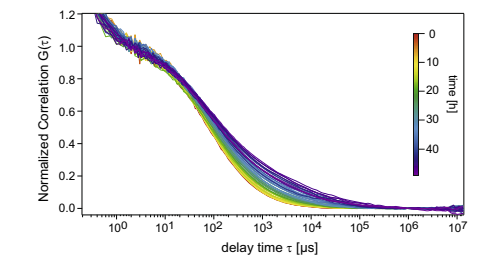


Fig. 2. Normalized average correlation curves over 48 h for a 20 μ M $A\beta_{1-42}$ sample (0.01% labeled). During the experiment the curves shift to the right and a buckling develops, indicating an increase in the number of different species and of particle sizes.

We first applied the MEMFCS fitting method [27,37] to autocorrelation functions at different time points throughout the experiment (Fig. 3A). A fit of the first measurement, reveals a single peak with a R_h maximum at 1.44 nm and a shoulder towards larger hydrodynamic radii. After 48 h, three peaks corresponding to spherical hydrodynamic radii of 2.09 nm, 101.17 nm and 4.5 μ m were observed (Fig. 3E).

Due to the assumption of maximum uncertainty and to avoid over interpretation of the data, MEMFCS fitting finds the widest size distribution that is consistent with the data [37]. Thus, the broad peaks obtained with MEMFCS are likely to include size distribution data for several different species in solution. Distribution curves resulting from MEMFCS analysis show Gaussian-type distribution features. Therefore, we used a Gaussian-shaped size distribution with a fixed number of peaks to fit our experimental data. This was inspired by initial work by Pal et al. [38], who used this approach as an alternative to MEMFCS for microemulsion droplets. The idea is that a component is not monodisperse with a single value for the diffusion time, τ_D , but rather a Gaussian distribution on a logarithmic time-scale with a peak diffusion time τ_p . The fit to the autocorrelation function is described by:

$$G(\tau) = \sum_{i=1}^n a_i(\tau_{Di}) \left(\frac{1}{1 + \frac{\tau}{\tau_{Di}}} \right) \left(\frac{1}{1 + \frac{\tau}{\tau_{Di}^2}} \right)^{\frac{1}{2}} \quad (1)$$

with the amplitude distribution

$$a_i(\tau_{Di}) = \sum_{n=1}^k A_n \exp \left[- \left(\frac{\ln(\tau_{Di}) - \ln(\tau_{pn})}{b_n} \right)^2 \right] \quad (2)$$

where A_n is the relative amplitude of the components, τ_{pn} is the peak diffusion time of the n th component and b_n is related to the width of the distribution. The τ_{p_i} 's have the same logarithmic quasi-continuous distribution as for MEMFCS. We have extended the work of Pal et al. by varying A_n , τ_{pn} and b_n rather than using only

a single peak. The fraction of each of the components was then determined by calculating the areas under the Gaussian peaks and normalizing them by the sum of the peak areas:

$$\text{Fraction}_n = \frac{\text{area}_n}{\sum_{n=1}^k \text{area}_n} \quad (3)$$

Hence, each distribution in the Gaussian distribution model (GDM) will represent a narrow range of particle sizes. The validity of the GDM was verified by extensive testing of the well-known dye Alexa 488 (using one distribution successfully, whereas a higher number of distributions were rejected by the model correctly). We choose to use five peaks for the fitting of A β since this was a good balance between distinguishing the different species in solution (monomer, small oligomer, larger oligomer, protofibril and fibril) and not having so many free variables that the outcome of the fits was physically unrealistic. Analysis of many autocorrelation curves using this method, gave consistent results. Less than five peaks led to an inappropriate description of the system (i.e. component sizes smaller than monomeric A β concomitant with very large particles at early time points).

In Fig. 3B the results of the analysis with the 5GDM are presented. There are a larger number of more sharply defined peaks representing different levels of A β_{1-42} aggregation than for MEMFCS. 5GDM fits reveal that two peaks at 1.17 nm and 1.62 nm are present at early time points in the experiment. If a weighted sum of these first two peaks is calculated using the relative amplitudes, a R_h of 1.44 nm is determined. This corresponds exactly to the diffusion time for the first peak obtained using MEMFCS fitting. In Fig. 3C–E, a direct comparison of the results of both fitting methods is shown for measurements taken at 0 h, 20 h and 48 h. For all three time points the results of 5GDM and MEMFCS are in good agreement and show the same trends for the aggregating system. However, at the later time points (48 h) significant differences for the calculated size of fibrils are observed ($R_h = 4.5 \mu$ m for MEMFCS and $R_h = 0.85 \mu$ m for 5GDM). These particle sizes are beyond

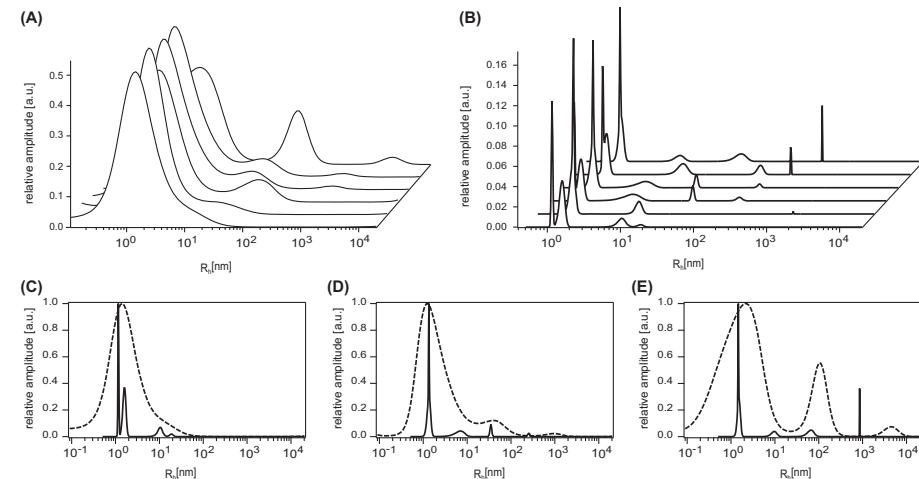


Fig. 3. Size distribution obtained with (A) MEMFCS and (B) 5GDM. Both fitting methods show similar trends, but the GDM fitting provides sharper and more defined peaks, especially in the range of low M_w oligomers. Measurements at 0 h, 5 h, 16 h, 20 h, 40 h and 48 h. (C–E) direct comparison of the results of MEMFCS (dashed) and 5GDM (line) for (C) 0 h, (D) 20 h and (E) 48 h. Both fitting methods show the same trends.

the reasonable measurable range for FCS and the values are artifacts of the fitting procedure in both methods. A comparison of the results obtained for each fitting procedure is shown in Fig. 3C–E. Clearly the general features of the aggregating system are consistent using both methods, but the 5GDM provides a more detailed and potentially a more realistic description of the aggregating system with better resolution of low M_w species.

3.3. Evaluation of the four fractions of A β_{1-42} aggregates

5GDM reveals a larger number of species within the system than MEMFCS, but each of these species represents a range of particle sizes. Since the first two peaks fuse and separate several times during the experiment, it was impossible to analyze these fractions separately (Fig. 3D and E). Hence, the percentages of the first two peaks were pooled and treated as one. This leads to a four level fraction model for A β_{1-42} aggregation (although a five peak fitting formula is used). The fusion of these first two peaks is probably due to a dynamic equilibrium that is assumed between monomers and very small oligomers [39,40]. We have therefore defined each of the size ranges obtained from the fitting as: (1) small components including monomers and low M_w oligomers; (2) higher M_w oligomers; (3) protofibrils and (4) fibrils. The fractions of the various A β particles in solution were determined from the 5GDM fitting and calculated using Eq. (3). The fractions were monitored over time and the averaged values are shown in Fig. 4.

The rate of aggregation is slower in the lower concentration samples and is consistent with previous experiments [32]. After 48 h, the proportion of fraction 1 (monomer and small oligomers) is higher in the lower concentration samples (72.4 for 10 μ M compared to 64.9% for 20 μ M), with a corresponding lower proportion of fibrils (3.6% for 10 μ M and 7.5% for 20 μ M). The proportion of fraction 1 decreases as fibrillogenesis proceeds (Fig. 4), while the R_h stays relatively constant (Fig. S1). Combined, these observations indicate a real decrease of the amount of monomer/small oligomers in solution. In Fig. S1 the evolution of the two peaks, which we have called fraction 1 (monomer and small oligomer) is shown. We observe that only a few data points lie in the monomer range between 0.8 and 1 nm [23], and most of the data points lie between 1 and 2 nm. This size range represents mixtures of monomers and small oligomers. Therefore with 5GDM it is not possible to differentiate between monomers and small oligomers and hence we have pooled this data in fraction 1. However, we can clearly separate a mixture of monomers and low M_w oligomers from larger aggregates. At the beginning of an experiment the dominating spe-

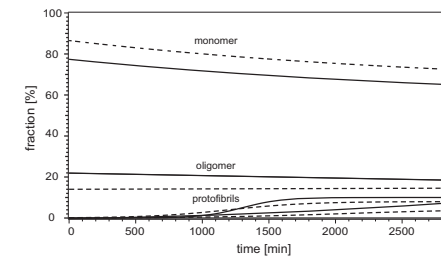


Fig. 4. Development of the fractions of the four aggregate levels of A β_{1-42} in sodium phosphate buffer, dashed lines represent 10 μ M A β samples, solid lines represent 20 μ M measurements. The amount of small components/monomers decreases over time, while the amount of protofibrils and fibrils increases after a certain lag time. The fraction of high M_w oligomers stays constant. The experiments were performed in triplicate to ensure reproducibility.

cies are small components (Fig. 4). This starting material consists of a mixture of monomer and small oligomers. Monomeric samples did not aggregate on a reasonable experimental time scale [23]. Examining fraction 2 (higher M_w oligomers), we see that these remain constant throughout the experiment (Fig. 4) (14% for 10 μ M and 19% for 20 μ M). For this fraction, the R_h grows slowly in size, and is in the range of 10 nm (Fig. S2). Hence, before the first measurement, equilibrium between small components (fraction 1) and high M_w oligomers (fraction 2) is established.

Protofibrils or fibrils are not present in FCS data at the beginning of the experiment (Fig. 4), but appear after a lag time, consistent with a nucleation-dependent polymerization model [41]. Both species show a sigmoidal behavior and a mean lag time of \sim 16 h. The fraction of protofibrils reaches a saturation level of 10% at 20 μ M and 8% at 10 μ M, respectively, while the proportion of fibrillar material continues to increase to the end of the experiment. Transmission electron microscopy (TEM) confirmed fibril formation (Fig. S3). The presence of fibrils is consistent with 5GDM analysis and the size values obtained for fibrils are in agreement with published studies [5,42,43].

3.4. Preliminary experiments in artificial CSF

Using artificial cerebrospinal fluid (ACSF), we assessed if the 5GDM fitting procedure is suitable for analysis in complex buffers and potentially in biological fluids. Large sedimenting particles are observed immediately after mixing stock A β with ACSF. During FCS measurements, this manifests as decreasing particle numbers due to loss of material to the large aggregates. The remaining monomeric material, now at much lower concentration, does not proceed to form higher M_w oligomers, since it is below the concentration required for the onset of fibrillogenesis. The higher ionic strength of ACSF leads to much faster kinetics for fibrillogenesis of A β_{1-42} in μ M concentrations [36]. An incremental decrease in A β , to nM concentrations, failed to find a regime in which a broader distribution of particle sizes was observed. Furthermore, adding labeled A β to pre-aggregated samples in ACSF produced similar results. In these experiments, only single events in the count rate plots were observed for 1 μ M, 500 nM and 50 nM A β_{1-42} , and these bursts corresponded to fibrils rather than to oligomers. A systematic evaluation with 5GDM was not performed, since these single events do not meet the requirements of the statistical basis needed for quantitative FCS analysis. These observations are consistent with Nag et al. [23]. They suggested that A β_{1-42} aggregation is dependent on physiological factors at low concentrations of A β_{1-42} and that aggregates dissociate below a certain concentration because they are thermodynamically unstable. However, beyond the limitation of this experimental system, there are no technical barriers to using 5GDM analysis in ACSF, CSF or other complex biological fluids.

A new fitting procedure for FCS (5GDM), allowing several differently sized components in solution to be analyzed simultaneously has been developed to study the fibrillogenesis of A β_{1-42} . Four A β_{1-42} aggregate types in solution were identified; small components (including monomer and low molecular weight oligomers), high M_w oligomers, protofibrils and fibrils. Each component was observed in solution over 48 h for a range of protein concentrations. A comparison with MEMFCS analysis confirmed that the results obtained with 5GDM are consistent with the established method, but that better resolution of particle size distributions in the nm range were obtained using 5GDM. Given that oligomers of A β in CSF have been found at picogram levels [44], concentration of the sample to pM levels could facilitate measurements in CSF using FCS with 5GDM. This analysis method could also be usefully employed to monitor the aggregation of other proteins, nanoparticles and colloids.

Acknowledgments

This work was made possible by funding from Science Foundation Ireland Stokes Lectureship (to J.J.McM), European Science Foundation networking programme "epitopeMap" (grant to J.O.R and J. J. McM), EU FP7 (NanoTransKinetics grant to JM, JOR), Deutsche Forschungsgemeinschaft (JM, travel grant) and the Foundation for Neurologic Diseases (DMW).

Appendix A. Supplementary data

Supplementary data associated with this article can be found, in the online version, at <http://dx.doi.org/10.1016/j.bbrc.2014.04.088>.

References

- CL. Masters, G. Simms, N.A. Weinman, et al., Amyloid plaque core protein in Alzheimer disease and Down syndrome, *Proc. Natl. Acad. Sci. U.S.A.* 82 (1985) 4245–4249.
- L.N. Zhao, H. Long, Y. Mu, et al., The toxicity of amyloid beta oligomers, *Int. J. Mol. Sci.* 13 (2012) 7303–7327.
- D.M. Walsh, D.J. Selkoe, A beta oligomers – a decade of discovery, *J. Neurochem.* 101 (2007) 1172–1184.
- I. Benilova, E. Karran, B. De Strooper, The toxic Abeta oligomer and Alzheimer's disease: an emperor in need of clothes, *Nat. Neurosci.* 15 (2012) 349–357.
- D.M. Walsh, D.M. Hartley, Y. Kusumoto, et al., Amyloid beta-protein fibrillogenesis. Structure and biological activity of protofibrillar intermediates, *J. Biol. Chem.* 274 (1999) 25945–25952.
- M. Hoshi, M. Sato, S. Matsumoto, et al., Spherical aggregates of beta-amyloid (amylopheroïd) show high neurotoxicity and activate tau protein kinase I/ glycogen synthase kinase-3beta, *Proc. Natl. Acad. Sci. U.S.A.* 100 (2003) 6370–6375.
- S. Barghorn, V. Nimrich, A. Striebing, et al., Globular amyloid beta-peptide oligomer – a homogenous and stable neuropathological protein in Alzheimer's disease, *J. Neurochem.* 95 (2005) 834–847.
- S. Lesne, M.T. Koh, L. Kotilinek, et al., A specific amyloid-beta protein assembly in the brain impairs memory, *Nature* 440 (2006) 352–357.
- G.M. Shankar, S. Li, T.H. Mehta, et al., Amyloid-beta protein dimers isolated directly from Alzheimer's brains impair synaptic plasticity and memory, *Nat. Med.* 14 (2008) 837–842.
- M. Lambert, A. Barlow, Diffusible, nonfibrillar ligands derived from A β_{1-42} are potent central nervous system neurotoxins, *Proc. Natl. Acad. Sci. U.S.A.* 95 (1998) 6448–6453.
- E. Portelius, A. Westman-Brinkmalm, H. Zetterberg, et al., Determination of beta-amyloid peptide signatures in cerebrospinal fluid using immunoprecipitation-mass spectrometry, *J. Proteome Res.* 5 (2006) 1010–1016.
- B. De Strooper, Proteases and proteolysis in Alzheimer disease: a multifactorial view on the disease process, *Physiol. Rev.* 90 (2010) 465–494.
- D.M. Holtzman, CSF biomarkers for Alzheimer's disease: current utility and potential future use, *Neurobiol. Aging* 32 (Suppl 1) (2011) S4–S9.
- R.J. Bateman, C. Xiong, T.L. Benzinger, et al., Dominantly inherited Alzheimer, clinical and biomarker changes in dominantly inherited Alzheimer's disease, *N. Engl. J. Med.* 367 (2012) 795–804.
- L.M. Peder Buchhave, K.B. Henrik Zetterberg, Asa K. Wallin, et al., Cerebrospinal fluid levels of beta-amyloid 1–42, but not of tau, are fully changed already 5–10 years before the onset of Alzheimer dementia, *Arch. Gen. Psychiatry* 69 (2012) 98–106.
- N.E. Pyyor, M.A. Moss, C.N. Hestekin, Unraveling the early events of amyloid-beta protein (Abeta) aggregation: techniques for the determination of Abeta aggregate size, *Int. J. Mol. Sci.* 13 (2012) 3038–3072.
- J.M. Paredes, S. Casares, M.J. Ruedas-Rama, et al., Early amyloidogenic oligomerization studied through fluorescence lifetime correlation spectroscopy, *Int. J. Mol. Sci.* 13 (2012) 9400–9418.
- S. Kumar, N. Rezaei-Ghaleh, D. Terwel, et al., Extracellular phosphorylation of the amyloid beta-peptide promotes formation of toxic aggregates during the pathogenesis of Alzheimer's disease, *EMBO J.* 30 (2011) 2255–2265.
- L.A. Munishkina, A.I. Fink, Fluorescence as a method to reveal structures and membrane-interactions of amyloidogenic proteins, *Biochim. Biophys. Acta* 1768 (2007) 1862–1885.
- Y. Liang, D.G. Lynn, K.M. Berland, Direct observation of nucleation and growth in amyloid self-assembly, *J. Am. Chem. Soc.* 132 (2010) 6306–6308.
- E. Hellstrand, B. Boland, D.M. Walsh, et al., Amyloid beta-protein aggregation produces highly reproducible kinetic data and occurs by a two-phase process, *ACS Chem. Neurosci.* 1 (2010) 13–18.
- S.I. Cohen, S. Linse, L.M. Luheshi, et al., Proliferation of amyloid-beta42 aggregates occurs through a secondary nucleation mechanism, *Proc. Natl. Acad. Sci. U.S.A.* 110 (2013) 9758–9763.
- S. Nag, B. Sarkar, A. Bandyopadhyay, et al., Nature of the amyloid-beta monomer and the monomer-oligomer equilibrium, *J. Biol. Chem.* 286 (2011) 13827–13833.
- Y. Takahashi, Y. Okamoto, H.A. Popiel, et al., Detection of polyglutamine protein oligomers in cells by fluorescence correlation spectroscopy, *J. Biol. Chem.* 282 (2007) 24039–24048.
- S. Nath, J. Meuniv, J. Hendrix, et al., Early aggregation steps in alpha-synuclein as measured by FCS and FRET: evidence for a contagious conformational change, *Biophys. J.* 98 (2010) 1302–1311.
- E. Rhoades, T.F. Ramlall, W.W. Webb, et al., Quantification of alpha-synuclein binding to lipid vesicles using fluorescence correlation spectroscopy, *Biophys. J.* 90 (2006) 4692–4700.
- K. Garai, B. Sahoo, P. Sengupta, et al., Quasihomogeneous nucleation of amyloid beta yields numerical bounds for the critical radius, the surface tension, and the free energy barrier for nucleus formation, *J. Chem. Phys.* 128 (2008) 045102.
- K. Wiesehan, J. Stohr, L. Nagel-Steger, et al., Inhibition of cytotoxicity and amyloid fibril formation by a D-amino acid peptide that specifically binds to Alzheimer's disease amyloid peptide, *Protein Eng. Des. Sel.* 21 (2008) 241–246.
- S. Hossain, M. Grande, G. Ahmadkhanov, et al., Binding of the Alzheimer amyloid beta-peptide to neuronal cell membranes by fluorescence correlation spectroscopy, *Exp. Mol. Pathol.* 82 (2007) 169–174.
- B. Sarkar, A.K. Das, S. Maiti, Thermodynamically stable amyloid-beta monomers have much lower membrane affinity than the small oligomers, *Front. Physiol.* 4 (2013) 84.
- L.O. Tjernberg, A. Pramantik, S. Bjorling, et al., Amyloid beta-peptide polymerization studied using fluorescence correlation spectroscopy, *Chem. Biol.* 6 (1999) 53–62.
- P. Sengupta, K. Garai, B. Sahoo, et al., The amyloid beta peptide (A beta(1–40)) is thermodynamically soluble at physiological concentrations, *Biochemistry-US* 42 (2003) 10506–10513.
- β -Amyloid (1–42), Hilyte Fluor™ 488-labeled Product Data Sheet, Anaspec Inc.
- P. Cizas, R. Budvytyte, R. Morkuniene, et al., Size-dependent neurotoxicity of beta-amyloid oligomers, *Arch. Biochem. Biophys.* 496 (2010) 84–92.
- C. Cabaleiro-Lago, F. Quinlan-Pluck, I. Lynch, et al., Dual effect of amino modified polystyrene nanoparticles on amyloid beta protein fibrillation, *ACS Chem. Neurosci.* 1 (2010) 279–287.
- V.H. FINDER, R. Glockshuber, Amyloid-beta aggregation, *Neurodegener. Dis.* 4 (2007) 13–27.
- P. Sengupta, K. Garai, J. Balaji, et al., Measuring size distribution in highly heterogeneous systems with fluorescence correlation spectroscopy, *Biophys. J.* 84 (2003) 1977–1984.
- N. Pal, S. Dev Verma, M.K. Singh, et al., Fluorescence correlation spectroscopy: an efficient tool for measuring size, size-distribution and polydispersity of microemulsion droplets in solution, *Anal. Chem.* 83 (2011) 7736–7744.
- A. Jan, D.M. Hartley, H.A. Lashuel, Preparation and characterization of toxic Abeta aggregates for structural and functional studies in Alzheimer's disease research, *Nat. Protoc.* 5 (2010) 1186–1209.
- S.A. Funke, Detection of soluble amyloid-beta oligomers and insoluble high-molecular-weight particles in CSF: development of methods with potential for diagnosis and therapy monitoring of Alzheimer's disease, *Int. J. Alzheimers Dis.* 2011 (2011) 151645.
- S. Kumar, J. Walter, Phosphorylation of amyloid beta (A β) peptides – a trigger for formation of toxic aggregates in Alzheimer's disease, *Aging (N.Y.)* 3(2011) 1–10.
- C. Sachse, Elektronenmikroskopie an Alzheimer-Fibrillen, *Bioforum* 32 (2009) 26–28.
- M. Fandrich, Oligomeric intermediates in amyloid formation: structure determination and mechanisms of toxicity, *J. Mol. Biol.* 421 (2012) 427–440.
- N. Salvadores, M. Shah Nawaz, E. Scarpini, et al., Detection of misfolded Abeta oligomers for sensitive biochemical diagnosis of Alzheimer's disease, *Cell Rep.* (2014) 1–8.

Supplementary Information

Simultaneous measurement of a range of particle sizes during A β ₁₋₄₂ fibrillogenesis quantified using fluorescence correlation spectroscopy

Judith J. Mittag¹, Silvia Milani¹, Dominic M. Walsh², Joachim O. Rädler¹, Jennifer J.

McManus^{3*}

¹Ludwig-Maximilians-Universität, Fakultät für Physik & CeNS, Geschwister-Scholl-Platz 1, 80539 München, Germany; judith.mittag@physik.lmu.de, silvia.milani@physik.lmu.de, raedler@lmu.de

²Laboratory for Neurodegenerative Research, Center for Neurologic Diseases, Brigham & Women's Hospital, Harvard Institutes of Medicine, Boston, MA 02115, USA dwalsh3@partners.org

³Department of Chemistry, National University of Ireland Maynooth, Maynooth, Co. Kildare, Ireland; Jennifer.mcmanus@nuim.ie

* **Corresponding author:** +353-1-7086926

Material & Methods

Transmission electron microscopy (TEM)

A 10 μ l A β ₁₋₄₂ solution from the FCS experiments was placed on a vacuum cleaned formvar/carbon coated grid (SPI supplies) and allowed to adhere for two minutes. The solution was removed and the grid washed with 7 μ l of 1% uranyl acetate solution. The grids were then stained with 7 μ l of 1% uranyl acetate solution for 20 seconds. After staining, the grids were allowed to dry for 45 minutes. Images were taken with a FastScan-F114camera (TVIPS) on a JEM1011 (JEOL) microscope operating at 80 keV.

FCS data analysis

Conventional FCS data analysis

The normalised autocorrelation function $G(\tau)$ is defined as

$$G(\tau) = \frac{\langle F(t)F(t+\tau) \rangle}{\langle F(t) \rangle^2} \quad (\text{SI Equation 1}),$$

where angular brackets denote the average over time t , $F(t)$ the fluorescence signal at time t and $F(t + \tau)$ the fluorescence signal at time $t + \tau$.

It is assumed that the confocal volume has an ideal three dimensional Gaussian shape. The structure parameter ω describes the ratio of the half axes z_0 to the radius of the laser beam w_0 . By fitting a model to the experimental data, physically relevant information can be extracted from the correlation curve. The autocorrelation curve for a single component freely diffusing in a 3D Gaussian element can be described by:

$$G(\tau) = \frac{1}{N} \left(\frac{1}{1+\frac{\tau}{\tau_D}} \right) \left(\frac{1}{1+\frac{\tau}{\omega^2 \tau_D}} \right)^{\frac{1}{2}} \quad (\text{SI Equation 2}),$$

where N is the number of particles in the confocal volume, τ_D is the translational diffusion time of the species, τ is the correlation time and ω the structure parameter.

The translational diffusion time describes the average dwell time of a molecule with diffusion constant D in the confocal volume

$$\tau_D = \frac{r^2}{4D} \quad (\text{SI Equation 3}) .$$

The hydrodynamic radius R_h of a spherical molecule can be determined with the Stokes-

Einstein-equation

$$R_h = \frac{k_B T}{6\pi\eta D} \quad (\text{SI Equation 4})$$

where k_B , is the Boltzman constant, T is the temperature in [K] and the viscosity of the surrounding medium η .

Maximum Entropy Method based fitting routine for FCS (MEMFCS)

Skilling and Bryan proposed the concept of maximum entropy method in 1984 [1]. This method was adapted by Sengupta [2] in 2003 for the analysis of FCS data of highly polydisperse samples. MEMFCS does not use any *a priori* assumptions to allow for a maximally wide distribution $a_i(\tau_{Di})$ that is consistent with the data. The fitting formula Eq. 2 changes to

$$G(\tau) = \sum_{i=1}^n a_i \left(\frac{1}{1+\frac{\tau}{\tau_{Di}}} \right) \left(\frac{1}{1+\frac{\tau}{\omega^2 \tau_{Di}}} \right)^{\frac{1}{2}} \quad (\text{SI Equation 5})$$

where n is the number of freely diffusing species and a_i the relative amplitude of the i^{th} component. The relative amplitude a_i includes variables such as the number of particles or the brightness and is a weighting factor for species i .

MEMFCS looks for a distribution of diffusion times $a_i(\tau_{Di})$ that minimizes X^2 and maximizes the entropy S at the same time.

The entropy is defined as

$$S = -\sum_i p_i \ln p_i \quad (\text{SI Equation 6})$$

with $p_i = a_i(\tau_{Di}) / \sum a_i(\tau_{Di})$ being the probability of finding a certain component i inside the confocal volume.

Since the range of possible aggregate sizes and therefore possible τ_{Di} 's spans several orders of magnitude, the range of possible τ_{Di} 's is transferred to a logarithmic scale for computational reasons. This range is then divided into n parts leading to a quasi-continuous distribution of particle sizes which is fixed during the fitting process. Only the amplitude $a_i(\tau_{Di})$ is varied.

Gaussian Distribution Model (GDM)

Pal et al. [3] showed that modelling with GDM can be an alternative for FCS analysis with MEMFCS for microemulsion droplets. They used a GDM for the analysis of the narrow size distribution of the droplets. The idea is that a component does not have a single sharp value for τ_D but instead a Gaussian distribution on a logarithmic time-scale around a peak diffusion time τ_p . In contrast to MEMFCS, the number of peaks and the shape of the distribution are determined. GDM only minimizes X^2 during fitting.

Equation 5 is modified to

$$G(\tau) = \sum_{i=1}^n a_i(\tau_{Di}) \left(\frac{1}{1+\frac{\tau}{\tau_{Di}}} \right) \left(\frac{1}{1+\frac{\tau}{\omega^2 \tau_{Di}}} \right)^{1/2} \quad (\text{SI Equation 7})$$

with the amplitude distribution

$$a_i(\tau_{Di}) = \sum_{n=1}^k A_n \exp \left[-\left(\frac{\ln(\tau_{Di}) - \ln(\tau_{pn})}{b_n} \right)^2 \right] \quad (\text{SI Equation 8})$$

Where A_n is the relative amplitude of the components, τ_{pn} is the peak diffusion time of the n^{th} component and b_n is related to the width of the distribution. The τ_{Di} 's have the same

logarithmic quasi-continuous distribution like for MEMFCS.

During our fitting A_n , τ_{pn} and b_n were varied, while Pal. *et al.* used only a single peak and fixed the peak diffusion time τ_p of it.

A total of 500 τ_{Dn} , logarithmically spaced between 10-10e⁶ μ s is used to cut of photophysical effects for short time-scales.

The fraction of the different components was determined by calculating the areas under the k Gaussian peaks and normalizing them by the sum of the k areas.

$$fraction_n = \frac{area_n}{\sum_{n=1}^k area_n} \quad (\text{SI Equation 9})$$

Results

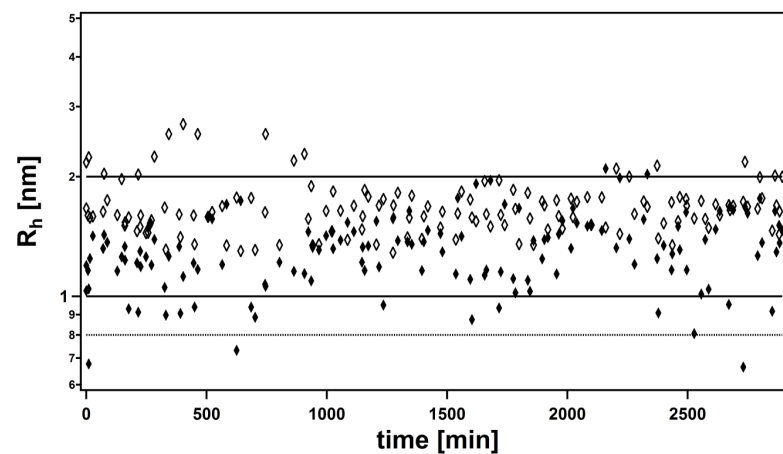


Figure S1: Evolution of the first (filled diamond) and second (open diamond) peak of 5GDM fitting. The horizontal lines at 0.8 nm, 1 nm and 2 nm are there to distinguish different components.

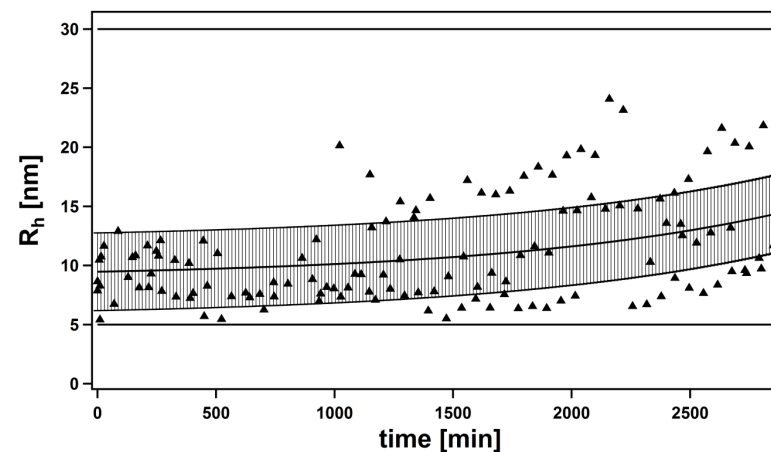


Figure S2: Development of the peak diffusion times of high MW oligomers in PB from 20 μ M $A\beta_{1-42}$ starting concentration. The black curve represents the fit of all three measurements at once, error bars are the mean deviation between the fit and the measured data points (3.4 nm). A slow, but steady increase in the hydrodynamic radius is observed

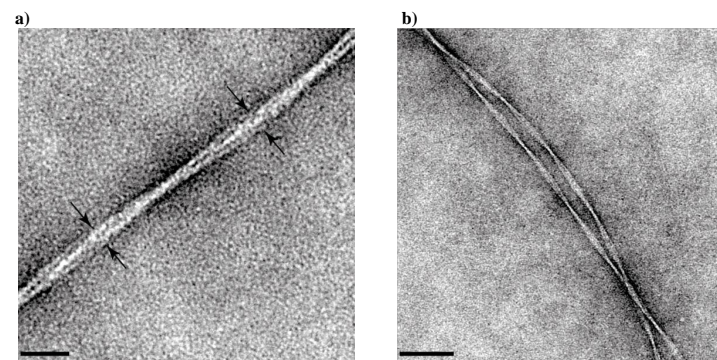


Figure S3: **a)** TEM picture of a fibril that was observed after a FCS experiment. The widths are indicated by arrows and have values of 15.64 nm and 13.91 nm (scale bar: 30 nm) **b)** Two amyloid fibrils starting to twist together.(scale bar: 90 nm)

References

- [1] J. Skilling, R.K. Bryan, Maximum-Entropy Image-Reconstruction - General Algorithm, Monthly Notices of the Royal Astronomical Society 211 (1984) 111-8.
- [2] P. Sengupta, K. Garai, J. Balaji, et al., Measuring size distribution in highly heterogeneous systems with fluorescence correlation spectroscopy, Biophys J 84 (2003) 1977-1984.
- [3] N. Pal, S. Dev Verma, M.K. Singh, et al., Fluorescence correlation spectroscopy: an efficient tool for measuring size, size-distribution and polydispersity of microemulsion droplets in solution, Anal Chem 83 (2011) 7736-7744.

M5 · Peptide Self-assembly Measured by Fluorescence Correlation Spectroscopy

J. J. Mittag, J. O. Rädler and J. J. McManus.

accepted, Methods in Molecular Biology, 2017.

Peptide self-assembly measured using fluorescence correlation spectroscopy

Judith J. Mittag¹, Joachim O. Rädler¹, Jennifer J. McManus^{2*}

¹Ludwig-Maximilians-Universität, Fakultät für Physik & CeNS, Geschwister-Scholl-Platz 1, 80539, München, Germany.

²Department of Chemistry, Maynooth University, Maynooth, Co. Kildare, Ireland.

Corresponding author:

Dr. Jennifer McManus,
Department of Chemistry,
Maynooth University,
Maynooth,
Co. Kildare,
Ireland.
Email: jennifer.mcmanus@nuim.ie

Running Head: A β_{1-42} self-assembly measured by FCS

Summary

Fluorescence correlation spectroscopy (FCS) is a flexible and powerful technique to measure the diffusion of fluorescently labeled particles. It has been important in examining a range of biological processes, from intracellular transport, to DNA hybridization. It is particularly suited to measuring the assembly of peptides, since peptides are often too small to be detected by standard light scattering methods, or may not contain aromatic amino acid residues, which limits the use of other spectroscopic techniques. In this protocol, we describe state-of-the-art sample preparation for A β_{1-42} peptide solutions and the measurement and analysis of the self-assembly of the peptide to form fibrils via a number of intermediate states using FCS.

Keywords (5-10): fluorescence correlation spectroscopy, peptide, self-assembly, size distribution, complex fluids, polydispersity, Gaussian distribution model

1. Introduction

Fluorescence correlation spectroscopy (FCS) is a sensitive and versatile technique allowing the diffusion of fluorescently labeled nano- and meso-scale objects in solution to be measured down to picomolar concentrations (1). The technique was first described in the early 1970s (2-4). FCS monitors the intensity fluctuations of a fluorescently labeled particle as it passes through a fixed volume (Fig. 1a and 1b). The use of a confocal microscope with FCS reduces the measurement volume to less than 1 femtolitre, allowing for single molecule detection (5, 6). By time averaging these fluorescence intensity fluctuations, an autocorrelation function is calculated (Fig. 1c), which contains information about the time taken for the labeled particle to pass through the measurement volume and the concentration of labeled particles in solution. This information in turn can be used to determine the particle size. One (a single label), two or more color FCS can be performed when the wavelengths of emission maxima of the different dyes are sufficiently separated (or that filters are used) to eliminate cross-talk. If two labeled components (of different colors) bind together, this can be detected by measuring a cross-correlation (7, 8). Hence, the variety of ways in which measurements can be performed has allowed the technique to be used for a diverse range of measurements including the hybridization of DNA (6), the binding of peptides to lipid membranes (9) and the assembly of virus capsids (10).

One of the limitations of FCS is that it works best for monodisperse solutions, or solutions in which there are large differences in sizes between the diffusing species. Recent developments in data analysis techniques however has made FCS better suited for measurements of assembly processes where heterogeneous particles sizes are obtained (11-15). The formation of a range of particles sizes is a typical occurrence in protein and peptide assembly and these more recent analysis techniques therefore offer new avenues to monitor the process. For these types of measurements, careful and consistent sample preparation is essential to ensure that the fitting methods are producing results based on robust data. We

have measured the assembly process (fibrillogenesis) of amyloid-beta ($A\beta$), a peptide associated with the pathogenesis of Alzheimer's disease by FCS (15).

Here we describe a protocol to prepare peptide solutions containing $A\beta_{1-42}$ and the methods and procedures to acquire robust and reliable data during aggregation and fibril formation of the peptide using FCS. Furthermore, we describe in some detail, the types of data analysis that can be performed on these heterogeneous solutions, including maximum entropy fitting (MEMFCS) and multi-Gaussian fitting (GDM), which recognize that the self-assembling peptide contains a number of different sized species, that are not captured well using single component fits.

2. Materials

Prepare all solutions using ultrapure Milli-Q water and analytical grade reagents.

1. Unlabeled $A\beta_{1-42}$ (see **Note 1**)
2. Labeled $A\beta_{1-42}$ (or labeling kit) (see **Note 2**)
3. Fluorescent dye with a known diffusion constant (for calibration), e.g. Alexa 488 (see **Note 3** and **Table 1**)
4. Measurement chambers, e.g. LabTek, Nunc 8-well-plates, borosilicate bottom, 200-400 μ l sample volume per well (Thermo Scientific) or Sensoplate plus, 20-100 μ l sample volume per well (384-well, black, 175 μ m glass bottom, Greiner Bio one) (see **Note 4**)
5. Poly-L-lysine coating solution: 100 μ g/ml poly-L-lysine in Milli-Q water (see **Note 5**)
6. Immersion oil (see **Note 6**)
7. UV Quartz cuvette (or whatever kind you use)
8. UV-vis spectrophotometer
9. Ice
10. 1% NH_4OH solution: 1 g of NH_4OH in 100 ml water
11. Tris buffer: 100 mM Tris, pH 7.4 (see **Note 7**)
12. Ultracentrifuge

13. Bench-top centrifuge
14. Ultra-filtration unit with a 10 kDa molecular weight cutoff (e.g. Amicon ultra-filtration devices), or syringe drive filters with a 0.02 μ m pore size (Whatman Anotop).
15. Glass vial (4ml volume)
16. Eppendorf tubes
17. Aluminum foil
18. Kimwipes
19. Nitrogen gas
20. Data Analysis Software, e.g. Origin, Matlab, Igor.

Methods

3.1 Sample preparation

3.1.1 Dissolution of peptide

1. To prepare unlabeled $A\beta_{1-42}$, add 1.8 ml of a 1% NH_4OH solution to 16 mg of the $A\beta_{1-42}$ peptide (Add 1.8 ml of Tris (pH 7.4)), which gives a 1 mM peptide solution (15). Ensure that all the solid material is dissolved and avoid the introduction of air bubbles where possible (see **Note 8**).
2. Dissolve the labeled peptide (e.g. $A\beta$ Hilyte, Anaspec Inc. Fremont, CA) per the supplier's instructions (see **Note 2**).

3.1.2 Removal of pre-existing peptide assemblies (e.g. oligomers or larger aggregates) (see **Note 9**)

Pre-existing assemblies can be present as artifacts of peptide lyophilization, sample preparation or concentration steps. These should be removed prior to measurements. One (or more) of the following procedures can be used:

1. Ultracentrifugation: For $A\beta$, pre-cool the rotor overnight at 4°C and set the centrifuge temperature to 4°C about 1 hour before use (cooling may take some time). Use centrifuge tubes designed for ultracentrifugation (not the standard lab variety). Ensure an appropriate counterweight is present in

the rotor. Centrifuge for 1h at 100,000 g. Remove only the upper 75% of the supernatant for further use and place on ice.

2. Ultra-filtration using e.g. Amicon ultra-filtration devices, to exclude components above a molecular weight cutoff (e.g. 10 kDa).
3. Filtration of samples through syringe drive filters e.g. Millipore Durapore 0.22µm filters or Whatman Anotop 0.02µm filters.

3.1.3 Concentration Determination

1. After removing pre-existing aggregates, determine the precise peptide concentration by measuring the absorbance at 280 nm for the unlabeled peptide and at 497 nm for the Hilyte 488-labeled Aβ₁₋₄₂ on a UV-vis spectrophotometer.
2. Measure the concentration of unlabeled peptide using the formula $c = A / \epsilon l$ where A is absorbance, ϵ is the molar extinction coefficient (equal to 1,400 M⁻¹ cm⁻¹ (at 280 nm) for Aβ₁₋₄₂) and l is the path length in cm. For labeled protein, calculate the molar concentration using the formula

$$c = \left(\frac{A_{280} - (A_{max,dye} - CF)}{\epsilon} \right) \cdot dilution\ factor$$

where $A_{max,dye}$ = absorbance maximum of dye, and CF is the correction factor for the dye (supplied by the manufacturer; for Hilyte 488, $CF = 0.19$).

3. Determine the labeling ratio using the formula:

$$\frac{dyes\ [moles]}{protein\ [moles]} = \left(\frac{A_{max,labeled}}{\epsilon' \cdot c \cdot dilution\ factor} \right)$$

where ϵ' is the extinction coefficient of the labeled peptide (e.g. For Hilyte 488 = 70,000 M⁻¹ cm⁻¹ at 497 nm).

3.2 Procedure for coating measurement chambers with Poly-L-lysine (16)– (see Note 5)

1. Dilute 0.5 mL poly-L-lysine stock solution into 2.83 ml water (or dilute to 15 µg/ml, total volume 3.33 ml).
2. Fill each chamber with 400 µl of the coating solution.
3. Incubate at room temperature for 1 hour in the dark.
4. Aspirate the solution completely and store it in a glass vial in the fridge. The coating solution can be reused for ~3 months. Wrap aluminum foil around the vial (or use an amber vial) to protect the solution from light.
5. Rinse the chambers carefully with 400 µl of Milli-Q water 20 times to remove all unbound poly-L-lysine.
6. Dry the glass bottom of the chamber slide carefully with a Kimwipe to avoid water marks.
7. Allow the chamber to dry in air at room temperature (or use a gentle stream of filtered nitrogen gas).

3.3 FCS setup and optimization

3.3.1 Preparation of FCS instrument

Specific instructions for performing steps 1 – 5 below will depend on the type of instrument used (see manufacturer instructions for assistance in performing these steps).

1. Switch on the laser 1 hour prior to setup.
2. Place a droplet of water or oil on the immersion objective of the microscope.
3. Place a chamber on the stage above the objective (if using an inverted microscope).
4. Search for the second reflection, optimize the quality of your signal with the objective collar ring and adjust the laser power to a suitable level.
5. Perform the pinhole alignment.
6. Calibrate the FCS set-up to determine the size of the confocal volume using a dye with a known diffusion constant (see **Table 1**). A concentration of 10-50 nM for the dye solution is typical (depending on the properties of the dye). Use the dilution buffer to dissolve the dye (see **Note 7**).

7. Add 200 μl of the dye solution to one of the chambers (or a suitable volume if different chambers are used).
8. Take 10 x 30 second measurements of the dye solution and determine the average.
9. Perform a one-component fit of the autocorrelation function using the instrumentation software (*see* 3.4.2) to determine the diffusion time (τ_D), and structure parameter (usually called S). Note these values.
10. Using D , the diffusion constant for the dye (from **Table 1**), first calculate r , using $\tau_D = r^2 / 4D$ and then z , using $S = z / r$. At this point do not change any of the components in the optical pathway or the calibration will need to be performed again.
11. Fix structure parameter (S) in the FCS software for the measurement of all other samples. (*see Note 10*).

3.3.2 Optimizing the labeled protein concentration (*see Note 7*)

1. Prepare your peptide samples (3.1.1 – 3.1.3). The labeled/unlabeled peptide ratio should be adjusted to achieve a labeled peptide concentration of ~ 10 nM (depending on the quality of the dye and the laser power used) to ensure a good signal to noise ratio.
2. If the measured signal is too weak or the signal to noise ratio is not good, increase the concentration of labeled peptide.

3.4 Sample measurement and analysis of FCS data

3.4.1 Measuring an autocorrelation function for a peptide solution.

1. Add the pre-prepared peptide solution to a sample chamber and seal with Parafilm or adhesive film to reduce evaporation.
2. Take a measurement (*see Notes 11, 12, 13 and 14*).

3.4.2 One component fitting

To extract physically relevant information from the autocorrelation curve, fit an appropriate model function to the experimental data. The simplest fitting formula is for a single component 3D freely diffusing species is:

$$G(\tau) = \frac{1}{N} \left(\frac{1}{1 + \frac{\tau}{\tau_D}} \right) \left(\frac{1}{1 + \frac{\tau}{S^2 \tau_D}} \right)^{\frac{1}{2}}$$

where N is the average number of particles inside the confocal volume, τ is the correlation time, S is the structure parameter and τ_D is the translational diffusion time of the molecule. An example of a “good” one-component fit is shown in **Fig. 2a**.

3.4.3 Two component fitting

For solutions containing two species, fit using a two-component method, which is performed using the following expression:

$$G(\tau) = \frac{1}{N} \left[(1 - y) \left(\frac{1}{1 + \frac{\tau}{\tau_{D1}}} \right) \left(\frac{1}{1 + \frac{\tau}{S^2 \tau_{D1}}} \right)^{\frac{1}{2}} + y \left(\frac{1}{1 + \frac{\tau}{\tau_{D2}}} \right) \left(\frac{1}{1 + \frac{\tau}{S^2 \tau_{D2}}} \right)^{\frac{1}{2}} \right] + 1$$

where τ_1 and τ_2 describe the diffusion times of the first and second diffusing species, y is the fraction of the second component in solution. This works particularly well if there is a significant difference in size between the two species. **Fig. 2b** shows a satisfactory two component fit. An example of a fit that does not accurately reflect the number of diffusing species in the solution is shown in **Fig. 2c** (*see Note 15*).

3.4.4 Higher order fitting: MEMFCS and GDM (multi-component fitting) (*see Note 16*)

When more than two components are required to achieve a satisfactory fit, the analysis becomes more complicated. Three main approaches for multi-component fits are used: CONTIN (11, 17), MEMFCS

(12, 13) and GDM (14, 15). The basis of each analysis method is the assumption of a quasi-continuous distribution of a large number of diffusing components. The major advantage of MEMFCS is that it provides a safe limit for interpretation of the data without any *a priori* assumptions and thereby reduces the risk of over-interpreting the data for highly polydisperse systems. GDM works in a similar way, but requires an assumption of the form of the amplitude distribution (i.e. the size ranges of the distributions used for the fit). While care must be exercised, it is faster and allows for better resolution of particle sizes than MEMFCS (Fig. 2d) (see Note 17).

3.4.5 Triplet decay

The fluorescence of a molecule can switch on and off several times while diffusing through the confocal volume by decay to the triplet (dark) state. These fluctuations can provide an additional contribution to the autocorrelation curve. To account for this, a function that describes the triplet decay can be integrated into the fitting equation for the model of 3D freely diffusing particles as follows:

$$G_{Triplet}(\tau) = \left(1 + \frac{T}{1-T} \exp\left(-\frac{\tau}{\tau_T}\right)\right)$$

where τ_T is the triplet state relaxation time and T is the fraction of fluorophores in the dark state. The total autocorrelation curve then becomes a product of the triplet function and the model $G(\tau)$ as follows:

$$G_{total}(\tau) = G_{Triplet}(\tau) \cdot G(\tau)$$

3.4.6 Determination of the hydrodynamic radius

Once a suitable fitting procedure has been established, the particle size can be derived from the fitting parameters. For spherical molecules the hydrodynamic radius R_h can be calculated using the Stokes-Einstein-equation:

$$R_h = \frac{k_B T}{6 \pi \eta D}$$

where k_B is the Boltzmann constant ($1.38 \times 10^{-23} \text{ J K}^{-1}$), T is temperature in Kelvin, η is the solvent viscosity (at temperature, T). It is also possible to insert correction factors to account for particles with non-spherical geometries (18).

4. Notes

1. A β_{1-42} is available commercially (e.g. Anaspec, Fremont, CA, USA) from a number of different sources or can be produced recombinantly. Other peptides can also be prepared using the same protocol.
2. FCS measurements are usually performed when only a small portion of the peptide used is labeled (and hence a mixture of labeled and unlabeled peptide is used). The lowest possible amount of labeled peptide should be used. If a labeling kit is used to tag the peptide of interest, there are two options; covalent attachment of a fluorescent molecule, usually by conjugation to either a primary amine or to a free cysteine; or the use of a binding dye, such as Thioflavin T, for which the fluorescence intensity increases significantly upon binding to amyloid-type assemblies. The choice will depend on the amino acid sequence of the peptide being examined and the types of assembly it will form. For methods that require covalent attachment of a dye, it is important to remove all excess (non-conjugated) dye. Exhaustive washing is required. The washings should be tested by measuring fluorescence intensity at the emission maximum of the dye in a fluorimeter to ensure that all excess dye has been removed. For both pre-labeled peptides and peptides labeled using a kit, the characteristics of the fluorescent label chosen should also be carefully evaluated for brightness, photostability (to ensure little or no bleaching), quantum efficiency, the size of dye (~1 nm) vs the size of peptide (often less than 1 nm), the ability to determine the concentration of the labeled peptide and dye/protein ratio.

3. To effectively calibrate the FCS instrument, the confocal volume is determined by measuring the diffusion of a fluorophore for which the diffusion coefficient is known. Choose a dye best suited to the excitation lasers available and the filter set installed for emission. The excitation maximum for the calibration dye should match the excitation maximum for the fluorescent label used with the peptide. A list of commonly used calibration dyes and their corresponding diffusion constants are listed in **Table 1**.
4. There are a number of possible sample chambers (or micro fluidic devices) that can be used for FCS measurements. It is possible to measure FCS in very small volumes and the choice of sample chamber may depend on the availability of material. At a minimum, the chamber should preferably have a glass base (but not too thick, since this will prohibit the adjustment of the collar ring of the objective lens).
5. FCS measurements are often performed in very low concentration samples. If the peptide binds to the sample chamber walls, this can reduce the bulk concentration significantly or indeed be responsible for the assembly of the peptide (*via* surface nucleation). The concentration of peptide (in a non-aggregating solution) can be monitored over time from the particle concentration data gathered in the autocorrelation function (as $1/N$). If the intercept of the autocorrelation function increases over time (without a concurrent increase in the diffusion time), peptide binding to the chamber walls should be suspected. If this occurs, surface binding can be pacified by coating the wells with a variety of other reagents. A procedure using poly-L-lysine has been described, but PEG, lipids or BSA can also be used (using the same procedure).
6. The water used for the objective should be dust free. If present, the measurements may be affected. Filter the water through 0.22 μm filters prior to use.
7. It is important to ensure compatibility of the fluorescent dye and the buffer used. The dye brightness can be pH-dependent or the dye may need specific ions to be present (e.g. calcium). The solution conditions required for the fluorescent dye may not be compatible with the peptide (e.g. close to the isoelectric point, or wrong ionic strength), which could affect the assembly

process. The selection of an appropriate buffer at a suitable pH and ionic strength should be given careful consideration.

8. Prepare a suitable buffer using analytical grade reagents. Filter through 0.22 μm filters (e.g. Millipore Durapore). It is also possible to perform measurements in complex fluids, such as blood plasma or cerebrospinal fluid. These are used instead of buffer. It is important that complex fluids are cell free, with no large particles (i.e. with sizes comparable to the confocal volume), as this will lead to light scattering.
9. The presence of dimers/oligomers and/or larger aggregates in the stock solution can make analysis of the data difficult. If possible, non-native higher order assemblies should be removed prior to the beginning of the measurement. If present, it will be difficult to accurately determine the size of the tagged peptide monomer and pre-existing assemblies can alter the kinetics of the assembly process. Prepare all samples consistently and just before measurements are performed.
10. If the laser power is increased (after the initial calibration), the calibration must be performed again. Increasing the laser power may lead to bleaching effects.
11. For measurements performed over several hours (typical for peptide assembly), sealing the sample chamber is important since evaporation will lead to an increase in concentration of the solutes and hence an overestimation of the number of particles. This may also mask a self-assembly process, which will decrease the particle number. The initial sample volume should also be large enough to ensure that evaporation doesn't dramatically alter the sample concentration.
12. For longer measurements, use oil immersion rather than water immersion for the objective. If one uses water, evaporation of the water droplet on the lens will occur. This needs to be monitored and re-applied if necessary. If the sample chamber is moved regularly throughout the experiment (e.g. if multiple wells are being measured simultaneously), re-application of the immersion fluid may also be required.
13. If large aggregates and/or dust are present in the sample during measurement, this will result in significant spikes in the intensity. Most software packages have integrated "dust filters". These

tools exclude count rates that are above a threshold level (that can be specified) and data above this threshold is not used in calculating the autocorrelation function.

14. A large decrease in number of particles may be due to the formation of very large aggregates (greater than 1 μm). If these particles are very large, sedimentation will occur and the formation will not be recorded in the autocorrelation function. Always visually inspect the sample chamber for large sedimented particles.
15. It can be very difficult to distinguish between a monomer and a dimer for the following reason. The autocorrelation function is an average of the time correlated intensity fluctuations of the diffusing species, where the intensity is proportional to the sixth power of the hydrodynamic radius. To distinguish clearly between two species in solution, one component should have twice the hydrodynamic radius of the other component. However, as a broad rule of thumb, a doubling in the hydrodynamic radius is equivalent to 8x increase in molecular weight. Therefore, a large increase in molecular weight is required to clearly distinguish different diffusing species using standard fitting procedures.
16. A multicomponent fit should be attempted when it is clear that either a one or two component fit do not accurately describe your system (i.e. the fit is bad, see **Fig. 2**). Sample polydispersity is indicated when there are significant deviations between the data and the one or two-component fits (see **Fig. 2c**). Even if the initial fit seems good (as indicated by the residuals), a multi-component fit may still be warranted if the sizes produced by the one or two-component fits are physically unrealistic (for example, smaller than either the peptide or the dye molecule), or if there is difficulty distinguishing between larger particles (those comparable in size to the confocal volume).
17. Fitting procedures for multi-component, polydisperse solutions e.g. MEMFCS and multi-Gaussian models require adequate computer power and fitting software (e.g. Igor or Matlab).

References

1. Ries, J. and Schwille, P. (2012) Fluorescence Correlation Spectroscopy. *Bioessays*, 34, 361-368.
2. Magde, D., Elson, E.L. and Webb, W. W. (1972) Thermodynamic Fluctuations in a Reacting System—Measurement by Fluorescence Correlation Spectroscopy. *Phys. Rev. Lett.*, 29 (11), 705-708.
3. Elson, E. L. and Magde D. (1974) Fluorescence Correlation Spectroscopy. I. Conceptual Basis and Theory. *Biopolymers*, 13, 1-27.
4. Magde, D., Elson, E. L. and Webb, W. W. (1974) Fluorescence Correlation Spectroscopy. II. An Experimental Realization. *Biopolymers*, 13, 29-61.
5. Rigler R., Mets, Ü., Widengren J. and Kask, P. (1993) Fluorescence correlation spectroscopy with high count rate and low background: analysis of translational diffusion. *Eur. Biophys. J.*, 22, 169-175.
6. Kinjo M. and Rigler, R. (1995) Ultrasensitive hybridization analysis using fluorescence correlation spectroscopy. *Nuc. Acids. Res.* 23 (10), 1795-1799.
7. Fitzpatrick J, Lillemeier B (2011) Fluorescence correlation spectroscopy: linking molecular dynamics to biological function *in vitro* and *in situ*. *Curr. Opin. Struct. Biol.* 21(5), 650–660.
8. Schwille, P. and Haustein, E. (2001) Fluorescence Correlation Spectroscopy - An Introduction to its Concepts and Applications. *Biophysics Textbook Online* 1 (3), 1-33.
9. Rusu, L., Gambhir, A., McLaughlin, S. and Rädler, J. O. (2004) Fluorescence correlation spectroscopy studies of peptide and protein binding phospholipid vesicles. *Biophys. J.* 87 (2), 1044-1053.
10. Comas-García, M., Garmann, R. F., Singaram, S. W., Ben-Shaul, A., Knobler, C. M. and Gelbart, W. M., Characterisation of Viral Capsid Protein Self-Assembly around Short Single-Stranded RNA.

11. Tjernberg, L.O., Pramanik, A., Björling, S. Thyberg, P., Thyberg, J., Nordstedt, C., Berndt, K.D., Terenius, L. and Rigler, R. (1999) Amyloid β -peptide polymerization studied using fluorescence correlation spectroscopy. *Chem. Biol.* 6 (1), 53-62.
12. Sengupta, P., Garai, K., Balaji, J., Periasamy, N. and Maiti, S. (2003). Measuring size distribution in highly heterogeneous systems with fluorescence correlation spectroscopy. *Biophys. J.* 84 (3), 1977–1984.
13. Garai, K., Sahoo, B., Sengupta, P. and Maiti, S. (2008) Quasihomogeneous nucleation of amyloid beta yields numerical bounds for the critical radius, the surface tension, and the free energy barrier for nucleus formation. *J. Chem. Phys.* 128 (4), 045102-1 - 7.
14. Pal, N., Verma, S.D., Singh, M. K., Singh, M. K. and Sobhan S. (2011) Fluorescence correlation spectroscopy: An efficient tool for measuring size, size-distribution and polydispersity of microemulsion droplets in solution. *Anal. Chem.* 83 (20), 7736–7744.
15. Mittag, J. J., Milani, S., Walsh, D. M., Rädler, J. O. and McManus J. J. (2014) Simultaneous measurement of a range of particle sizes during $A\beta_{1-42}$ fibrillogenesis quantified using fluorescence correlation spectroscopy. *Biochem. Biophys. Res. Comm.* 448 (2), 195-199.
16. www.ibidi.com/service/application_notes/AN08_Coating.pdf
17. Provencher, S. W. (1982) Contin: A general purpose constrained regularization program for inverting noisy linear algebraic and integral equations. *Comput. Phys. Comm.* 27: 229-242
18. Tirado, M., Lopez Martinez, C., Garcia de la Torre, J. (1984) Comparison of theories for the translational and rotational diffusion coefficients for rod-like macromolecules. Application to short DNA fragments. *J. Chem. Phys.* 81 (4), 2047-2052.
19. Petrášěk, Z. and Schwille, P. (2008) Precise measurement of diffusion coefficients using scanning fluorescence correlation spectroscopy. *Biophys. J.* 94, 1437-1448.
20. Dertinger, T., Loman, A., Ewers, B., Müller, C. B., Krämer, B. and Enderlein, J. (2008) The optics and performance of dual-focus fluorescence correlation spectroscopy. *Optics Express* 16 (19), 14353-14368.

21. Kapusta, P. (2010) Absolute diffusion coefficients: Compilation of reference data for FCS calibration. PicoQuant GmbH Application Note.
22. Dertinger, T., Pacheco, V., von der Hocht, I., Hartman, R.H., Gregor, I. and Enderlein, J. (2007) Two-focus fluorescence correlation spectroscopy: A new tool for accurate and absolute diffusion measurement. *Chem. Phys. Chem.* 8 (3), 433-443.

Acknowledgements:

This work was made possible by funding from Science Foundation Ireland Stokes Lectureship (to J. J. McM); European Science Foundation networking programme “epitopeMap” (grant to J.O. R. and J. J. McM); EU FP7 (NanoTransKinetics grant to JJM, JOR), Deutsche Forschungsgemeinschaft (JJM, travel grant).

Figures:

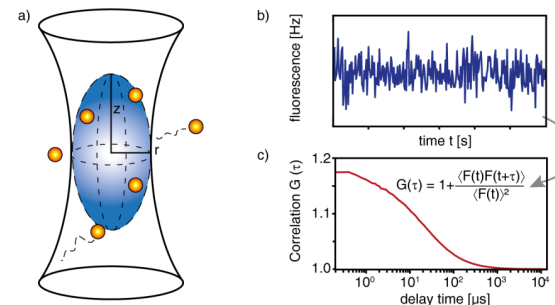


Figure 1: a) Confocal volume for a FCS experiment: fluorescently labeled particles diffuse through the confocal volume leading to fluctuations in the fluorescence intensity, b) The fluctuations are recorded over the time of the experiment and c), the time averaged intensity fluctuations are recorded as an autocorrelation function, which can be used to determine the diffusion time and concentration of diffusing particles and therefore their size.

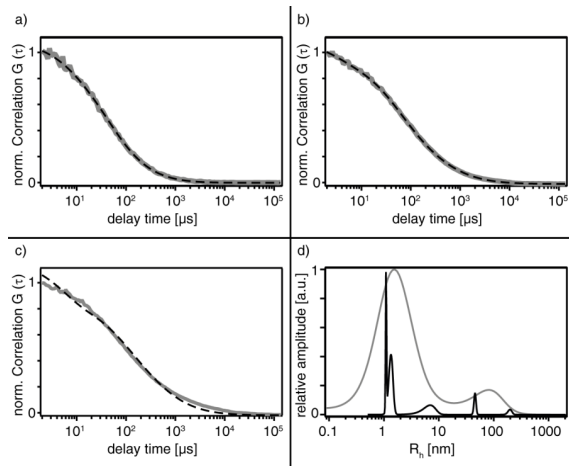


Figure 2: Examples for data fitting. (a) An example of a “good” one-component fit. (b) A successful two-component fit, (c) A “bad” two component fit that deviates from the measured data. This may indicate that a higher number of components are required to obtain a satisfactory fit of the data. (data in gray, fit as black dashed line) (d) Amplitude distribution of a polydisperse $A\beta_{1-42}$ solution after 16 hours analyzed using MEMFCS (gray) and GDM (black). While both results show similar overall trends, the GDM analysis gives more defined peaks than MEMFCS.

Table 1: Diffusion coefficients for a number of fluorescent small molecules that can be used for calibrating the FCS instrument.

Dye	diffusion constant $[\mu\text{m}^2/\text{s}]$	laser wavelength [nm]	temperature $[\text{°C}]$	Reference
Alexa488	435	488	$22.5 + 2\%/\text{°C}$	(19)
Alexa546	341	543	$22.5 + 2\%/\text{°C}$	(19)
eGFP	95	488	$22.5 + 2\%/\text{°C}$	(19)
Fluorescein	436	488	$22.5 + 2\%/\text{°C}$	(19)
Rhodamine 6G	426	543	$22.5 + 2\%/\text{°C}$	(19)
Cy5	370 ± 15	633	25	(20)
Alexa633	340 ± 10	633	25	(21)
Atto655	390	633	25	(22)

P6 · Quantitative Thermophoretic Study of Disease-related Protein Aggregates

M. Wolff, **J. J. Mittag**, T. W. Herling, E. De Genst, C. M. Dobson, T. P. J. Knowles, D. Braun and A. K. Buell.

Scientific Reports, 2016.

licensed under a Creative Commons Attribution 4.0 International Licence

<http://creativecommons.org/licenses/by/4.0/>

SCIENTIFIC REPORTS

OPEN Quantitative thermophoretic study of disease-related protein aggregates

Received: 24 November 2015
Accepted: 22 February 2016
Published: 17 March 2016

Manuel Wolff¹, Judith J. Mittag², Therese W. Herling³, Erwin De Genst³,
Christopher M. Dobson³, Tuomas P. J. Knowles³, Dieter Braun¹ & Alexander K. Buell^{3,†}

Amyloid fibrils are a hallmark of a range of neurodegenerative disorders, including Alzheimer's and Parkinson's diseases. A detailed understanding of the physico-chemical properties of the different aggregated forms of proteins, and of their interactions with other compounds of diagnostic or therapeutic interest, is crucial for devising effective strategies against such diseases. Protein aggregates are situated at the boundary between soluble and insoluble structures, and are challenging to study because classical biophysical techniques, such as scattering, spectroscopic and calorimetric methods, are not well adapted for their study. Here we present a detailed characterization of the thermophoretic behavior of different forms of the protein α -synuclein, whose aggregation is associated with Parkinson's disease. Thermophoresis is the directed net diffusional flux of molecules and colloidal particles in a temperature gradient. Because of their low volume requirements and rapidity, analytical methods based on this effect have considerable potential for high throughput screening for drug discovery. In this paper we rationalize and describe in quantitative terms the thermophoretic behavior of monomeric, oligomeric and fibrillar forms of α -synuclein. Furthermore, we demonstrate that microscale thermophoresis (MST) is a valuable method for screening for ligands and binding partners of even such highly challenging samples as supramolecular protein aggregates.

Protein aggregation into highly ordered, insoluble amyloid fibrils and their oligomeric precursors is a hallmark of a range of disorders, many of them neurodegenerative in nature, such as Alzheimer's and Parkinson's diseases¹. In the latter condition, intracellular amyloid deposits, known as Lewy bodies, of the intrinsically disordered protein α -synuclein form a major characteristic of the pathology². To date, no cure for this disease exists, a consequence at least in part of the lack of fundamental understanding of the mechanism of aggregation and its associated toxicity, as well as the incomplete characterization of the interactions between aggregates of α -synuclein and other compounds, including small molecules and proteins.

Such interactions are important for both diagnostic (e.g. for positron emission tomography³) and therapeutic purposes (e.g. for targeted aggregation inhibitors⁴). In this context there is an urgent need for experimental techniques that can be used for high throughput screening to identify such compounds. Standard techniques, such as isothermal titration calorimetry (ITC)⁵ or surface plasmon resonance (SPR)⁶ can provide important information, but suffer from a number of limitations, including high levels of sample consumption (ITC), potential surface artifacts (SPR) and high sensitivity to solution conditions (both ITC and SPR).

Analytical methods based on thermophoresis have recently been introduced as alternatives to these established methods for the measurement of binding interactions of biomolecular compounds^{7,8}. Thermophoresis, also known as the Soret effect⁹, corresponds to the directed net diffusional flux of particles under the influence of a temperature gradient. If the temperature gradient is stationary, the molecular concentration eventually reaches a steady state through the simultaneous and opposite effects of thermal diffusion (with coefficient D_T) and standard (Fick) diffusion (with coefficient D). The phenomenon of thermophoresis was first described in the 19th

¹Systems Biophysics, Physics Department, Nanosystems Initiative Munich and Center for NanoScience, Ludwig-Maximilians-Universität München, Amalienstr. 54, 80799 München, Germany. ²Faculty of Physics and Center for NanoScience (CeNS), Ludwig Maximilians University, Geschwister-Scholl-Platz 1, 80539 München, Germany. ³Department of Chemistry, University of Cambridge, Lensfield Road, Cambridge CB2 1EW, UK. [†]Present address: Institute of Physical Biology, University of Düsseldorf, Universitätsstr. 1, 40225 Düsseldorf, Germany. Correspondence and requests for materials should be addressed to D.B. (email: dieter.braun@lmu.de) or A.K.B. (email: alexander.buell@uni-duesseldorf.de)

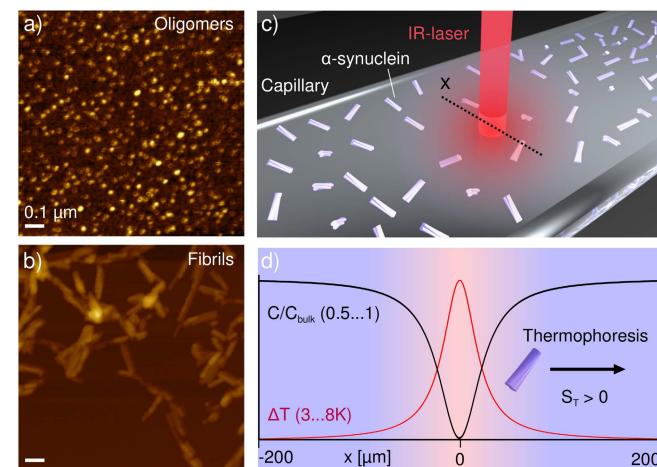


Figure 1. Quantitative thermophoresis of proteins. AFM images of oligomeric (a) and fibrillar (b) forms of the protein α -synuclein, associated with Parkinson's disease. The oligomers have an average diameter of 15 nm in solution, as determined by fluorescence correlation spectroscopy. (c) An initially homogeneous solution, or a suspension of a protein species, here illustrated with fibrillar aggregates, is subjected to localized heating by an IR-laser inside a borosilicate capillary, which leads to directed movement of molecules and complexes along the temperature gradient, until a steady state is established. (d) The radially averaged temperature profile (typically established within less than a second after turning on the laser), and the concentration profile (usually established within seconds to minutes) are illustrated schematically at steady state. A schematic fibril is displayed undergoing positive thermophoresis, i.e. migrating away from the heated spot.

century^{9,10} and has recently seen a surge in attention, due to its many potential biophysical applications¹¹ and even possible role in the origins of life¹².

In a thermophoretic experiment, the concentration of thermally diffusing particles or molecules, c , can be described by a combination of local equilibrium and non-equilibrium effects, and follows an exponential distribution: $c(\vec{x})/c_0(\vec{x}_0) = \exp(-S_T(T(\vec{x}) - T_0(\vec{x}_0)))^{13}$, where $S_T = D_T/D$ is the Soret coefficient. Through the creation of well-defined temperature gradients and the subsequent measurement of concentration distributions at steady state, the intrinsic propensities of particles to exhibit thermophoresis can be determined. Temperature gradients can be created through joule heating¹⁴, the generation of a hot reservoir¹⁵ or by absorption of infrared (IR) laser radiation (Fig. 1c)¹⁶, and the concentration profiles of the species undergoing thermophoresis can be mapped via measurements of variations in refractive index¹⁷, light scattering¹⁸ or fluorescence intensity¹⁶, provided that the species are suitably labeled or show intrinsic fluorescence¹¹.

The increasing recognition of the potential importance of thermophoresis for the characterization of biomolecular binding equilibria is paralleled by extensive fundamental research activity on the thermophoretic properties of polymeric and colloidal systems^{16,19–21}, as well as solvent mixtures²². Despite the current lack of an overarching theory of thermophoresis of different systems, interesting trends have been observed in a variety of systems. For nonionic polymers a saturation of the thermal diffusion coefficient after several Kuhn segments has been found in a large set of nonpolar solvents²³ as well as in water^{20,24}. Nevertheless, no general tendency of increasing or decreasing Soret coefficient with size for uncharged polymers has been observed^{20,25} and theoretical models are still under debate^{26,27}. For charged polymers, substantial progress has been made in the understanding of ionic effects in recent years. Thermal gradients lead to the development of concentration gradients for the ionic species²⁸, which contribute to the movement of charged polymers by the build-up of electric fields^{16,29} and diffusiophoresis³⁰. Furthermore, thermal gradients also introduce contributions to the Soret coefficient which arise from the change in free energy of the Debye layer associated with the temperature change³¹ and can be described by considering local equilibrium¹³. These models have been successfully tested for spherical particles by variation of ionic strength^{16,32,33} and extended to elongated structures, such as viruses³⁴ and DNA³⁵. The Soret coefficients of proteins and various other charged polymers have also been found to increase with temperature in a manner that is described by an empirical formula¹⁷. Although fundamental research into the origin of this temperature dependence is ongoing, the Soret effect has already been exploited for particle separation¹⁵ and the detection of phase transitions³⁶.

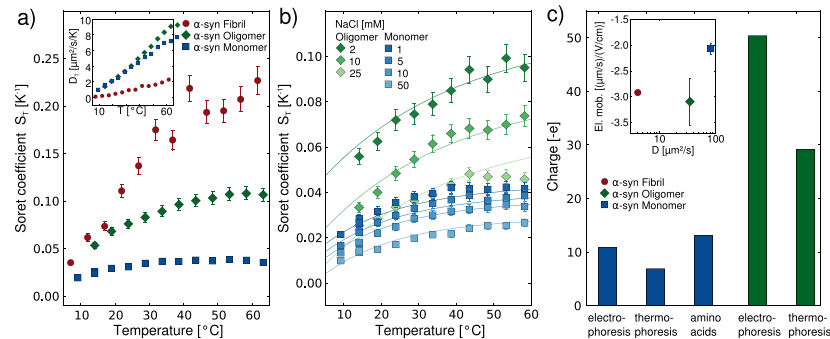


Figure 2. Thermophoretic characterization of three distinct α -synuclein species. (a) The Soret coefficients, S_T , of monomeric, oligomeric and fibrillar α -synuclein (in 1 mM Tris buffer at pH 7.4) as a function of temperature, showing their strong size-dependence. Inset: The thermal diffusion coefficient, $D_T = DS_T$, as a function of temperature. (b) Fit of the temperature dependence of S_T of α -synuclein monomers (blue) and oligomers (green) at different concentrations of added NaCl. The data are globally fitted to a model that includes the electrostatic effects relevant for thermophoresis and where the effective charges of the species and the Soret coefficient of the Tris ion are the only free parameters. (c) The charges determined from the fits in (b) compared with the charges determined from an analysis of the electrophoretic mobilities (supplementary section 6). For the monomer, the charge expected from the amino acid composition is also plotted. Inset: The free flow electrophoretic mobilities³³ of fluorescently labeled monomeric, oligomeric and fibrillar α -synuclein (in 5 mM Tris buffer pH 7.4) are plotted against their diffusion coefficients (from FCS measurements⁴², and supplementary section 5).

The binding of a ligand to a biomolecule can in many cases induce a change in thermophoretic behavior that is sufficiently large to be detected, and hence a binding curve can be obtained through measurements of a dilution series of one of the binding partners. It has been shown, for example, that binding constants for protein-ligand interactions can be obtained rapidly in this way, even under the most challenging solution conditions and using only minute quantities of sample⁸.

Despite the increasing attention being focused on such effects and the great potential of thermophoresis for high throughput screening, it is not yet possible to predict from first principles the value of the Soret coefficient of any protein under a given set of conditions, or even the sign and magnitude of a change in the Soret coefficient induced by the binding of a ligand. Indeed, very few studies have so far addressed the problem of quantitative measurements of the thermophoresis of proteins¹⁷ or protein assemblies³⁷. The aim of the studies described here is to advance our fundamental understanding of protein thermophoresis through the study of distinct forms of the protein α -synuclein. We have chosen this protein because of its relevance to Parkinson's disease, as well as its well-established ability to form different types of stable aggregates, such as oligomeric structures³⁸ and mature amyloid fibrils³⁹. In addition, the monomeric protein is kinetically highly stable in bulk solution, and in the absence of catalytic surfaces it does not aggregate at a detectable rate even at high concentrations^{40,41}, facilitating its study by biophysical techniques. Therefore, α -synuclein represents an excellent system through which to study the influence of the size and nature of protein assemblies on their thermophoretic behavior. In particular, we have used a combination of fluorescence correlation spectroscopy (FCS)⁴² and microfluidic free flow electrophoresis⁴³, along with measurements of the Soret coefficients of fluorescently labeled monomeric and aggregated α -synuclein to examine the importance of electrostatic effects in protein thermophoresis. We find that while the different aggregated species cannot be discriminated based on their electrophoretic mobilities, they exhibit very distinct thermophoretic mobilities. In addition, we show that the binding of a high affinity single domain antibody (nanobody) as well as of a natural small molecule, epigallocatechin gallate (EGCG^{44,45}) to α -synuclein aggregates can be probed by exploiting changes in thermophoretic behavior upon binding. These results establish thermophoresis as a useful method for binding studies to a highly challenging class of target structures.

Results

Thermophoresis of protein structures is size-dependent. We have produced fluorescently labeled monomeric, oligomeric and fibrillar α -synuclein (see supplementary section 2 for detailed protocols) and characterized these different species by atomic force microscopy (AFM, Fig. 1) and FCS (supplementary section 5). For the aggregated forms of the protein, we used a minimally invasive labeling strategy, in which only a small fraction of the protein molecules within each aggregate is labeled. We then measured the Soret coefficients, S_T , of these three distinct and well-defined forms of α -synuclein at low ionic strength (1 mM Tris buffer) as a function of temperature (Fig. 2a), using a thermophoresis setup with laser heating and a camera¹⁶ (see supplementary

section 4) to record the time evolution and steady-state distribution of the concentration of fluorescently labeled protein aggregates. In these experiments unlabeled protein molecules and aggregates are invisible. The absolute magnitude of S_T was found to increase with the size of the α -synuclein structure (Fig. 2a). A size dependence of the Soret coefficient has been observed previously^{13,21,46}, but the question of whether or not the thermal diffusion coefficient $D_T = DS_T$ also depends on size has been controversial, although most results point towards the size independence of D_T for simple colloid systems^{24,46}. We find here that while monomeric and oligomeric forms of α -synuclein have very similar thermal diffusion coefficients, D_T is markedly smaller for the fibrillar form of the protein (Inset to Fig. 2a). In order to investigate the origin of the size dependence of S_T in more detail, therefore, we have performed experiments under a range of different solution conditions.

The thermophoresis of proteins is dominated by electrostatic effects. We first explored the effects of variations in ionic strength on the thermophoretic behavior of the various proteinaceous species studied here, as significant effects have been observed previously for DNA¹⁶. The magnitude of the Soret coefficient decreases when the ionic strength is increased for monomeric and oligomeric α -synuclein species (Fig. 2b). The absolute change in S_T for a given variation in ionic strength is, however, observed to depend on the size and charge of the α -synuclein species, with a more pronounced dependence being observed for the oligomers. Similar experiments for fibrillar α -synuclein were not pursued because an increase in ionic strength can induce higher order assembly of fibrils, as reported previously³⁹, making an accurate determination of the absolute Soret coefficient difficult.

We have recently presented a theoretical description that for DNA quantitatively captures the various electrostatic effects important in thermophoresis, such as the capacitor effect and the Seebeck effect¹⁶ and (see supplementary section 7). The most important parameters in this model are the size, charge and electrophoretic mobility of the macromolecule under investigation. We have here been able to determine all of these parameters independently for the three distinct types of α -synuclein species (inset to Fig. 2c) by using FCS⁴² to measure the standard (Fick) diffusion coefficients (supplementary section 5); the latter can be used to determine the dimensions of the structures. Assuming spherical geometry³⁸, we obtain hydrodynamic diameters of 5.6 nm and 15 nm for the monomeric and oligomeric α -synuclein, respectively. In addition, the (sonicated) fibril length distributions were characterized in detail by AFM and we found an average length of ~ 200 nm and a diameter of ~ 8 nm. Furthermore, we used microfluidic free flow electrophoresis⁴³ and (supplementary section 6) to determine the electrophoretic mobility of each species (inset to Fig. 2c). We have fitted the data to a model that takes both the capacitor and Seebeck effects into account (supplementary section 7), allowing us to decompose the Soret coefficient into charge-dependent effects and non-ionic contributions. The fits yield an effective charge that appears to be responsible for the strong dependence of the thermophoresis on the ionic strength of the solution. We can also estimate the charges of the distinct α -synuclein species from their electrophoretic mobilities. To that end, the monomeric and oligomeric forms of α -synuclein were approximated as spheres and the fibrils as rods, enabling us to use the theoretical framework already developed for colloids⁴⁷, yielding charges of -10.9 e for the monomer, -50.4 e for the oligomer and a value in the range from -200 e to -300 e for the fibrils (supplementary section 6). The value for the monomer is in good agreement with that calculated from the amino acid composition at this pH (-9.1 e) in addition to the charges carried by the fluorescent label (-4 e). It is interesting to see that the oligomers, despite being composed of ca. 30 monomers on average³⁸, have a net charge only about 5 times higher than that of the monomer. This difference between expected and determined charge, which is even more pronounced for fibrillar α -synuclein, can be explained through a shift of the pK_a values of the ionizable residues in the aggregates with respect to the monomeric state, as well as the absorption and incorporation of counter ions into the oligomers and fibrils⁴⁸. The values of the effective charges (see Fig. 2c for an overview) of the α -synuclein monomers and oligomers calculated from the thermophoretic data (-6.9 e and -29.2 e) are significantly smaller than those resulting from the fits to the electrophoretic mobilities (-10.9 e and -50.4 e). Due to the lack of experimental data on the ionic strength dependence of the S_T values of the fibrils, we cannot estimate the thermophoretic charge of the fibrils. Since studies that directly compare effective charges determined from electrophoretic and thermophoretic measurements are rare^{40,33}, the data shown here provide an important benchmark through which to improve the theoretical descriptions of both electrophoretic and thermophoretic phenomena of complex biomolecular structures such as protein molecules and supramolecular protein aggregates. Note that the Soret coefficient of the positively charged Tris ion was determined from a global fit to the ionic strength dependence of the thermophoresis of monomeric and oligomeric α -synuclein to be 0.0031/K, and the value obtained is at least comparable in magnitude to the one of the sodium ion with 0.00469/K^{16,49}.

We next tested whether or not the presence of an excess of unlabeled monomeric α -synuclein leads to a change in the thermophoresis of the fluorescently labeled monomeric, oligomeric and fibrillar α -synuclein (Fig. 3). We find that the thermophoresis of both labeled monomeric and oligomeric α -synuclein is decreased by the presence of an excess (70 μM) of unlabeled monomeric α -synuclein (Fig. 3a). Furthermore, we find that the Soret coefficient of fibrillar α -synuclein at 20 °C in the presence of 40 μM unlabeled monomeric α -synuclein shows also a decreased value compared to the sample without added monomeric protein (Fig. 3b). Under these conditions of low ionic strength and relatively low temperature, the rate of incorporation of monomeric protein into the amyloid fibrils is negligibly slow³⁹. However, when we heat the samples for 20 min to 70 °C, and again determine the Soret coefficient (Fig. 3b), we find that S_T has significantly increased for the sample with the added monomer, whereas the increase is smaller for the sample without any added monomer. Analysis of the length distributions of the amyloid fibrils before and after the incubation at 70 °C illustrates that the fibrils have increased in length due to monomer incorporation (Fig. 3c). As the temperature is increased, the structural rearrangements and/or desolvation necessary for the incorporation reaction of the α -synuclein monomers into the fibrils are significantly accelerated^{39,50}.

These results suggest that the presence of unlabeled monomeric α -synuclein does indeed affect the thermophoresis of monomeric and aggregated α -synuclein. In order to elucidate the physical origin of this effect, we have

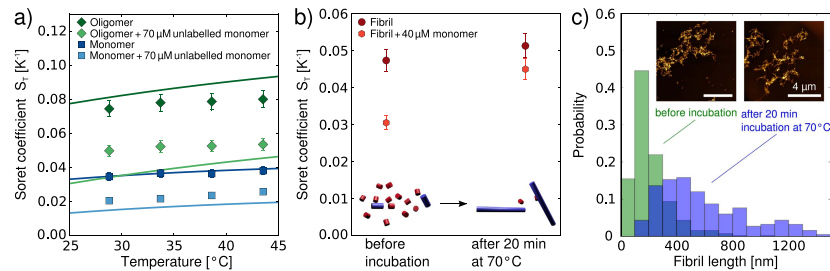


Figure 3. The effect of unlabeled (and hence invisible) monomeric α -synuclein on the thermophoresis of the distinct α -synuclein species. (a) Temperature dependence of S_T for labeled monomeric and oligomeric α -synuclein in the presence and absence of a high background concentration (70 μ M) of unlabeled monomeric α -synuclein in 1 mM Tris buffer pH 7.4. The solid lines are predictions if the unlabeled monomer is treated as an ionic species within the theoretical thermophoretic model used here (see main text and supplementary section 7). (b) The Soret coefficient of fibrillar α -synuclein at 20 $^{\circ}$ C, in the presence and absence of 40 μ M unlabeled monomeric α -synuclein, before and after a 20 min period of heating to 70 $^{\circ}$ C. (c) Length distributions of the α -synuclein fibrils with added unlabeled monomer before and after 20 min heating to 70 $^{\circ}$ C.

computed the predicted decrease in Soret coefficient due to the additional Seebeck and capacitor effects caused by the presence of the unlabeled monomer, treating the latter as an additional salt species with the Soret coefficient and charge as determined above for labeled monomer (mean value over the examined temperature range: $S_T^{mon} = 0.031/\text{K}$). The predictions are shown in Fig. 3a as solid lines and show that the decrease in Soret coefficient induced by the presence of the unlabeled monomer can be quantitatively described by treating the unlabeled α -synuclein monomer as a dissolved electrolyte. It is surprising that this simple approximation yields a relatively good description of the observed behavior, given the limited validity of Debye Hückel theory when treating highly charged macromolecules, such as the α -synuclein monomers, as counterions in the capacitor effect. Indeed, the Debye length at the ionic strength that can be formally attributed to the presence of the 70 μ M unlabeled α -synuclein (ca. 5 nm) is much shorter than the average distance between the protein molecules at this concentration (ca. 30 nm). Nevertheless, based on the agreement between the experiments and the modeling, the decrease in Soret coefficient of the three α -synuclein species in the presence of an excess of unlabeled monomeric α -synuclein appears to be caused, at least in part, by the electrostatic effects exerted by the latter on the former. In the case of labeled α -synuclein monomer, the addition of unlabeled monomer is of course equivalent to an increase in the total concentration of the protein, and it has been reported previously that an increase in concentration of a charged species decreases the Soret coefficient¹⁶. Since the concentration of unlabeled monomer is far below the overlap concentration (~ 0.01 Mol/l), effects of the added species upon viscosity are expected to play a minor role here. Furthermore, even at higher viscosities, the steady state distributions of molecules in a temperature gradient are not necessarily affected, due to the dependence of both D and D_T on viscosity²³, which can lead to viscosity independent Soret coefficients S_T . Therefore the results of our particular experimental design where only part of the protein molecules are visible allow us to conclude that the effect of an increase in concentration on thermophoresis can be understood in the general framework of electrostatic interactions in the dilute regime.

Measurement of ligand binding constants to monomeric and aggregated α -synuclein. Having established the general principles governing the thermophoresis of protein aggregates, we proceeded to investigate the application of this technique for ligand screening and characterization of the binding of ligands to the aggregates. For this purpose, we investigated the effects of the binding of a single domain camelid antibody (nanobody), which has been shown to bind to the disordered C-terminal region of α -synuclein³, on the thermophoresis of different α -synuclein species. We first determined the S_T values of monomeric and oligomeric α -synuclein in the presence of a saturating concentration of the nanobody (Fig. 4a) and found that in both cases the bound state displays a reduced thermophoretic effect. The nanobody is positively charged at neutral pH (+1.5 e), and therefore the net global charge of the protein-nanobody complex is lower than that of the protein alone. If the observed decreases in Soret coefficient are attributed solely to decreases in charge, it would correspond to a change in charge of +2.7 e for the monomer and +7.0 e for the oligomer (compare solid lines in Fig. 4a). Therefore, at least for the monomer, which is known to bind with a stoichiometry of 1:1 to the nanobody, the observed effect appears larger than expected purely on electrostatic grounds. One reason for this enhanced effect might be the change in overall size and hydrophobicity⁵¹ associated with the binding of the nanobody. For the oligomers, the value of the reduced charge suggests a stoichiometry much larger than 1:1, which is consistent with the fact that the oligomers consist on average of 30 monomers. However, due to lack of detailed structural information for the oligomer, and hence the accessibility of the binding epitopes, it is difficult to estimate the stoichiometry. We were unable to perform similar experiments with fibrillar α -synuclein, as the charge reduction associated with the binding of

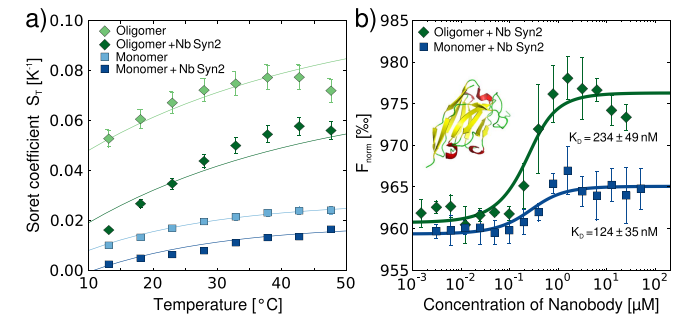


Figure 4. Measurements of the effects of the binding of an antibody on the different α -synuclein species. (a) Temperature dependence of S_T for monomeric and oligomeric α -synuclein in the presence and absence of the single domain camelid antibody (nanobody) Nb Syn2 (structure of Nb Syn2 with coordinates taken from PDB 2X6M⁵³). The solid lines are fits that allow the determination of the reduction in effective charge due to the binding of the nanobody. (b) Binding curves of Nb Syn2 to monomeric and oligomeric α -synuclein obtained with a thermophoresis setup that monitored the time course of the fluorescence intensity at the position of heating. Each data set combines the results from three independent experiments. The data for the monomer were shifted up by 40% for better clarity.

the nanobody led to almost instantaneous formation of macroscopic assemblies of fibrils, that rendered accurate determination of the Soret coefficient impossible.

Based on the observed change in Soret coefficient upon nanobody binding, however, we tested if the binding constant of the nanobody to both monomeric and oligomeric α -synuclein could be measured by using a simplified thermophoresis setup that monitors the time evolution of the total fluorescence intensity in the area of elevated temperature, rather than the full spatial distribution as in the setup used for the determination of the Soret coefficients (integrated vs. spatially resolved approach, see supplementary section 4). In Fig. 4b, we show the corresponding binding curves from the integrated measurements. We obtain binding affinities of the nanobody to monomeric α -synuclein that are in excellent agreement with a previously determined value, obtained from ITC measurements (124 ± 35 nM vs. 130 ± 23 nM⁵²). The binding affinity to the oligomers (234 ± 49 nM) had not previously been reported, partly due to the challenge of obtaining sufficient quantities of pure oligomers, which we have been able to overcome by exploiting the low sample requirements of thermophoresis. Interestingly, the thermophoresis values of the oligomer-nanobody system in the fully bound state do not reach a stable plateau, but rather decrease linearly. This effect could be caused by the electrostatic influence of the excess free nanobody on the thermophoresis of the oligomer-nanobody complex. In general, electrostatic effects of free ligand molecules might in this way be able to distort binding curves of charged molecules determined by thermophoresis, if the affinity is sufficiently low such that high ligand concentrations need to be employed. However, in the present case, we do not expect a significant influence on the K_D value, due to the small net charge of the nanobody and the relatively high affinity.

We then investigated the binding of the small molecule epigallocatechin gallate (EGCG), one of the main constituents of green tea, to α -synuclein aggregates. This molecule has been reported to bind to various species on the aggregation pathway of α -synuclein and even to remodel mature amyloid fibrils⁴⁴. We again first probed whether or not the binding to fibrillar and oligomeric α -synuclein manifests itself in a change in Soret coefficient. Despite the fact that EGCG is not charged, we measured a decrease in Soret coefficient upon its binding to both oligomeric and fibrillar α -synuclein (Fig. 5a). The global charge of the aggregates is not expected to change upon binding; indeed, the electrophoretic mobilities of the oligomers and fibrils of α -synuclein are very similar with and without bound EGCG (see inset of Fig. 5a). Therefore it is likely that changes in the overall protein-solvent interactions are responsible for the observed change in S_T . Indeed, it has been proposed that thermophoresis represents a way of probing interactions of particles and molecules with the solvent². Such a proposition is rendered plausible by a significant, temperature-dependent non-electrostatic contribution to S_T (see supplementary section 7) that we were able to determine by subtracting the electrostatic contributions from the overall value of S_T .

Furthermore, as in the case of the nanobody, the binding constant of EGCG to oligomeric and fibrillar α -synuclein can be determined by using the rapid and straightforward integrated approach (Fig. 5b). In these experiments, we found that the ratio of labeled to unlabeled protein within the aggregates is an important experimental parameter, in particular in the case of a compound that is able to influence the fluorescence intensity of the label upon binding, such as EGCG. In addition, if the ratio of the labeled to the unlabeled protein is too high, the surface properties, and hence the binding behavior of α -synuclein aggregates can change significantly as compared to a completely unlabeled structure (supplementary section 4). Using an optimized ratio of labeled to unlabeled protein of ~ 0.02 – 0.03 for both aggregate species, we determined the binding constant of EGCG to α -synuclein amyloid fibrils and oligomers under these conditions to be 2.5 ± 0.4 μ M and 4.3 ± 0.8 μ M,

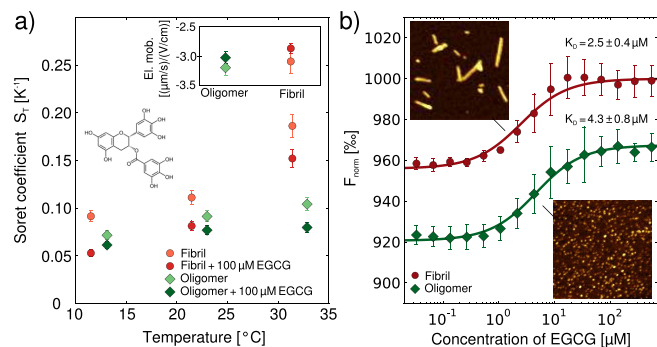


Figure 5. Measurement of binding of EGCG (structure shown in a) to α -synuclein aggregates. (a) Measurements of the Soret coefficients of oligomeric and fibrillar α -synuclein in the presence and absence of 100 μM EGCG. In contrast to thermophoresis, the electrophoretic mobilities remain virtually unchanged in the presence of EGCG (see inset). (b) Binding constants for the interactions of EGCG with oligomeric and fibrillar α -synuclein were measured using the integrated thermophoresis approach. Each data set is an average of three independent experiments. The insets show AFM images (image sizes are $1 \mu\text{m} \times 1 \mu\text{m}$) taken after incubation of oligomers and fibrils for 12 h with 100 μM EGCG. No morphological changes could be detected (compare with Fig. 1a,b).

respectively. The affinity for the fibrils is approximately one order of magnitude lower than the value reported previously under conditions of higher ionic strength⁴⁴, whereas the affinity of EGCG for oligomers has not previously been measured. It has, however, been reported that EGCG can induce structural changes in amyloid fibrils and other protein aggregates⁴⁴, and such a substantial structural rearrangement can be expected to affect the thermophoretic behavior, complicating the determination of binding constants. In order to test whether or not such effects occurred during our binding studies, we incubated oligomeric and fibrillar α -synuclein for 12 h in the presence of 100 μM EGCG followed by AFM imaging, to allow for sufficient time for even slow remodeling processes to take place. The resulting images are shown as insets in Fig. 5b and reveal no noticeable change in morphology compared to freshly prepared oligomers and fibrils (compare with Fig. 1c,d), suggesting that under the conditions employed here, no significant remodeling of fibrils and oligomers is induced by EGCG.

Discussion

We describe in this paper the results of a comprehensive experimental approach that has allowed substantial progress to be made towards a quantitative understanding of the thermophoresis of monomeric and aggregated forms of proteins. The approach consists of a combination of precise control of sample preparation (solution conditions, labeling position and density), independent and quantitative measurements of size, electrophoretic mobility and thermophoretic mobility, as well as theoretical modeling. With this strategy, we have shown that electrostatic effects, in particular electrophoresis in the field created by the temperature-induced ion gradient ('Seebeck effect'), as well as the temperature dependence of the ion cloud extension and its associated electrostatic energy ('capacitor effect') (supplementary section 7 and for details of the modeling process)¹⁶, are important factors in the thermophoresis of proteins and protein aggregates. These conclusions are consistent with those reported previously for nucleic acids^{16,32}, and therefore suggest that there may be universal principles that govern the thermophoresis of charged macromolecules. Such a general understanding of the well-established physico-chemical phenomenon of thermophoresis represents an important step in the further development of this technique as an experimental strategy for characterizing biomolecular interactions.

We were able to combine the advances made using custom built research tools, which allow for the characterization of a range of well-defined physical properties (diffusion coefficient, electrophoretic mobility and Soret coefficient), with the ease of use of a simplified thermophoresis setup that can be applied in a straightforward manner for the determination of binding constants. This dual strategy has allowed us to exploit the precise control of sample preparation for the detection and characterization of the binding of a range of ligands (small molecules and macromolecules) to different types of disease-related protein aggregates. Indeed, we were able to investigate structures ranging from soluble monomeric protein molecules to oligomeric structures and mature amyloid fibrils. Because of the importance of electrostatic effects in defining the magnitude of the observed thermophoretic effect, these results show that thermophoresis is very well suited for the study of binding events that lead to a change in charge.

Even in cases where there is no change in global charge, however, we found that thermophoresis allowed for detection of binding events, due to the additional dependence on parameters such as size and interaction with the solvent. Indeed, we observed that protein aggregates that are very different in size and structure, but which display a very similar electrophoretic mobility, such as oligomeric and fibrillar α -synuclein, show a marked difference

in thermophoretic mobility. Furthermore, the binding of a ligand that does not lead to a change in global charge and electrophoretic mobility, such as of the compound EGCG, to oligomeric and fibrillar α -synuclein leads to a detectable change in thermophoretic behavior. It has recently been shown in this regard that the binding of EGCG to α -synuclein oligomers changes their surface properties significantly, and renders them less disruptive to lipid membranes⁴⁵. The thermophoretic response to changes in surface hydrophobicity reflects the physical complexity of systems with non-uniform temperature that leads to a potentially greater discriminatory power compared to other separation techniques based only on size or electrophoretic mobility.

Conclusions

The results of this study have contributed significantly to the rationalization of the size and charge-dependence of protein thermophoresis, and therefore have significantly advanced our fundamental understanding of this phenomenon and enabled a general strategy to be outlined that would deepen this understanding further in the future. This strategy consists of specifically designed sample preparation and labeling strategies, combined with state-of-the-art thermophoretic, electrophoretic and size measurements of the structures under study and theoretical analysis and modeling of the physico-chemical factors that determine thermophoresis. We have been able to show that species such as oligomeric and fibrillar protein aggregates show very similar electrophoretic, but very distinct thermophoretic behavior.

Equally importantly, we have also established the possibility of using thermophoresis for the screening and characterization of ligand binding to disease-related protein aggregates. Despite the fact that microscale thermophoresis is in the process of becoming a well-established experimental technique for protein-ligand binding affinity measurements, it has not previously been reported for the study of ligand binding to supramolecular aggregates, such as amyloid fibrils. Due to their polymeric nature these types of samples are substantially more challenging to handle than most soluble monomeric proteins and we present here a comprehensive protocol for the use of microscale thermophoresis for amyloid-ligand binding assays. The possibility of characterizing novel types of ligands that bind to protein aggregates, both small and large molecules, at high throughput and using minute sample quantities is a highly valuable addition to the experimental toolbox available for the development of diagnostic and therapeutic strategies against protein misfolding diseases. In particular, we would like to emphasize that oligomeric structures, which have been highlighted as the most toxic species on the aggregation pathway²³, often occur only at low concentration and with short lifetimes and hence experimental methods that are rapid and require only small amounts of sample are vital for their study.

Materials and Methods

Detailed protocols for sample preparation and for the measurements of diffusion coefficients, electrophoretic mobilities, Soret coefficients and binding curves can be found in the supplementary materials.

References

- Knowles, T. P. J., Vendruscolo, M. & Dobson, C. M. The amyloid state and its association with protein misfolding diseases. *Nat Rev Mol Cell Biol* **15**, 384–396 (2014).
- Spillantini, M. G. *et al.* Alpha-synuclein in lewy bodies. *Nature* **388**, 839–840 (1997).
- Klunk, W. E., Debnath, M. L. & Pettegrew, J. W. Development of small molecule probes for the beta-amyloid protein of Alzheimer's disease. *Neurobiol Aging* **15**, 691–698 (1994).
- Mirecka, E. A. *et al.* Sequestration of a β -hairpin for control of α -synuclein aggregation. *Angew Chem Int Ed Engl* **53**, 4227–4230 (2014).
- Guilliams, T. *et al.* Nanobodies raised against monomeric α -synuclein distinguish between fibrils at different maturation stages. *J Mol Biol* **425**, 2397–2411 (2013).
- Ge, J.-F., Qiao, J.-P., Qi, C.-C., Wang, C.-W. & Zhou, J.-N. The binding of resveratrol to monomer and fibril amyloid beta. *Neurochem Int* **61**, 1192–1201 (2012).
- Jerabek-Willemsen, M., Wienken, C. J., Braun, D., Baaske, P. & Duhr, S. Molecular interaction studies using microscale thermophoresis. *Assay Drug Dev Technol* **9**, 342–353 (2011).
- Seidel, S. A. *et al.* Microscale thermophoresis quantifies biomolecular interactions under previously challenging conditions. *Methods* **59**, 301–315 (2013).
- Soret, C. *Archives des Sciences Physiques et Naturelles de Genève* **11**, 48–61 (1879).
- Ludwig, C. *Sitzungber Bayer Akad Wiss Wien - Math-Naturwiss Kl* **20**, 539 (1856).
- Seidel, S. A. *et al.* Label-free microscale thermophoresis discriminates sites and affinity of protein-ligand binding. *Angew Chem Int Ed Engl* **51**, 10656–10659 (2012).
- Braun, D. & Libchaber, A. Thermal force approach to molecular evolution. *Phys. Biol.* **1**, 1–8 (2004).
- Duhr, S. & Braun, D. Thermophoretic depletion follows Boltzmann distribution. *Phys Rev Lett* **96**, 168301 (2006).
- de Mello, A. J., Habgood, M., Lancaster, N. L., Welton, T. & Wootton, R. C. R. Precise temperature control in microfluidic devices using joule heating of ionic liquids. *Lab Chip* **4**, 417–419 (2004).
- Vigolo, D., Rusconi, R., Stone, H. A. & Piazza, R. Thermophoresis: microfluidics characterization and separation. *Soft Matter* **6**, 3489–3493 (2010).
- Reich, M., Herzog, M., Gütz, A. & Braun, D. Why charged molecules move across a temperature gradient: the role of electric fields. *Phys Rev Lett* **112**, 198101 (2014).
- Iacopini, S. & Piazza, R. Thermophoresis in protein solutions. *Europhys. Lett.* **63**(2), 247–253 (2003).
- Wiegand, S., Ning, H. & Krieger, H. Thermal diffusion forced Rayleigh scattering setup optimized for aqueous mixtures. *J Phys Chem B* **111**, 14169–14174 (2007).
- Würger, A. Transport in charged colloids driven by thermoelectricity. *Phys Rev Lett* **101**, 108302 (2008).
- Wang, Z., Afanasenkau, D., Dong, M., Huang, D. & Wiegand, S. Molar mass and temperature dependence of the thermomodification of polyethylene oxide in water/ethanol mixtures. *The Journal of Chemical Physics* **141**(6), 064904 (2014).
- Braibanti, M., Vigolo, D. & Piazza, R. Does thermophoretic mobility depend on particle size? *Phys Rev Lett* **100**, 108303 (2008).
- Hartmann, S. *et al.* Thermophobility of liquids: Heats of transport in mixtures as pure component properties. *Phys. Rev. Lett.* **109**, 065901 (2012).
- Stadelmaier, D. & Köhler, W. Thermal diffusion of dilute polymer solutions: The role of chain flexibility and the effective segment size. *Macromolecules* **42**(22), 9147–9152 (2009).

24. Chan, J., Popov, J. J., Kolsinek-Kehl, S. & Least, D. G. Soret coefficients for aqueous polyethylene glycol solutions and some tests of the segmental model of polymer thermal diffusion. *J. Sol. Chem.* **32**(3), 197–214 (2003).
25. Kishikawa, Y. *et al.* Temperature dependence of thermal diffusion for aqueous solutions of monosaccharides, oligosaccharides, and polysaccharides. *Phys. Chem. Chem. Phys.* **14**, 10147–10153 (2012).
26. Würger, A. Molecular-weight dependent thermal diffusion in dilute polymer solutions. *Physical Review Letters* **102**, 078302 (2009).
27. Morozov, K. I. & Köhler, W. Thermophoresis of polymers: nondraining vs draining coil. *Langmuir* **30**, 6571–6576 (2014).
28. Römer, F., Wang, Z., Wiegand, S. & Bresme, F. Alkali halide solutions under thermal gradients: Soret coefficients and heat transfer mechanisms. *J Phys Chem B* **117**, 8209–8222 (2013).
29. Vigolo, D., Buzzaccaro, S. & Piazza, R. Thermophoresis and thermoelectricity in surfactant solutions. *Langmuir: the ACS journal of surfaces and colloids* **26**, 7792–7801 (2010).
30. Eslahian, K. A., Majeed, A., Maskos, M. & Würger, A. Specific salt effects on thermophoresis of charged colloids. *Soft Matter* **10**, 1931 (2014).
31. Dhont, J. K. G., Wiegand, S., Duhr, S. & Braun, D. Thermodiffusion of charged colloids: single-particle diffusion. *Langmuir* **23**, 1674–1683 (2007).
32. Duhr, S. & Braun, D. Why molecules move along a temperature gradient. *Proc Natl Acad Sci USA* **103**, 19678–19682 (2006).
33. Ning, H., Dhont, J. K. G. & Wiegand, S. Thermal-diffusive behavior of a dilute solution of charged colloids. *Langmuir* **24**, 2426–2432 (2008).
34. Wang, Z., Krieger, H., Buitenhuis, J., Dhont, J. K. G. & Wiegand, S. Thermophoresis of charged colloidal rods. *Soft Matter* **9**, 8697–8704 (2013).
35. Reichl, M., Herzog, M., Greiss, F., Wolff, M. & Braun, D. Understanding the similarity in thermophoresis between single- and double-stranded DNA or RNA. *Phys. Rev E* **91**, 062709 (2015).
36. Wolf, M., Braun, D. & Nash, M. A. Detection of thermoresponsive polymer phase transition in dilute low-volume format by microscale thermophoretic depletion. *Anal Chem* **86**, 6797–6803 (2014).
37. Blanco, P., Krieger, H., Lettinga, M. P., Holmqvist, P. & Wiegand, S. Thermal diffusion of a stiff rod-like mutant Y21M fd-virus. *Biomacromolecules* **12**, 1602–1609 (2011).
38. Lorenzen, N. *et al.* The role of stable α -synuclein oligomers in the molecular events underlying amyloid formation. *J Am Chem Soc* **136**, 3859–3868 (2014).
39. Buell, A. K. *et al.* Solution conditions determine the relative importance of nucleation and growth processes in α -synuclein aggregation. *Proc Natl Acad Sci USA* **111**(21), 7671–7676 (2014).
40. Campioni, S. *et al.* The presence of an air-water interface affects formation and elongation of alpha-synuclein fibrils. *J Am Chem Soc* **136**(7), 2866–2875 (2014).
41. Galvagnion, C. *et al.* Lipid vesicles trigger α -synuclein aggregation by stimulating primary nucleation. *Nat Chem Biol* **11**, 229–234 (2015).
42. Mittag, J. J., Milani, S., Walsh, D. M., Rädler, J. O. & McManus, J. J. Simultaneous measurement of a range of particle sizes during A β 1–42 fibrillogenesis quantified using fluorescence correlation spectroscopy. *Biochem Biophys Res Commun* **448**, 195–199 (2014).
43. Herling, T. W. *et al.* Integration and characterization of solid wall electrodes in microfluidic devices fabricated in a single photolithography step. *Applied physics letters* **102**, 184102 (2013).
44. Bieschke, J. *et al.* ECGG remodels mature alpha-synuclein and amyloid-beta fibrils and reduces cellular toxicity. *Proc Natl Acad Sci USA* **107**, 7710–7715 (2010).
45. Lorenzen, N. *et al.* How epigallocatechin gallate can inhibit α -synuclein oligomer toxicity *in vitro*. *J Biol Chem* **289**, 21299–21310 (2014).
46. Vigolo, D., Brambilla, G. & Piazza, R. Thermophoresis of microemulsion droplets: size dependence of the Soret effect. *Phys Rev E Stat Nonlin Soft Matter Phys* **75**, 040401 (2007).
47. Hunter, R. J. *Zeta Potential in Colloid Science: Principles and Applications* (Academic Press, 1981).
48. Manning, G. S. Limiting laws and counterion condensation in polyelectrolyte solutions. V. Further development of the chemical model. *Biophys Chem* **9**, 65–70 (1978).
49. Takeyama, N. & Nakashima, K. Proportionality of intrinsic heat of transport to standard entropy of hydration for aqueous ions. *Journal of Solution Chemistry* **17**(4), 305–325 (1988).
50. Buell, A. K. *et al.* Detailed analysis of the energy barriers for amyloid fibril growth. *Angew Chem Int Ed Engl* **51**, 5247–5251 (2012).
51. Maeda, K., Shinyashiki, N., Yagihara, S., Wiegand, S. & Kita, R. Ludwig-Soret effect of aqueous solutions of ethylene glycol oligomers, crown ethers, and glycerol: Temperature, molecular weight, and hydrogen bond effect. *J. Chem. Phys.* **143**, 124504 (2015).
52. Kaye, R. *et al.* Common structure of soluble amyloid oligomers implies common mechanism of pathogenesis. *Science* **300**, 486–489 (2003).
53. Genst, E. J. D. *et al.* Structure and properties of a complex of α -synuclein and a single-domain camelid antibody. *J Mol Biol* **402**, 326–343 (2010).

Acknowledgements

This work was supported by the Nanosystems Initiative, Munich (DB), the Deutsche Forschungsgemeinschaft (SFB 1032 Project A4, DB, MW), the European Research Council (DB, MW), a grant from the Simons Foundation (SCOL 327125, DB, MW), the UK BBSRC (CMD, TPJK, TWH), the Wellcome Trust (CMD, TPJK), The Frances and Augustus Newman Foundation (TPJK), Magdalene College, Cambridge (AKB), the Federation of European Biochemical Societies (AKB) and the Leverhulme Trust (AKB). We thank Beata Blaszczyk and Sam Ness for help with the protein expression, Tom Nikolaus for help with the protein purification and Daniel Otzen, Ehud Yariv and Hiroyuki Ohshima for helpful discussions. We thank Jonathan Liu for proofreading the article.

Author Contributions

A.K.B., M.W. and D.B. conceived and designed the study. A.K.B., M.W., J.J.M. and T.W.H. performed the experiments and analysed the data. E.D.G. contributed reagents. A.K.B., M.W., D.B., T.P.J.K. and C.M.D. wrote the manuscript. The authors declare no conflicts of interest.

Additional Information

Supplementary information accompanies this paper at <http://www.nature.com/srep>

Competing financial interests: The authors declare no competing financial interests.

How to cite this article: Wolff, M. *et al.* Quantitative thermophoretic study of disease-related protein aggregates. *Sci. Rep.* **6**, 22829; doi: 10.1038/srep22829 (2016).



This work is licensed under a Creative Commons Attribution 4.0 International License. The images or other third party material in this article are included in the article's Creative Commons license, unless indicated otherwise in the credit line; if the material is not included under the Creative Commons license, users will need to obtain permission from the license holder to reproduce the material. To view a copy of this license, visit <http://creativecommons.org/licenses/by/4.0/>

Supplementary information: Quantitative thermophoretic study of disease-related protein aggregates

Manuel Wolff¹, Judith J. Mittag², Therese W. Herling³, Erwin De Genst³, Christopher M. Dobson³, Tuomas P.J. Knowles³, Dieter Braun^{1,*} and Alexander K. Buell^{3,4,*}

¹Systems Biophysics, Physics Department, Nanosystems Initiative Munich and Center for NanoScience, Ludwig-Maximilians-Universität München, Amalienstr. 54, 80799 München, Germany

²Faculty of Physics and Center for Nanoscience (CeNS), Ludwig Maximilians University, Geschwister-Scholl-Platz 1, 80539 Munich, Germany

³Department of Chemistry, University of Cambridge, Lensfield Road, Cambridge CB2 1EW, UK

⁴Present address: Institute of Physical Biology, University of Düsseldorf, Universitätsstr.1, 40225 Düsseldorf, Germany

*authors to whom correspondence should be addressed: dieter.braun@lmu.de, alexander.buell@uni-duesseldorf.de

Content

1. Chemicals and reagents
2. Preparation of protein samples and protein labeling
3. Atomic force microscopy
4. Thermophoresis experiments
5. Fluorescence correlation spectroscopy of monomeric and aggregated α -synuclein
6. Free flow electrophoresis measurements of monomeric and aggregated α -synuclein
7. Modeling the electrostatic effects in protein thermophoresis
8. ComSol simulations of the thermophoresis setup

1 Chemicals and reagents

Thioflavin-T (ThT), Epigallocatechin gallate (EGCG), NaCl, Na₂HPO₄, NaH₂PO₄, PBS tablets and Tris-HCl were purchased from Sigma Aldrich. BCECF, Alexa Fluor[®] 568 C₅ maleimide and Alexa Fluor[®] 647 C₂ maleimide were purchased from Life Technologies Ltd (Paisley, UK).

2 Preparation of protein samples and protein labeling

2.1 Monomeric unlabeled and labeled α -synuclein

Wild type α -synuclein (α -syn) was recombinantly expressed and purified as reported previously [1]. After the last step of the purification protocol, the protein solution (in 20 mM phosphate buffer) was divided into aliquots of 500-1000 μ l at concentrations between 200 and 300 μ M, flash frozen with liquid nitrogen and stored at -80 °C. When the monomeric protein was required in a different buffer, it was dialysed for 24 h against a thousandfold larger volume of the required buffer. For the fluorescent labeling, we used the N122C variant [2], in order to be able to attach the fluorescent label. This variant was expressed and purified similarly to the wild type protein, except that the lysis buffer and all subsequent buffers contained 1 mM EDTA and 1 mM DTT. For the labeling, ca. 0.2 μ mol of N122C variant α -syn in 500 μ l buffer was injected into a Superdex 200 Increase 10/300 GL gel filtration column (GE Healthcare, Little Chalfont, UK) that had been incubated with labeling buffer (Tris or phosphate buffer at ~pH 7, 5-20 mM). The fluorescent dyes (maleimide derivatives) were dissolved at 10 mg/ml in DMSO or DMF and 100 μ l of this stock solution were added to the combined protein fractions immediately after elution. The protein was left to react with the label for 1 h at room temperature and afterwards for 12 h at 4 °C. Then the solution was concentrated to 500 μ l

using Amicon centrifugal concentrators with 3 kDa MW cut-off (Millipore, Watford, UK) and injected into a Superdex 200 Increase 10/300 GL gel filtration column that had been incubated with the buffer the protein was required in, i.e. 20 mM PB buffer pH 6.5 or 5 mM Tris buffer pH 7.4. The most concentrated fractions of the labeled protein were combined and divided into aliquots of 25 μ l. The aliquots were flash frozen in liquid nitrogen and stored at -80 °C until use. Labeling efficiency was evaluated with mass spectrometry (Figure 1 a) and the protein concentration was determined using amino acid analysis (both services provided by PNAC facility, Department of Biochemistry, University of Cambridge). We also kept some of the fractions of free dye label for control experiments (see below). The single chain camelid antibody NbSyn2 was expressed and purified as described in [3].

2.2 Preparation of labeled α -synuclein oligomers

The preparation of stable α -synuclein oligomers is similar to the protocol described in detail in [4]. In short, monomeric α -synuclein is dialysed for 1-3 days against pure water. The solution is then freeze-dried and the lyophilized protein is stored at -80 °C until use. For oligomer formation, the dry protein is dissolved in phosphate buffer saline (PBS) at concentrations between 600 and 800 μ M and incubated at 37 °C for several hours (10-20 h) under quiescent conditions. In most cases, the protein solution had not visibly aggregated/gelled despite the high protein concentration after this incubation period. It has been shown that quiescent α -synuclein solutions in the absence of pre-formed seeds [5] and of other aggregation stimulating conditions, such as lipid bilayers [6] aggregate only very slowly, due to the fact that the fibril nucleation is a heterogeneous process that requires catalytic interfaces, such as the air-water interface [7]. 500 μ l of the protein solution are then injected into a Superdex 200 Increase 10/300 GL gel filtration column, which had been incubated with 5 mM Tris buffer. The protein is eluted at 0.5 ml/min and the oligomers elute as a small peak of ca. 0.75 ml volume after ca. 20 min, followed by a largely dominant monomer peak (Figure 1 b). In order to produce fluorescently labeled oligomers, we reasoned that it would be best to minimize the labeling density; the lowest possible label density corresponds to one dye molecule per oligomer. Using various light scattering techniques, we have in previous work determined these stable α -synuclein oligomers to consist of ~30 monomers on average [4]. Therefore, we used ratios of unlabeled to labeled protein of 30 or higher. Figure 1 b shows an example of a chromatogram illustrating the relative populations of oligomers and monomers and giving an idea about the labeling density.

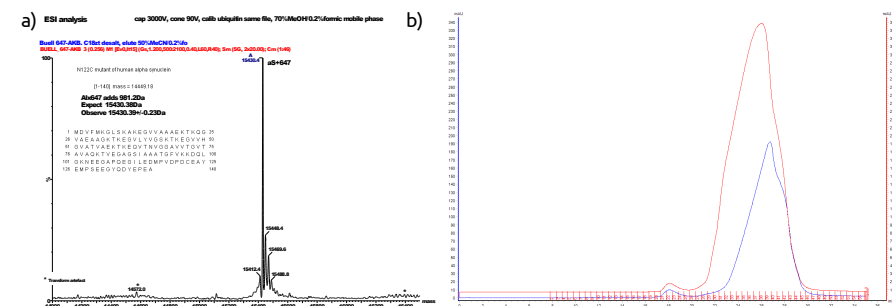


Figure 1: a) Mass spectrum of α -synuclein N122C labeled with Alexa Fluor[®] 647, showing the essentially quantitative labeling. b) Example of a size exclusion chromatogram of a mixture of labeled (with Alexa Fluor[®] 647) and unlabeled α -synuclein, treated according to the protocol described above. The small peak to the left of the large monomer peak corresponds to the oligomers (red: absorption at 647 nm; blue: absorption at 280 nm). Fractions 22 and 23 were combined and used as the oligomeric species. It can be seen that the labeled and unlabeled monomers have slightly different retention times. Also, the relative absorptions at 280 and 647 nm are comparable for the monomer and oligomer peaks, suggesting that the labeled monomer is incorporated statistically into the oligomers and that therefore the labeling density of the oligomers corresponds to the initial proportion of labeled monomer.

Our attempts to label the oligomers proved insightful regarding their mechanism of formation. Adding the labeled protein at different points in the oligomer formation protocol led to very different incorporation efficiencies. When the labeled protein was added after the freeze-dried unlabeled protein had been dissolved in PBS, virtually no labeled oligomers were obtained. Furthermore, the duration of the incubation had very little effect on the labeling yield.

However, the best incorporation efficiency (equal to the ratio of added labeled protein) was achieved when labeled and unlabeled protein were mixed before the dialysis against water. These findings strongly suggest that these stable α -synuclein oligomers form during the process of dialysis and/or lyophilisation and are therefore possibly not directly connected with the molecular pathway that leads to the formation of amyloid fibrils; we have drawn similar conclusions in the past based on kinetic experiments with these oligomers [4].

After gel filtration, the most concentrated oligomer fractions were combined (typically $\sim 500 \mu\text{l}$) and concentrated to about ten times the eluted concentration, using Amicon centrifugal concentrators with 3 kDa MW cut-off (see above). For the measurements of the Soret coefficients, we required the oligomers in 1 mM Tris buffer. In those cases we diluted the concentrated oligomers 1:4 into water and re-concentrated them to the desired final concentration. Once the oligomers were purified and concentrated, they were stable and could be used for several days, as confirmed by fluorescence correlation spectroscopy (see below).

2.3 Preparation of labeled α -synuclein fibrils

Fibrils with varying labeling densities were prepared by seeding a mixture of labeled and unlabeled protein with small percentages (5% or less) of unlabeled fibrils prepared at pH 6.5 and sonicated to create short seeds as described in [5]. For the accurate measurements of S_T , the seeds were incubated with the monomeric fractions (either directly as eluted or concentrated) from the oligomer purification experiments, yielding the same range of labeling densities as for the oligomers ($\leq 1:30$). Under the conditions of low ionic strength (5 mM Tris buffer, pH 7.4) under which the oligomers were purified, the growth of the seed fibrils is relatively slow, due to electrostatic repulsion between the monomer and the fibril end [8]. Therefore we incubated the seeded protein solution at elevated temperature (50 °C) for 2-3 days under heavy stirring with a magnetic stirrer. We verified by fluorescence correlation spectroscopy (FCS, see below) that the monomer content of these fibril samples was below 20%. Under those conditions of very low ionic strength, that have to our knowledge not been studied in detail before, α -synuclein appears to have a relatively high concentration of free monomer at equilibrium, presumably because the free energy of aggregation has an unfavorable electrostatic component [9] that contributes more strongly at lower ionic strength. The yield can be improved by adding NaCl (10 mM) to the seeded protein solution, which can be tolerated as the subsequent dilution of the fibril sample for the thermophoretic measurement will sufficiently dilute the NaCl. Due to the slow dissociation of monomer from the fibril ends, such a diluted fibril suspension will not immediately re-equilibrate to a high free monomer concentration. For the measurements of the Soret coefficients and for FCS measurements, the fibrils were diluted 30-60 fold (to achieve suitable signal intensity and particle counts) into 1 mM Tris buffer pH 7.4 and sonicated for 5 min with a Sonopuls 2070 sonicator with a MS 72 tip (Bandelin electronic, Berlin, Germany) at minimal power and 30% pulses.

Our overall strategy of the production of labeled fibrils was based on our previous extensive studies of α -synuclein fibril formation and growth [5]. We avoided the production of labeled fibrils at higher values of the ionic strength, as we had previously found that the higher order assembly ("flocculation") of fibrils induced at higher ionic strength values is only partly reversible upon dilution into lower ionic strength buffer, even after sonication. In all cases, we produced labeled fibrils by seeded growth reactions, as we have previously shown that in seeded growth, the kinetics of aggregation is independent of the ratio of labeled to unlabeled monomer [2]. Therefore, it is reasonable to assume that the labeled monomer will be incorporated statistically into the growing fibrils, and that therefore the labeling densities correspond to the initial proportions of labeled to unlabeled monomer.

For the measurements of small molecule binding using the commercially available Monolith instrument (Nanotemper, Munich, Germany), the absolute concentration of the amyloid fibrils is an important parameter, and hence we prepared the fibrils from mixtures of unlabeled and labeled protein solutions at known concentrations. 5% seed fibrils were incubated with a total of 50 μM of monomeric protein with varying proportions of labeled and unlabeled α -synuclein molecules in 20 mM phosphate buffer pH 6.5. The samples were incubated at 37 °C overnight, then they were diluted 1:2 into H_2O , sonicated for 3 s and incubated at room temperature overnight. Then the samples were flash frozen in liquid nitrogen and stored at -80 °C until used. No differences in morphology were observed by AFM between fibrils prepared with different proportions of labeled protein.

3 Atomic force microscopy (AFM)

AFM images of purified oligomers and sonicated fibrils were taken using a Nanowizard II atomic force microscope (JPK, Berlin, Germany) using tapping mode in air. The samples were diluted to $\sim 1 \mu\text{M}$ total protein concentration in water and 10 μl were deposited on freshly cleaved mica (Agar Scientific, Stansted, UK) and left to dry. The length distributions were extracted with in-house written Python code, where the ends of the fibrils were manually selected and the program then draws a line onto the fibril, in order to avoid double-counting of fibrils.

4 Thermophoresis experiments

We pursued a dual strategy in this work in order to both improve our fundamental understanding of the physical origins of protein thermophoresis and to demonstrate its usefulness in screening strategies for ligands of disease-related protein aggregates. We performed measurements of the Soret coefficients of different types of aggregates under different conditions in order to test the applicability to proteins of the theoretical description of biomolecular thermophoresis that we have presented in the past for the simpler case of nucleic acids [10, 11]. These experiments were performed using a home-built setup, based on an inverted fluorescence microscope [11], that records the full spatial distribution of fluorescence intensity, and hence concentration of α -synuclein species, as a function of time. Having optimized our experimental protocols (labeling density, solution conditions etc.), we then performed detailed binding experiments with monomeric, oligomeric and fibrillar α -synuclein and small molecule and protein ligands using a commercially available instrument, that measures the total fluorescence intensity in the region of interest as a function of time. For the measurements of Soret coefficients, the concentration of labeled α -synuclein was between 0.1 and 1 μM . Correspondingly, the total protein concentration (by mass) was 30-50 fold higher in the case of the oligomers and fibrils, as these species were produced from mixtures of unlabeled protein doped with 2-3% fluorescently labeled monomer. For the measurements of the binding constants of the antibody NbSyn2 and the small molecule EGCG to oligomeric and fibrillar aggregates, the total protein concentrations by mass were between 0.2 and 0.5 μM with the concentration of labeled protein accordingly 30-50 times lower. For accurate measurements of binding constants, it is important to keep the concentration of one binding partner constant at a value at or below the expected K_D . The resulting low concentrations of labeled α -synuclein were compatible with the sensitivity of the instrument (see below).

4.1 Measurements of Soret coefficients of monomeric and aggregated α -synuclein

Measurements were performed with an upright fluorescence microscope (Zeiss Vario Scope.A1) using an air objective (Zeiss EC-Plan NeoFluar, 40x, NA=0.9), a CCD camera (Andor Luca DL-658M-TiL) and heating from an infrared laser (Fibotec, $\lambda = 1480 \text{ nm}$ absorbed in water) [11], coupled into the optical path right above the objective. To keep convection artifacts below experimental error, measurements were performed in borosilicate capillaries with an inner rectangular cross section of 50 x 500 μm^2 (VitroCom Vitrotubes #5005-050). The thin sample, low numerical aperture and moderate concentration depletion (<50%) ensured that temperature and concentration profiles were equally averaged along the optical axis. For a sketch of the setup, see Figure 2.

The chamber base temperature was controlled by a PID loop using Peltier elements (Telemeter Electronic GmbH, PC-128-10-05) and a heat bath. The chamber height of 50 μm and the moderate temperature rise of less than 9 K above base temperature kept thermal convection small. The measurement was automated and the LED, IR, motorized stage, temperature, and camera trigger were controlled with LabVIEW. The response of the concentration of labeled protein in space and time was recorded at 2.5 Hz by fluorescence imaging. Ten seconds of the equilibrated sample were imaged, followed by different time periods of thermophoretic depletion (depending on the nature of the sample) under optical heating and different time periods to monitor the back-diffusion after switching off the laser.

The profile of the intermittent local optical heating was measured using the temperature dependent fluorescence of the dye BCECF (acid form, Invitrogen B-1151) at a concentration of 50 μM in 10 mM Tris, pH 7.8 (Figure 3a and b). First the peak temperature ΔT for the applied laser power was determined in two dimensions by the assumption of Lorentzian temperature profile $T(r) = T_0 + \Delta T \frac{w^2}{(r^2 + w^2)}$. Second the temperature dependence of ΔT as a function of base temperature was assumed as predicted by COMSOL simulations and confirmed by measurements (supplementary section 8). The Soret coefficient was deduced by evaluating the radial concentration profile at steady state in correspondence to the image after temperature jump according to $S_T \Delta T(T, r) = -\log\left(\frac{c(r)}{c_0}\right)$ (Figure 3c and d). The error bars for individual Soret coefficients are based on the uncertainties of the temperature jump ΔT (see also supplementary section 8).

4.2 Measurements of ligand binding affinities of monomeric, oligomeric and fibrillar α -synuclein

The measurements of the ligand binding constants were performed with a Monolith NT.115 instrument (Nanotemper, Munich, Germany). We obtained the best experimental results (complete absence of sample adsorption onto the inner walls of the glass capillaries) using the hydrophobically coated glass capillaries provided by Nanotemper. The binding experiments between monomeric/oligomeric α -synuclein and the nanobody NbSyn2 were performed as follows. A dilution series was prepared in PBS buffer of the Nb (from 202 μM -6.2 nM, 10 μl at each concentration). The labeled monomers (in PB pH 6.5) were diluted to a concentration of 0.4 μM into H_2O , and then 10 μl of the diluted protein solution were added to the 10 μl aliquots of the NbSyn2 dilution series, yielding a final monomer concentration

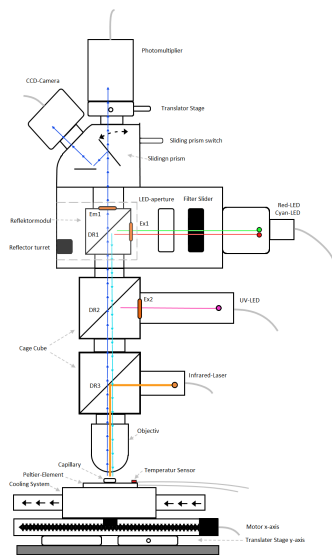


Figure 2: Schematic illustration [12] of the thermophoresis setup for quantitative measurements of the Soret coefficients of protein aggregates. The setup is based on a fluorescence microscope. The heating is carried out with an infrared laser that is coupled into the light path. Detection can be performed either with a CCD camera or with a PMT.

of 0.2 μM . The glass capillaries were filled through capillary action and thermophoretic measurements were performed (25 $^{\circ}\text{C}$, 15% red LED intensity, 20 and 40% IR laser intensity, 30 s laser on). The labeled oligomers were diluted in 5 mM Tris buffer pH 7.4 to a concentration of approximately 1 μM , as estimated from the size chromatogram during the isolation and purification of the oligomers. Then 10 μl of the oligomer solution were added to the 10 μl of the NbSyn 2 dilution series and the capillaries were filled and thermophoresis measurements performed analogously to the monomer case, except that the LED intensity was 60%. Representative data for nanobody binding to monomeric and oligomeric α -synuclein are shown in Figure 4. In the case of the oligomers, the thermophoretic amplitude was measured before steady state was reached (ca. 5 s after the heating laser was switched on), due to the fact that the data became noisier at later times. This is presumably due to the higher order assembly of the oligomers, that experience a decrease in charge due to the nanobody binding. In the case of the monomer, the thermophoretic amplitude was measured at steady state, 30 s after the heating laser was switched on.

For the experiments with EGCG, we first prepared stock solutions of 50 mg/ml (109.08 mM) in dimethylsulfoxide (DMSO) and then diluted it 50-fold into water to reach a concentration of 2.18 mM with 2% residual DMSO. We then prepared a dilution series into water with 2% DMSO (10 μl per sample) and added 10 μl of the monomer (1.5 μM total monomer, 2% labeled, 98% unlabeled monomer), oligomer or fibril (1.5 μM total protein, 2% labeling density) samples. Then we performed thermophoresis experiments at 25 $^{\circ}\text{C}$ and 20 as well as 40% of the IR laser power.

During our experiments that probed EGCG binding to oligomeric and fibrillar α -synuclein, we noticed that the apparent binding constant changed during the first hour after sample preparation; the binding was observed to become tighter (Figure 5). While we are not certain about the origin of this change in apparent affinity, it is unlikely to be caused by a pronounced change in aggregate structure (see AFM images in Figure 5 of main manuscript), but could indicate multi-step binding with rapid kinetics of initial and slower kinetics of later stages. An alternative explanation could also be a chemical modification of the fluorescent label by the bound ligand. The experiments shown in the main manuscript were performed after 1 h incubation of the samples.

For all the measurements of binding constants, we combined data from three independent experiments.

We also performed binding and stability time course experiments with fibrils prepared with different percentages of

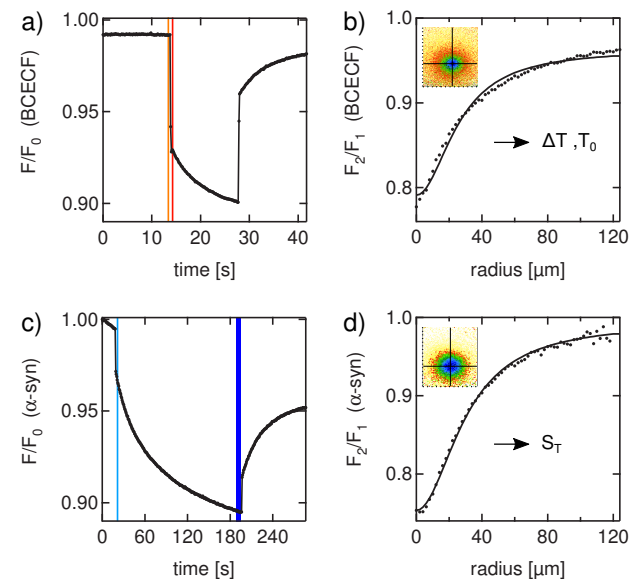


Figure 3: Data evaluation for the quantitative measurements of the Soret coefficient. The temperature gradient which was induced by the IR-laser was determined by BCECF fluorescence. a) The mean fluorescence on the CCD camera drops when the temperature gradient is established within 300 ms. Afterwards thermophoresis takes place. When the IR-laser is turned off the mean fluorescence recovers due to back diffusion. Dividing the picture after the temperature jump (red bar) by the one beforehand (orange bar) gives the radial fluorescence profile as indicated in b). The radial fluorescence profile is approximated by a Lorentzian function and the temperature gradient is then determined with the help of a calibration curve. c) For the α -synuclein species, here illustrated with monomer, the mean fluorescence is monitored over a longer period of time to reach a steady state. The change of concentration due to thermophoresis is obtained by division of the mean picture at the steady state (dark blue bar) by the one after temperature jump (light blue bar). d) The radial concentration profile together with the temperature profile gives the respective Soret coefficient. Here the measurement of α -synuclein monomer at 1 mM Tris pH 7.4 is shown. The base temperature is set to 25 $^{\circ}\text{C}$ in the presented examples.

incorporated labeled protein. Figure 6 a) shows a comparison of experiments with fibrils with 2% and 50% labeling density. It can be seen that the apparent affinity and the time-dependent behavior depend on the labeling density. The overall result of these studies was that the labeling density should be minimized. Obviously, it is always desirable to minimize the impact that any label might have on the process under study, but if the label concentration is decreased too much, then the signal is too weak at the low (μM) total protein concentrations that needed to be used in order to probe the binding affinity accurately. We found that 2% of labeled protein in the fibrils gave consistently the best results.

We also performed oligomer binding experiments with Thioflavin-T instead of EGCG (Figure 6 b), starting with a 2.33 mM ThT solution in H_2O with 2% DMSO. A weak interaction could be detected, that displays no time dependence. Furthermore, we found that also monomeric α -synuclein interacts with EGCG (Figure 6 c), whereas the free dye label shows no change in thermophoresis upon incubation with an EGCG concentration series, confirming that the binding curves presented in this work are not artifacts from ligand-label interactions.

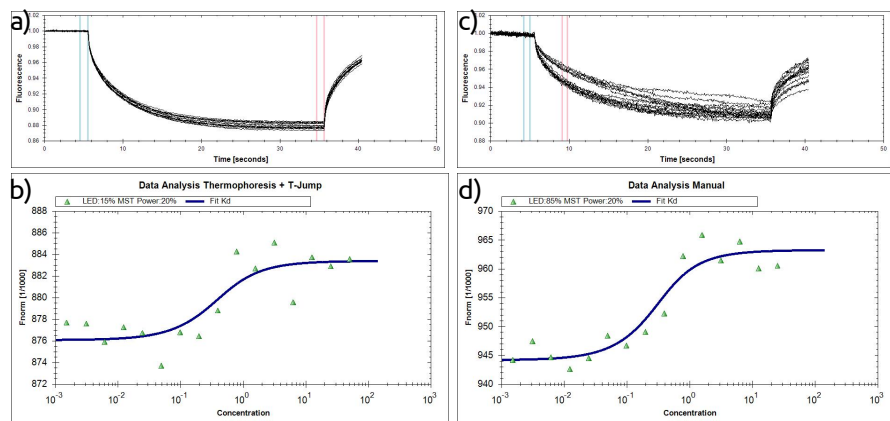


Figure 4: Microscale thermophoresis (MST) binding data of monomeric and oligomeric α -synuclein with the nanobody NbSyn2. a) Raw MST curves for monomeric α -synuclein. b) Binding curve for monomeric α -synuclein. c) Raw MST curves for oligomeric α -synuclein. d) Binding curve for oligomeric α -synuclein.

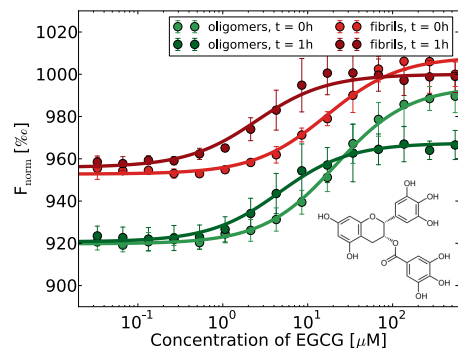


Figure 5: Change in apparent binding affinity of EGCG to oligomeric and fibrillar α -synuclein. For both species, the binding appears to become tighter over the course of an hour, changing from $16.5 \pm 1.6 \mu\text{M}$ and $21.2 \pm 2 \mu\text{M}$, for fibrils and oligomers, respectively, to $2.5 \pm 0.4 \mu\text{M}$ and $4.3 \pm 0.8 \mu\text{M}$.

5 Fluorescence correlation spectroscopy (FCS) of monomeric and aggregated α -synuclein

FCS measurements were performed on a Axiovert 200 microscope equipped with a ConfoCor2 unit (Carl Zeiss Jena, Germany), a 543 nm and 633 nm helium-neon laser and an apochromatic 40x water-immersion objective with a NA of 1.2 (Carl Zeiss). Fluorescence emission was separated from laser light using a bandpass filter (560-615 nm) for excitation with 543nm and a long pass filter (650 nm) for excitation with 633 nm. Calibration was performed with Alexa546 or Alexa633, respectively, to determine the dimensions of the observation volume. Samples were filled in NUNC 8-Well-Plates (Thermo Scientific). All measurements were performed at room temperature (22°C , air conditioned). For analysis the ConfoCor2 software was used.

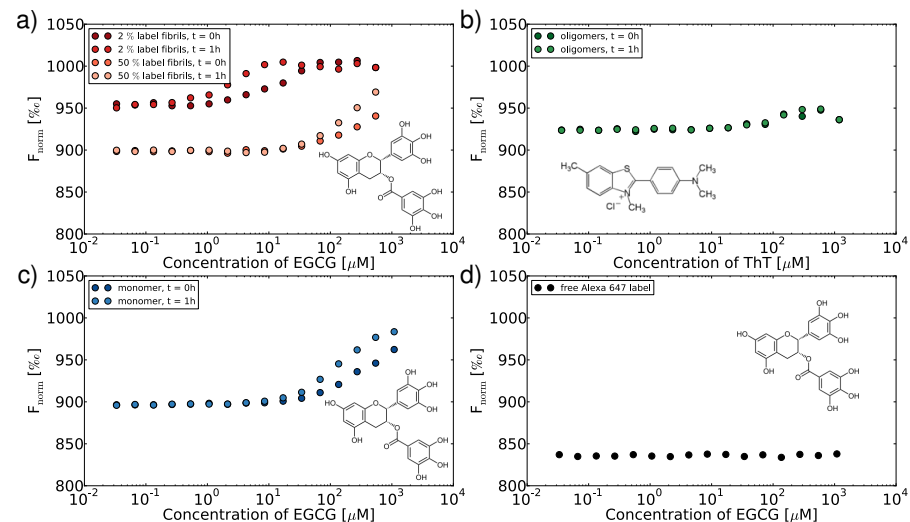


Figure 6: a) α -synuclein amyloid fibrils with either 2% or with 50% of the constituent monomers labeled with Alexa 647 are incubated with increasing concentrations of EGCG. Thermophoresis measurements were performed immediately after sample preparation and again after 1 h incubation period. It is apparent from this data that the labeling density is an important experimental parameter, and that it should be minimized as much as possible. b) α -synuclein oligomers show a weak interaction with Thioflavin-T, that does not change over time. c) Monomeric α -synuclein shows a weak interaction with EGCG, which also displays some time dependence. d) Free Alexa Fluor[®] 647 malimide does not display any interactions with EGCG.

5.1 Data analysis

We follow here the procedures outlines in [13]. The normalized correlation function $G(\tau)$ is defined as:

$$G(\tau) = \frac{\langle F(t)F(t+\tau) \rangle}{\langle F(t) \rangle^2} \quad (1)$$

where angular brackets denote the average over time, $F(t)$ the fluorescence signal at time t and $F(t+\tau)$ the fluorescence signal at a later time $t+\tau$. An ideal three dimensional Gaussian shape is assumed for the confocal volume. The structure parameter ω describes the ratio of the half axis z_0 to the radius of the laser beam w_0 . By fitting a model to the experimental data, physically relevant information can be extracted from the correlation curve. The autocorrelation curve for a single component freely diffusing in a 3D Gaussian element can be described by:

$$G(\tau) = \frac{1}{N} \left(\frac{1}{1 + \frac{\tau}{\tau_D}} \right) \left(\frac{1}{1 + \frac{\tau}{\omega^2 \tau_{D1}}} \right)^{\frac{1}{2}} + 1 \quad (2)$$

where N is the number of particles inside the confocal volume, τ_D is the translational diffusion time of the species, τ is the correlation time and ω the structure parameter. For samples containing two components of different size a two component fit is used:

$$G(\tau) = \frac{1}{N} \left[(1-y) \left(\frac{1}{1 + \frac{\tau}{\tau_{D1}}} \right) \left(\frac{1}{1 + \frac{\tau}{\omega^2 \tau_{D1}}} \right)^{\frac{1}{2}} + y \left(\frac{1}{1 + \frac{\tau}{\tau_{D2}}} \right) \left(\frac{1}{1 + \frac{\tau}{\omega^2 \tau_{D2}}} \right)^{\frac{1}{2}} \right] + 1 \quad (3)$$

where τ_{D1} and τ_{D2} are the diffusion times of the two components and y is the fraction of the second component. To take optical dark states of the dye into account, a function that describes the triplet can be integrated into the fitting equation:

$$G_{\text{Triplet}}(\tau) = \left(1 + \frac{T}{1-T} \exp\left(-\frac{\tau}{\tau_T}\right)\right) \quad (4)$$

τ_T is the triplet state relaxation time and T the fraction of fluorophores in the dark state. The total correlation curve then becomes a product of the triplet function and the model $G(\tau)$:

$$G_{\text{total}}(\tau) = G_{\text{Triplet}}(\tau)G(\tau) \quad (5)$$

The translational diffusion time describes the average dwell time of a molecule with diffusion constant D in the confocal volume:

$$\tau_D = \frac{w_0^2}{4D} \quad (6)$$

The hydrodynamic radius R_h of a spherical molecule can be determined with the Stokes-Einstein-equation:

$$R_h = \frac{k_B T}{6\pi\eta D} \quad (7)$$

where k_B , is the Boltzman constant, T is the temperature in [K] and η the viscosity of the surrounding medium.

5.2 Results

We have determined the sizes of fluorescently labeled monomeric, oligomeric and fibrillar α -synuclein using FCS. Figure 7 shows the normalized correlation functions that clearly illustrate the difference in diffusion behavior between the different species.

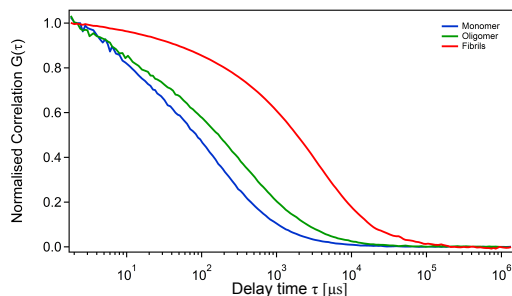


Figure 7: Normalized correlation curves of monomeric (blue), oligomeric (green) and fibrillar (red) α -synuclein. FCS measurements enable accurate determination of the diffusion coefficient and hence the (effective) hydrodynamic radii of the different species, using the Stokes-Einstein equation (Equation 7). The shift to the right towards longer diffusion times is an indicator for an increase in size.

The experiment shown in Figure 7 yields values of the diffusion coefficient of $8.2 \pm 0.34 \cdot 10^{-11} \frac{m^2}{s}$ (monomer), $3.5 \pm 0.34 \cdot 10^{-11} \frac{m^2}{s}$ (oligomer) and $4.1 \pm 0.4 \cdot 10^{-12} \frac{m^2}{s}$ (fibrils). In the case of the monomers and oligomers, the Stokes-Einstein equation (Eq. 7) can be directly applied in order to determine the hydrodynamic radii, as these species can be approximated as spheres. As averages from several independent experiments, we obtain $R_M = 2.8 \pm 0.1$ nm for the hydrodynamic radius of the monomer and $R_O = 7.5 \pm 0.7$ nm for the hydrodynamic radii of the oligomers. The average diffusion coefficient measured for the sonicated fibrils is $4.1 \pm 0.4 \cdot 10^{-12} \frac{m^2}{s}$. In all cases when fibrillar samples were measured by FCS, the quality of a two-component fit was considerably better, where the second component was fixed to have the size of the monomer. The monomer component of the fibril samples varied between 15 and 23%, which also introduces an error into the values of the Soret coefficients measured for the fibrils. In order to calculate the diffusion coefficient

and subsequently the dimensions of the fibrils, we make use of the AFM images that we have taken of these fibrils (see Figure 3 of main manuscript). These images in principle already provide us with the necessary information about the dimensions of the fibrils, but we will nevertheless check whether the results of the FCS measurements that are performed under the same conditions as the thermophoresis and electrophoresis experiments, are consistent with the AFM images. According to the detailed analysis of the AFM images, the sonicated fibrils have an average length of 171 nm and a thickness of approximately 8 nm. With these dimensions, we can calculate the rotational diffusion coefficient, according to:

$$D_r = \frac{k_B T}{\gamma_r} \quad (8)$$

where γ_r is the rotational friction coefficient, given according to Broersma [14] by:

$$\gamma_r = \frac{\pi\eta L^3}{3(\log(2L/D) - c_r)} \quad (9)$$

where L is the length of the rod, D is its diameter and c_r is a numerical factor that corrects for end effects:

$$c_r = 1.57 - 7 \left(\frac{1}{\log(2L/D)} - 0.28 \right)^2 \quad (10)$$

The rotational diffusion coefficient has units of radians²/s. We obtain a value of ~ 1725 rad²/s. The diffusion time of a fibril through the confocal volume of the FCS instrument is approximately 5 ms, a value directly obtainable from the FCS measurements. During this time, the fibril will rotate on average about 168° . This is probably not enough to assume complete orientational averaging, but some degree of averaging can be assumed. We can therefore expect the difference between the measured apparent diffusion coefficient of the fibrils and the calculated diffusion coefficient of a rod with 171 nm length and 8 nm thickness to be not too large. In order to calculate the translational diffusion coefficient of a rod, we use the results by de la Torre [15]:

$$D_t = \frac{k_B T (\log(L/D) + c_t)}{3\pi\eta L} \quad (11)$$

where c_t is again a numerical correction factor for end effects:

$$c_t = \frac{c_{t,\perp} + c_{t,\parallel}}{2} \quad (12)$$

with

$$c_{t,\perp} = 0.5 + 4.2 \left(\frac{1}{\log(2L/D)} - 0.39 \right)^2 \quad (13)$$

and

$$c_{t,\parallel} = -0.58 + 7.4 \left(\frac{1}{\log(2L/D)} - 0.34 \right)^2 \quad (14)$$

We obtain $c_t = 0.0122$ and $D_t = 8.1 \cdot 10^{-12} \frac{m^2}{s}$. This value is in acceptable agreement with the value determined from FCS ($4.1 \pm 0.4 \cdot 10^{-12} \frac{m^2}{s}$, see above). The difference in these values is likely to stem from the polydispersity of the fibrillar sample. The FCS measurements are likely to be biased towards the shorter fibrils, due to faster diffusion and less likely absorption on the walls etc., whereas the AFM measurements might be biased towards the longer fibrils, due to preferential absorption on the AFM substrate.

We have also performed FCS measurements of α -synuclein fibrils before and after incubation with additional unlabeled monomeric protein at 70°C , as in the experiment shown in Figure 3 of the main manuscript. The correlation data of this experiment is shown in Figure 8, and the growth of the fibrils is clearly apparent from this data. Finally, we also used FCS in order to probe the temporal stability of the purified oligomers. We measured a sample of oligomers continuously for more than 60 h at RT (Figure 9) and found only a very slight trend towards increasing sizes. This result confirms that the oligomers are thermodynamically highly stable and display negligible kinetics of dissociation on the time scale of days. Therefore purified samples of oligomers were stored during up to several days (at RT or 4°C) and used for thermophoresis experiment throughout this period.

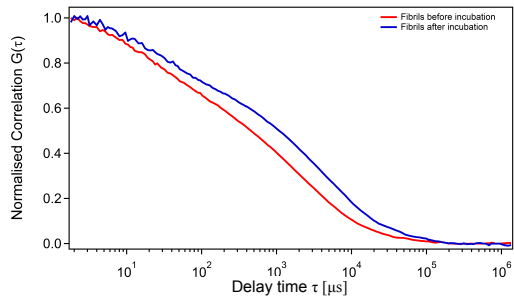


Figure 8: Normalized correlation curves from FCS experiments of α -synuclein amyloid fibrils before and after a 20 min incubation period with 70 μ M added unlabeled monomeric protein at 70 $^{\circ}$ C. The shift to the right towards longer diffusion times is an indicator for an increase in size. This shift corresponds to a change in diffusion coefficient from $3.8 \pm 0.2 \cdot 10^{-12} \frac{m^2}{s}$ to $2.4 \pm 0.2 \cdot 10^{-12} \frac{m^2}{s}$.

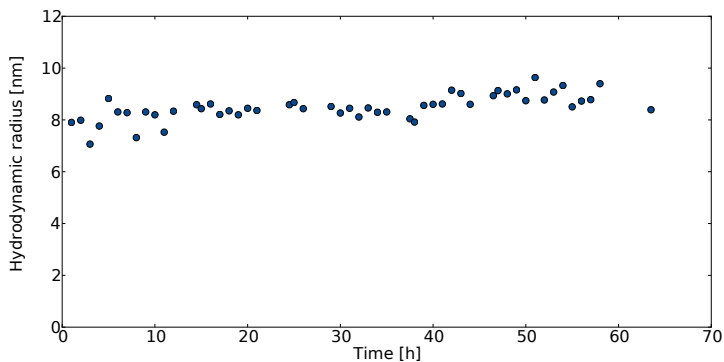


Figure 9: Time course of FCS size measurements of labeled α -synuclein oligomers over more than 60 h, confirming the high structural stability of these types of aggregates.

6 Free flow electrophoresis measurements of monomeric and aggregated α -synuclein

As will be discussed in detail in the next section, the net charge and electrophoretic mobility are important parameters for the quantitative description of thermophoresis. The thermophoresis of the salt ions in solution creates a macroscopic electric field at steady state that leads to electrophoresis of the macromolecule under study, such as the monomeric or aggregated α -synuclein in the present case. Furthermore, the potential energy stored in the double layer depends on both the charge and the temperature and hence yields another temperature-dependent contribution to the Soret coefficient. Therefore, independent estimates of the effective charges of the different α -synuclein species are important for the quantitative analysis and understanding of the thermophoretic behavior.

We used a variant of microfluidic free flow electrophoresis that was recently developed in our laboratory [16] in order to measure the electrophoretic mobilities of monomeric, oligomeric and fibrillar α -synuclein in 5 mM Tris buffer at pH 7.4 (Figure 10).

The measured electrophoretic mobilities are $-2.06 \pm 0.11 \frac{\mu m/s}{\sqrt{cm}}$ (labeled monomers), $-3.09 \pm 0.46 \frac{\mu m/s}{\sqrt{cm}}$ (oligomers) and

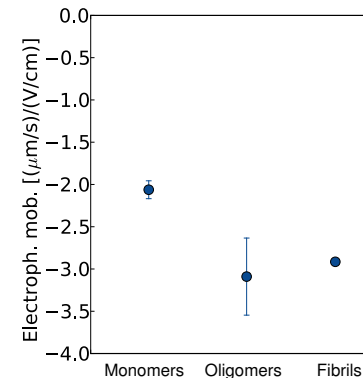


Figure 10: Electrophoretic mobilities, measured via microfluidic free-flow electrophoresis [16]. The mobilities were measured in 5 mM Tris buffer, pH 7.4. Error bars come from two independent repeats with independent sample preparations.

$-2.91 \pm 0.02 \frac{\mu m/s}{\sqrt{cm}}$ (fibrils). The values for both monomeric and fibrillar α -synuclein are well-defined and display a trend of increasing mobility with increasing size. However, the variation in the values measured for the oligomers is much larger, potentially reflecting a degree of polydispersity of the oligomer preparations [4]. In particular, oligomeric and fibrillar α -synuclein display an essentially identical electrophoretic mobility. In the light of the very different sizes and structures of oligomers and fibrils, this is a very interesting finding which highlights the power of thermophoresis to discriminate more easily between different types of particles, compared to electrophoresis. For our quantitative modeling of the thermophoresis data, we require the surface charge density or the absolute charge of the protein monomers and aggregates, in addition to the electrophoretic mobilities. A comprehensive theoretical framework for relating mobilities to surface potentials for colloid-like systems of all sizes has been first presented by Henry [17]. In particular for particles that can be approximated as spheres, such as monomeric and oligomeric α -synuclein, this is well-established.

6.1 From electrophoretic mobility to effective charge for monomeric and oligomeric α -synuclein

The ζ -potential is the potential difference between the (neutral) bulk solution and the surface of a charged particle, including tightly absorbed counter ions [18], and is therefore a measure for the charge density of the particle surface. The electrophoretic mobility and the ζ -potential are related through Henry's formula [17]:

$$\mu_e = \frac{2\epsilon_0\epsilon_r\zeta f(\kappa R)}{3\eta} \quad (15)$$

where ζ is the ζ -potential, η the viscosity and $f(\kappa R)$ is Henry's function with the argument κR , the product of inverse Debye length κ and particle radius R . Henry's function varies from $1.0 \leq f(\kappa R) \leq 1.5$. For $\kappa R \ll 1$, $f(\kappa R) = 1.0$ (Hückel limit) and for $\kappa R \gg 1$, $f(\kappa R) = 1.5$ (Smoluchowski limit). Ohshima has presented a formula for $f(\kappa R)$ that is valid for all values of κR and accurate to within 1% [19]:

$$f(\kappa R) = 1 + 0.5 \frac{1}{\left(1 + \frac{2.5}{\kappa R(1+2e^{-\kappa R})}\right)^3} \quad (16)$$

However, the applicability of Henry's expression for the particle mobility depends on the absolute value of the charge and mobility, due to the fact that Henry's treatment neglects relaxation effects of the counterion atmosphere [18]. We can define a reduced mobility:

$$\mu_{red} = \frac{3\eta e}{2\epsilon_0\epsilon_r k_B T} \mu_e \quad (17)$$

Depending on the relative values of μ_{red} and κR , either Henry's simplified treatment or a more sophisticated one has to be applied. We obtain $\mu_{\text{red},M} = -1.74$ and $\mu_{\text{red},O} = -2.62$. From the FCS measurements (see above), we know that the radius of the monomeric protein, R_m , is ca. 2.8 nm and the radius of the oligomers, R_o , is ca. 7.5 nm. The free flow electrophoresis experiments were carried out in 5 mM Tris buffer pH 7.4, where the Debye length $\lambda = 1/\kappa = 4.7$ nm. Hence $\kappa R = 0.6$ for monomeric α -synuclein and 1.6 for oligomeric α -synuclein. It turns out that Henry's simplified treatment for the calculation of the ζ -potential is applicable for the monomer (with $f(\kappa R)=1.02$), but for the oligomer, we need to use Hunter's inversion [18] of Booth's formula [20]:

$$\zeta_r = \frac{\mu_{\text{red}}}{f(\kappa R)} - \left[\frac{C_3(\mu_{\text{red}}/f(\kappa R))^3 + C_4(\mu_{\text{red}}/f(\kappa R))^4}{f(\kappa R) + 3C_3(\mu_{\text{red}}/f(\kappa R))^2 + 4C_4(\mu_{\text{red}}/f(\kappa R))^3} \right] \quad (18)$$

where ζ_r is the reduced ζ -potential:

$$\zeta_r = \frac{\zeta e}{k_B T} \quad (19)$$

and where C_3 and C_4 are numerical coefficients that depend on the product κR and the limiting molar conductance of the counter- and coions. Hunter [18] gives the expressions for these coefficients that we are not reproducing here. The limiting conductances of the Tris⁺ ion and the Cl⁻ ion are $2.97 \cdot 10^{-3} \Omega^{-1} \text{m}^2 \text{mol}^{-1}$ [21] and $7.64 \cdot 10^{-3} \Omega^{-1} \text{m}^2 \text{mol}^{-1}$ [22].

We are now in a position to calculate the ζ -potentials for monomeric (44.0 mV) and oligomeric (40.3 mV) α -synuclein. In order to calculate the charges from these values of the ζ -potentials, we follow the methodology outlined by Ohshima [23]. We define the dimensionless surface charge density Σ :

$$\Sigma = \frac{e\sigma}{\epsilon_0 \epsilon_r \kappa k_B T} \quad (20)$$

where σ is the surface charge density. Ohshima derives the following expression relating reduced ζ -potential and reduced surface charge density:

$$\Sigma = 2 \sinh(\zeta_r/2) \left[1 + \frac{2}{\kappa R \cosh^2(\frac{\zeta_r}{4})} + \frac{8 \log(\cosh(\frac{\zeta_r}{4}))}{(\kappa R)^2 \sinh^2(\frac{\zeta_r}{2})} \right]^{\frac{1}{2}} \quad (21)$$

The absolute charge Q can be computed from the surface charge density σ as $Q = 4\pi R^2 \sigma$. Using these expressions, we obtain values for the absolute charge of $Q_M = -10.9 e$ for the monomeric protein and $Q_O = -50.4 e$ for the oligomers. The value of the monomer is in good agreement with theoretical predictions, based on the combined charge of the individual amino acids at this pH value (-9.1 e) and the charge of the Alexa 647 label (-4 e). For the oligomers, on the other hand, the effective charge corresponds to only ~ 5 times the charge of a monomer, while each oligomer consists on average of ~ 30 monomers. This strong difference can be explained through processes such as counter ion incorporation into the oligomer structure, as well as Manning condensation of counterions [24] onto the surface of the oligomer. Indeed, without such charge compensation mechanisms, the electrostatic contribution to the formation of an oligomer would render such a structure highly energetically unfavorable.

6.2 Free flow electrophoresis of rod-like particles

The determination of effective charges from electrophoretic mobilities of rod-like particles represents an additional difficulty, due to the anisotropic nature of the rod and the possibility of alignment in the electric field. In addition, if the electrophoretic mobility is measured in free (shear) flow, alignment could also occur in the flow direction. We start by evaluating whether or not alignment effects have to be taken into account in our setup. Dhont and Briels [25] have given a comprehensive treatment of the behavior of Brownian rods in shear flow. A rotational Péclet number can be defined that quantifies the relative importance of shear forces and random Brownian rotational motion:

$$\text{Pe}_r = \frac{\dot{\gamma}}{D_r} \quad (22)$$

where $\dot{\gamma} = \frac{du_x}{dy}$ is the shear rate, u_x is the flow velocity and y is a direction perpendicular to the flow. The microfluidic channel is 2200 μm wide and 25 μm high. It is therefore clear that in the horizontal direction, the shear rate will be negligibly small in the center of the channel, while it might be considerable in the vertical direction. Therefore we limit our treatment to this direction. The flow rate is 500 μl per hour, corresponding to an average flow velocity of $2.5 \cdot 10^{-3} \frac{\text{m}}{\text{s}}$. We take the flow rate to be approximately constant throughout the wide dimension of the channel and approximate the parabolic flow profile across the narrow dimension by a linear one, and therefore the maximum flow velocity is twice the average flow velocity. Hence we obtain a shear rate of $4 \cdot 10^2 \text{s}^{-1}$. The rotational diffusion coefficient

has been determined above to be $1700 \frac{\text{rad}^2}{\text{s}}$, and hence we obtain $\text{Pe}_r \approx 0.24$. This is smaller than the threshold for the beginning of orientation, $\text{Pe}_r \sim 1$ [26]. Therefore, shear alignment is negligible in our setup for short amyloid fibrils.

Next, we investigate whether the α -synuclein fibrils can be aligned by the electric field applied during the electrophoretic measurements. Alignment in an electric field can occur by means of a permanent or an induced electric dipole. We can apply phenomenological, as well as theoretical arguments. Phenomenologically, the electrophoretic mobility is expected to increase with the applied voltage in the case of significant alignment, as the degree of alignment should increase with the field strength and aligned rods have a lower friction factor - this argument has been given in favor of alignment in the case of tobacco mosaic viruses [27]. However, as can be seen in Figure 11, the electrophoretic velocity increases linearly with the electric field, and therefore an increase in mobility is not detected. This observation hints towards no significant alignment effects.

Next, we treat the question of whether alignment by the field plays a role or not theoretically. The first question is whether the fibrils possess a permanent dipole moment. Measurements of permanent dipole moments of rod-like protein aggregates are rare. It has been reported that β -lactoglobulin amyloid fibrils with an average length of ca. 4 μm have a permanent dipole moment of $3.1 \cdot 10^{-19} \text{Cm}$. This value, which agrees remarkably well with the value calculated for a chain-like assembly of monomers, has been obtained from electric field-induced birefringence at pH 2.0, where the protein carries a significant net charge of $\sim +20 e$. On the other hand, it has been reported that the tobacco mosaic virus, a rod-like structure of ~ 300 nm in length and 18 nm in diameter, possesses a permanent dipole moment of only $8.3 \cdot 10^{-26} \text{Cm}$ [28] at pH 7.5, where the virus coat protein carries a net charge of $-3.4 e$. It therefore seems likely that the α -synuclein fibrils possess a permanent dipole moment, but it is difficult to estimate its magnitude, especially as no detailed structural information is available for the fibrils.

Furthermore, fibrillar protein structures display a polarizability due to the mobile counterions that are associated with the charged rod, leading to an induced dipole moment. An expression for this induced dipole moment has been given by Fixman [29, 30]:

$$\mu_{\text{ind}} = \frac{4\pi\epsilon_0\epsilon_r L K z_1 E_0}{\gamma^2(z_1 - z_2)} \left(1 - \frac{\tanh(\gamma L/2)}{\gamma L/2} \right) \quad (23)$$

where z_1 and z_2 are the counter- and co-ion valencies and γ is a characteristic length scale:

$$\gamma^2 = \frac{4\pi c_1 K b}{\phi} \quad (24)$$

where c_1 is the bulk concentration of counter ions, K is a numerical factor, given by:

$$K = \frac{1}{2 \log(2L/D) - 14/3} \quad (25)$$

The fraction of bound counter ions ϕ depends on the mean spacing between charges on the rod-like macromolecule, b , and the Bjerrum length, $\lambda_B = \frac{e^2}{4\pi\epsilon_0\epsilon_r k_B T}$, according to:

$$\phi = 1 - \frac{b}{\lambda_B} \quad (26)$$

With a fibril diameter of 8 nm, a fibril density of 1.35 g/cm³, a molecular mass and charge of the α -synuclein monomer of 14.46 kDa and -9 e, respectively, we obtain a mean spacing of the charges of 0.4 Å. The Bjerrum length in water at room temperature is ~ 0.7 nm and hence $\phi \approx 0.945$. Using those values, we obtain an induced dipole moment of $\sim 1.1 \cdot 10^{-27} \text{Cm}$. This value is negligible compared to the potential permanent dipole moments mentioned above. We can now compute the orientational order parameter Φ ($\Phi \in [0,1]$) for various values of μ_0 , the permanent dipole moment. The orientational order parameter can be calculated as [31]:

$$\Phi = 1 - 3 \frac{\coth(\beta) - 1/\beta}{\beta} \quad (27)$$

with β defined as $\beta = \frac{\mu_0 E}{k_B T}$. If we take the range of values for μ_0 from the ones reported above: $10^{-25} \text{Cm} < \mu_0 < 10^{-20} \text{Cm}$, we obtain values of Φ that vary between 0.0008 and 0.9997, and hence between negligible and complete alignment. Therefore it is impossible to say from theoretical arguments alone, without a more precise estimate of the fibrils' permanent dipole moment, whether or not alignment with the field direction occurs. We will therefore analyze the electrophoresis data assuming complete and no alignment and compare the results. Expressions relating the electrophoretic mobilities of aligned and randomly oriented rods have been given by Ohshima [32]:

$$\mu_{\parallel} = \frac{\epsilon_0 \epsilon_r \zeta}{\eta} \quad (28)$$

and

$$\mu_{\text{rand}} = \frac{\epsilon_0 \epsilon_r}{3\eta} \zeta (1 + 2f(\kappa R)) \quad (29)$$

where $f(\kappa R)$ is Henry's function for a cylinder, that varies between 0.5 and 1. Therefore

$$\frac{\mu_{\parallel}}{\mu_{\text{rand}}} = \frac{3}{1 + 2f(\kappa R)} \quad (30)$$

varies between 1.5 and 1.0. Henry's function for a cylinder is given by [32]:

$$f(\kappa R) = 0.5 + 0.5 \frac{1}{\left(1 + \frac{2.55}{\kappa R(1 + e^{-\kappa R})}\right)^2} \quad (31)$$

which yields $f(\kappa R) = 0.55$ in the case of fibrils of a radius of $R = 4$ nm in 5 mM Tris buffer. With this value of $f(\kappa R)$, we can calculate the ζ -potential for the cases of complete alignment (42.2 mV) and random orientation (60.2 mV). Hunter [18] gives the relationship between the total charge of a cylinder and the ζ -potential:

$$\zeta = \frac{2Q_F K_0(\kappa R)}{4\pi\epsilon_0\epsilon_r\kappa R(2R + L)K_1(\kappa R)} \quad (32)$$

where $K_0(\kappa R)$ and $K_1(\kappa R)$ are the modified Bessel functions of the second kind ($K_0(\kappa R)/K_1(\kappa R) \approx 0.85$ under these conditions [18]). Using this relationship, we can calculate average total charges of the fibrils of -205 e (aligned case) and -292 e (random orientation). Both of these values are in good agreement with a rough estimate of the total charge based on the fraction of condensed counter ions calculated above. A fraction of bound counterions of 0.945 leaves the fibrils with a net charge of -238 e. This analysis is therefore consistent with both aligned and randomly oriented fibrils and we conclude that the fibrils possess a net charge of between 200-300 e.

6.3 Electrophoresis under different solution conditions

In order to check this analysis for its robustness and consistency, we have also performed similar electrophoresis experiments in 10 mM Tris buffer instead of 5 mM Tris. We obtain electrophoretic mobilities of $-1.20 \frac{\mu\text{m/s}}{\text{V/cm}}$ and $-1.95 \frac{\mu\text{m/s}}{\text{V/cm}}$ for monomeric and oligomeric α -synuclein under these conditions. This translates into charges of -7.2 e and -37.3 e. This apparent decrease in charge compared to the conditions of lower ionic strength might have its origin in more pronounced counter-ion binding, but could also stem from the fact that the measurement become more difficult and inaccurate at higher ionic strengths. The contribution of the fluorescent sample to the overall current, and hence the measured deflection of the sample beam, decreases with increasing solution ionic strength. Furthermore, we have also performed experiments in 5 mM Tris buffer in the presence of 100 μM EGCG, and we found that the measured values for the mobilities are almost indistinguishable in the presence and absence of EGCG for all α -synuclein species.

7 Modeling electrostatic effects in protein thermophoresis

One of the aims of this study is to be able to quantitatively understand and model the effects of changes in solution conditions on the thermophoresis of proteins. We have recently presented an analysis of nucleic acid thermophoresis that highlighted the importance of electrostatic effects [11]. We apply this model to the thermophoresis of proteins and protein aggregates in the present study.

In our model the Soret coefficient of a biopolymer consists of three main contributions. For charged biomacromolecules, the capacitor effect (S_T^M) and Seebeck effect (S_T^{EL}) play an important role.

$$S_T = S_T^M + S_T^{EL} + S_T^{NI} \quad (33)$$

The nonionic contribution (S_T^{NI}) cannot, at present, be modeled and is likely to involve surface properties of the molecule undergoing thermophoresis, such as its hydrophobicity. We shown in the present study that changes in such properties lead to changes in thermophoretic behavior (e.g. the binding of the neutral molecule EGCG to α -synuclein oligomers and fibrils).

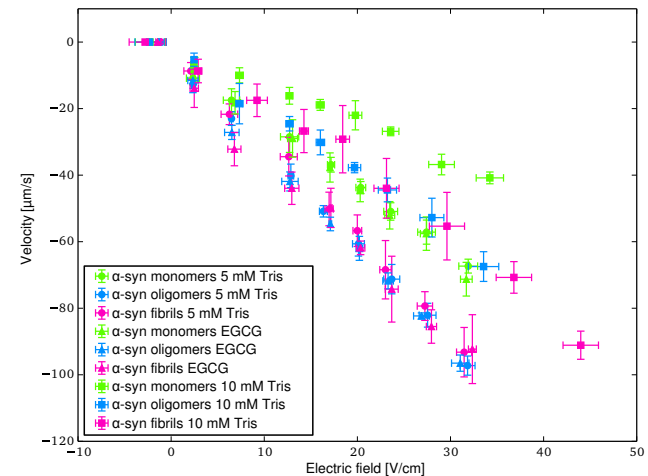


Figure 11: Plot of electrophoretic velocities vs. electric field. Shown is data for monomeric, oligomeric and fibrillar α -synuclein, in 5 and 10 mM Tris buffer, pH 7.4, as well as in 5 mM Tris buffer in the presence of 100 μM EGCG.

7.1 Capacitor effect

One important contribution to S_T of charged macromolecules is given by the capacitor effect S_T^M . It results from the change in free energy of the molecule's ion cloud upon temperature variation and is dependent on the properties of the Debye layer [11, 33]. The crucial parameters are the Debye length λ_D , as well as the polymer's charge Q and radius R . In addition the density ρ , permittivity $\epsilon = \epsilon_0 \epsilon_r$, and temperature T of the solvent water affect the magnitude of S_T^M . Therefore the Soret coefficient of a charged biopolymer at any given temperature is a function of the ionic strength. For spherical particles or molecules, as monomers and oligomers the capacitor model yields a contribution to S_T of:

$$S_T^M = \frac{(Qe)^2}{16\pi k_B T^2 \epsilon \lambda_D (1 + R/\lambda_D)^2} \left(1 - \frac{\partial \log[\rho(T)]}{\partial \log[T]} - \frac{\partial \log[\epsilon(T)]}{\partial \log[T]} \left(1 - \frac{2\lambda_D}{R} \right) \right) \quad (34)$$

For rodlike structures, such as amyloid fibrils, the capacitance can be expressed as a superposition of a spherical and a cylindrical capacitor [34].

7.2 Seebeck effect

The salt ions in solution have themselves different Soret coefficients and are therefore affected differently by thermophoresis. As a consequence, a macroscopic electric field builds up if a thermal gradient is applied to a salt solution [11, 35, 36]. The charged macromolecules under study will undergo electrophoresis in the electric field thus created. This dependence, which in analogy to solid state thermoelectric phenomena has been dubbed the Seebeck effect, can be expressed as:

$$S_T^{EL} = -\frac{k_B T \mu}{eD} \frac{\sum_i z_i c_i S_{Ti}}{\sum_i z_i^2 c_i} \quad (35)$$

The mobility is related to the zeta potential via Eq. 15 and $\zeta = \frac{Qe}{4\pi\epsilon r(1+r/\lambda)}$. For the Soret coefficients of single ions in water, S_{Ti} , literature values according to the reduction rule were applied ([37] and see also Reichl et al. [11])

$$S_T^{Cl^-} = 7.18 \cdot 10^{-4} / K \quad (36)$$

$$S_T^{Na^+} = 4.69 \cdot 10^{-3}/K \quad (37)$$

7.3 Nonionic contribution

The non-ionic contribution to the Soret coefficient of biomacromolecules is likely to be linked to surface properties of the molecule, such as hydrophobicity and hydrogen bonding capacity with water [10]. At present, no general framework exists that is able to describe these effects quantitatively. Therefore we restrict our theoretical description to the ideal gas contribution and an empirical temperature dependent part according to Piazza [38].

$$S_T^{NI} = \frac{1}{T} + S_T^\infty (1 - e^{-(T-T_0)/T^*}) \quad (38)$$

Here S_T^∞ denotes the empirical Soret coefficient at infinite temperature, T_0 the temperature where the Soret coefficient changes sign and T^* is a measure for the broadness of the range where S_T increases with temperature.

7.4 Determination of 'thermophoretic charge' and nonionic contribution

On the basis of the model for the electrostatic contributions to the Soret coefficient of the protein molecules and aggregates outlined above, the 'thermophoretic charges', Q_T , and nonionic contributions, S_T^{NI} , are determined from the ionic strength series for the monomeric and oligomeric α -synuclein species (Figure 2 of the main manuscript). Taking into account the temperature dependent physical parameters of water (viscosity, permittivity, density), as well as salt concentration, concentration and size of the protein species an optimization of χ^2 for the measured data yields the parameters listed below for monomers and oligomers. Unfortunately it was not possible to perform measurements of the Soret coefficient as a function of the ionic strength for the α -synuclein amyloid fibrils due to higher order assembly of the fibrils at higher ionic strengths [5] and sticking interactions with the capillary walls. For Soret coefficient of the Tris ion, individual parametric sweeps were performed on the salt series of monomeric and oligomeric α -synuclein. For the two α -synuclein species the best fits yields $S_T(Tris)^{Mon} = 0.0024/K$ and $S_T(Tris)^{Oligo} = 0.0038/K$. Consequently the Soret coefficient was set to the median of both measurements $S_T(Tris) = 0.0031/K$. This value is reasonable since it is quantitatively comparable to the one of sodium with $0.00469/K$ [11, 37].

The best fit of the model to the data yields the following effective thermophoretic charges and nonionic contributions for monomeric and oligomeric α -synuclein:

	Q_T	$S_T^\infty [1/K]$	$T_0 [K]$	$T^* [K]$
Monomer	-6.9 e	0.0126	292.4	20.7
Oligomer	-29.2 e	0.0161	320.6	33.4

Nonionic Contribution: Interestingly S_T^{NI} is higher for the monomers in the observed temperature range, but increases more strongly for the oligomers over base temperature (Figure 12). Whether hydrophobic effects play a role here is not clear. It is also under discussion whether the strong temperature dependence of the empirical nonionic contribution is connected to additional electrostatic effects not currently included. The thermophoresis of salt ions changes over temperature [39] and can result in further diffusiotheretic or electrophoretic influence on S_T of the macromolecule [36].

Thermophoretic charge Q: Overall the obtained charges on the basis of thermophoresis measurements are significantly smaller than the charges determined from electrophoretic measurements: $Q_T^{Mon} = -6.9$ e, $Q_T^{Oligo} = -29.2$ e from thermophoresis vs. $Q_E^{Mon} = -10.9$ e, $Q_E^{Oligo} = -50.4$ e from electrophoresis. This difference might originate in an incomplete description of the electrostatic effects involved in thermophoresis and does indeed provide an important comparison that will be helpful for further theoretical studies of protein electrophoresis and thermophoresis.

Influence of unlabeled monomers (Fig 3a of main manuscript): The Soret coefficient of the additional unlabeled monomer was set according to the expected contribution for labeled monomers in 1mM Tris: $S_T^{nl.mon} = S_T^{NI-mon.} + S_T^{C-M-mon.} = 0.031/K$. Note that this Soret coefficient corresponds to the median value over the observed temperature range in Figure 3a of main manuscript. The monomers were then incorporated as additional salt species in the Seebeck effect and taken into account for the Debye length (Capacitor Model). The observed decrease in the Soret coefficient of the labeled monomers and oligomers in the presence of unlabeled monomers coincides with similar findings on DNA [34] in the dilute regime.

Influence of the nanobody Syn2 (Fig 4a of main manuscript): In the case of nanobodies present, the best fit to the data yields the following charges:

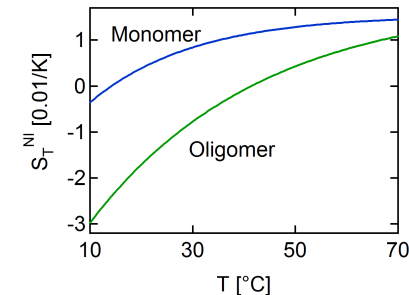


Figure 12: The non-ionic contribution to the Soret coefficient, S_T^{NI} , for monomeric and oligomer α -synuclein as a function of temperature.

	Monomer	Oligomer
No nanobody	-4.5 e	-27.6 e
Nanobody	-1.8 e	-20.6 e

The reason for the differences in charge listed here in the absence of nanobody and the charge determined for the monomers and oligomers stated above is likely to be due to the modified solution conditions (presence of phosphate ions in the nanobody solution and respectively also added to the control) and the associated altered Seebeck effect. For monomers, we obtain a $\Delta Q = +2.7$ e, which is in reasonable agreement with the expected binding of one nanobody (+1.5 e). In the case of the oligomers, the observed value of $\Delta Q = +7$ e is consistent with the attachment of more than one molecule of nanobody. It is difficult to estimate the expected stoichiometry of binding of nanobody to the oligomers, due to lack of detailed structural information of the oligomer and hence of the accessibilities of the epitopes.

8 ComSol simulations of the thermophoresis setup

The Soret coefficient determined from the experimentally measured concentration depletion value depends linearly on the magnitude of the induced temperature jump ΔT . In order to obtain insight into the experimental uncertainty of the induced temperature gradient, we performed a finite element simulation and compared the results with the measured values for ΔT . The decrease of ΔT with increasing base temperature T for simulation is in good agreement with the measurements. Furthermore the effect of errors in capillary thickness ($\pm 10\%$) could be tested in the simulations and the resulting error for ΔT deduced.

The simulation was performed in COMSOL Multiphysics (COMSOL Inc., USA) whereby the physics of infrared-absorption and heat transfer were incorporated (Figure 13 a). In our simulation we assumed radial symmetry and incorporated the capillary with dimensions of $50 \mu\text{m} \times 500 \mu\text{m}$. The capillary is coupled to a silicon wafer of $350 \mu\text{m}$ thickness with high thermal conductivity. For borosilicate, silicon and water standard material properties were used. Only temperature dependent absorption of water in the IR at the wavelength was additionally incorporated into the model [40]. As heating source a Gaussian laser profile was assumed with a beam waist of $30 \mu\text{m}$.

As boundary conditions the bottom of the silicon was set to a base temperature and the top of the capillary thermally insulated since heat conduction of the air above is very low. Individual simulation runs were performed for base temperatures in the range of $T = 5-65$ °C. ΔT was extracted by line averaging in the water region over capillary height and subtracting temperatures at the inner and the outer boundary. It can be observed that ΔT decreases with increasing base temperature (Figure 13 b). The main reason is found in the decreasing infrared-absorption coefficient of water with increasing temperature. The result of the numerical evaluation is in good agreement with our measurements of ΔT which was obtained using the temperature sensitive fluorescence of the dye (2',7'-Bis-(2-Carboxyethyl)-5-(and-6)-Carboxyfluorescein) (BCECF). Additionally we probed the effect of variations in capillary thickness ($\pm 10\%$, as stated by the manufacturer). The resulting shift in ΔT is of the order of $\pm 6.3\%$ and was assumed as statistical error for our experiments.

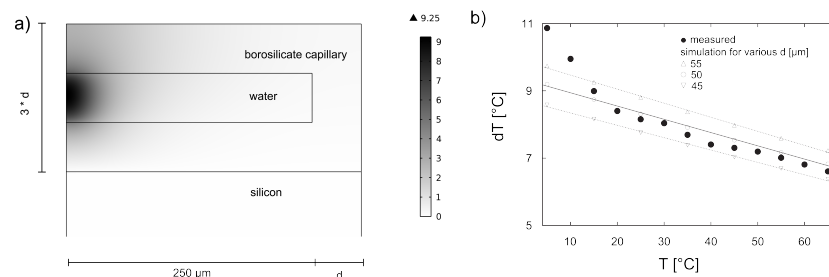


Figure 13: a) Finite Element Simulation for a capillary filled with water which is heated by an infrared (IR)-laser. In this example the temperature at the bottom of the silicon wafer was set to $T = 25\text{ }^{\circ}\text{C}$ and the resulting shift by line averaging is $\Delta T \sim 8\text{ }^{\circ}\text{C}$. b) Since the IR absorbance of water is decreasing with increasing temperature [40], the extracted values for ΔT decrease with increasing base temperature T . Experimental results are in good agreement with our simulation results. The numerical evaluation was also performed for varying capillary thickness d of 45, 50 and 55 μm (variation stated by the supplier). A variation of capillary thickness by 10% entails a variation of ΔT of $\pm 6.3\%$ around the mean temperature. This value is used as statistical error of our experiments.

References

- [1] Hoyer, W. *et al.* Dependence of α -synuclein aggregate morphology on solution conditions. *J Mol Biol* **322**, 383–393 (2002).
- [2] Pinotsi, D. *et al.* Direct observation of heterogeneous amyloid fibril growth kinetics via two-color super-resolution microscopy. *Nano Lett* **14**, 339–345 (2014).
- [3] Guillems, T. *et al.* Nanobodies raised against monomeric α -synuclein distinguish between fibrils at different maturation stages. *J Mol Biol* **425**, 2397–2411 (2013).
- [4] Lorenzen, N. *et al.* The role of stable α -synuclein oligomers in the molecular events underlying amyloid formation. *J Am Chem Soc* **136**, 3859–3868 (2014).
- [5] Buell, A. K. *et al.* Solution conditions determine the relative importance of nucleation and growth processes in α -synuclein aggregation. *Proc Natl Acad Sci U S A* **111**(21), 7671–7676 (2014).
- [6] Galvagnion, C. *et al.* Lipid vesicles trigger α -synuclein aggregation by stimulating primary nucleation. *Nat Chem Biol* **11**, 229–234 (2015).
- [7] Campioni, S. *et al.* The presence of an air-water interface affects formation and elongation of alpha-synuclein fibrils. *J Am Chem Soc* **136**(7), 2866–2875 (2014).
- [8] Buell, A. K. *et al.* Electrostatic effects in filamentous protein aggregation. *Biophys J* **104**, 1116–1126 (2013).
- [9] Shammas, S. L. *et al.* Perturbation of the stability of amyloid fibrils through alteration of electrostatic interactions. *Biophys J* **100**, 2783–2791 (2011).
- [10] Duhr, S. & Braun, D. Why molecules move along a temperature gradient. *Proc Natl Acad Sci U S A* **103**, 19678–19682 (2006).
- [11] Reichl, M., Herzog, M., Götz, A. & Braun, D. Why charged molecules move across a temperature gradient: the role of electric fields. *Phys Rev Lett* **112**, 198101 (2014).
- [12] Keil, L. A setup for RNA melting curves and label free thermophoresis: Bachelor thesis (2011).
- [13] Mittag, J. J., Milani, S., Walsh, D. M., Rädler, J. O. & McManus, J. J. Simultaneous measurement of a range of particle sizes during A β 1–42 fibrillogenesis quantified using fluorescence correlation spectroscopy. *Biochem Biophys Res Commun* **448**, 195–199 (2014).
- [14] Broersma, S. Rotational diffusion constant of a cylindrical particle. *J. Chem. Phys.* **32**, 1626–1631 (1960).
- [15] de la Torre, J. G. G. & Bloomfield, V. A. Hydrodynamic properties of complex, rigid, biological macromolecules: theory and applications. *Q Rev Biophys* **14**, 81–139 (1981).
- [16] Herling, T. W. *et al.* Integration and characterization of solid wall electrodes in microfluidic devices fabricated in a single photolithography step. *Applied physics letters* **102**, 184102 (2013).
- [17] Henry, D. C. The cataphoresis of suspended particles. Part I. The equation of cataphoresis. *Proc R Soc Lond A* **133**, 106–129 (1931).
- [18] Hunter, R. J. *Zeta Potential in Colloid Science: Principles and Applications* (Academic Press, 1981).
- [19] Ohshima, H. J. A simple expression for Henry’s function for the retardation effect in electrophoresis of spherical colloidal particles. *J. Colloid Interf. Sc.* **168**, 269–271 (1994).
- [20] Booth, F. The cataphoresis of spherical, solid non-conducting particles in a symmetrical electrolyte. *Proc R Soc Lond A* **203**, 514–533 (1950).
- [21] Klein, S. D. & Bates, R. G. Conductance of tris(hydroxymethyl)-aminomethane hydrochloride (TrisHCl) in water at 25 and 37 $^{\circ}\text{C}$. *J Sol Chem* **9**(4), 289–292 (1980).
- [22] Quist, A. S. & Marshall, W. L. Assignment of limiting equivalent conductances for single ions to 400 $^{\circ}\text{C}$. *J. Phys. Chem.* **69**(9), 2984–2987 (1965).
- [23] Ohshima, H., Healy, T. W. & White, L. R. Accurate analytic expressions for the surface charge density/surface potential relationship and double-layer potential distribution for a spherical colloidal particle. *J. Colloid Interf. Sc.* **90**(1), 17–26 (1982).
- [24] Manning, G. S. Limiting laws and counterion condensation in polyelectrolyte solutions. V. Further development of the chemical model. *Biophys Chem* **9**, 65–70 (1978).
- [25] Dhont, J. K. G. & Briels, W. J. *Rod-like Brownian Particles in Shear Flow* (WILEY-VCH Verlag Berlin GmbH, 2004).
- [26] Tannous, C. Orientation control of rodlike objects by flow. *arXiv:0905.0091v3* (2009).
- [27] Grossman, P. D. & Soane, D. S. Orientation effects on the electrophoretic mobility of rod-shaped molecules in free solution. *Anal Chem* **62**, 1592–1596 (1990).
- [28] Newman, J. & Swinney, H. L. Length and dipole moment of tmv by laser signal-averaging transient electric birefringence. *Biopolymers* **15**, 301–315 (1976).
- [29] Fixman, M. Charged macromolecules in external fields. 2. preliminary remarks on the cylinder. *Macromolecules* **13**, 711–716 (1980).
- [30] Rogers, S. S. *et al.* Electric birefringence study of an amyloid fibril system: the short end of the length distribution. *Eur Phys J E Soft Matter* **18**, 207–217 (2005).
- [31] O’Konski, C. T., Yoshioka, K. & Orttung, W. H. Electric properties of macromolecules. IV. Determination of electric and optical parameters from saturation of electric birefringence in solutions. *J. Phys. Chem.* **63**(10), 1558–1565 (1959).
- [32] Ohshima, H. Henry’s function for electrophoresis of a cylindrical colloidal particle. *J. Colloid Interf. Sc.* **180**, 299–301 (1996).
- [33] Dhont, J. K. G., Wiegand, S., Duhr, S. & Braun, D. Thermodiffusion of charged colloids: single-particle diffusion. *Langmuir* **23**, 1674–1683 (2007).
- [34] Reichl, M., Herzog, M., Greiss, F., Wolff, M. & Braun, D. Understanding the similarity in thermophoresis between single- and double-stranded DNA or RNA. *Phys. Rev. E* **91**, 062709 (2015).
- [35] Guthrie Jr., G., Wilson, J. N. & Schomaker, V. Theory of the thermal diffusion of electrolytes in a Clusius column. *J. Chem. Phys.* **17**, 310 (1949).

- [36] Eslahian, K. A., Majee, A., Maskos, M. & Würger, A. Specific salt effects on thermophoresis of charged colloids. *Soft Matter* **10**, 1931 (2014).
- [37] Takeyama, N. & Nakashima, K. Proportionality of intrinsic heat of transport to standard entropy of hydration for aqueous ions. *J. Sol. Chem.* **17**(4), 305-325 (1988).
- [38] Iacopini, S., Rusconi, R. & Piazza, R. The "macromolecular tourist": universal temperature dependence of thermal diffusion in aqueous colloidal suspensions. *Eur Phys J E Soft Matter* **19**, 59-67 (2006).
- [39] Römer, F., Wang, Z., Wiegand, S. & Bresme, F. Alkali halide solutions under thermal gradients: Soret coefficients and heat transfer mechanisms. *J Phys Chem B* **117**, 8209-8222 (2013).
- [40] Goldstein, R. & Penner, S. The near-infrared absorption of liquid water at temperatures between 27 and 209°C. *Journal of Quantitative Spectroscopy and Radiative Transfer* **4**(3), 441-451 (1964).

Abbreviations

Aβ	amyloid beta
AD	Alzheimer's Disease
AFM	atomic force microscopy
APD	avalanche photodiode
ApoA1	apolipoprotein A1
α-syn	α -synuclein
β-gal	β -galactosidase
BSA	bovine serum albumin
CF	carboxyfluorescein
CSF	cerebrospinal fluid
DCS	differential centrifugation sedimentation
DLS	dynamic light scattering
DNA	deoxyribonucleic acid
DPPC	1,2-dipalmitoyl-sn-glycero-3-phosphocholine
DPPG₂	1,2-dipalmitoyl-sn-glycero-3-phosphodiglycerol
DSPC	1,2-distearoyl-sn-glycero-3-phosphocholine
EDTA	ethylenediaminetetraacetic acid

FBS	fetal bovine serum, also known as fetal calf serum
FCS	fluorescence correlation spectroscopy
FCCS	fluorescence cross correlation spectroscopy
FDG	fluorescein di- β -D-galactopyranoside
Fib	fibrinogen
FN	fibronectin
FS	fluorescence spectroscopy
GDM	Gaussian distribution model
GFP	green fluorescent protein
HBS	hepes buffered saline
HDL	high-density lipoprotein
HSA	human serum albumin
ISC	intersystem crossing
MEMFCS	maximum entropy method for FCS data analysis
MST	microscale thermophoresis
NLDRE	non-Langmuir differential rate equation
NP	nanoparticle
PBS	phosphate buffered saline
PIE	pulsed-interleaved excitation
R_h	hydrodynamic radius
SA	serum albumin
SDS-PAGE	sodium dodecyl-sulphate polacrylamide gel electrophoresis
Tf	transferrin

T_m	melting phase-transition temperature
TSL	thermosensitive liposome

Bibliography

- [1] ASTRUC, D.: Transition-metal nanoparticles in catalysis: From historical background to the state-of-the art. *Nanoparticles and Catalysis*. Wiley-VCH, 2008, 1–48
- [2] STRATAKIS, E. ; KYMAKIS, E.: Nanoparticle-based plasmonic organic photovoltaic devices. *Materials Today* 16 (2013), 133–146
- [3] FURUKAWA, H. ; CORDOVA, K. ; O'KEEFFE, M. ; YAGHI, O. M. O.: The chemistry and applications of metal-organic frameworks. *Science* 341 (2013), 974–990
- [4] DONALDSON, K. ; SEATON, A.: The Janus faces of nanoparticles. *Journal of Nanoscience and Nanotechnology* 7 (2007), 4607–4611
- [5] BORM, P. J. ; MÜLLER-SCHULTE, D.: Nanoparticles in drug delivery and environmental exposure: Same size, same risks? *Nanomedicine* 1 (2006), 235–249
- [6] DONALDSON, K.: Resolving the nanoparticles paradox. *Nanomedicine* 1 (2006), 229–234
- [7] STIFTUNG-WARENTEST: Die Welt ist klein. *Test* 10/2012 (2012), 64–65
- [8] CEDERVALL, T. ; LYNCH, I. ; LINDMAN, S. ; BERGGÅRD, T. ; THULIN, E. ; NILSSON, H. ; DAWSON, K. A. ; LINSE, S.: Understanding the nanoparticle-protein corona using methods to quantify exchange rates and affinities of proteins for nanoparticles. *Proceedings of the National Academy of Sciences of the United States of America* 104 (2007), 2050–2055
- [9] LUNDQVIST, M. ; STIGLER, J. ; CEDERVALL, T. ; BERGGÅRD, T. ; FLANAGAN, M. B. ; LYNCH, I. ; ELIA, G. ; DAWSON, K.: The evolution of the protein corona around nanoparticles: A test study. *ACS Nano* 5 (2011), 7503–7509

- [10] AGGARWAL, P. ; HALL, J. B. ; MCLELAND, C. B. ; DOBROVOLSKAIA, M. A. ; MCNEIL, S. E.: Nanoparticle interaction with plasma proteins as it relates to particle biodistribution, biocompatibility and therapeutic efficacy. *Advanced Drug Delivery Reviews* 61 (2009), 428–437
- [11] NEL, A. E. ; MÄDLER, L. ; VELEGOL, D. ; XIA, T. ; HOEK, E. M. V. ; SOMASUNDARAN, P. ; KLAESSIG, F. ; CASTRANOVA, V. ; THOMPSON, M.: Understanding biophysicochemical interactions at the nano-bio interface. *Nature Materials* 8 (2009), 543–557
- [12] MAHMOUDI, M. ; SAEEDI-ESLAMI, S. N. ; SHOKRGOZAR, M. A. ; AZADMANESH, K. ; HASSANLOU, M. ; KALHOR, H. R. ; BURTEA, C. ; ROTHEN-RUTISHAUSER, B. ; LAURENT, S. ; SHEIBANI, S. ; VALI, H.: Cell “vision”: Complementary factor of protein corona in nanotoxicology. *Nanoscale* 4 (2012), 5461–5468
- [13] RÖDER, R. ; PREISS, T. ; HIRSCHLE, P. ; STEINBORN, B. ; ZIMPEL, A. ; HOEHN, M. ; RÄDLER, J. O. ; BEIN, T. ; WAGNER, E. ; WUTTKE, S. ; LÄCHELT, U.: Multi-functional nanoparticles by coordinative self-assembly of His-tagged units with metal-organic frameworks. *Journal of the American Chemical Society* 139 (2017), 2359–2368
- [14] PREISS, T. ; ZIMPEL, A. ; WUTTKE, S. ; RÄDLER, J.: Kinetic analysis of the uptake and release of fluorescein by metal-organic framework nanoparticles. *Materials* 10 (2017), 216
- [15] WUTTKE, S. ; BRAIG, S. ; PREISS, T. ; ZIMPEL, A. ; SICKLINGER, J. ; BELLOMO, C. ; RÄDLER, J. O. ; VOLLMAR, A. M. ; BEIN, T.: MOF nanoparticles coated by lipid bilayers and their uptake by cancer cells. *Chemical Communication* 51 (2015), 15752–15755
- [16] HIRSCHLE, P. ; PREISS, T. ; AURAS, F. ; PICK, A. ; VÖLKNER, J. ; VALDEPÉREZ, D. ; WITTE, G. ; PARAK, W. J. ; RÄDLER, J. O. ; WUTTKE, S.: Exploration of MOF nanoparticle sizes using various physical characterization methods – is what you measure what you get? *CrystEngComm* 18 (2016), 4359–4368
- [17] ZIMPEL, A. ; PREISS, T. ; RÖDER, R. ; ENGELKE, H. ; INGRISCH, M. ; PELLER, M. ; RÄDLER, J. O. ; WAGNER, E. ; BEIN, T. ; LÄCHELT, U. ; WUTTKE, S.: Imparting func-

- tionality to MOF nanoparticles by external surface selective covalent attachment of polymers. *Chemistry of Materials* 28 (2016), 3318–3326
- [18] FAN, K. ; CAO, C. ; PAN, Y. ; LU, D. ; YANG, D. ; FENG, J. ; SONG, L. ; LIANG, M. ; YAN, X.: Magnetoferritin nanoparticles for targeting and visualizing tumour tissues. *Nature Nanotechnology* 7 (2012), 459–464
- [19] KINJO, M. ; RIGLER, R.: Ultrasensitive hybridization analysis using fluorescence correlation spectroscopy. *Nucleic Acids Research* 23 (1995), 1795–9
- [20] MARGEAT, E. ; POUJOL, N. ; BOULAHTOUF, A. ; CHEN, Y. ; MÜLLER, J. D. ; GRATTON, E. ; CAVAILLES, V. ; ROYER, C.: The human estrogen receptor alpha dimer binds a single SRC-1 coactivator molecule with an affinity dictated by agonist structure. *Journal of Molecular Biology* 306 (2001), 433–442
- [21] MILANI, S. ; BOMBELLI, F. B. ; PITEK, A. S. ; DAWSON, K. A. ; RÄDLER, J.: Reversible versus irreversible binding of transferrin to polystyrene nanoparticles: Soft and hard corona. *ACS Nano* 6 (2012), 2532–2541
- [22] LIPPOK, S. ; RADTKE, M. ; OBSER, T. ; KLEEMEIER, L. ; SCHNEPPENHEIM, R. ; BUDDE, U. ; NETZ, R. R. ; RÄDLER, J. O.: Shear-induced unfolding and enzymatic cleavage of full-length VWF multimers. *Biophysical Journal* 110 (2016), 545–554
- [23] KOL, N. ; ADLER-ABRAMOVICH, L. ; BARLAM, D. ; SHNECK, R. Z. ; GAZIT, E. ; ROUSSO, I.: Self-assembled peptide nanotubes are uniquely rigid bioinspired supramolecular structures. *Nano Letters* 5 (2005), 1343–1346
- [24] KNOWLES, T. P. J. ; OPPENHEIM, T. W. ; BUELL, A. K. ; CHIRGADZE, D. Y. ; WELLAND, M. E.: Nanostructured films from hierarchical self-assembly of amyloidogenic proteins. *Nature Nanotechnology* 5 (2010), 204–207
- [25] ADLER-ABRAMOVICH, L. ; MARCO, P. ; ARNON, Z. A. ; CREASEY, R. C. G. ; MICHAELS, T. C. T. ; LEVIN, A. ; SCURR, D. J. ; ROBERTS, C. J. ; KNOWLES, T. P. J. ; TENDLER, S. J. B. ; GAZIT, E.: Controlling the physical dimensions of peptide nanotubes by supramolecular polymer coassembly. *ACS Nano* 10 (2016), 7436–7442
- [26] BOLISSETY, S. ; MEZZENGA, R.: Amyloid–carbon hybrid membranes for universal water purification. *Nature Nanotechnology* 11 (2016), 365–371

- [27] SCHWILLE, P. ; HAUSTEIN, E.: Fluorescence correlation spectroscopy. An introduction to its concepts and applications. *Biophysics Textbook Online* 94 (2001), 1–33
- [28] LAKOWICZ, J.: *Principles of Fluorescence Spectroscopy*. Springer US, 2006
- [29] FITZPATRICK, J. A. J. ; LILLEMEIER, B. F.: Fluorescence correlation spectroscopy: Linking molecular dynamics to biological function in vitro and in situ. *Current Opinion in Structural Biology* 21 (2011), 650–660
- [30] PETRÁSEK, Z. ; SCHWILLE, P.: Precise measurement of diffusion coefficients using scanning fluorescence correlation spectroscopy. *Biophysical Journal* 94 (2008), 1437–1448
- [31] KAPUSTA, P.: Absolute diffusion coefficients: Compilation of reference data for FCS. *PicoQuant GmbH Application Note* (2010)
- [32] WIDENGREN, J. ; RIGLER, R. ; METS, Ü.: Triplet-state monitoring by fluorescence correlation spectroscopy. *Journal of Fluorescence* 4 (1994), 255–258
- [33] WIDENGREN, J. ; METS, U. ; RIGLER, R.: Fluorescence correlation spectroscopy of triplet-states in solution - a theoretical and experimental-study. *Journal of Physical Chemistry* 99 (1995), 13368–13379
- [34] CRAENENBROECK, E. V. ; MATTHYS, G. ; BEIRLANT, J. ; ENGELBORGHES, Y.: A statistical analysis of fluorescence correlation data. *Journal of Fluorescence* 9 (1999), 325–331
- [35] PROVENCHER, S. W.: CONTIN: A general purpose constrained regularization program for inverting noisy linear algebraic and integral equations. *Computer Physics Communications* 27 (1982), 229–242
- [36] TJERNBERG, L. O. ; PRAMANIK, A. ; BJORLING, S. ; THYBERG, P. ; THYBERG, J. ; NORDSTEDT, C. ; BERNDT, K. D. ; TERENIUS, L. ; RIGLER, R.: Amyloid beta-peptide polymerization studied using fluorescence correlation spectroscopy. *Chemistry & Biology* 6 (1999), 53–62
- [37] PRAMANIK, A. ; THYBERG, P. ; RIGLER, R.: Molecular interactions of peptides with phospholipid vesicle membranes as studied by fluorescence correlation spectroscopy. *Chemistry and Physics of Lipids* 104 (2000), 35–47

- [38] MATSUMUR, S. ; SHINODA, K. ; YAMADA, M. ; YOKOJIMA, S. ; INOUE, M. ; OHNISHI, T. ; SHIMADA, T. ; KIKUCHI, K. ; MASUI, D. ; HASHIMOTO, S. ; SATO, M. ; ITO, A. ; AKIOKA, M. ; TAKAGI, S. ; NAKAMURA, Y. ; NEMOTO, K. ; HASEGAWA, Y. ; TAKAMOTO, H. ; INOUE, H. ; NAKAMURA, S. ; NABESHIMA, Y.-i. ; TEPLow, D. B. ; KINJO, M. ; HOSHIA, M.: Two distinct amyloid beta-protein (A β) assembly pathways leading to oligomers and fibrils identified by combined fluorescence correlation spectroscopy, morphology, and toxicity analyses. *Journal of Biological Chemistry* 286 (2011), 11555–11562
- [39] SENGUPTA, P. ; GARAI, K. ; BALAJI, J. ; PERIASAMY, N. ; MAITI, S.: Measuring size distribution in highly heterogeneous systems with fluorescence correlation spectroscopy. *Biophysical Journal* 84 (2003), 1977–1984
- [40] SAHOO, B. ; BALAJI, J. ; NAG, S. ; KAUSHALYA, S. K. ; MAITI, S.: Protein aggregation probed by two-photon fluorescence correlation spectroscopy of native tryptophan. *Journal of Chemical Physics* 129 (2008), 075103
- [41] GARAI, K. ; SENGUPTA, P. ; SAHOO, B. ; MAITI, S.: Selective destabilization of soluble amyloid beta oligomers by divalent metal ions. *Biochemical and Biophysical Research Communications* 345 (2006), 210–215
- [42] ZHONG, Z.-H. ; PRAMANIK, A. ; EKBERG, K. ; JANSSON, O. T. ; JÖRNVALL, H. ; WAHREN, J. ; RIGLER, R.: Insulin binding monitored by fluorescence correlation spectroscopy. *Diabetologia* 44 (2001), 1184–1188
- [43] PRASHANTHI, S. ; LANKE, S. R. ; KUMAR, P. H. ; SIVA, D. ; BANGAL, P. R.: Determination of hydrodynamic properties of bare gold and silver nanoparticles as a fluorescent probe using its surface-plasmon-induced photoluminescence by fluorescence correlation spectroscopy. *Applied Spectroscopy* 66 (2012), 835–841
- [44] DONG, C. ; IRUDAYARAJ, J.: Hydrodynamic size-dependent cellular uptake of aqueous QDs probed by fluorescence correlation spectroscopy. *Journal of Physical Chemistry B* 116 (2012), 12125–12132
- [45] CHEN, J. ; WANG, C. ; IRUDAYARAJ, J.: Ultrasensitive protein detection in blood serum using gold nanoparticle probes by single molecule spectroscopy. *Journal of Biomedical Optics* 14 (2009), 040501

- [46] BHOWMIK, D. ; DAS, A. K. ; MAITI, S.: Rapid, cell-free assay for membrane-active forms of amyloid- β . *Langmuir* 31 (2015), 4049–4053
- [47] PAL, N. ; VERMA, S. ; SINGH, M. M. K. ; SEN, S. ; DEV VERMA, S. ; SINGH, M. M. K. ; SEN, S.: Fluorescence correlation spectroscopy: An efficient tool for measuring size, size-distribution and polydispersity of microemulsion droplets in solution. *Analytical Chemistry* 83 (2011), 1–7
- [48] NAG, S. ; CHEN, J. ; IRUDAYARAJ, J. ; MAITI, S.: Measurement of the attachment and assembly of small amyloid- β oligomers on live cell membranes at physiological concentrations using single-molecule tools. *Biophysical Journal* 99 (2010), 1969–1975
- [49] MITTAG, J. J. ; MILANI, S. ; WALSH, D. M. ; RÄDLER, J. O. ; MCMANUS, J. J.: Simultaneous measurement of a range of particle sizes during Abeta 1 – 42 fibrillogenesis quantified using fluorescence correlation spectroscopy. *Biochemical and Biophysical Research Communications* 448 (2014), 195–199
- [50] TIRADO, M. M. ; MARTINEZ, C. L. ; TORRE, J. G. I.: Comparison of theories for the translational and rotational diffusion coefficients of rod-like macromolecules. Application to short DNA fragments. *The Journal of Chemical Physics* 81 (1984), 2047–2052
- [51] LUMMA, D. ; KELLER, S. ; VILGIS, T. ; RÄDLER, J. O. ; RA, J. O.: Dynamics of large semiflexible chains probed by fluorescence correlation spectroscopy. *Physical Review Letters* 90 (2003), 218301
- [52] WINKLER, R. G. ; KELLER, S. ; RÄDLER, J. O.: Intramolecular dynamics of linear macromolecules by fluorescence correlation spectroscopy. *Physical Review E* 73 (2006), 1–14
- [53] STARCHEV, K. ; ZHANG, J. ; BUFFLE, J.: Applications of fluorescence correlation spectroscopy - particle size effect. *Journal of Colloid and Interface Science* 203 (1998), 189–196
- [54] WU, B. ; CHEN, Y. ; MÜLLER, J. D.: Fluorescence correlation spectroscopy of finite-sized particles. *Biophysical Journal* 94 (2008), 2800–2808

- [55] DEPTUŁA, T. ; BUITENHUIS, J. ; JARZEBSKI, M. ; PATKOWSKI, A. ; GAPINSKI, J.: Size of submicrometer particles measured by FCS: correction of the confocal volume. *Langmuir* 31 (2015), 6681–6687
- [56] GAPINSKI, J. ; JARZEBSKI, M. ; BUITENHUIS, J. ; DEPTUŁA, T. ; MAZURYK, J. ; PATKOWSKI, A.: Structure and dimensions of core - shell nanoparticles comparable to the confocal volume studied by means of fluorescence correlation spectroscopy. *Langmuir* 32 (2016), 2482–2491
- [57] PHILLIPS, R. ; KONDEV, J. ; THERIOT, J. ; GARCIA, H.: *Physical Biology of the Cell*. 2nd ed. New York : Garland Science, Taylor & Francis Group, LLC, 2012
- [58] LANGMUIR, I.: *Surface chemistry. Nobel lecture, december 14, 1932*. 1966
- [59] HILL, A.: The possible effects of the aggregation of the molecules of hæmoglobin on its dissociation curves. *The Journal of Physiology* 40 (1910), iv–vii
- [60] WEISS, J. N.: The Hill equation revisited: Uses and misuses. *The FASEB Journal* 11 (1997), 835–841
- [61] STEFAN, M. I. ; LE NOVÈRE, N.: Cooperative binding. *PLoS Computational Biology* 9 (2013), 1–6
- [62] GESZTELYI, R. ; ZSUGA, J. ; KEMENY-BEKE, A. ; VARGA, B. ; JUHASZ, B. ; TOSAKI, A.: The Hill equation and the origin of quantitative pharmacology. *Archive for History of Exact Sciences* 66 (2012), 427–438
- [63] NELSON, D. L. ; COX, M. M.: *Lehninger principles of biochemistry*. 6th ed. Worth Publishing Inc, 2013. – 1–1198 S
- [64] BIETH, J. G.: In vivo significance of kinetic constants of protein proteinase inhibitors. *Biochemical Medicine* 32 (1984), 387–397
- [65] WALCZYKX, D. ; BOMBELLI, F. ; MONOPOLI, M. P. ; LYNCH, I. ; DAWSON, K.: What the cell "sees" in bionanoscience. *Journal of the American Chemical Society* 132 (2010), 5761–5768
- [66] RUSU, L. ; GAMBHIR, A. ; MCLAUGHLIN, S. ; RÄDLER, J.: Fluorescence correlation spectroscopy studies of peptide and protein binding to phospholipid vesicles. *Biophysical Journal* 87 (2004), 1044–1053

- [67] DORN, I. T. ; NEUMAIER, K. R. ; TAMPÉ, R.: Molecular recognition of histidine-tagged molecules by metal-chelating lipids monitored by fluorescence energy transfer and correlation spectroscopy. *Journal of the American Chemical Society* 120 (1998), 2753–2763
- [68] RHOADES, E. ; RAMLALL, T. F. ; WEBB, W. W. ; ELIEZER, D.: Quantification of alpha-synuclein binding to lipid vesicles using fluorescence correlation spectroscopy. *Biophysical Journal* 90 (2006), 4692–4700
- [69] GRUNWALD, D. ; CARDOSO, M. C. ; BUSCHMANN, H. L. ; V: Diffusion and binding properties investigated by fluorescence correlation spectroscopy (FCS). *Current Pharmaceutical Biotechnology* 6 (2005), 381–386
- [70] BEN-TAL, N. ; HONIG, B. ; PEITZSCH, R. ; DENISOV, G. ; MCLAUGHLIN, S.: Binding of small basic peptides to membranes containing acidic lipids: Theoretical models and experimental results. *Biophysical Journal* 71 (1996), 561–575
- [71] LUDWIG, C.: Diffusion zwischen ungleich erwärmten Orten gleich zusammengesetzter Lösung. *Aus der K.K. Hof- und Staatsdruckerei, in Commission bei W. Braumüller, Buchhändler des K.K. Hofes und der K. Akademie der Wissenschaften* (1856)
- [72] WIENKEN, C. J. ; BAASKE, P. ; ROTHBAUER, U. ; BRAUN, D. ; DUHR, S.: Protein-binding assays in biological liquids using microscale thermophoresis. *Nature Communications* 1 (2010), 1–7
- [73] SEIDEL, S. A. I. ; DIJKMAN, P. M. ; LEA, W. A. ; BOGAART, G. van d. ; JERABEK-WILLEMSEN, M. ; LAZIC, A. ; JOSEPH, J. S. ; SRINIVASAN, P. ; BAASKE, P. ; SIMONOV, A. ; KATRITCH, I. ; MELO, F. A. ; LADBURY, J. E. ; SCHREIBER, G. ; WATTS, A. ; BRAUN, D. ; DUHR, S.: Microscale thermophoresis quantifies biomolecular interactions under previously challenging conditions. *Methods* 59 (2013), 301–315
- [74] DUHR, S. ; BRAUN, D.: Why molecules move along a temperature gradient. *Proceedings of the National Academy of Sciences of the United States of America* 103 (2006), 19678–19682
- [75] DUHR, S. ; BRAUN, D.: Thermophoretic depletion follows boltzmann distribution. *Physical Review Letters* 96 (2006), 168301

- [76] REICHL, M. ; HERZOG, M. ; GÖTZ, A. ; BRAUN, D.: Why charged molecules move across a temperature gradient: The role of electric fields. *Physical Review Letters* 112 (2014), 198101
- [77] DENG, J. ; YU, D. ; GAO, C.: Biological identity of nanomaterials: Opportunities and challenges. *Science China Chemistry* 56 (2013), 1533–1541
- [78] MONOPOLI, M. P. ; ÅBERG, C. ; SALVATI, A. ; DAWSON, K. A.: Biomolecular coronas provide the biological identity of nanosized materials. *Nature Nanotechnology* 7 (2012), 779–786
- [79] CASALS, E. ; PFALLER, T. ; DUSCHL, A. ; OOSTINGH, G. J. ; PUNTES, V.: Time evolution of the nanoparticle protein corona. *ACS Nano* 4 (2010), 3623–3632
- [80] GREEN, R. ; DAVIES, M. ; ROBERTS, C. ; TENDLER, S.: Competitive protein adsorption as observed by surface plasmon resonance. *Biomaterials* 20 (1999), 385–391
- [81] MONOPOLI, M. P. ; WAN, S. ; BOMBELLI, F. B. ; MAHON, E. ; DAWSON, K.: Comparisons of nanoparticle protein corona complexes isolated with different methods. *Nano LIFE* 3 (2013), 1343004
- [82] DOCTER, D. ; WESTMEIER, D. ; MARKIEWICZ, M. ; STOLTE, S. ; KNAUER, S. K. ; STAUBER, R. H.: The nanoparticle biomolecule corona: Lessons learned - challenge accepted? *Chemical Society Reviews* 44 (2015), 6094–6121
- [83] LESNIAK, A. ; SALVATI, A. ; SANTOS-MARTINEZ, M. J. ; RADOMSKI, M. W. ; DAWSON, K. A. ; ÅBERG, C.: Nanoparticle adhesion to the cell membrane and its effect on nanoparticle uptake efficiency. *Journal of the American Chemical Society* 135 (2013), 1438–1444
- [84] TREUEL, L. ; BRANDHOLT, S. ; MAFFRE, P. ; WIEGELE, S. ; SHANG, L. ; NIENHAUS, G. U.: Impact of protein modification on the protein corona on nanoparticles and nanoparticle-cell interactions. *ACS Nano* 8 (2014), 503–513
- [85] VROMAN, L.: Effect of adsorbed proteins on the wettability of hydrophilic and hydrophobic solids. *Nature* 196 (1962), 476–477
- [86] VROMAN, L. ; ADAMS, A. L.: Identification of rapid changes at plasma-solid interfaces. *Journal of Biomedical Materials Research* 3 (1969), 43–67

- [87] DELL'ORCO, D. ; LUNDQVIST, M. ; OSLAKOVIC, C. ; CEDERVALL, T. ; LINSE, S.: Modeling the time evolution of the nanoparticle-protein corona in a body fluid. *PLoS ONE* 5 (2010), 1–8
- [88] RÖCKER, C. ; PÖTZL, M. ; ZHANG, F. ; PARAK, W. J. ; NIENHAUS, G. U.: A quantitative fluorescence study of protein monolayer formation on colloidal nanoparticles. *Nature Nanotechnology* 4 (2009), 577–580
- [89] CEDERVALL, T. ; LYNCH, I. ; FOY, M. ; BERGGÅRD, T. ; DONNELLY, S. C. ; CAGNEY, G. ; LINSE, S. ; DAWSON, K. A.: Detailed identification of plasma proteins adsorbed on copolymer nanoparticles. *Angewandte Chemie - International Edition* 46 (2007), 5754–5756
- [90] ANDERSON, N. L. ; ANDERSON, N. G.: The human plasma proteome: History, character, and diagnostic prospects. *Molecular & Cellular Proteomics* 1 (2002), 845–867
- [91] MONOPOLI, M. P. ; WALCZYK, D. ; CAMPBELL, A. ; ELIA, G. ; LYNCH, I. ; BOMBELLI, F. ; DAWSON, K.: Physical-chemical aspects of protein corona: relevance to in vitro and in vivo biological impacts of nanoparticles. *Journal of the American Chemical Society* 133 (2011), 2525–3254
- [92] HELLSTRAND, E. ; LYNCH, I. ; ANDERSSON, A. ; DRAKENBERG, T. ; DAHLBÄCK, B. ; DAWSON, K. A. ; LINSE, S. ; CEDERVALL, T.: Complete high-density lipoproteins in nanoparticle corona. *The FEBS Journal* 276 (2009), 3372–3381
- [93] TENZER, S. ; DOCTER, D. ; ROSFA, S. ; WLODARSKI, A. ; KUHAREV, J. ; REKIK, A. ; KNAUER, S. K. ; BANTZ, C. ; NAWROTH, T. ; BIER, C. ; SIRIRATTANAPAN, J. ; MANN, W. ; TREUEL, L. ; ZELLNER, R. ; MASKOS, M. ; SCHILD, H. ; STAUBER, R. H.: Nanoparticle size is a critical physicochemical determinant of the human blood plasma corona: A comprehensive quantitative proteomic analysis. *ACS Nano* 5 (2011), 7155–7167
- [94] TENZER, S. ; DOCTER, D. ; KUHAREV, J. ; MUSYANOVYCH, A. ; FETZ, V. ; HECHT, R. ; SCHLENK, F. ; FISCHER, D. ; KIOUPTSI, K. ; REINHARDT, C. ; LANDFESTER, K. ; SCHILD, H. ; MASKOS, M. ; KNAUER, S. K. ; STAUBER, R. H.: Rapid formation of plasma protein corona critically affects nanoparticle pathophysiology. *Nature Nanotechnology* 8 (2013), 772–81

- [95] MIRSHAFIEE, V. ; KIM, R. ; MAHMOUDI, M. ; KRAFT, M. L.: The importance of selecting a proper biological milieu for protein corona analysis in vitro: Human plasma versus human serum. *The International Journal of Biochemistry & Cell Biology* 75 (2016), 188–195
- [96] JEYACHANDRAN, Y. L. ; MIELCZARSKI, E. ; RAI, B. ; MIELCZARSKI, J.: Quantitative and qualitative evaluation of adsorption/desorption of bovine serum albumin on hydrophilic and hydrophobic surfaces. *Langmuir* 25 (2009), 11614–11620
- [97] MINCHIOTTI, L. ; GALLIANO, M. ; KRAGH-HANSEN, U. ; WATKINS, S. ; MADISON, J. ; PUTNAM, F. W.: A genetic variant of albumin (albumin asola; Tyr140Cys) with no free-SH group but with an additional disulfide bridge. *European Journal of Biochemistry* 228 (1995), 155–159
- [98] KRAGH-HANSEN, U.: Molecular and practical aspects of the enzymatic properties of human serum albumin and of albumin-ligand complexes. *Biochimica et Biophysica Acta (BBA)* 1830 (2013), 5535–5544
- [99] SAVAGE, B. ; BOTTINI, E. ; RUGGERI, Z. M.: Interaction of integrin α IIb β 3 with multiple fibrinogen domains during platelet adhesion. *Journal of Biological Chemistry* 270 (1995), 28812–28817
- [100] KIM, J. ; SOMORJAI, G. A.: Molecular packing of lysozyme, fibrinogen, and bovine serum albumin on hydrophilic and hydrophobic surfaces studied by infrared-visible sum frequency generation and fluorescence microscopy. *Journal of the American Chemical Society* 125 (2003), 3150–3158
- [101] ALTIERI, D. C. ; BADER, R. ; MANNUCCI, P. M. ; EDINGTON, T. S.: Oligospecificity of the cellular adhesion receptor Mac-1 encompasses an inducible recognition specificity for fibrinogen. *The Journal of Cell Biology* 107 (1988), 1893–1900
- [102] TREZZINI, C. ; JUNGI, T. W. ; KUHNERT, P. ; PETERHANS, E.: Fibrinogen association with human monocytes: Evidence for constitutive expression of fibrinogen receptors and for involvement of Mac-1 (CD18, CR3) in the binding. *Biochemical and Biophysical Research Communications* 156 (1988), 477–484
- [103] PANKOV, R. ; YAMADA, K. M.: Fibronectin at a glance. *Journal of Cell Science* 115 (2002), 3861–3863

- [104] JANDL, J. H. ; KATZ, J. H.: The plasma-to-cell cycle of transferrin. *Journal of Clinical Investigation* 42 (1963), 314–326
- [105] FINCH, C. ; HUEBERS, H. A. ; ENG, M. ; MILLER, L.: Effect of transfused reticulocytes on iron exchange. *Blood* 59 (1982), 364–369
- [106] HUEBERS, H. A. ; FINCH, C. A.: The physiology of transferrin and transferrin receptors. *Physiological Reviews* 67 (1987), 520–582
- [107] AISEN, P. ; LEIBMAN, A. ; ZWEIER, J.: Stoichiometric and site characteristics of the binding of iron to human transferrin. *Journal of Biological Chemistry* 253 (1978), 1930–1937
- [108] AISEN, P. ; LISTOWSKY, I.: Iron transport and storage proteins. *Annual Review of Biochemistry* 49 (1980), 357–393
- [109] SHONGWE, M. S. ; SMITH, C. a. ; AINSCOUGH, E. W. ; BAKER, H. M. ; BRODIE, a. M. ; BAKER, E. N.: Anion binding by human lactoferrin: Results from crystallographic and physicochemical studies. *Biochemistry* 31 (1992), 4451–4458
- [110] ZAK, O. ; TRINDER, D. ; AISEN, P.: Primary receptor-recognition site of human transferrin is in the C-terminal lobe. *Journal of Biological Chemistry* 269 (1994), 7110–7114
- [111] ROTHENBERGER, S. ; IACOPETTA, B. J. ; KÜHN, L. C.: Endocytosis of the transferrin receptor requires the cytoplasmic domain but not its phosphorylation site. *Cell* 49 (1987), 423–431
- [112] MCGRAW, T. E. ; MAXFIELD, F. R.: Human transferrin receptor internalization is partially dependent upon an aromatic amino acid on the cytoplasmic domain. *Cell Regulation* 1 (1990), 369–377
- [113] RENSWOUDE, J. van ; BRIDGES, K. R. ; HARFORD, J. B. ; KLAUSNER, R. D.: Receptor-mediated endocytosis of transferrin and the uptake of fe in K562 cells: Identification of a nonlysosomal acidic compartment. *Proceedings of the National Academy of Sciences of the United States of America* 79 (1982), 6186–6190
- [114] DAUTRY-VARSAT, A. ; CIECHANOVER, A. ; LODISH, H. F.: pH and the recycling of transferrin during receptor-mediated endocytosis. *Proceedings of the National Academy of Sciences of the United States of America* 80 (1983), 2258–2262

- [115] BAKER, E. N. ; RUMBALL, S. V. ; ANDERSON, B. F.: Transferrins: Insights into structure and function from studies on lactoferrin. *Trends in Biochemical Sciences* 12 (1987), 350–353
- [116] BALI, P. K. ; ZAK, O. ; AISEN, P.: A new role for the transferrin receptor in the release of iron from transferrin. *Biochemistry* 30 (1991), 324–328
- [117] SIPE, D. M. ; MURPHY, R. F.: Binding to cellular receptors results in increased iron release from transferrin at mildly acidic pH. *Journal of Biological Chemistry* 266 (1991), 8002–8007
- [118] KLAUSNER, R. D. ; RENSWOUDE, J. van ; ASHWELL, G. ; KEMPF, C. ; SCHECHTER, A. N. ; DEAN, A. ; BRIDGES, K. R.: Receptor-mediated endocytosis of transferrin in K562 cells. *Journal of Biological Chemistry* 258 (1983), 4715–4724
- [119] HÖGEMANN-SAVELLANO, D. ; BOS, E. ; BLONDET, C. ; SATO, F. ; ABE, T. ; JOSEPHSON, L. ; WEISSLEDER, R. ; GAUDET, J. ; SGROI, D. ; PETERS, P. J. ; BASILION, J. P.: The transferrin receptor: A potential molecular imaging marker for human cancer. *Neoplasia* 5 (2003), 495–506
- [120] PACK, D. W. ; HOFFMAN, A. S. ; PUN, S. ; STAYTON, P. S.: Design and development of polymers for gene delivery. *Nature Reviews Drug Discovery* 4 (2005), 581–593
- [121] TORTORELLA, S. ; KARAGIANNIS, T. C.: Transferrin receptor-mediated endocytosis: A useful target for cancer therapy. *Journal of Membrane Biology* 247 (2014), 291–307
- [122] MACEDO, M. F. ; SOUSA, M. de: Transferrin and the transferrin receptor: Of magic bullets and other concerns. *Inflammation & Allergy-Drug Targets* 7 (2008), 41–52
- [123] VILASECA, P. ; DAWSON, K. A. ; FRANZESE, G.: Understanding and modulating the competitive surface-adsorption of proteins through coarse-grained molecular dynamics simulations. *Soft Matter* 9 (2013), 6978
- [124] SVENSSON, O. ; ARNEBRANT, T.: Adsorption of serum albumin on silica - The influence of surface cleaning procedures. *Journal of Colloid and Interface Science* 344 (2010), 44–47
- [125] KOTELIANSKY, V. E. ; GLUKHOVA, M. A. ; BENJAMIN, M. V. ; SMIRNOV, V. N. ; FILIMONOV, V. V. ; ZALITE, O. M. ; VENYAMINOV, S. Y.: A study of the structure of fibronectin. *European Journal of Biochemistry* 119 (1981), 619–624

- [126] ARCIELLO, A. ; PICCOLI, R. ; MONTI, D. M.: Apolipoprotein A-I: The dual face of a protein. *The FEBS Journal* 590 (2016), 4171–4179
- [127] KANE, J. P. ; MALLOY, M. J.: Prebeta-1 HDL and coronary heart disease. *Current Opinion in Lipidology* 23 (2012), 367–371
- [128] RYE, K.-A. ; BARTER, P. J.: Formation and metabolism of prebeta-migrating, lipid-poor apolipoprotein A-I. *Arteriosclerosis, Thrombosis, and Vascular Biology* 24 (2004), 421–428
- [129] CAVIGIOLIO, G. ; GEIER, E. G. ; SHAO, B. ; HEINECKE, J. W. ; ODA, M. N.: Exchange of apolipoprotein A-I between lipid-associated and lipid-free states. *Journal of Biological Chemistry* 285 (2011), 18847–18857
- [130] RAMELLA, N. A. ; RIMOLDI, O. J. ; PRIETO, E. D. ; SCHINELLA, G. R. ; SANCHEZ, S. A. ; JAUREGUIBERRY, M. S. ; VELA, M. E. ; FERREIRA, S. T. ; TRICERRI, M. A.: Human apolipoprotein A-I-derived amyloid: Its association with atherosclerosis. *PLoS ONE* 6 (2011), e22532
- [131] RADER, D. J.: Molecular regulation of HDL metabolism and function: Implications for novel therapies. *The Journal of Clinical Investigation* 116 (2006), 3090–3100
- [132] MEISTER, S. ; ZLATEV, I. ; STAB, J. ; DOCTER, D. ; BACHES, S. ; STAUBER, R. H. ; DEUTSCH, M. ; SCHMIDT, R. ; ROPELE, S. ; WINDISCH, M. ; LANGER, K. ; WAGNER, S. ; BRIESEN, H. von ; AND, S. W. ; PIETRZIK, C. U. ; BRIESEN, H. von ; WEGGEN, S. ; PIETRZIK, C. U.: Nanoparticulate flurbiprofen reduces amyloid- β 42 generation in an in vitro blood–brain barrier model. *Alzheimer's Research & Therapy* 5 (2013), 1–12
- [133] PAULA-LIMA, A. C. ; TRICERRI, M. A. ; BRITO-MOREIRA, J. ; BOMFIM, T. R. ; OLIVEIRA, F. F. ; MAGDESIAN, M. H. ; GRINBERG, L. T. ; PANIZZUTTI, R. ; FERREIRA, S. T.: Human apolipoprotein A-I binds amyloid- β and prevents A β -induced neurotoxicity. *International Journal of Biochemistry and Cell Biology* 41 (2009), 1361–1370
- [134] ZAMANIAN-DARYOUSH, M. ; LINDNER, D. ; TALLANT, T. C. ; WANG, Z. ; BUFFA, J. ; KLIPFELL, E. ; PARKER, Y. ; HATALA, D. ; PARSONS-WINGERTER, P. ; RAYMAN, P. ; YUSUFISHAQ, M. S. S. ; FISHER, E. A. ; SMITH, J. D. ; FINKE, J. ; DIDONATO, J. A. ; HAZEN, S. L.: The cardioprotective protein apolipoprotein A1 promotes potent anti-tumorigenic effects. *The Journal of Biological Chemistry* 288 (2013), 21237–21252

- [135] KREUTER, J. ; SHAMENKOV, D. ; PETROV, V. ; RAMGE, P. ; CYCHUTEK, K. ; KOCH-BRANDT, C. ; ALYAUTDIN, R.: Apolipoprotein-mediated transport of nanoparticle-bound drugs across the blood–brain barrier. *Journal of Drug Targeting* 10 (2002), 317–325
- [136] MARUYAMA, M. ; ARAI, H. ; SUGITA, M. ; TANJI, H. ; HIGUCHI, M. ; OKAMURA, N. ; MATSUI, T. ; HIGUCHI, S. ; MATSUSHITA, S. ; YOSHIDA, H. ; SASAKI, H.: Cerebrospinal fluid amyloid beta(1-42) levels in the mild cognitive impairment stage of Alzheimer’s disease. *Experimental Neurology* 172 (2001), 433–436
- [137] FAGAN, A. M. ; HEAD, D. ; SHAH, A. R. ; MARCUS, D. ; MINTUN, M. ; MORRIS, J. C. ; HOLTZMAN, D. M.: Decreased cerebrospinal fluid A β (42) correlates with brain atrophy in cognitively normal elderly. *Annals of Neurology* 65 (2009), 176–183
- [138] KUMAR, S. ; WALTER, J.: Phosphorylation of amyloid beta (A β) peptides – A trigger for formation of toxic aggregates in Alzheimer’s disease. *Aging* 3 (2011), 1–10
- [139] NAG, S. ; SARKAR, B. ; BANDYOPADHYAY, A. ; SAHOO, B. ; SREENIVASAN, V. K. a. ; KOMBRABAIL, M. ; MURALIDHARAN, C. ; MAITI, S.: Nature of the amyloid- β monomer and the monomer-oligomer equilibrium. *The Journal of Biological Chemistry* 286 (2011), 13827–13833
- [140] GALANTE, D. ; CORSARO, A. ; FLORIO, T. ; VELLA, S. ; PAGANO, A. ; SBRANA, F. ; VASSALLI, M. ; PERICO, A. ; D’ARRIGO, C.: Differential toxicity, conformation and morphology of typical initial aggregation states of A β 1-42 and A β py3-42 beta-amyloids. *The International Journal of Biochemistry & Cell Biology* 44 (2012), 2085–2093
- [141] FINDER, V. H. ; GLOCKSHUBER, R.: Amyloid- β aggregation. *Neurodegenerative Diseases* 4 (2007), 13–27
- [142] GANDY, S.: The role of cerebral amyloid beta accumulation in common forms of Alzheimer disease. *The Journal of Clinical Investigation* 115 (2005), 1121–1129
- [143] PITSCHKE, M. ; PRIOR, R. ; HAUPT, M. ; RIESNER, D.: Detection of single amyloid beta-protein aggregates in the cerebrospinal fluid of Alzheimer’s patients by fluorescence correlation spectroscopy. *Nature Medicine* 4 (1998), 832–834

- [144] WALSH, D. M. ; THULIN, E. ; MINOGUE, A. M. ; GUSTAVSSON, N. ; PANG, E. ; TEPLOW, D. B. ; LINSE, S.: A facile method for expression and purification of the Alzheimer's disease-associated amyloid β -peptide. *The FEBS Journal* 276 (2009), 1266–1281
- [145] SIDHU, A. ; WERSINGER, C. ; VERNIER, P.: Alpha-Synuclein regulation of the dopaminergic transporter: A possible role in the pathogenesis of Parkinson's disease. *The FEBS Journal* 565 (2004), 1–5
- [146] PEREZ, R. G. ; HASTINGS, T. G.: Could a loss of α -synuclein function put dopaminergic neurons at risk? *Journal of Neurochemistry* 89 (2004), 1318–1324
- [147] BONINI, N. M. ; GIASSON, B. I.: Snaring the function of alpha-synuclein. *Cell* 123 (2005), 359–361
- [148] JENCO, J. M. ; RAWLINGSON, A. ; DANIELS, B. ; MORRIS, A. J.: Regulation of phospholipase D2: Selective inhibition of mammalian phospholipase D isoenzymes by α - and β -synucleins. *Biochemistry* 37 (1998), 4907–4909
- [149] PENG, X. M. ; TEHRANIAN, R. ; DIETRICH, P. ; STEFANIS, L. ; PEREZ, R. G.: α -Synuclein activation of protein phosphatase 2A reduces tyrosine hydroxylase phosphorylation in dopaminergic cells. *Journal of Cell Science* 118 (2005)
- [150] JO, E. ; MCLAURIN, J. ; YIP, C. M. ; ST GEORGE-HYSLOP, P. ; FRASER, P. E.: alpha-Synuclein membrane interactions and lipid specificity. *The Journal of Biological Chemistry* 275 (2000), 34328–34
- [151] PERNI, M. ; GALVAGNION, C. ; MALTSEV, A. ; MEISL, G. ; MÜLLER, M. B. D. ; CHALLA, P. K. ; KIRKEGAARD, J. B. ; FLAGMEIER, P. ; COHEN, S. I. A. ; CASCELLA, R. ; CHEN, S. W. ; LIMBOKER, R. ; SORMANNI, P. ; HELLER, G. T. ; APRILE, F. A. ; CREMADES, N. ; CECCHI, C. ; CHITI, F. ; NOLLEN, E. A. A. ; KNOWLES, T. P. J. ; VENDRUSCOLO, M. ; BAX, A. ; ZASLOFF, M. ; DOBSON, C. M.: A natural product inhibits the initiation of α -synuclein aggregation and suppresses its toxicity. *Proceedings of the National Academy of Sciences of the United States of America* (2017), 201610586
- [152] CABIN, D. E. ; SHIMAZU, K. ; MURPHY, D. ; COLE, N. B. ; GOTTSCHALK, W. ; MCILWAIN, K. L. ; ORRISON, B. ; CHEN, A. ; ELLIS, C. E. ; PAYLOR, R. ; LU, B. ;

- NUSSBAUM, R. L.: Synaptic vesicle depletion correlates with attenuated synaptic responses to prolonged repetitive stimulation in mice lacking α -synuclein. *Journal of Neuroscience* 22 (2002), 8797–8807
- [153] CASTAGNET, P. I. ; GOLOVKO, M. Y. ; BARCELÓ-COBLIJN, G. C. ; NUSSBAUM, R. L. ; MURPHY, E. J.: Fatty acid incorporation is decreased in astrocytes cultured from α -synuclein gene-ablated mice. *Journal of Neurochemistry* 94 (2005), 839–849
- [154] WEINREB, P. H. ; ZHEN, W. ; POON, A. W. ; CONWAY, K. A. ; LANSBURY, P. T. J.: NACP, a protein implicated in alzheimer's disease and learning, is natively unfolded. *Biochemistry* 35 (1996), 13709–13715
- [155] LENDEL, C. ; BERTONCINI, C. W. ; CREMADES, N. ; WAUDBY, C. A. ; VENDRUSCOLO, M. ; DOBSON, C. M. ; SCHENK, D. ; CHRISTODOULOU, J. ; TOTH, G.: On the mechanism of nonspecific inhibitors of protein aggregation: Dissecting the interactions of α -synuclein with congo red and lacmoid. *Biochemistry* 48 (2009), 8322–8334
- [156] DAVIDSON, W. S. ; JONAS, A. ; CLAYTON, D. F. ; GEORGE, J. M.: Stabilization of alpha-synuclein secondary structure upon binding to synthetic membranes. *The Journal of Biological Chemistry* 273 (1998), 9443–9449
- [157] ELIEZER, D. ; KUTLUAY, E. ; BUSSELL, R. ; BROWNE, G.: Conformational properties of α -synuclein in its free and lipid-associated states. *Journal of Molecular Biology* 307 (2001), 1061–1073
- [158] GIASSON, B. I. ; MURRAY, I. V. ; TROJANOWSKI, J. Q. ; LEE, V. M.: A hydrophobic stretch of 12 amino acid residues in the middle of alpha-synuclein is essential for filament assembly. *The Journal of Biological Chemistry* 276 (2001), 2380–2386
- [159] DÖRNER, K.: *Klinische Chemie und Hämatologie*. Stuttgart : Thieme, 2013
- [160] FASS, D. N. ; KNUTSON, G. J. ; KATZMANN, J. A.: Monoclonal antibodies to porcine factor VIII coagulant and their use in the isolation of active coagulant protein. *Blood* 59 (1982), 594–600
- [161] SEELIG, H. P.: *Präanalytik*. 3. ed. Karlsruhe, 2008
- [162] ANDERSON, P. J. ; KOKAME, K. ; SADLER, J. E.: Zinc and calcium ions cooperatively modulate ADAMTS13 activity. *The Journal of Biological Chemistry* 281 (2006), 850–857

- [163] APONTE-SANTAMARÍA, C. ; LIPPOK, S. ; MITTAG, J. J. ; OBSER, T. ; SCHNEPPENHEIM, R. ; BALDAUF, C. ; GRÄTER, F. ; BUDDE, U. ; RÄDLER, J. O.: Mutation G1629E increases von Willebrand factor cleavage via a cooperative destabilization mechanism. *Biophysical Journal* 112 (2017), 57–65
- [164] HALEEM J. ISSAQ ; XIAO, Z. ; VEENSTRA, T. D.: Serum and plasma proteomics. *Chemical Reviews* 107 (2007), 3601–3620
- [165] OLSON, E. ; TORRES, R. ; LEVENE, M. J.: Integrated fluorescence correlation spectroscopy device for point-of-care clinical applications. *Biomedical Optics Express* 4 (2013), 1074–1082
- [166] ENGELKE, H. ; LIPPOK, S. ; DORN, I. ; NETZ, R. R. ; RÄDLER, J. O.: FVIII binding to PS membranes differs in the activated and non-activated form and can be shielded by annexin A5. *The Journal of Physical Chemistry B* 115 (2011), 12963–12970
- [167] ELLIS, R.: Macromolecular crowding: An important but neglected aspect of the intracellular environment. *Current Opinion in Structural Biology* 11 (2001), 114–119
- [168] ELLIS, R. J. ; MINTON, A. P.: Cell biology: Join the crowd. *Nature* 425 (2003), 27–28
- [169] ZHOU, H.-X. ; RIVAS, G. ; MINTON, A. P.: Macromolecular crowding and confinement: Biochemical, biophysical, and potential physiological consequences. *Annual Review of Biophysics* 37 (2008), 375–397
- [170] ENGELKE, H. ; DORN, I. ; RÄDLER, J. O. ; JOACHIM, O. R.: Diffusion and molecular binding in crowded vesicle solutions measured by fluorescence correlation spectroscopy. *Soft Matter* 5 (2009), 4283–4289
- [171] ENGELKE, H. ; HEINRICH, D. ; RÄDLER, J. O.: Probing GFP-actin diffusion in living cells using fluorescence correlation spectroscopy. *Physical Biology* 7 (2010), 46014
- [172] FENOLLOSA, R. ; GARCIA-RICO, E. ; ALVAREZ, S. ; ALVAREZ, R. ; YU, X. ; RODRIGUEZ, I. ; CARREGAL-ROMERO, S. ; VILLANUEVA, C. ; GARCIA-ALGAR, M. ; RIVERA-GIL, P. ; LERA, A. R. ; PARAK, W. J. ; MESEGUER, F. ; ALVAREZ-PUEBLA, R.: Silicon particles as trojan horses for potential cancer therapy. *Journal of Nanobiotechnology* 12 (2014), 1–10

- [173] NAPIERSKA, D. ; LEEN THOMASSEN ; LISON, D. ; MARTENS, J. A. ; HOET, P. H. ; THOMASSEN, L. C. ; LISON, D. ; MARTENS, J. A. ; HOET, P. H.: The nanosilica hazard: Another variable entity. *Particle and Fibre Toxicology* 7 (2010), 1–32
- [174] BHARTI, C. ; NAGAICH, U. ; PAL, A. K. ; GULATI, N.: Mesoporous silica nanoparticles in target drug delivery system: A review. *International Journal of Pharmaceutical Investigation* 5 (2015), 124–33
- [175] MCCARTHY, J. R. ; WEISSLEDER, R.: Multifunctional magnetic nanoparticles for targeted imaging and therapy. *Advanced Drug Delivery Reviews* 60 (2008), 1241–1251
- [176] THOENY, H. C. ; TRIANTAFYLLOU, M. ; BIRKHAUSER, F. D. ; FROELICH, J. M. ; TSHERING, D. W. ; BINSER, T. ; FLEISCHMANN, A. ; VERMATHEN, P. ; STUDER, U. E.: Combined ultrasmall superparamagnetic particles of iron oxide-enhanced and diffusion-weighted magnetic resonance imaging reliably detect pelvic lymph node metastases in normal-sized nodes of bladder and prostate cancer patients. *European Urology* 55 (2009), 761–769
- [177] LOOSLI, F. ; VITORAZI, L. ; BERRET, J.-F. ; STOLL, S.: Isothermal titration calorimetry as a powerful tool to quantify and better understand agglomeration mechanisms during interaction processes between TiO₂ nanoparticles and humic acids. *Environmental Science: Nano* 2 (2015), 541–550
- [178] ARMAND, L. ; BIOLA-CLIER, M. ; BOBYK, L. ; COLLIN-FAURE, V. ; DIEMER, H. ; STRUB, J. M. ; CIANFERANI, S. ; VAN DORSSELAER, A. ; HERLIN-BOIME, N. ; RABILLOUD, T. ; CARRIERE, M.: Molecular responses of alveolar epithelial A549 cells to chronic exposure to titanium dioxide nanoparticles: A proteomic view. *Journal of Proteomics* 134 (2016), 163–173
- [179] SHI, H. ; MAGAYE, R. ; CASTRANOVA, V. ; ZHAO, J.: Titanium dioxide nanoparticles: A review of current toxicological data. *Particle and Fibre Toxicology* 10 (2013), 1–33
- [180] ORIEKHOVA, O. ; STOLL, S.: Effects of pH and fulvic acids concentration on the stability of fulvic acids - cerium (IV) oxide nanoparticle complexes. *Chemosphere* 144 (2016), 131–137
- [181] KELLER, J. ; WOHLLEBEN, W. ; MA-HOCK, L. ; STRAUSS, V. ; GRÖTERS, S. ; KÜTTLER, K. ; WIENCH, K. ; HERDEN, C. ; OBERDÖRSTER, G. ; RAVENZWAAY,

- B. van ; LANDSIEDEL, R.: Time course of lung retention and toxicity of inhaled particles: Short-term exposure to nano-Ceria. *Archives of Toxicology* 88 (2014), 2033–2059
- [182] RODRÍGUEZ, J. A. ; WANG, X. ; HANSON, J. C. ; LIU, G. ; IGLESIAS-JUEZ, A. ; FERNANDEZ-GARCIA, M.: The behavior of mixed-metal oxides: Structural and electronic properties of $Ce_{1-x}Ca_xO_2$ and $Ce_{1-x}Ca_xO_{2-x}$. *Journal of Chemical Physics* 119 (2003), 5659–5669
- [183] VILANOVA, O. ; MITTAG, J. J. ; KELLY, P. M. ; MILANI, S. ; DAWSON, K. A. ; RÄDLER, J. O. ; DAWSON, A. ; JOACHIM, O. R.: Understanding the kinetics of protein-nanoparticle corona formation. *ACS Nano* 10 (2016), 10842–10850
- [184] SALVATI, A. ; PITEK, A. S. ; MONOPOLI, M. P. ; PRAPAINOP, K. ; BOMBELLI, F. B. ; HRISTOV, D. R. ; KELLY, P. M. ; ÅBERG, C. ; MAHON, E. ; DAWSON, K. a.: Transferrin-functionalized nanoparticles lose their targeting capabilities when a biomolecule corona adsorbs on the surface. *Nature Nanotechnology* 8 (2013), 137–43
- [185] PITEK, A. S. ; O'CONNELL, D. ; MAHON, E. ; MONOPOLI, M. P. ; BALDELLI, F. ; DAWSON, K.: Transferrin coated nanoparticles: Study of the bionano interface in human plasma. *PLoS ONE* 7 (2012)
- [186] KRPETIĆ, Ž. ; DAVIDSON, A. M. ; VOLK, M. ; LÉVY, R. ; BRUST, M. ; COOPER, D. L.: High-resolution sizing of monolayer-protected gold clusters by differential centrifugal sedimentation. *ACS Nano* 7 (2013), 8881–8890
- [187] DING, H. M. ; MA, Y. Q.: Computer simulation of the role of protein corona in cellular delivery of nanoparticles. *Biomaterials* 35 (2014), 8703–8710
- [188] DARABI SAHNEH, F. ; SCOGLIO, C. ; RIVIERE, J.: Dynamics of nanoparticle-protein corona complex formation: Analytical results from population balance equations. *PLoS ONE* 8 (2013), e64690
- [189] PATRA, A. ; DING, T. ; ENGUDAR, G. ; WANG, Y. ; DYKAS, M. M. ; LIEDBERG, B. ; KAH, J. C. Y. ; VENKATESAN, T. ; DRUM, C. L.: Component-specific analysis of plasma protein corona formation on gold nanoparticles using multiplexed surface plasmon resonance. *Small* 12 (2016), 1174–1182

- [190] MAFFRE, P. ; BRANDHOLT, S. ; NIENHAUS, K. ; SHANG, L. ; PARAK, W. J. ; NIENHAUS, G. U.: Effects of surface functionalization on the adsorption of human serum albumin onto nanoparticles – a fluorescence correlation spectroscopy study. *Beilstein Journal of Nanotechnology* 5 (2014), 2036–2047
- [191] NIENHAUS, G. U. ; MAFFRE, P. ; NIENHAUS, K.: Studying the protein corona on nanoparticles by FCS. *Methods in Enzymology* 519 (2013), 115–137
- [192] JIANG, X. ; WEISE, S. ; HAFNER, M. ; RÖCKER, C. ; ZHANG, F. ; PARAK, W. J. ; NIENHAUS, G. U.: Quantitative analysis of the protein corona on FePt nanoparticles formed by transferrin binding. *Journal of The Royal Society Interface* 7 (2010), S5–S13
- [193] HUHN, J. ; FEDELI, C. ; ZHANG, Q. ; MASOOD, A. ; DEL PINO, P. ; KHASHAB, N. M. ; PAPINI, E. ; PARAK, W. J.: Dissociation coefficients of protein adsorption to nanoparticles as quantitative metrics for description of the protein corona: A comparison of experimental techniques and methodological relevance. *The International Journal of Biochemistry & Cell Biology* 75 (2016), 148–161
- [194] LIEDL, T. ; KELLER, S. ; SIMMEL, F. C. ; RADLER, J. O. ; PARAK, W. J.: Fluorescent nanocrystals as colloidal probes in complex fluids measured by fluorescence correlation spectroscopy. *Small* 1 (2005), 997–1003
- [195] CANOA, P. ; SIMÓN-VÁZQUEZ, R. ; POPPLEWELL, J. ; GONZÁLEZ-FERNÁNDEZ, Á.: A quantitative binding study of fibrinogen and human serum albumin to metal oxide nanoparticles by surface plasmon resonance. *Biosensors and Bioelectronics* 74 (2015), 376–383
- [196] BOULOS, S. P. ; DAVIS, T. A. ; YANG, J. A. ; LOHSE, S. E. ; ALKILANY, A. M. ; HOLLAND, L. A. ; MURPHY, C. J.: Nanoparticle–protein interactions: A thermodynamic and kinetic study of the adsorption of bovine serum albumin to gold nanoparticle surfaces. *Langmuir* 29 (2013), 14984–14996
- [197] LI, N. ; ZENG, S. ; HE, L. ; ZHONG, W.: Probing nanoparticle-protein interaction by capillary electrophoresis. *Analytical Chemistry* 82 (2010), 7460–7466
- [198] ZHANG, H. ; WU, P. ; ZHU, Z. ; WANG, Y.: Interaction of gamma-Fe(2)O(3) nanoparticles with fibrinogen. *Spectrochimica Acta Part A: Molecular and Biomolecular Spectroscopy* 151 (2015), 40–47

- [199] CAI, H. ; YAO, P.: Gold nanoparticles with different amino acid surfaces: Serum albumin adsorption, intracellular uptake and cytotoxicity. *Colloids and Surfaces B: Biointerfaces* 123 (2014), 900–906
- [200] GREGORIADIS, G. ; RYMAN, B. E.: Liposomes as carriers of enzymes or drugs: A new approach to the treatment of storage diseases. *The Biochemical Journal* 124 (1971), 58
- [201] GREGORIADIS, G.: Drug entrapment in liposomes. *The FEBS Journal* 36 (1973), 292–296
- [202] PERRIE, Y.: Gregory Gregoriadis: Introducing liposomes to drug delivery. *Journal of Drug Targeting* 16 (2008), 518–519
- [203] LASIC, D. D.: Doxorubicin in sterically stabilized liposomes. *Nature* 380 (1996), 561–562
- [204] LASIC, D. D. ; NEEDHAM, D.: The “stealth” liposome: A prototypical biomaterial. *Chemical Reviews* 95 (1995), 2601–2628
- [205] SLINGERLAND, M. ; GUCHELAAR, H. J. ; GELDERBLOM, H.: *Liposomal drug formulations in cancer therapy: 15 years along the road*
- [206] SARRIS, A. H. ; HAGEMEISTER, F. ; ROMAGUERA, J. ; RODRIGUEZ, M. A. ; MCLAUGHLIN, P. ; TSIMBERIDOU, A. M. ; MEDEIROS, L. J. ; SAMUELS, B. ; PATE, O. ; OHOLENDT, M. ; KANTARJIAN, H. ; BURGE, C. ; CABANILLAS, F.: Liposomal vincristine in relapsed non-Hodgkin’s lymphomas: Early results of an ongoing phase II trial. *Annals of Oncology* 11 (2000), 69–72
- [207] RODRIGUEZ, M. A. ; PYTLIK, R. ; KOZAK, T. ; CHANABHAI, M. ; GASCOYNE, R. ; LU, B. ; DEITCHER, S. ; WINTER, J. ; INVESTIGATORS, M.: Vincristine sulfate liposomes injection (Marqibo) in heavily pretreated patients with refractory aggressive non-Hodgkin lymphoma. *Cancer* 115 (2009), 3475–3482
- [208] KNEIDL, B. ; PELLER, M. ; WINTER, G. ; LINDNER, L. H. ; HOSSANN, M.: Thermosensitive liposomal drug delivery systems: State of the art review. *International Journal of Nanomedicine* 9 (2014), 4387–4398

- [209] MANZOOR, A. A. ; LINDNER, L. H. ; LANDON, C. D. ; PARK, J. Y. ; SIMNICK, A. J. ; DREHER, M. R. ; DAS, S. ; HANNA, G. ; PARK, W. ; CHILKOTI, A. ; KONING, G. A. ; TEN HAGEN, T. L. M. ; NEEDHAM, D. ; DEWHIRST, M. W.: Overcoming limitations in nanoparticle drug delivery: Triggered, intravascular release to improve drug penetration into tumors. *Cancer Research* 72 (2012), 5566–5575
- [210] SMET, M. D. ; HEIJMAN, E. ; LANGEREIS, S. ; HIJNEN, N. M. ; GRÜLL, H.: Magnetic resonance imaging of high intensity focused ultrasound mediated drug delivery from temperature-sensitive liposomes: An in vivo proof-of-concept study. *Journal of Controlled Release* 150 (2011), 102–110
- [211] NEGUSSIE, A. H. ; YARMOLENKO, P. S. ; PARTANEN, A. ; RANJAN, A. ; JACOBS, G. ; WOODS, D. ; BRYANT, H. ; THOMASSON, D. ; MARK, W. ; WOOD, B. J. ; DREHER, M. R. ; NEGUSSIE, A. H. ; YARMOLENKO, P. S. ; PARTANEN, A. ; RANJAN, A. ; JACOBS, G. ; WOODS, D. ; BRYANT, H. ; THOMASSON, D. ; DEWHIRST, M. W. ; NEGUSSIE, A. H. ; YARMOLENKO, P. S. ; PARTANEN, A. R. I. ; THOMASSON, D. ; DEWHIRST, M. W. ; WOOD, B. J.: Formulation and characterisation of magnetic resonance imageable thermally sensitive liposomes for use with magnetic resonance-guided high intensity focused ultrasound. *International Journal of Hyperthermia* 27 (2011), 140–155
- [212] LINDNER, L. H. ; EICHHORN, M. E. ; EIBL, H. ; TEICHERT, N. ; SCHMITT-SODY, M. ; ISSELS, R. D. ; DELLIAN, M.: Novel temperature-sensitive liposomes with prolonged circulation time. *Clinical Cancer Research* 10 (2004), 2168–2178
- [213] HOSSANN, M. ; WIGGENHORN, M. ; SCHWERDT, A. ; WACHHOLZ, K. ; TEICHERT, N. ; EIBL, H. ; ISSELS, R. D. ; LINDNER, L. H.: In vitro stability and content release properties of phosphatidylglyceroglycerol containing thermosensitive liposomes. *Biochimica et Biophysica Acta (BBA) - Biomembranes* 1768 (2007), 2491–2499
- [214] HOSSANN, M. ; SYUNYAEVA, Z. ; SCHMIDT, R. ; ZENGERLE, A. ; EIBL, H. ; ISSELS, R. D. ; LINDNER, L. H. ; HEALTH, E.: Proteins and cholesterol lipid vesicles are mediators of drug release from thermosensitive liposomes. *Journal of Controlled Release* 162 (2012), 400–406
- [215] LIMMER, S. ; HAHN, J. ; SCHMIDT, R. ; WACHHOLZ, K. ; ZENGERLE, A. ; LECHNER, K. ; EIBL, H. ; ISSELS, R. D. ; HOSSANN, M. ; LINDNER, L. H.: Gemcitabine treatment

- of rat soft tissue sarcoma with phosphatidylglycerol-based thermosensitive liposomes. *Pharmaceutical Research* 31 (2014), 2276–2286
- [216] ZIMMERMANN, K. ; HOSSANN, M. ; HIRSCHBERGER, J. ; TROEDSON, K. ; PELLER, M. ; SCHNEIDER, M. ; BRÜHSCHWEIN, A. ; MEYER-LINDENBERG, A. ; WESS G, WERGIN M, DÖRFELT R, KNÖSEL T, SCHWAIGER M, BAUMGARTNER C, BRANDL J, SCHWAMBERGER S, L. L.: A pilot trial of doxorubicin containing phosphatidylglycerol based thermosensitive liposomes in spontaneous feline soft tissue sarcoma. *International Journal of Hyperthermia* (2016)
- [217] JULIANO, R. L. ; BONTÉ, F.: Interactions of liposomes with serum proteins. *Chemistry and Physics of Lipids* 40 (1986), 359–372
- [218] GABER, M. H. ; HONG, K. ; HUANG, S. K. ; PAPAHAJIOPOULOS, D.: Thermosensitive sterically stabilized liposomes: Formulation and in vitro studies on mechanism of doxorubicin release by bovine serum and human plasma. *Pharmaceutical Research* 12 (1995), 1407–1416
- [219] HOSOKAWA, T. ; SAMI, M. ; KATO, Y. ; HAYAKAWA, E.: Alteration in the temperature-dependent content release property of thermosensitive liposomes in plasma. *Chemical & Pharmaceutical Bulletin* 51 (2003), 1227–1232
- [220] ALLEN, T. M. ; CLELAND, L. G.: Serum-induced leakage of liposome contents. *Biochimica et Biophysica Acta (BBA)* 597 (1980), 418–426
- [221] WEINSTEIN, J. N. ; YOSHIKAMI, S. ; HENKART, P. ; BLUMENTHAL, R. ; HAGIS, W. A.: Liposome-cell interaction: Transfer and intracellular release of a trapped fluorescent marker. *Science* 2 (1977), 489–492
- [222] BARBET, J. ; MACHY, P. ; TRUNEH, A. ; LESERMAN, L. E. E. D.: Weak acid-induced release of liposome-encapsulated carboxyfluorescein. *Biochimica et Biophysica Acta (BBA)* 772 (1984), 347–356
- [223] AUSBORN, M. ; SCHREIER, H. ; BREZESINSKI, G. ; FABIAN, H. ; MEYER, H. W. ; NUHN, P.: The protective effect of free and membrane-bound cryoprotectants during freezing and freeze-drying of liposomes. *Journal of Controlled Release* 30 (1994), 105–116

- [224] CROWE, J. H. ; CROWE, L. M.: Factors affecting the stability of dry liposomes. *Biochimica et Biophysica Acta (BBA)* 939 (1988), 327–34
- [225] WOLFRAM, J. ; SURI, K. ; YANG, Y. ; SHEN, J. ; CELIA, C. ; FRESTA, M. ; ZHAO, Y. ; SHEN, H. ; FERRARI, M.: Shrinkage of pegylated and non-pegylated liposomes in serum. *Colloids and Surfaces B: Biointerfaces* 114 (2004), 294–300
- [226] RAYNOR, A. ; JANTSCHKEFF, P. ; ROSS, T. ; SCHLESINGER, M. ; WILDE, M. ; HAASIS, S. ; DRECKMANN, T. ; BENDAS, G. ; MASSING, U.: Saturated and mono-unsaturated lysophosphatidylcholine metabolism in tumour cells: A potential therapeutic target for preventing metastases. *Lipids in Health and Disease* 14 (2015), 69–84
- [227] CARACCILO, G.: Liposome-protein corona in a physiological environment: Challenges and opportunities for targeted delivery of nanomedicines. *Nanomedicine* 11 (2015), 543–557
- [228] CAPRIOTTI, A. L. ; CARACCILO, G. ; CAVALIERE, C. ; FOGLIA, P. ; POZZI, D. ; SAMPERI, R. ; LAGANÀ, A.: Do plasma proteins distinguish between liposomes of varying charge density? *Journal of Proteomics* 75 (2012), 1924–1932
- [229] LUNDQVIST, M. ; STIGLER, J. ; ELIA, G. ; LYNCH, I. ; CEDERVALL, T. ; DAWSON, K.: Nanoparticle size and surface properties determine the protein corona with possible implications for biological impacts. *Proceedings of the National Academy of Sciences of the United States of America* 105 (2008), 14265–14270
- [230] KHANDELIA, H. ; IPSEN, J. H. ; MOURITSEN, O. G.: The impact of peptides on lipid membranes. *Biochimica et Biophysica Acta (BBA) - Biomembranes* 1778 (2008), 1528–1536
- [231] ZLATANOV, I. ; POPOVA, A.: Penetration of lysozyme and cytochrome C in lipid bilayer: Fluorescent study. *The Journal of Membrane Biology* 242 (2011), 95–103
- [232] SABÍN, J. ; PRIETO, G. ; RUSO, J. M. ; MESSINA, P. V. ; SALGADO, F. J. ; NOGUEIRA, M. ; COSTAS, M. ; SARMIENTO, F.: Interactions between DMPC liposomes and the serum blood proteins HSA and IgG. *The Journal of Physical Chemistry B* 113 (2009), 1655–1661

- [233] WOLFF, M. ; MITTAG, J. J. ; HERLING, T. W. ; GENST, E. D. ; DOBSON, C. M. ; KNOWLES, T. P. J. ; BRAUN, D. ; BUELL, A. K.: Quantitative thermophoretic study of disease-related protein aggregates. *Scientific Reports* 6 (2016), 22829
- [234] COHEN, S. I. A. ; LINSE, S. ; LUHESHI, L. M. ; HELLSTRAND, E. ; WHITE, D. a. ; RAJAH, L. ; OTZEN, D. E. ; VENDRUSCOLO, M. ; DOBSON, C. M. ; KNOWLES, T. P. J.: Proliferation of amyloid- β 42 aggregates occurs through a secondary nucleation mechanism. *Proceedings of the National Academy of Sciences of the United States of America* 110 (2013), 9758–9763
- [235] DAUER, W. ; PRZEDBORSKI, S.: Parkinson's disease: Mechanisms and models. *Neuron* 39 (2003), 889–909
- [236] BLENNOW, K. ; LEON, M. J. ; ZETTERBERG, H.: Alzheimer's disease. *Lancet* 368 (2006), 387–403
- [237] BATES, G. ; TABRIZI, S. ; JONES, L. ; BATES, G. ; TABRIZI, S. ; JONES, L.: *Huntington's disease*. 4th. Oxford Monographs on Medical Genetics, 2014. – 502 S
- [238] SUNDE, M. ; SERPELL, L. C. ; BARTLAM, M. ; FRASER, P. E. ; PEPYS, M. B. ; BLAKE, C. C.: Common core structure of amyloid fibrils by synchrotron X-ray diffraction. *Journal of Molecular Biology* 273 (1997), 729–739
- [239] AROSIO, P. ; KNOWLES, T. P. J. ; LINSE, S.: On the lag phase in amyloid fibril formation. *Physical Chemistry Chemical Physics* 17 (2015), 7606–7618
- [240] KNOWLES, T. P. J. ; VENDRUSCOLO, M. ; DOBSON, C. M.: The amyloid state and its association with protein misfolding diseases. *Nature Reviews Molecular Cell Biology* 15 (2014), 384–396
- [241] GILLAM, J. E. ; MACPHEE, C. E.: Modelling amyloid fibril formation kinetics: Mechanisms of nucleation and growth. *Journal of Physics: Condensed Matter* 25 (2013), 373101
- [242] WETZEL, R.: For protein misassembly, it's the "I" decade. *Cell* 86 (1996), 699–702
- [243] ROBERTS, C. J.: Non-native protein aggregation kinetics. *Biotechnology and Bioengineering* 98 (2007), 927–938

- [244] SACHSE, C.: Elektronenmikroskopie an Alzheimer-Fibrillen. *Bioforum* 32 (2009), 26–28
- [245] HELLSTRAND, E. ; BOLAND, B. ; WALSH, D. M. ; LINSE, S.: Amyloid β -protein aggregation produces highly reproducible kinetic data and occurs by a two-phase process. *ACS Chemical Neuroscience* 1 (2010), 13–18
- [246] WALSH, D. M. ; HARTLEY, D. M. ; KUSUMOTO, Y. ; FEZOU, Y. ; CONDRON, M. M. ; LOMAKIN, A. ; BENEDEK, G. B. ; SELKOE, D. J. ; TEPLow, D. B.: Amyloid β -protein fibrillogenesis: Structure and biological activity of protofibrillar intermediates. *Journal of Biological Chemistry* 272 (1999), 22364–22372
- [247] WETZEL, R. ; KHETERPAL, I.: *Amyloid, prions, and other protein aggregates*. 1st ed. Academic Press, 1999
- [248] COHEN, S. I. ; VENDRUSCOLO, M. ; DOBSON, C. M. ; KNOWLES, T. P.: From macroscopic measurements to microscopic mechanisms of protein aggregation. *Journal of Molecular Biology* 421 (2012), 160–171
- [249] MORRIS, A. M. ; WATZKY, M. a. ; FINKE, R. G.: Protein aggregation kinetics, mechanism, and curve-fitting: A review of the literature. *Biochimica et Biophysica Acta (BBA)* 1794 (2009), 375–397
- [250] ANDERSEN, C. B. ; YAGI, H. ; MANNO, M. ; MARTORANA, V. ; BAN, T. ; CHRISTIANSEN, G. ; OTZEN, D. E. ; GOTO, Y. ; RISCHER, C.: Branching in Amyloid Fibril Growth. *Biophysical Journal* 96 (2009), 1529–1536
- [251] BUELL, A. K. ; GALVAGNION, C. ; GASPAR, R. ; SPARR, E. ; VENDRUSCOLO, M. ; KNOWLES, T. P. J. ; LINSE, S. ; DOBSON, C. M.: Solution conditions determine the relative importance of nucleation and growth processes in α -synuclein aggregation. *Proceedings of the National Academy of Sciences of the United States of America* 111 (2014), 7671–7676
- [252] PRYOR, N. E. ; MOSS, M. a. ; HESTEKIN, C. N.: Unraveling the early events of amyloid- β protein ($A\beta$) aggregation: Techniques for the determination of $A\beta$ aggregate size. *International Journal of Molecular Sciences* 13 (2012), 3038–3072

- [253] NATH, S. ; MEUVIS, J. ; HENDRIX, J. ; CARL, S. a. ; ENGELBORGH, Y.: Early aggregation steps in alpha-synuclein as measured by FCS and FRET: Evidence for a contagious conformational change. *Biophysical Journal* 98 (2010), 1302–1311
- [254] CIZAS, P. ; BUDVYTYTE, R. ; MORKUNIENE, R. ; MOLDOVAN, R. ; BROCCIO, M. ; LÖSCHE, M. ; NIAURA, G. ; VALINCIUS, G. ; BORUTAITE, V.: Size-dependent neurotoxicity of beta-amyloid oligomers. *Archives of Biochemistry and Biophysics* 496 (2010), 84–92
- [255] CABALEIRO-LAGO, C. ; QUINLAN-PLUCK, F. ; LYNCH, I. ; DAWSON, K. A. ; LINSE, S.: Dual effect of amino modified polystyrene nanoparticles on amyloid β protein fibrillation. *ACS Chemical Neuroscience* 1 (2010), 279–287
- [256] GARAI, K. ; SAHOO, B. ; SENGUPTA, P. ; MAITI, S.: Quasihomogeneous nucleation of amyloid beta yields numerical bounds for the critical radius, the surface tension, and the free energy barrier for nucleus formation. *The Journal of Chemical Physics* 128 (2008), 045102 1–7
- [257] JAN, A. ; HARTLEY, D. M. ; LASHUEL, H.: Preparation and characterization of toxic Abeta aggregates for structural and functional studies in Alzheimer's disease research. *Nature Protocols* 5 (2010), 1186–209
- [258] FUNKE, S. A.: Detection of soluble amyloid- β oligomers and insoluble high-molecular-weight particles in CSF: Development of methods with potential for diagnosis and therapy monitoring of Alzheimer's disease. *International Journal of Alzheimer's Disease* 2011 (2011), 151645
- [259] SENGUPTA, P. ; GARAI, K. ; SAHOO, B.: The amyloid peptide (A 1-40) is thermodynamically soluble at physiological concentrations. *Biochemistry* (2003), 10506–10513
- [260] FÄNDRICH, M.: Oligomeric intermediates in amyloid formation: Structure determination and mechanisms of toxicity. *Journal of Molecular Biology* 421 (2012), 427–440
- [261] IACOPINI, S. ; PIAZZA, R.: Thermophoresis in protein solutions. *Europhysics Letters (EPL)* 63 (2007), 247–253

- [262] BLANCO, P. ; KRIEGS, H. ; LETTINGA, M. P. ; HOLMQVIST, P. ; WIEGAND, S.: Thermal diffusion of a stiff rod-like mutant Y21M fd-virus. *Biomacromolecules* 12 (2011), 1602–1609
- [263] HERLING, T. W. ; MÜLLER, T. ; RAJAH, L. ; SKEPPER, J. N. ; VENDRUSCOLO, M. ; KNOWLES, T. P. J.: Integration and characterization of solid wall electrodes in microfluidic devices fabricated in a single photolithography step. *Applied Physics Letters* 102 (2013), 1–5
- [264] LORENZEN, N. ; BUELL, A. K. ; KASPERSEN, J. D. ; AROSIO, P. ; VAD, B. S. ; PASLAWSKI, W. ; CHRISTIANSEN, G. ; VALNICKOVA-HANSEN, Z. ; ANDREASEN, M. ; ENGHILD, J. J. ; PEDERSEN, J. S. ; DOBSON, C. M. ; KNOWLES, T. P. J. ; OTZEN, D. E.: The role of stable α -synuclein oligomers in the molecular events underlying amyloid formation. *Journal of the American Chemical Society* 136 (2014), 3859–3868
- [265] BUELL, A. K. ; DHULESIA, A. ; WHITE, D. a. ; KNOWLES, T. P. J. ; DOBSON, C. M. ; WELLAND, M. E.: Detailed analysis of the energy barriers for amyloid fibril growth. *Angewandte Chemie - International Edition* (2012), 1–6
- [266] MÜLLER, B. K. ; ZAYCHIKOV, E. ; BRÄUCHLE, C. ; LAMB, D. C.: Pulsed interleaved excitation. *Biophysical Journal* 89 (2005), 3508–22
- [267] HENDRIX, J. ; SCHRIMPF, W. ; HÖLLER, M. ; LAMB, D. C.: Pulsed interleaved excitation fluctuation imaging. *Biophysical Journal* 105 (2013), 848–861